AN ENGINEERING APPROACH TO MODELLING THE IMPACT AND BALLISTIC RESPONSE OF LAMINATED COMPOSITE STRUCTURES

by

XIANGYANG QUAN

B.Sc., East China Institute of Technology, Nanjing, China, 1984
M.Sc., East China Institute of Technology, Nanjing, China, 1987

A THESIS SUBMITTED IN PARTIAL FULFILLMENT OF

THE REQUIREMENTS FOR THE DEGREE OF

DOCTOR OF PHILOSOPHY

in

THE FACULTY OF GRADUATE STUDIES

(Department of Civil Engineering)

We accept this thesis as confirming
to the required standard

THE UNIVERSITY OF BRITISH COLUMBIA

November 1998

In presenting this thesis in partial fulfilment of the requirements for an advanced degree at the University of British Columbia, I agree that the Library shall make it freely available for reference and study. I further agree that permission for extensive copying of this thesis for scholarly purposes may be granted by the head of my department or by his or her representatives. It is understood that copying or publication of this thesis for financial gain shall not be allowed without my written permission.

Department of Civil Engineering

The University of British Columbia
Vancouver, Canada

Date November 27, 1998

DE-6 (2/88)

Abstract

A super finite element program, SENACS, that was previously developed for transient non-linear analysis of isotropic structures, has been modified to handle the structural response of layered (laminated) composite materials. Both material and geometric non-linearities have been taken into account in the formulation. The structural analysis capabilities of the code have been demonstrated by successfully comparing the predictions with other experimental, analytical, and numerical results in the literature.

Impact problems have been subdivided into two groups: nonpenetrating and penetrating. In each case, appropriate contact laws are introduced to evaluate the local impact load on the structure while the structural analysis part of SENACS computes the target global response.

In nonpenetrating impact events, where there is only elastic indentation in the targets, the Hertzian contact law has been employed to establish the impact force as a function of the local indentation. Predictions of the nonpenetrating impact response of plain and stiffened laminated composite plate and shell structures have been found to be in good agreement with the experimental measurements previously reported in the literature.

Modelling of penetrating impact problems has been guided by experimental investigations. A phenomenological analytical model for static penetration of composite materials has been developed. In this model, three major penetration mechanisms have been accounted for: hole expansion, flexural deformation of a delaminated plate (split-plate), and transverse plugging.

The parameters of the model have been determined through material characterisation tests. The penetration model is introduced as a local contact behaviour in SENACS, and used to predict the penetrating impact response of composites to projectiles with different conical nose shapes. Ballistic impact response of two different material systems, IM7/8551-7 Carbon Fibre-Reinforced Polymer (CFRP) and S2-glass/phenolic resin Glass Fibre-Reinforced Polymer (GFRP) laminates provides the physical background and experimental verifications for the present model. Finally, a number of numerical ballistic simulations have been carried out to investigate the influence of structural shapes and sizes, loading conditions, projectile geometry, and impact velocity on the energy absorption capability of composite materials.

Table of Contents

List of Tables

List of Figures

Nomenclature

a	Length of a plain or stiffened cylindrical shell panel in the x axis
a_j	Outer radius of the j'th split in a split-plate (delaminated plate)
A	Mid-plane area of super shell and beam elements
$[A]$	In-plane stiffness matrix of a laminate
A_b	Cross-sectional area of a super beam element
A_p	Projected area of the projectile (indenter) in a target
A_{ij}	Anisotropic yielding and hardening parameters which describe the shape of the initial yield and subsequent hardening surface
$[B]$	Coupling (bending-stretching) matrix in the strain-displacement relationship of a laminate
$[B_c]$	Strain-displacement matrix for infinitesimal bending strain $z\{\kappa\}$
$[B_m]$	Strain-displacement matrix for infinitesimal membrane strain $\{\varepsilon^0\}$
$[B_x]$	Strain-displacement matrix for infinitesimal membrane strain of a straight super beam element
$[B_y]$	Strain-displacement matrix for infinitesimal membrane strain of a curved super beam element
b	Circumferential length of a plain or stiffened cylindrical shell panel in the y axis
b_0	Bluntness of a projectile (indenter) cone
b_j	Inner radius of the j'th split in a split-plate (delaminated plate)
$[C]$	Strain-displacement matrix of the von-Karman strains in a super shell element.
$[C_x]$	Strain-displacement matrix of the von-Karman strains of a straight super beam element

$[C_y]$	Strain-displacement matrix of the von-Karman strains of a curved super beam element
D	A reduction parameter for the hole expansion pressure
$\{D\}$	Assembled global equivalents of $\{d_e\}$ and $\{\bar{d}_e\}$
$[D]$	Bending stiffness matrix of a laminate
D_{dj}	Bending rigidity of the j'th split in a split-plate (delaminated plate)
$\{d_e\}$	Nodal displacement vector of a super shell element
$\{\bar{d}_e\}$	Nodal displacement vector of a super beam element
E	Elastic modulus of a laminate
E_{perf}	Perforation energy of a target
E_c	Energy dissipated in indenting a target
E_d	Energy dissipated in delamination
E_f	Maximum strain energy absorbed by a target
E_p	Energy dissipated in plugging of a target
E_r	Projectile residual (exit) kinetic energy
E_s	Projectile striking (impact) kinetic energy
e	Eccentricity of the beam centroidal axis from the mid-plane of a shell panel
F	Contact (impact) force
F_f	Friction force between the projectile (indenter) shaft and the target material
F_m	Maximum contact (impact) force
F_{pf}	Friction force between the plug and the rest of the target material
F_s	Force due to flexural deformation of a split-plate (delaminated plate)
F_{s0}	Penetration force when projectile (indenter) shaft reaches the frontal surface of the target ($\alpha = L_c$)

$\{F^c\}$	Assembled global equivalents of $\{f_e^c\}$.
$\{F^t\}$	Assembled global equivalents of $\{f_e^t\}$
$[F^{eff}]$	Effective load vector during the Newmark-β time integration
f	Total compliance of a split-plate (delaminated plate)
f_j	Compliance of the j'th split in a split-plate (delaminated plate)
$\{f_e^c\}$	Elemental contact (impact) force vector
$\{f_e^t\}$	External force vector of a super shell or beam element
G	Shear modulus
G_z	Transverse shear modulus of a single layer of the target
h	Thickness of a cylindrical shell panel
h_j	Distance in thickness direction between the j'th and $(j+1)$'th delaminations
I_{zz}	Moment of inertia about the z axis
J	Torsional constant
J_c	Polar moment of inertia about the centroid of a super beam element
$[K^{eff}]$	Effective stiffness matrix in Newmark-β time integration
$[K_T]$	Tangent stiffness matrix assembled from elemental stiffness matrix $[k_e]_T$ in a Newton-Raphson iterative scheme for non-linear problems
$[\overline{K}_{TB}]$	Stiffness matrix of a beam element due to the beam torsion and lateral bending effects
k	Stiffness coefficient of the Hertzian contact law
k_h	Spring stiffness due to hole expansion
k_p	Spring stiffness due to transverse plugging
k_s	Spring stiffness due to flexural deformation of a split-plate (delaminated plate)

k_y	Effective size of the yield surface
$[k_e]$	Elemental stiffness matrix of a super shell or beam element
$[k_e]_T$	Elemental tangent stiffness matrix in Newton-Raphson iterative scheme for non-linear problems
L_c	Length of projectile (indenter) conical head
L_{f1}	Maximum length in the target over which friction is operative.
L_{f2}	A length used to check the start of friction and perforation of the target
L_p	Projectile length
l	Length of a beam stiffener in a stiffened cylindrical shell panel
$[M]$	Assembled global equivalents of $[m_e]$
$\{M\}$	Bending moment resultant
$[\overline{M}_{TB}]$	Elemental mass matrix due to the effects of beam torsion and lateral bending for a super beam element
m	Projectile mass
$[m_e]$	Elemental consistent mass matrix of a super shell or beam element
N	Number of orthotropic layers in a laminated composite shell panel
N_0	Number of total time steps
$[N]$	Matrix of shape functions of a super shell element
$\{N\}$	Stress resultant
$[\overline{N}]$	Matrix of shape functions of a super beam element
n_s	Total number of splits in a split-plate (delaminated plate)
n	Time step number
$\{P\}$	Assembled global equivalents of $\{p_e\}$

$\{p_e\}$	Internal resistance force vector of a super shell or beam element
Q	Transverse shear force per unit length
$[Q_e]^k$	Matrix of elastic constitutive relation of the k'th layer in a laminate
$[Q_p]^k$	Matrix of plastic constitutive relation of the k'th layer in a laminate
$[Q_e^x]$	Matrix of elastic constitutive relation in the laminate co-ordinates
$[Q_p^x]$	Matrix of plastic constitutive relation in the laminate co-ordinates
$[Q_{ep}^x]$	Elasto-plastic constitutive matrix in the laminate co-ordinates
q	Exponent of Hertzian contact law during the unloading phase
R	Shell radius of curvature
R_1	Radius of curvature of a projectile head
R_2	Radius of curvature of a target
R_p	Radius of projectile (indenter) shaft
R_b	Radius of the curvature of a super beam element
$\{R^{err}\}$	Residual force vector in Newton-Raphson iterative scheme
S	Boundary surface area of super shell and beam elements
T	Kinetic energy due to the effects of beam torsion and lateral bending of a super beam element
$\{T\}$	Vector of applied boundary surface tractions
Tol	Tolerance of the solution
t_0	Thickness of one layer in a laminated composite shell panel (ply thickness)
t	Time
U	Strain energy of a beam element due to torsion, lateral bending, and warping for a super beam element

u	In-plane displacement of the mid-plane of a laminated shell panel in the x direction
$u_{,x}$	1st order derivative of u with respect to x
$u_{,y}$	In-plane rotation of axial displacement u to the y axis
$\{u\}$	Displacement vector of a super shell element
$\{\overline{u}\}$	Displacement vector of a super beam element
V	Volume of super shell and beam elements
V_{cr}	Ballistic limit of a target
V_n	Projectile velocity at time t_n
V_r	Projectile residual (exit) velocity from a target
V_s	Projectile striking (impact) velocity on a target
v	In-plane displacement of the mid-plane of a laminated shell panel in the y direction
$v_{,x}$	In-plane rotation of circumferential displacement v to the x axis
$v_{,y}$	1st order derivative of v with respect to y
w	Out-of-plane displacement of the mid-plane of a laminated shell panel or of the centroidal line of a beam stiffener in the z direction
w_0	Transverse deflection of a target at the impact site
w_s	Flexural deflection of a split-plate (delaminated plate) at the impact site
w_{s0}	Flexural deflection of a split-plate (delaminated plate) at the impact site when a projectile (or indenter) shaft reaches the frontal surface of a target
$w_{,x}$	Bending slope of transverse displacement w to the x axis
$w_{,xx}$	Curvature of a super shell element in the x axis
$w_{,y}$	Bending slope of transverse displacement w to the y axis
$w_{,yy}$	Curvature of a super shell element in the y axis

$w_{,xy}$	Bending twist of transverse displacement w
x	Longitudinal axis of curvilinear co-ordinate system for a cylindrical shell
y	Circumferential axis of curvilinear co-ordinate system for a cylindrical shell
z	Radial axis of curvilinear co-ordinate system for a cylindrical shell
α	Local indentation (or penetration depth) in a target
α_0	Penetration depth in a target when delamination or transverse plugging initiates
α_c	Constant in calculating permanent indentation by Chen and Sun (1985)
α_m	Maximum indentation in a target
α_p	Permanent indentation in a target
β	Constant in Newmark-β method
$2\beta_0$	Included cone angle of a projectile (indenter)
β_p	Constant in calculating permanent indentation by Chen and Sun (1985)
Δ	Projectile displacement
Δt	Time step
$\{\varepsilon\}$	Strain vector of a super shell element
$\{\bar{\varepsilon}\}$	Strain vector of a super beam element
$\{\varepsilon^0\}$	Strain vector on mid-plane of a super shell element
ε_x	Normal component of strain vector $\{\varepsilon\}$ in the x axis of a super shell element
$\bar{\varepsilon}_x$	Normal component of strain vector $\{\varepsilon\}$ in the x axis of a super beam element
ε_x^0	Normal component of strain vector $\{\varepsilon^0\}$ in the x axis of a super shell element
ε_y	Normal component of strain vector $\{\varepsilon\}$ in the y axis of a super shell element
ε_y^0	Normal component of strain vector $\{\varepsilon^0\}$ in the y axis of a super shell element

$\overline{\varepsilon}_y$	Normal component of strain vector $\{\varepsilon\}$ in the y axis of a super beam element
Γ	Warping constant
γ	Constant in Newmark-β method
γ_{xy}	Shear component of strain vector $\{\varepsilon\}$ of a super shell element
γ_{xy}^0	Shear component of strain vector $\{\varepsilon^0\}$ of a super shell element
$\{\kappa\}$	Curvature vector on the mid-plane of a super shell element
$_x$	Curvature of a super shell element in the x axis
$_y$	Curvature of a super shell element in the y axis
$_{xy}$	Bending twist of the transverse displacement w
μ	Coefficient of friction between a projectile (indenter) head and the local damage area of a target due to hole expansion
ν_z	Transverse Poisson's ratio of a single layer of a target
φ	Fibre orientation angle of one layer to the x axis in a laminated composite shell panel
$_0$	Angle of local deformed zone
θ	Rotation of the cross-section of a super beam element
$\theta_{,x}$	Slope of torsion angle θ to the x axis
$\theta_{,y}$	Slope of torsion angle θ to the y axis
ρ	Mass density
ρ_L	Mass density per unit length for a super beam element
$\{\sigma\}$	Stress vector
σ_0	Hole expansion pressure of a laminate
σ_i	Stress components of $\{\sigma\}$
σ_m	Mean indentation pressure of a laminate

σ_m'	Modified mean indentation pressure of a laminate
σ_Y	Yield stress of target material
τ	Transverse shear stress
ω	Natural circular frequency

Acknowledgement

I wish to express my greatest appreciation and thanks to my supervisors, Dr. R. Vaziri, and Dr. M.D. Olson, for their constant guidance and encouragement both technically and personally. I remember when I did the first presentation on the thesis proposal, how nervous I was and how the instructions from Dr. Vaziri helped me to make a good presentation. I also won't forget that in the first month I arrived at UBC from the other side of the Pacific Ocean, how the personal check from Dr. Olson helped me to overcome my financial difficulty in that month.

I would also like to thank my supervisory committee members, Dr. A. Poursartip, Dr. R.O. Foschi, and Dr. D.L. Anderson, for their precious time and helpful suggestions. Without the enlightenment on the physical nature of impact phenomenon and many good discussions with Dr. Poursartip, this work would not have been as successful.

The financial support provided by the Natural Sciences and Engineering Research Council of Canada and the Canadian Department of National Defence is also appreciated.

I also give my thanks to the people whose excellent work created the experimental data for this thesis: Mr. R. Bennett, Dr. D. Delfosse, Tim Sanders, Elvis Cepus, Dan Ursenbach, Mike Pierson, Walter Lau, Edward Fidler, and Etinne Lecomte. My thanks extend to all the current and previous members of the composites group for their help and friendship.

Finally, I would like to thank my wife, Ru Sun, and my son, Wei Quan, for their loving and understanding. I would also like to thank my parents for bringing me into this mysterious world full of unknowns for PhDs to write their theses on.

Chapter One: Introduction

1.1 Impact Events in Applications of Composite Materials

Laminated composite materials have been used extensively in many engineering applications as light-weight structures to provide high specific strength and stiffness. For example, the wings and fuselages in aeroplanes are made of composite materials in order to reduce their weight and increase load-carrying capability. However, during their service life these structures will likely encounter many kinds of impact loadings, such as dropped tools, flying birds, fired projectiles, and so forth.

Impact on composite structures by foreign objects will cause significant internal and external damages and both types of damage will reduce the structural strength and stiffness. For example, dropped tools will cause delaminations in composites which sometimes cannot be detected by visual inspection and thus may be neglected. If such structures are still in service and not repaired or replaced, the growth of damage will trigger the ultimate failure of the structures and cause financial and human loss. Fired projectiles with high kinetic energy will perforate the structure and lead to its ultimate failure. The projectiles with low kinetic energy may not perforate the structure but may still lead to some other forms of undesirable damage.

Therefore, it is necessary to study the initiation and development of damage in composite structures during foreign object impact and in doing so understand the manner in which they

absorb the impact energy, and finally to predict the structural behaviour of damaged composites to subsequent loading.

1.2 General Approaches to Impact Problems

There are three ways to approach impact problems. The first way is experimental investigation, where the structures are impacted by instrumented or free-flying projectiles. The loss of projectile kinetic energy and impact damage in the targets are measured during and after the projectile penetration. Simple empirical curves or equations are generated for the tested targets and projectiles. These empirical results are only accurate when they are applied to similar impact conditions and similar structures to those in the original tests. Their predictive capability are doubtful if the structure type, material type, geometric sizes of the targets, and projectile size and head shape are different from the original test conditions. Therefore, they have limited applications. Some empirical equations can be found in Zukas *et al.* (1982) and Backman and Goldsmith (1978).

The second way is analytical modelling. Based upon careful examinations of the initiation, development, and progression of impact damage in the structures during projectile penetration, the associated damage modes and penetration mechanisms are found from these impact tests. Then, analytical models for penetration problems are developed using these penetration mechanisms by applying mechanistic theories. This kind of modelling is the most versatile and effective way when evaluating the ballistic performance of a wide range of projectiles and targets, because the damage mechanisms used in the models allow for many

impact and structural parameters to be considered. However, the validity of the analysis is highly dependent on the reliability of original assumptions, or the appropriateness of penetration mechanisms used in the models.

The third approach is numerical modelling. Finite element or finite difference analyses are applied to penetration problems. The impact response, and damage initiation and growth in structures are calculated using computer codes. This kind of modelling provides detailed stress and strain distributions in the structures and thus provides more information than experimental investigation and analytical modelling. However, they are dependent on reliable constitutive models that are often difficult to formulate and calculate.

In the present approach, the above three methods are combined together in the way which the advantages of each method are used to complement the disadvantages of another method or methods. The objective is to arrive at efficient ways of analysing impact behaviour of composite structures. At first, impact tests are conducted by Delfosse (1994b) and Sanders (1997) to identify the damage modes and penetration mechanisms in the composite targets during projectile penetration, where projectiles are assumed to be rigid so that they do not deform throughout the whole penetration process. Due to the ease with which one can run tests statically, static penetration tests on the same kind of targets are also performed by Delfosse (1994b) and Sanders (1997) to discover the initiation, evolution, and progression of damage in the targets.

Then, penetration mechanisms and damage modes are proposed based upon these experimental studies to model the initiation and growth of impact damage in the structures.

Material characterisation tests are also conducted to obtain the required empirical parameters. Finally, the analytical model is developed and implemented into the finite element program developed in Chapter Two and Three, which can take into account the different structural shapes, boundary conditions, sizes, and material properties.

1.3 Objectives and Scope of the Present Research

There are two kinds of targets in impact problems: semi-infinite and finite thickness targets (Zukas *et al.*, 1982). In finite thickness targets, the distal surface of the targets have significant effects on the penetration mechanisms and damage modes, which leads to a more complicated problem and for which it is difficult to find closed-form solutions (Corbett *et al.*, 1996). However, finite thickness targets are of far greater practical interest and therefore are studied in the present work.

The objective of this thesis is to develop an efficient approach to modelling the impact of laminated composite plates and cylindrical shells. In this approach, the local damages due to projectile penetration in the impacted structures are modelled by simple analytical methods, while the finite element modelling takes into account the variations in structural dimensions, geometric and boundary conditions. The whole thesis is presented in eight chapters and five appendices.

The finite element formulation, time integration method, and Newton-Raphson iterative scheme for non-linear problems in numerical modelling are presented in the second chapter. The numerical verifications and applications of the associated computer code in calculating

the non-linear structural response of composite plates and cylindrical shells are presented in Appendix C.

The Hertzian contact law and the iterative scheme used for solution of nonpenetrating impact problems for laminated composite structures are discussed in Chapter Three. The present approach is verified by comparing the predicted results with available experimental measurements, analytical solutions, and other finite element results in the literature. The prediction of nonpenetrating impact response of stiffened laminated composite plates and shells is also presented there and parametric studies are performed for stiffened structures.

A literature review on penetration mechanisms and models is presented in Chapter Four. Then guided by experimental observations, a penetration model for laminated composite materials is presented in the fifth and sixth chapters. In addition to predicting the energy absorption in impacted composite structures, this model is aimed at capturing the essence of damage patterns in composites during projectile penetration and considers the transitions of penetration mechanisms with different head shapes and sizes of projectiles and different target thicknesses. Two different material systems, IM7/8551-7 Carbon Fibre-Reinforced Polymer (CFRP) and S2-glass/phenolic resin Glass Fibre-Reinforced Polymer (GFRP) laminates, are studied and provide the experimental verifications for the present model.

In Chapter Seven, the penetration model developed in Chapter Six is implemented into the finite element code. The dynamic penetration study on IM7/8551-7 CFRP and S2-glass/resin GFRP laminates is presented in this chapter. The energy absorption and penetration force histories of different laminated composites under different impact conditions, geometric sizes

of targets, and geometric shapes of projectiles are calculated using this code and compared with the experimental measurements.

The analytical and numerical studies in the present thesis are summarised in Chapter Eight. The major achievements and contributions are highlighted along with the weaknesses of the present approach. A proposal for future improvement of the present model is finally presented.

Chapter Two: Super Finite Element Formulation

2.1 Introduction

Finite element method (FEM) has proved to be an effective numerical tool for solving structural problems over the last few decades. However, in order to model real engineering structures traditional FEM generally requires many elements with a huge amount of data preparation and computing time, thus rendering the analysis impractical for preliminary engineering design.

To improve this situation, super finite elements (SFE) have been introduced in the conventional finite element formulation, *e.g.* Olson (1991) and Koko *et al.* (1991a) among others. Through the use of SFE, engineering design accuracy can be achieved by only a few elements. The inherent accuracy arises from the displacement functions adopted for these elements. These displacement functions are typically polynomial functions that are selected from the basic analytical solutions to provide a good approximation of the linear and non-linear deformation modes that may occur in beam, plain and stiffened plate and cylindrical shell structures.

Super finite elements have been applied to isotropic materials for non-linear structural analysis in Koko *et al.* (1991 a-b), Koko *et al.* (1992), and Jiang *et al.* (1993). Recently, failure and post-failure models have been proposed for plain and stiffened plates by incorporating interactive failure criteria in SFE analyses in Rudrapatna *et al.* (1996).

In the present study, the super finite element method developed previously is extended to take into account the structural response of orthotropic laminated composite materials. This code, called SENACS, will be used as a test bed for all the theoretical developments discussed in this thesis.

2.2 Finite Element Equations

Formulating finite element equations for super elements follows the same procedure as in conventional FEM for the purposes of this study.

Laminated composite plates and cylindrical shells are assumed to be thin and in the case of stiffened structures the beam stiffeners are considered to be slender so that the effect of transverse shear deformation is negligible. The von-Karman assumptions for strains are employed to take account of the effect of large deflections in the structures.

When ductile materials, such as metals, are used as the matrix material in composites, the plasticity effects in the matrix cannot be ignored in formulating the finite element equations. Due to anisotropy of composite materials, the elasto-plastic constitutive relations with anisotropic hardening rule (Vaziri *et al.*, 1992) has been applied instead of the conventional rule of isotropic hardening.

2.2.1 Strain-Displacement Relations

A stiffened laminated composite cylindrical shell panel as shown schematically in Figure 2.1 is stiffened by a set of orthogonally placed beams, which can be attached from above or

below the panel. The beams are usually placed along the axial and circumferential directions of the shell.

Consider an isolated panel bay with two adjacent stiffeners (one straight and one curved) shown in Figure 2.2. The local curvilinear co-ordinate system (x, y, z) is attached to the mid-surface of the shell panel. For simplicity, it is also assumed in a shell and beam element that the local x-axis is always parallel to the shell axis, while the y and z axes are defined in the circumferential and radial directions, respectively. Figure 2.3 shows the nodal configuration of super elements.

The shell panel with thickness h is composed of N orthotropic layers with their reinforced directions oriented at different angles φ to the laminate co-ordinate x as shown in Figure 2.4. In the laminated panels, it is assumed that all the layers are perfectly bonded together and each layer is of uniform thickness (ply thickness) t_0. Thus the strains are continuous through the shell thickness, including the interfaces between each layer. For linear-elastic materials, this assumption will allow us to replace a laminated panel with an equivalent single layer whose material properties are averaged over the thickness (see section 2.2.2). Thus this will simplify the analysis and still give good results in modelling the global response of the laminated panel.

In practical structural design, a laminate is attached to the shell panel as beam stiffeners on its lateral surface as shown in Figure 2.5 (Dost *et al.*, 1991). Therefore, a layered approach is not suitable for formulating finite element equations of beam elements. The beam stiffeners will be treated as isotropic materials. Their elastic modulus and Poisson's ratio are calculated from lamination theory.

2.2.1.1 Element Displacement Fields

The displacement fields within a super shell element can be written as

$$\{u\} = \begin{Bmatrix} u \\ v \\ w \end{Bmatrix} = [N]\{d_e\} \tag{2.1}$$

where u, v are the in-plane and w is the out-of-plane displacements of the mid-plane of a laminated shell panel in the x, y, and z directions, respectively; $[N]$ is the matrix of shape functions with details shown in Appendix A; $\{d_e\}$ is the elemental nodal displacement vector which has 59 components as shown in Table 2.1, where $u_{,y}$ and $v_{,x}$ are the in-plane rotations, $w_{,x}$ and $w_{,y}$ are the bending slopes, and $w_{,xy}$ is the twist.

The displacement fields within a straight super beam element can be written as

$$\{\bar{u}\} = \begin{Bmatrix} u \\ w \\ v \\ \theta \end{Bmatrix} = [\bar{N}]\{\bar{d}_e\} \tag{2.2}$$

where u, w, and v represent the axial, vertical bending (in z direction), and lateral bending (in y direction) displacements, respectively; and θ is the rotation of the cross-section. The beam shape function matrix $[\bar{N}]$ is also shown in Appendix A. The total number of beam nodal displacement components in $\{\bar{d}_e\}$ is 19 and shown in Table 2.2, where $\theta_{,x}$ and $\theta_{,y}$ are slopes of the torsion angle, which denote the rates of twist. The element formulation of a curved super beam element can be obtained by a proper transformation of coordinates.

2.2.1.2 Strain-Displacement Relations For Super Shell Elements

The strain-displacement relations employed in the present formulation are based upon Love and Timoshenko's shell theory:

$$\begin{aligned}
\varepsilon_x &= u_{,x} - zw_{,xx} + \frac{(w_{,x})^2}{2} \\
\varepsilon_y &= v_{,y} + \frac{w}{R} - z(w_{,yy} - \frac{v_{,y}}{R}) + \frac{(w_{,y})^2}{2} \\
\gamma_{xy} &= u_{,y} + v_{,x} - 2z(w_{,xy} - \frac{v_{,x}}{R}) + w_{,x}w_{,y}
\end{aligned} \tag{2.3}$$

where R is the shell radius of curvature and z is the radial co-ordinate measured from the mid-plane of the shell.

In terms of the mid-plane strains $\{\varepsilon^0\}$ and curvatures $\{\kappa\}$, we can write Equation (2.3) as follows

$$\{\varepsilon\} = \begin{Bmatrix} \varepsilon_x \\ \varepsilon_y \\ \gamma_{xy} \end{Bmatrix} = \{\varepsilon^0\} + z\{\kappa\} \tag{2.4}$$

where

$$\{\varepsilon^0\} = \begin{Bmatrix} \varepsilon_x^0 \\ \varepsilon_y^0 \\ \gamma_{xy}^0 \end{Bmatrix} = \begin{Bmatrix} u_{,x} + \frac{(w_{,x})^2}{2} \\ v_{,y} + \frac{w}{R} + \frac{(w_{,y})^2}{2} \\ u_{,y} + v_{,x} + w_{,x}w_{,y} \end{Bmatrix} \tag{2.5a}$$

$$\{\kappa\} = \begin{Bmatrix} \kappa_x \\ \kappa_y \\ \kappa_{xy} \end{Bmatrix} = \begin{Bmatrix} -w_{,xx} \\ \frac{v_{,y}}{R} - w_{,yy} \\ \frac{2v_{,x}}{R} - 2w_{,xy} \end{Bmatrix} \tag{2.5b}$$

After Equation (2.1) is substituted into Equation (2.4), the relations between strains $\{\varepsilon\}$ and nodal displacement $\{d_e\}$ will be in the form of

$$\{\varepsilon\} = \left([B_m] + \frac{1}{2}[C] + z[B_c] \right) \{d_e\} \tag{2.6}$$

where $[B_m]$ and $[B_c]$ denote strain-displacement matrices for infinitesimal membrane and bending strains, respectively; and strain-displacement matrix $[C]$ denotes the von-Karman components.

2.2.1.3 Strain-Displacement Relations for Super Beam Elements

The strain-displacement relations for super beam elements are based upon Bernoulli-Euler's beam theory. For example, for a straight beam in the x-direction,

$$\bar{\varepsilon}_x = u_{,x} - z w_{,xx} + \frac{(w_{,x})^2}{2} \tag{2.7}$$

and for a curved beam in the y-direction,

$$\bar{\varepsilon}_y = v_{,y} + \frac{w}{R_b} - z(w_{,yy} - \frac{v_{,y}}{R_b}) + \frac{(w_{,y})^2}{2} \tag{2.8}$$

In Equation (2.8), $R_b = R - e$ is the radius of the curvature of the beam element with e representing the eccentricity of the beam centroidal axis from the mid-plane of the shell panel. Also, overbar denotes quantities associated with the beam.

After Equation (2.2) is substituted into Equation (2.7) and (2.8), the relations between strains $\{\bar{\varepsilon}\}$ and nodal displacement $\{\bar{d}_e\}$ will be written in the form of

$$\bar{\varepsilon}_x = \left([\bar{B}_x] + [\bar{C}_x]\right)\{\bar{d}_e\} \tag{2.9}$$

$$\bar{\varepsilon}_y = \left([\bar{B}_y] + [\bar{C}_y]\right)\{\bar{d}_e\} \tag{2.10}$$

Details of the matrices of strain-displacement relations $[\bar{B}_x]$, $[\bar{B}_y]$, $[\bar{C}_x]$, and $[\bar{C}_y]$ for beam elements are shown in Jiang *et al.* (1993).

The geometric compatibility is applied to satisfy the displacement continuity on the interface between the shell panel and beam stiffener (Jiang *et al.*, 1993).

2.2.2 Constitutive Relations

The stress and bending moment resultants $\{N\}$ and $\{M\}$ can be written in terms of the stress vector $\{\sigma\}$ as

$$\{N\} = \int_{-h/2}^{h/2} \{\sigma\} dz = \sum_{k=1}^{N} \int_{z_k}^{z_{k+1}} \{\sigma\}^k dz \tag{2.11}$$

$$\{M\} = \int_{-h/2}^{h/2} \{\sigma\} z dz = \sum_{k=1}^{N} \int_{z_k}^{z_{k+1}} \{\sigma\}^k z dz \tag{2.12}$$

There are two ways to evaluate the integrations in the above equations. One method is to calculate the stress components in each layer and then integrate them through the thickness of that layer. The other method, is used for linear-elastic material behaviour, to express the stresses in terms of the displacements where the integral before the displacement vector can be integrated through the laminate thickness in the first step and then saved for the subsequent steps.

In the analysis of elasto-plastic materials, the material constitutive relations vary with the stress state. The first method is necessary in order to capture the plastic stress components in each layers through the thickness. For linear-elastic materials, where the material constitutive relations are constant in the analysis, the second method will improve the computing efficiency and save the CPU time in integrations through the shell thickness.

Therefore a linear-elastic material, whether it involves small deflection or large deflection analysis, the stress and moment resultants $\{N\}$ and $\{M\}$ will be written in the following form

$$\begin{Bmatrix} N \\ M \end{Bmatrix} = \begin{bmatrix} [A] & [B] \\ [B] & [D] \end{bmatrix} \begin{Bmatrix} \varepsilon^0 \\ \kappa \end{Bmatrix} \tag{2.13}$$

where $[A]$, $[B]$, and $[D]$ are the usual in-plane, coupling (bending-stretching) and bending stiffness matrices of the laminate [*e.g.*, Ochoa *et al.* (1992) and Whitney (1987)].

For elasto-plastic materials, the yield function for anisotropic yielding and hardening under plane stress conditions can be written as

$$f(\sigma_i, A_{ij}, k_y) = A_{ij}\sigma_i\sigma_j - k_y^2 = 0 \tag{2.14}$$

where A_{ij} denotes the anisotropic yielding and hardening parameters which describe the shape of the yield surface, σ_i denotes the stress components, and k_y is the effective size of the yield surface. Both k_y and A_{ij} are updated with the stress state σ_i as plasticity progresses. The subscripts i, j in Equation (2.14) are numbered as 1, 2, and 6, referring to the three in-plane stress components in the principal material directions.

The mathematical derivation from yield criterion and hardening rule to stress-strain relationship was shown in Vaziri *et al.* (1992) and has been briefly summarised in Appendix B. Thus, the incremental stress-strain relationship in the k-th layer of the laminate can be written as

$$d\{\sigma\}^k = ([Q_e]^k - [Q_p]^k) d\{\varepsilon\}^k \tag{2.15}$$

where $[Q_e]^k$ and $[Q_p]^k$ are matrices of elastic and plastic constitutive relations, respectively; and $\{\varepsilon\}^k$ is the strain tensor in the principal material directions of the shell panel. The details of matrices $[Q_e]^k$ and $[Q_p]^k$ are given in Appendix B.

2.2.3 Virtual Work Principle

Neglecting structural damping, the principle of virtual work for super elements can be written as

$$\int_V \{\delta u\}^T \rho \{\ddot{u}\} dV + \int_A \left[\{\delta \varepsilon^0\}^T \{N\} + \{\delta \kappa\}^T \{M\} \right] dA = \int_S \{\delta u\}^T \{T\} dS \tag{2.16}$$

where ρ is the mass density; V, A, and S are, respectively, the volume, mid-plane area, and the boundary surface area of the shell and beam elements; $\{T\}$ is the vector of applied

boundary surface tractions; overdots denote differentiation with respect to time; and δ denotes a virtual change in the quantity to which it is attached.

Substituting the strain-displacement relations [Equations (2.6), (2.9), and (2.10)] into Equation (2.16), and noting that the virtual changes in the nodal displacements $\{\delta d_e\}$ are arbitrary, the following set of discretized equations of motion for a single element can be obtained:

$$[m_e]\{\ddot{d}_e\}+\{p_e\}=\{f_e^t\} \tag{2.17}$$

where $[m_e]$, $\{p_e\}$, and $\{f_e^t\}$ are the elemental consistent mass matrix, internal resistance force vector, and external force vector, respectively.

The elemental tangent stiffness matrix can be determined as the derivative of the internal force with respect to the nodal displacements. For linear-elastic materials and a shell element, it is

$$[k_e]_T=\frac{\partial\{p_e\}}{\partial\{d_e\}}=\frac{\partial\int_A(\{\varepsilon^0\}^T\{N\}+\{\kappa\}^T\{M\})dA}{\partial\{d_e\}} \tag{2.18a}$$

After substituting Equations (2.5a), (2.5b), and (2.13) into (2.18a), the stiffness matrix can be written as

$$[k_e]_T=\int_A([B_m]^T[A][B_m]+[B_m]^T[B][B_c]+[B_c]^T[B][B_m]$$

$$+[B_c]^T[D][B_c])dA+\int_A([B_m]^T[A][C]+[C]^T[A][B_m]+ \tag{2.18b}$$

$$[C]^T[A][C]+[B_c]^T[B][C]+[C]^T[B][B_c])dA$$

where the first integration on the right-hand side of the above equation is the linear part of the tangent stiffness matrix while the second integration is its non-linear part taking account of large deflections. For elasto-plastic materials, it is

$$[k_e]_T = \frac{\partial\{p_e\}}{\partial\{d_e\}} = \int_V \{([B_m]+z[B_c]+[C])^T[Q_{ep}^x]([B_m]+z[B_c]+[C])$$

$$+\frac{\partial[C]^T}{\partial\{\delta\}}\{\sigma\}\}dV \tag{2.19}$$

where $[Q_{ep}^x]$ is the elasto-plastic constitutive matrix in the laminate co-ordinates ($[Q_{ep}^x]=[Q_e^x]-[Q_p^x]$).

Adding the element contributions in the usual manner, the discretized equations of motion for the shell structure can be written as

$$[M]\{\ddot{D}\}+\{P\}=\{F^t\} \tag{2.20}$$

where $[M]$, $[D]$, $\{P\}$, and $\{F^t\}$ are the assembled global equivalents of $[m_e]$, $[d_e]$, $\{p_e\}$, and $\{f_e^t\}$.

For a super beam element, elemental mass and stiffness matrices are calculated first on an element basis in the same way as a shell element and then added into the global mass and stiffness matrices. The virtual work principle shown above in Equation (2.16) is based solely on beam bending theory so that the effects of beam torsion and lateral bending have not yet

been taken into account. In order to consider these effects, the formulation of mass and stiffness matrices developed in Jiang *et al.* (1993) is used in the present analysis.

Considering a beam element vibrating at a circular frequency ω, when the effect of rotary inertia is ignored, the kinetic energy due to the effects of beam torsion and lateral bending can be written as

$$T = \frac{1}{2}\omega^2 \rho_L \int_0^l (A_b v^2 + J_c \theta^2) dx \tag{2.21}$$

where ρ_L is the mass density per unit length, A_b is the cross-sectional area, J_c is the polar moment of inertia about the centroid, and l is the length of the beam. Using Equation (2.2), the matrix form of Equation (2.21) can be written as

$$T = \frac{1}{2}\omega^2 \{\bar{d}_e\}^T [\bar{M}_{TB}] \{\bar{d}_e\} \tag{2.22}$$

Thus the total beam mass matrix is obtained by combining $[\bar{M}_{TB}]$ with elemental mass matrix due to beam bending and adding them together into the global mass matrix.

The strain energy of a beam element due to torsion, lateral bending, and warping for a straight beam element in the x-direction, is calculated from

$$U = \frac{1}{2} GJ \int_0^l (\frac{d\theta}{dx})^2 dx + \frac{1}{2} EI_{zz} \int_0^l (\frac{d^2 v}{dx^2})^2 dx + \frac{1}{2} E\Gamma \int_0^l (\frac{d^2 \theta}{dx^2})^2 dx \tag{2.23}$$

while for a curved beam element it is

$$U = \frac{1}{2} GJ \int_0^l (\frac{d\theta}{dx} + \frac{1}{R_b}\frac{dv}{dx})^2 dx + \frac{1}{2} EI_{zz} \int_0^l (\frac{\theta}{R_b} - \frac{d^2 v}{dx^2})^2 dx$$

$$+\frac{1}{2}E\Gamma\int_0^l\left(\frac{d^2\theta}{dx^2}+\frac{1}{R_b}\frac{d^2v}{dx^2}\right)^2 dx \tag{2.24}$$

where G, E are, respectively, the shear and elastic moduli; J is the torsional constant; I_{zz} is the moment of inertia about the z axis; and Γ is the warping constant. After Equation (2.2) is applied, the matrix form of equation (2.23) and (2.24) will become

$$U=\frac{1}{2}\{\bar{d}_e\}^T[\bar{K}_{TB}]\{\bar{d}_e\} \tag{2.25}$$

where $[\bar{K}_{TB}]$ is the stiffness matrix of a beam element due to the beam torsion and lateral bending effects and will be assembled in the same way as the beam mass matrix.

2.3 Solution Scheme

The Gauss integration method is used to evaluate the mass and stiffness matrices and all the consistent force vectors. A 5×5 Gauss integration rule is applied to the mid-plane of the shell element and a minimum of one Gauss point per layer is used for integrations through the thickness of the laminate for elasto-plastic analysis. The Gauss integration rule for a beam element is 5×1 where 5 Gauss integration points are placed along the beam axis. The number of Gauss integration points through the beam thickness depends on the cross-sectional shape of beams as shown in Jiang *et al.* (1993).

Because the number of layers making up a laminate panel may be very large, it is necessary to use different number of Gauss integration points through the thickness of each layer for

elasto-plastic problems to improve the computational efficiency. The Gauss integration rule used in the present formulation and computer program SENACS, is shown in Table 2.3.

2.3.1 Time Integration Method

The general Newmark-β method is used to integrate the global equations of motion [Equation (2.20)] in the time domain. Accordingly, the generalised nodal velocity and displacement vectors at time $t_{n+1} = t_n + \Delta t$ can be written as

$$\begin{aligned} \{\dot{D}\}_{n+1} &= \{\dot{D}\}_n + \Delta t[(1-\gamma)\{\ddot{D}\}_n + \gamma\{\ddot{D}\}_{n+1}] \\ \{D\}_{n+1} &= \{D\}_n + \Delta t\{\dot{D}\}_n + \frac{(\Delta t)^2}{2}[(1-2\beta)\{\ddot{D}\}_n + 2\beta\{\ddot{D}\}_{n+1}] \end{aligned} \tag{2.26}$$

where Δt is the integration time step, and the subscripts n and n+1 denote quantities evaluated at time t_n and t_{n+1}, respectively. When $\beta = 0.25$ and $\gamma = 0.5$, Equation (2.26) will be degenerated to the case which has no artificial damping. When $\gamma > 0.5$, artificial damping will be introduced to filter out the high-frequency vibrations in the structure. The high-frequency dissipation will be maximised for $\gamma > 0.5$ when β is taken to be related to γ as [Cook *et al.* (1989)]

$$\beta = \frac{1}{4}(\gamma + 0.5)^2 \tag{2.27}$$

For any values of β and γ satisfying $2\beta \geq \gamma \geq 0.5$, the solution of Equation (2.20) will be unconditionally stable when its velocity and acceleration are expressed as in Equation (2.26). It should also be noted that for a structure which has a maximum natural frequency ω_{max}, the

time step Δt chosen in the analysis should satisfy the convergence criterion in Newmark (1959) as follows

$$\Delta t < \frac{1}{\omega_{\max}\sqrt{\beta}} \tag{2.28}$$

2.3.2 Newton-Raphson Iteration Scheme

The non-linearities arising from the combination of large deflections and plasticity lead to a set of non-linear algebraic equations that need to be solved at each time or loading step using an iterative scheme. In the current formulation, the equation of motion [Equation (2.20)] at time t_{n+1} is solved by forming an effective static problem which is then solved using a Newton-Raphson solution procedure. Thus, solution of the following equation is sought

$$\left[K^{eff}\right]_n \{\Delta D\}_{n+1} = \{F^{eff}\}_{n+1} \tag{2.29}$$

where

$$\begin{aligned} &\{\Delta D\}_{n+1} = \{D\}_{n+1} - \{D\}_n, \\ &\left[K^{eff}\right]_n = \frac{1}{\beta \Delta t^2}[M] + [K_T]_n, \\ &\{F^{eff}\}_{n+1} = \{F^t\}_{n+1} - \{P\}_n + [M]\left(\frac{1}{\beta \Delta t}\{\dot{D}\}_n + \frac{1-2\beta}{2\beta}\{\ddot{D}\}_n\right). \end{aligned} \tag{2.30}$$

In Equation (2.30), $[K_T]$ is the tangent stiffness matrix resulting from the non-linear strain-displacement or stress-strain relations, and can be assembled from elemental stiffness matrix $[k_e]_T$. For linear-elastic and small deflection analysis, $[K_T]$ will remain a constant throughout the solution process.

The residual force vector in the structure is calculated as

$$\{R^{err}\} = \{F^t\} - [M]\{\ddot{D}\} - \{P\} \tag{2.31}$$

at each iteration within the time or loading step. When the required tolerance *Tol* given by

$$Tol = \frac{\|R^{err}\|}{\|F^t\|} \tag{2.32}$$

is reached at an iteration, the iteration will end and then the analysis proceeds to the next step. In the present study $Tol = 0.01$.

The tangent stiffness matrix for large deflection and/or elasto-plastic analysis can be updated in each iteration or just the first iteration of a given time or loading step. If the non-linearity in the problem is not very severe, $[K_T]$ is suggested to be updated only in the first iteration of each time step and maintained constant for each subsequent iterations to maintain computational efficiency.

2.4 Summary

A computer program, SENACS (Super Elements for Non-linear Analysis of Cylindrical Shells-Version for Composite Materials), has been written based upon the above finite element formulations using FORTRAN language. Figure 2.6 shows the flow chart of the program.

The structural geometry, element mesh, boundary conditions, material properties, and external load condition are inputted first. Because only a few elements are needed to model

the problem, it is very easy to generate the input of nodal and element data to the program without any pre-processor.

After initialising all the arrays and parameters used in the analysis, the program starts the loops for time or load steps and iterations. The elemental mass (only for eigenvalue and transient problems) and stiffness matrices, as well as force vector are generated first and then assembled into the global mass matrix, stiffness matrix, and force vector. The effective stiffness matrix and load vector are calculated if a transient analysis is required. The solutions are attained by solving the finite element equations. If the solutions satisfy the required convergence tolerance, the iteration loop ends and the final solutions are written into pre-assigned files. Otherwise, more iterations are performed until the solution converges. After all the required time or load steps are looped over, the program stops.

The numerical verifications of SENACS have been conducted by comparing the predicted results with available experimental, analytical, and numerical results. The comparisons show good agreement [see Appendix C] and thus verify the program. This instils confidence in using the program SENACS for linear and non-linear static and transient structural analysis of laminated composite plates and shells. In the next chapter, details of adding impact analysis capability to SENACS will be presented.

Table 2.1 Nodal degrees of freedom for a super shell element (Jiang *et al.*, 1993).

Node Number	Degrees of Freedom
1	$u_1, v_1, w_1, u_{,y1}, v_{,x1}, w_{,x1}, w_{,y1}, w_{,xy1}$
2	$u_2, v_2, w_2, u_{,y2}, v_{,x2}, w_{,x2}, w_{,y2}, w_{,xy2}$
3	$u_3, v_3, w_3, u_{,y3}, v_{,x3}, w_{,x3}, w_{,y3}, w_{,xy3}$
4	$u_4, v_4, w_4, u_{,y4}, v_{,x4}, w_{,x4}, w_{,y4}, w_{,xy4}$
5	$u_5, w_5, w_{,y5}, u_8, u_{11}$
6	$v_5, w_6, w_{,x6}, v_9, v_{12}$
7	$u_6, w_7, w_{,y7}, u_9, u_{12}$
8	$v_6, w_8, w_{,x8}, v_8, v_{11}$
9	$u_7, v_7, w_9, u_{10}, v_{10}, u_{13}, v_{13}$

Table 2.2 Nodal degrees of freedom for a super beam element (Jiang *et al.*, 1993).

Type	Direction	Node Number	Degrees of Freedom
straight	x	1	$u_1, v_1, w_1, v_{,x1}, w_{,x1}, \theta_1, \theta_{,x1}$
		2	$u_2, v_2, w_2, v_{,x2}, w_{,x2}, \theta_2, \theta_{,x2}$
		3	$u_3, w_3, \theta_3, u_4, u_5$
curved	y	1	$v_1, u_1, w_1, u_{,y1}, w_{,y1}, \theta_1, \theta_{,y1}$
		2	$v_2, u_2, w_2, u_{,y2}, w_{,y2}, \theta_2, \theta_{,y2}$
		3	$v_3, w_3, \theta_3, v_4, v_5$

Table 2.3 Gauss integration rule used in SENACS for a super shell element.

Axial	Circumferential	Through the thickness of each layer		
		Linear Elastic	Elasto-Plastic	No. of Layers
5	5	none	4	1
5	5	none	2	2-10
5	5	none	1	>10

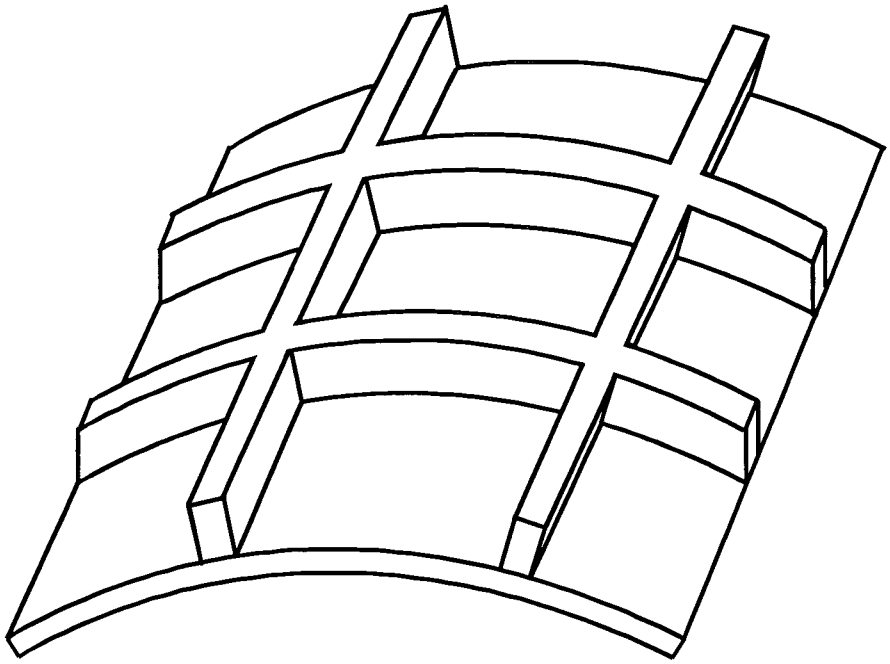

Figure 2.1 Schematic illustration of an orthogonally stiffened laminated composite cylindrical shell.

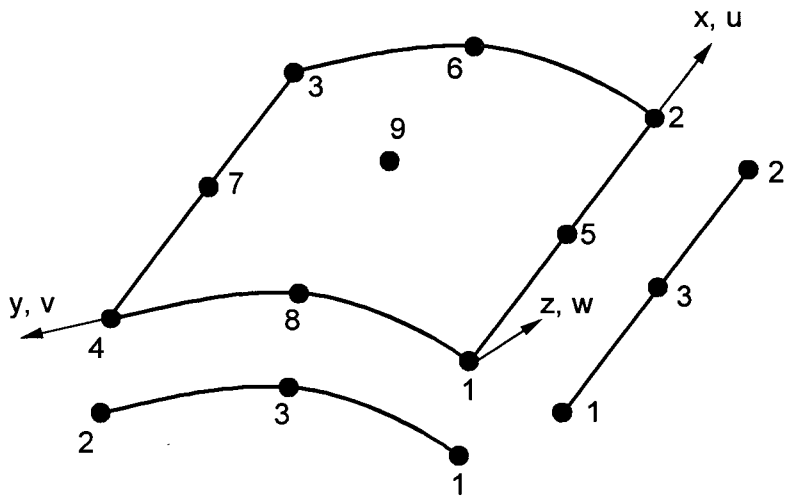

Figure 2.2 Illustration of element connection between a super shell element and a super beam element (straight and curved).

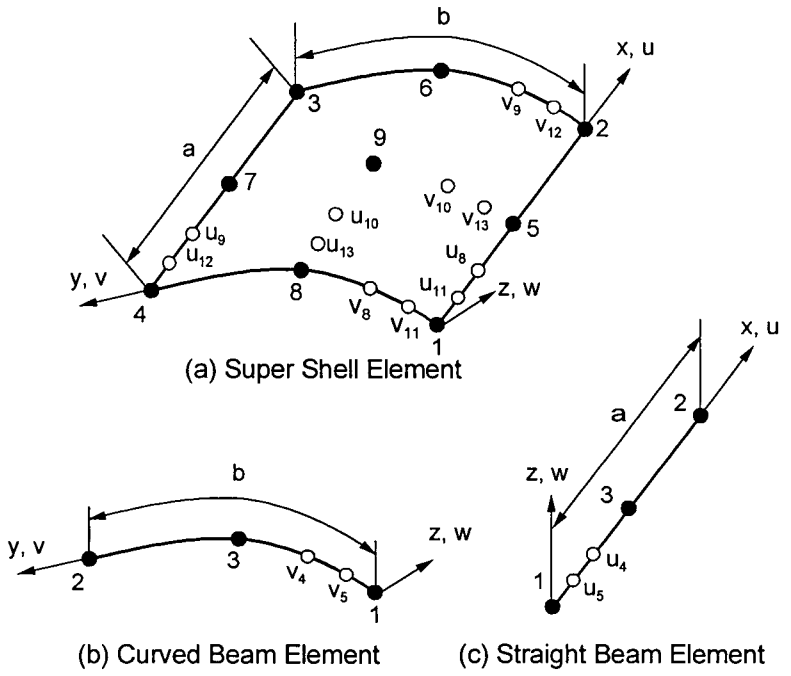

Figure 2.3 Nodal configuration of super elements.

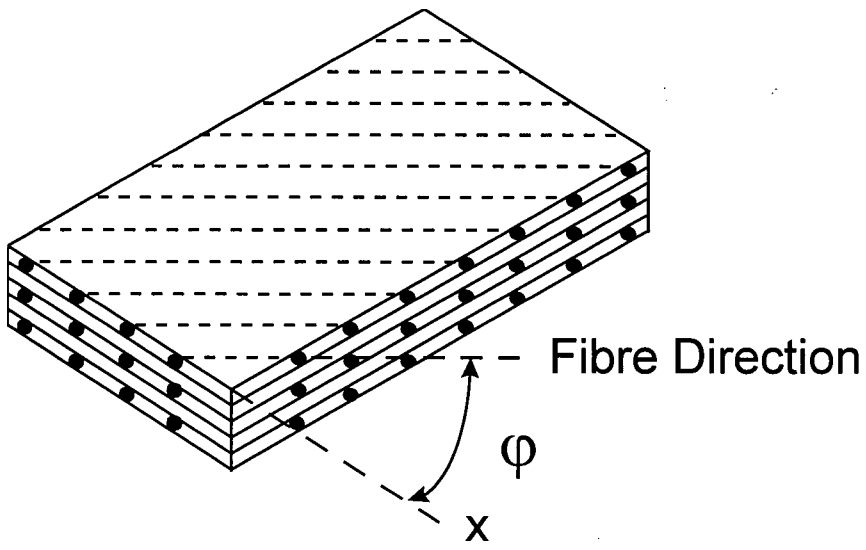

Figure 2.4 Schematic illustration of a laminated composite plate.

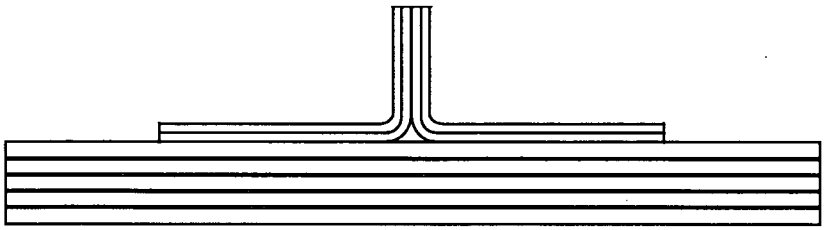

Figure 2.5 Schematic illustration of a stiffened laminated composite plate where a laminated stiffener is attached to a laminated skin (Dost *et al.*, 1991).

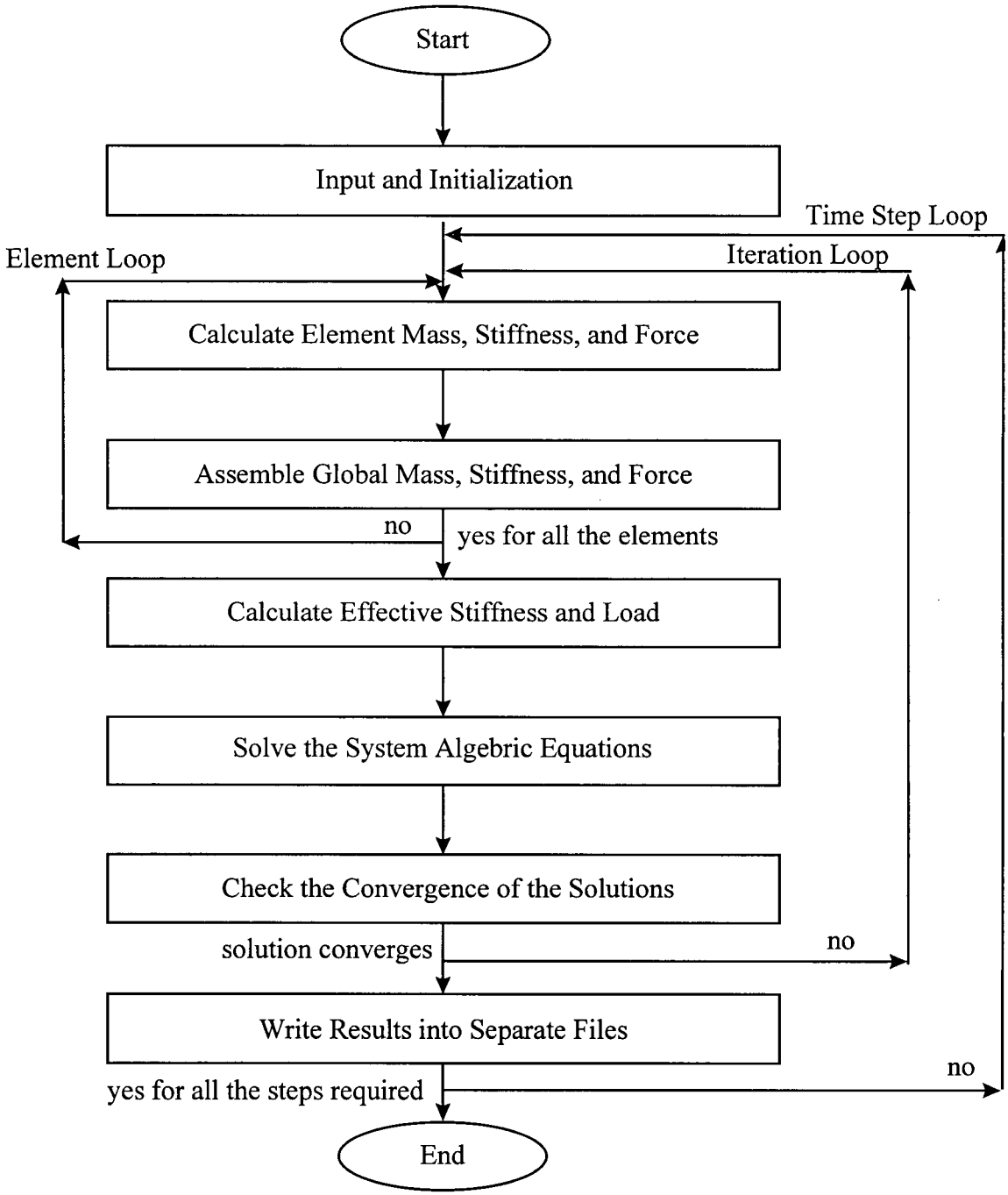

Figure 2.6 Flow chart of structural response calculation using SENACS.

Chapter Three: Nonpenetrating Impact Response

3.1 Literature Review

The transient response of structures subjected to impact can be assumed to occur at two levels: a global response of the overall structure and a local response under the point of impact (Pierson *et al.*, (1993). Thus, the first step in understanding the impact response of structures is to accurately predict their transient global response (i.e., nonpenetrating impact response).

Numerous works have been done in the area of impact of laminated composite materials. They have been carefully reviewed in Abrate (1991 and 1994). Only selected work on analytical modelling and finite element modelling of nonpenetrating impact response of plain and stiffened laminated composite plates and shells will be reviewed here.

3.1.1 Analytical Work on Plates and Shells

As one of the earliest work on the analytical treatment of the impact behaviour of composite plates, Sun and Chattopadhyay (1975) used a Mindlin-type laminated plate theory originally developed by Whitney and Pagano (1970) to solve the resulting equations of motion by a modal analysis technique. A similar approach was also used by Dobyns (1981), and Qian and Swanson (1990) to study the impact response of laminates. Matsuhashi *et al.* (1993) included the effects of large deflections within a Rayleigh-Ritz procedure to investigate the

sensitivity of the impact response to partial in-plane constraints at the supports. Pierson and Vaziri (1996) presented an efficient modal analysis procedure for predicting the impact response of simply-supported composite plates. Their analytical formulation took into account the combined effects of transverse shear deformation, rotary inertia, and the non-linear Hertzian contact law.

The analytical technique to solve nonpenetrating impact problems for laminated composite shells generally employs Fourier series expansion. Ramkumar and Thakar (1987) predicted the transient response of a cylindrical shell under an impact loading, which was assumed to be a known input. Christoforou and Swanson (1990) applied a double Fourier series expansion to the time histories of the impact load and transverse deflection to obtain a closed-form solution for the impact response of cylindrical shells under simply-supported boundary conditions. Their analysis neglected the effects of in-plane and rotary inertia as well as the contact stiffness. High-order shear deformation theory was utilised in Gong *et al.* (1995) to predict the transient response of simply-supported, doubly curved shells excited by an impact from a blunt-ended projectile. The impact force history was calculated based on the spring-mass model developed in Gong *et al.* (1994) and the equations of motion were solved by Fourier series expansion of in-plane orthogonal curvilinear co-ordinates and time.

3.1.2 Numerical Work on Plates and Shells

For more complex structures with more general boundary conditions, one has to resort to numerical methods such as the finite element method to model the impact response of these structures.

Sun and Chen (1985) developed a two-dimensional finite element procedure to analyse the impact response of initially stressed laminated composite plates. The plates were modelled by a nine-node isoparametric plate element accounting for the transverse shear deformations. The contact phenomenon was simulated using an experimentally determined static indentation law proposed by Tan and Sun (1985). The Newmark constant-acceleration time integration scheme was used to solve the equilibrium equations of both projectile and plate. Furthermore, based on the above finite element formulation and contact law, the large deflection response of composite laminates subjected to impact was investigated by Chen and Sun (1985). Montermurro *et al.* (1995) studied the impact response and damage progression of laminated plates and shells using isoparametric Mindlin plate elements. The Newton-Raphson iterative method was used to solve the non-linearities caused by the contact effects and large deflections.

Bachrach and Hansen (1989) developed a mixed finite element method for a composite cylinder subjected to impact. The projectile displacement and the deflection at the impact point of the cylinder were approximated using the Wilson-θ method and a finite difference method, respectively, to solve the non-linear equations arising from contact effects. Lee *et al.* (1993) performed finite element analyses of cylindrical shells subjected to impact using a non-linear contact law that took into account the curvatures of the contacting bodies. The effect of large deflections was also investigated in their analysis. The large deflection response of laminated cylindrical and doubly curved shells to impact was also investigated in Chandrashekhara and Schroeder (1995) using a shear flexible finite element method. The

time histories of impact force and central deflection were presented for various projectile parameters, shell geometries, and boundary conditions.

3.1.3 Experimental, Analytical, and Numerical Work on Stiffened Structures

The research on the impact response of stiffened composite structures initiated in recent years due to extensive applications of these structures. Madan and Shuart (1990), and Madan (1991) studied the influence of impact on blade-stiffened graphite/epoxy plates experimentally. In their tests, the stiffened flat panels were impacted by a drop-weight projectile at various energy levels. The impact points were either at the midbay or at the middle of the panel over the centreline of the stiffener. Damaged specimens were then loaded uniaxially and tested to failure by slowly applying a compression load. A simple analytical model was proposed to calculate the residual strength of the stiffened plates in post-impact compression. Basque and Aoki (1993) presented a phenomenological study on the impact damaged CFRP blade-stiffened flat panels. Their experimental results showed that the impact damage occurred first in the region of the blade stiffener and panel joint. Then the impact on the plates was approximated by a transverse load neglecting the dynamic effects and plugged into finite element analysis to model damage development in the joint region between the panel and the blade with more than two thousand 3-D elements.

Bucci and Mercurio (1994) studied the static and fatigue behaviour of CFRP panels with bead stiffeners under compression loads. The influence of impact damage from low velocity impact on buckling threshold load was also investigated. Scott and Rees (1995) analysed the post-buckling behaviour of carbon/epoxy panels with blade stiffeners experimentally and

numerically. The experimental results of damage development in CFRP stiffened plates with impact damage under compression loads was also presented in Aoki (1995).

Although these studies dealt with the impact response of stiffened composite plates, their emphasis was on the damage development or buckling threshold of the stiffened structures with impact damages. No contact and dynamic effects were considered in their analytical models and numerical analyses.

3.2 Contact Law

According to the indentation law developed by Tan and Sun (1985), the contact force F is given by the following modified non-linear Hertzian-type relations

$$F = \begin{cases} k\alpha^{3/2}, & \text{loading} \\ F_m\left(\dfrac{\alpha-\alpha_p}{\alpha_m-\alpha_p}\right)^q, & \text{unloading} \\ F_m\left(\dfrac{\alpha-\alpha_p}{\alpha_m-\alpha_p}\right)^{3/2}, & \text{reloading} \end{cases} \tag{3.1}$$

where α denotes the local indentation in the target, k is a contact stiffness coefficient, and F_m denotes the maximum contact force reached before unloading. k depends on the material properties and interface curvature between the two contacting bodies, which are assumed as cylindrical or spherical. The permanent indentation in the target, α_p, was found to vary with the material systems and in a linear relationship with the maximum indentation α_m. In Equation (3.1), q is the exponent of contact law during the unloading phase which is

generally taken as 2.5 based upon experimental measurements. Note that because the indentation law is based on static test results, the target inertia due to the local indentation is ignored here.

Various analytical and experimental techniques have been proposed for determination of k in the literature. In the present approach, the following explicit expressions taken from Hills *et al.* (1992) for contact between a spherical indentor and a transversely isotropic medium are employed,

$$k = \frac{8}{3} \frac{1}{\frac{1-\nu_z}{G_z} \sqrt{\frac{1}{R_1} + \frac{1}{R_2}}} \tag{3.2}$$

where G_z and ν_z are the transverse shear modulus and Poisson's ratio of a single layer of the target; and R_1 and R_2 are the radii of curvature of the projectile and the target, respectively. For simplicity, the transverse Poisson's ratio and shear modulus are assumed to be equal to their corresponding in-plane values.

The projectile is assumed to be rigid in the present approach and the effect of its elastic properties on contact stiffness coefficient is thus ignored in Equation (3.2).

3.3 Solution Scheme

Similar to Equation (2.16) in Section 2.2.3, the virtual work principle for the target can be written as

$$\int_V \{\delta u\}^T \rho \{\ddot{u}\}\, dV + \int_A \left[\{\delta \varepsilon^0\}^T \{N\} + \{\delta \kappa\}^T \{M\} \right] dA - \int_S \{\delta u\}^T \{T\}\, dS - F\delta\Delta = 0 \qquad (3.3)$$

where Δ and m are the projectile displacement and mass, respectively. The local indentation of the target, α, satisfies the following constraint condition at the contact point (x_c, y_c),

$$\Delta = \alpha + w_0 \qquad (3.4)$$

where $w_0 = w(x_c, y_c)$ is the transverse displacement of the target at the impact point. The other parameters and symbols, ρ, V, A, S, $\{T\}$, and δ are the same as those used in Chapter Two.

Applying the same derivations in Chapter Two for the target and the Newton's 2nd law for the projectile, the discretized equations of motion for a single element and the projectile can be written as:

$$[m_e]\{\ddot{d}_e\} + \{p_e\} = \{f_e^t\} + \{f_e^c\} \qquad (3.5)$$

$$m\ddot{\Delta} + F = 0 \qquad (3.6)$$

where $\{f_e^c\}$ denotes the elemental contact force vector. It should be noted that Equations (3.5) and (3.6) are coupled through the compatibility condition of Equation (3.4).

The assembled discretized equations of motion for the target can be written as

$$[M]\{\ddot{D}\} + \{P\} = \{F^t\} + \{F^c\} \qquad (3.7)$$

where $[M], \{P\}, \{F^t\}$, and $\{F^c\}$ are the assembled global equivalents of $[m_e]$, $\{p_e\}$, $\{f_e^t\}$, and $\{f_e^c\}$.

In the differential equation (3.7), the contact force term $\{F^c\}$ contains the deflection at the impact site of the structure. However, to solve for the deflection of the structure we need to know the magnitude of the contact force $\{F^c\}$. Therefore, Equation (3.7) is a non-linear equation even for small deflection analysis and linear-elastic materials and an iterative scheme should be used to solve it.

Generally, the Newton-Raphson iterative method is employed to perform this kind of task. Updating the stiffness matrix at each time step (for initial stiffness method) or at each iteration (for tangent stiffness method) reduces the computational efficiency of super finite element analysis. Thus, the contact non-linearity is linearized in the present analysis using the finite difference method.

At time t_{n+1}, the projectile displacement Δ_{n+1} is given by the solution of Equation (3.6) as

$$\Delta_{n+1} = \Delta_n + V_n \Delta t - \frac{F_n \Delta t^2}{2m} \tag{3.8}$$

where V_n and F_n are the projectile velocity and the contact force evaluated at time t_n. The deflection at the impact point of the target at time t_{n+1} is approximated by using the finite difference method,

$$w_{0_{n+1}} = w_{0_n} + \dot{w}_{0_n} \Delta t + \frac{1}{2} \ddot{w}_{0_n} (\Delta t)^2 \tag{3.9}$$

The indentation of the target at time t_{n+1} is thus given by

$$\alpha_{n+1} = \Delta_{n+1} - w_{0_{n+1}} \tag{3.10}$$

Therefore, the contact force at time t_{n+1} can be explicitly written in terms of known quantities at time t_n and thus there will be no need for any iterations.

3.4 Results for Laminated Plates and Shells

In this section, nonpenetrating impact model is verified by comparing the predicted results with experimental, analytical, and other numerical results available in literature. Some of them have already been published in Vaziri *et al.* (1996). Numerical experiments are also carried out for parametric studies.

3.4.1 Small Deflection Analysis

3.4.1.1 Impact Response of $[0/90/0/90/0]_s$ CFRP Plate

The response of a simply-supported T300/934 CFRP square plate with a lay-up of $[0/90/0/90/0]_s$ impacted by a 8.54 g steel ball with a striking velocity of 3.0 m/s will be considered here. The orthotropic material properties of the constituent layers and the geometric sizes of the plates are defined in Table 3.1.

Fundamental frequency

The fundamental frequency of the plate calculated using different mesh densities as shown in Table 3.2 is compared with the analytical solution by Pierson and Vaziri (1996) which accounts for transverse shear deformations. Present results, even using the coarsest mesh (1×1 for the whole plate), give a good estimation of the fundamental frequency of the plate.

Impact analysis

The transient analysis of the same laminate defined in Table 3.1 involving the impact of a 12.7 mm diameter steel ball with a mass of 8.54 g and velocity of 3.0 m/s is carried out using different mesh densities. The predicted force-time histories are shown in Figure 3.1. It can be seen that the results obtained from 4×4 and 5×5 grids for a quarter plate are almost indiscernible. The contact stiffness coefficient used in the present analysis is the same as that used in Pierson and Vaziri (1996), namely, $k = 3.14\times10^8$ N/m$^{3/2}$. The time step is taken to be $\Delta t = 0.3\ \mu s$.

Figure 3.2 and Figure 3.3 show, respectively, the predicted time histories of the impact force and central plate deflection using a 4×4 mesh for a quarter plate. No artificial damping is introduced in this case in order to verify the present approach. The present prediction is seen to be reasonably close to the modal analysis results of Pierson and Vaziri (1996) and the finite element results of Sun and Chen (1985). The discrepancies can be attributed to the fact that, unlike the other two approaches, the present model does not include the effect of transverse shear deformations and thus leads to somewhat stiffer results.

3.4.1.2 Impact Response of [45/90/-45/0]$_{3s}$ T800H/3900-2 CFRP Plate

Comparison with instrumented impact tests

To validate the predictive capability of the present approach, present results are compared with instrumented impact test data reported in Delfosse *et al.* (1993a). Comparisons between the predicted and measured results are shown in Figure 3.4 to Figure 3.7, inclusive. The

properties of the target plate used here are shown in Table 3.3. The numerical simulations are conducted using the option of small deflection analysis and a uniform 4×4 mesh for a quarter-plate. The fundamental frequency of the plate is calculated as 2.95 kHz and the time step used is $\Delta t = 1$ μs. Also, a contact stiffness value of $k = 6.0\times10^8$ N/m$^{3/2}$ is used in the simulations. This value was found to fit the static indentation test results quite accurately (Delfosse *et al.*, 1993a).

The trends of the predicted contact force histories are seen to be in fair agreement with the experimental results for both the low-velocity/large mass (Figure 3.4 and Figure 3.5) and high-velocity/small mass (Figure 3.6 and Figure 3.7) impact events. In most of the cases considered, peak values of the impact force are overpredicted while the impact durations are underpredicted; all indications of the response of a stiff system. It should be remarked that the multiple oscillations in the predicted force-time histories caused by high frequency vibrations of the projectile/target system have been smoothed by introducing artificial damping with $\gamma = 5.0$ and then $\beta = 7.5625$ from Equation (2.27). In the experiments presented here, some of these oscillations had also been filtered out as high frequency noise (see Delfosse *et al.*, 1993a).

Bucinell *et al.* (1991) proposed a two degree of freedom spring-mass system to model the nonpenetrating impact response of plates. The time periods of the high frequency oscillations (without artificial damping) in the present force time history are found to be close to the second vibration period of the Bucinell's spring-mass system. More details on how artificial damping affects the impact force history in the present approach is presented in Appendix D along with the Bucinell's spring-mass model.

Response under different impact velocities

In this section, the same laminate is used to investigate the impact response under different striking velocities. The impact energy is taken to be the same as that in the instrumented impact tests shown in Figure 3.5 and Figure 3.7, *i.e.*, 22 J.

Experimental studies [see Delfosse *et al.*, (1994b)] indicated that the force-displacement curves generated from high velocity impact events initially followed the same curve as the static indentation curves and then deviated from it when flexural waves that had initiated at the impact site had time to travel to the boundary and reflect back.

Figure 3.8 shows the relationship between the impact force and the projectile displacement under impact velocities ranging from 59.25 m/s to 296 m/s. Superposed on the same graph is the static indentation curve. It can be seen that for high velocity impacts, the initial part of the force-displacement curve coincides with the static indentation curve. Therefore at high velocity impacts, the target has very little time to bend and the impact behaviour resembles that of a projectile striking an infinite or semi-infinite target.

For very high velocity impact events, such as 132.5 m/s and 296.3 m/s, there is only one peak in the force-displacement curve, which corresponds to the maximum indentation depth.

For intermediate impact velocities, such as 59.25 m/s, there are two more peaks in the force-displacement curve, which are caused by interaction of the projectile motion and the plate vibration (also see Figure 3.9 and Figure 3.10). It should be noted that the projectile continues to decelerate during the impact. After the first peak of the impact force, both the

projectile and plate decelerate. Their rates of deceleration are different and vary with the time. Near to the time when the plate velocity is equal to the projectile velocity again ($t = 0.095\ ms$), there is a second peak of the impact force. Shortly after that, the projectile starts to retreat, moves backward and its velocity increases negatively. At the same time, the plate velocity decreases to zero and continues to increase in the opposite direction. The plate moves faster than the projectile and results in an increase of the impact force. When the projectile moves with the same velocity as the plate (*i.e.,* the velocity of indentation depth $\dot{\alpha} = \dot{\Delta} - \dot{w}_0$ is zero), the third peak force is reached. Then, the projectile moves away from the plate and the impact force decreases and reduces to zero. The time at which peak forces occur are indicated in Figures 3.8 and 3.9.

For low velocity impacts in Figures 3.4 and 3.5, the target deforms in a way that is similar to a quasi-static deformation. Thus there is only one peak force in their force-displacement curves.

Figure 3.11 shows the deflection profiles at the instant when maximum deflection occurs for three typical impacts: low velocity impact (5.30 m/s), intermediate velocity impact (59.25 m/s), and high velocity impact (296.3 m/s). As expected, the low velocity impact will cause much more deformation in the target than the intermediate and high velocity impacts.

3.4.1.3 Impact Response of $[90/\pm22]_{2T}$ IM7/55A CFRP Cylinder

Christoforou *et al.* (1989) experimentally studied the transverse impact behaviour of $[90/\pm22]_{2T}$ IM7/55A CFRP laminated composite cylinder impacted by a 32 g steel ball at 3

m/s. In a subsequent paper, Christoforou and Swanson (1990) presented analytical solutions for some simple boundary conditions that were different from those used in their experimental set-up. The cylindrical shell problem is shown in Figure 3.12(a) and the material constants, geometric dimensions, and laminate lay-up are listed in Table 3.4.

A series of transient analyses for a prescribed load-time history have been performed first to study the convergence of the numerical results and hence arrive at a desirable mesh geometry. Three uniform meshes (2×2, 2×4, and 4×4) and one non-uniform mesh (4×4) in which the elements were gradually refined near the impact site [Figure 3.12(b)] are considered for discretization of a quarter-cylinder. The transient response of the shell to a given force-time history [Figure 2 in Christoforou and Swanson (1990)] is carried out using the above mesh configurations. It has been found that the 4×4 non-uniform mesh arrangement yields results that agree more closely with the analytical predictions and is therefore used in subsequent impact simulations.

Before conducting the impact analyses, the contact stiffness coefficient between the target and the projectile have to be determined. However, this information was not available from the paper by Christoforou and Swanson (1990) as their analysis neglected the local contact deformation in the target and only considered its bending response. Using a projectile diameter of 15.9 mm (taken from Christoforou *et al.*, 1989), the contact stiffness coefficient is found to be $k = 1.58 \times 10^9$ N/m$^{3/2}$ which is calculated from Equation (3.2). The first natural frequency of the cylinder is 0.99 kHz and the time step size used is $\Delta t = 1$ μs.

An impact simulation with the conditions described in Table 3.4 was performed. The time history of the normalised transverse deflection of the shell at the impact point is shown in Figure 3.12(c). The predicted deflection-time history agrees well with the analytical solutions.

As noted before, the analytical model did not consider the indentation response and therefore resulted in a higher peak value of central deflection.

3.4.2 Large Deflection Analysis

3.4.2.1 Impact Response of $[0/45/0/-45/0]_{2s}$ T300/934 CFRP Laminated Plate

Large deflection response of laminated composite plates subjected to impact loads was first investigated by Chen and Sun (1985) using the finite element method. For comparison, the same problem is analysed using the present formulation. The laminated plate considered in this case has a $[0/45/0/-45/0]_{2S}$ lay-up with the same basic layer properties as those shown in Table 3.1. The plate dimensions are 15.24 cm × 10.16 cm × 0.269 cm and the boundary conditions are simply-supported and immovable in the plane of the plate along all the edges. The laminate is considered to be impacted by a 8.54 g ball fired at a velocity of 30.0 m/s. The contact stiffness coefficient is the same as that used in the Section 3.3.4.1.1. The permanent indentation is determined by

$$\alpha_p = \beta_p (\alpha_m - \alpha_c), \quad \text{if } \alpha_m \geq \alpha_c$$
$$\alpha_p = 0, \quad \text{if } \alpha_m \leq \alpha_c$$

where $\beta_p = 0.094$, $\alpha_c = 1.667\times10^{-2}$ cm [Chen and Sun (1985)], α_m is the maximum indentation depth, and the unloading index of the contact law $q = 2.5$.

A 2×2 mesh for a quarter plate is used in the analysis. The fundamental frequency of the plate is calculated to be 0.78 kHz and the time step used is $\Delta t = 4$ μs. No artificial damping is introduced in the time integration scheme.

The time histories of the target deflection at the impact point are shown in Figure 3.13, where present results using both small and large deflection analyses are compared with corresponding results in Chen and Sun (1985). The present results agree very well with the predictions of Chen and Sun (1985), thus validating the large deflection analysis capability of the present model. It should be pointed out that the present analysis uses larger time steps than those used in Chen and Sun (1985), leading to more computational efficiency.

3.3.1.1 Impact Response of $[\pm45_2/0_2]_S$ AS4/3501-6 CFRP Plate

Matsuhashi *et al.* (1993) investigated the impact response of a $[\pm45_2/0_2]_s$ laminated CFRP plate both experimentally and analytically. The same problem is studied here and present results are compared with experimental results reported in Matsuhashi *et al.* (1993). The material properties, geometrical dimensions, boundary conditions, and laminate lay-up are shown in Table 3.5. The mass of the projectile is 1.53 kg and its velocity is 3.0 m/s. The contact stiffness coefficient, k, used in the present analysis is the same as in Matsuhashi *et al.* (1993), namely, $k = 5.0\times10^8 N/m^{3/2}$.

A 2×2 mesh for a quarter-plate is used. The fundamental frequency of the plate is 1.33 kHz and the time step used is 1.5 μs. No artificial damping is introduced in the time integration scheme. A comparison of the present results with experimental results of Matsuhashi *et al.* (1993) is shown in Figure 3.14. The present large deflection analysis results are stiffer than the experimental results because the clamped boundary condition cannot be realised in the experiments, especially when the deflection is very large. However, the present small deflection results are on the "soft" side of the experimental results. This indicates that the present small and large deflection results are reasonable bounds on the real behaviour. Also, in the analytical study of Matsuhashi *et al.* (1993), the fully clamped boundary condition was not applied and a flexibility factor for the in-plane boundary condition was introduced to approach the experimental results.

3.4 Results for Stiffened Plates and Shells

After verifying the ability of the computer program in calculating the nonpenetrating impact response of plain plates and shells, the nonpenetrating impact response of stiffened plates and shells is carried out in this section. Following the verifications of the model, some numerical experiments (parametric studies) will be performed here as well.

3.4.1 Verification

Consider a stiffened laminated structure, IM7/977-2 CFRP laminated plate with a $[45/90/-45/0/45/90/-45/0/90/0/90/0]_s$ lay-up. The plate dimensions are 17.8 cm × 50.8 cm × 0.451

cm. The finite element mesh used in the present analysis consists of 2×2 shell elements and 2×1 beam elements for a quarter-plate as shown in Figure 3.15. The plate is simply-supported along two opposite stiffeners. The other two opposite edges are free. The elastic properties of the lamina are listed in Table 3.6.

There are two T-shape stiffeners beneath the skin in the stiffened plate. These stiffeners are made of the same laminate material as the skin with a $[22.5/90/-22.5/0]_{2s}$ lay-up. The elastic modulus and Poisson's ratio for the stiffeners are evaluated by classical laminate plate theory as $E = 68.3$ GPa and $\nu = 0.26$.

The impact point is at the midbay of the stiffened panel. The projectile mass and velocity are $m = 6.347$ kg, $V_s = 2.74$ m / s. The diameter of the spherical projectile is 25.4 mm. Then, the coefficient of contact stiffness k is calculated using Equation (3.2) to be $k = 4.68$ GN / m$^{3/2}$.

The present contact force history is compared with the experimental data measured from the instrumented impact tests at the University of British Columbia (Dost *et al.*, 1991) in Figure 3.16 and fairly good agreement is attained. The artificial damping ($\gamma = 8.0$ and $\beta = 18.0$) is introduced to filter out the spurious high frequency oscillations.

3.4.2 Numerical Experiments

Having validated the present approach, a variety of example problems in this section are considered to study the impact response of stiffened laminated plates and cylindrical shells using small and large deflection analysis. These are hypothetical problems which have not been reported in the literature. The purpose of the analyses is to identify the influence of

various parameters on the impact response of stiffened plates and shells. For all the problems considered, the material properties and geometric sizes are defined in Table 3.6. The projectile mass is $m = 0.635$ kg and projectile velocity is $V_s = 8.7$ m / s. Unless mentioned otherwise, all the impact sites are taken to be at the midbay of the stiffened panel.

3.4.2.1 Effect of Curvature

Consider a stiffened shell panel with the ratio of shell radius to arc length as infinity (i.e., flat plate), 5, and 1. The boundary conditions and stiffener arrangements are the same as in the problem considered in section 3.5.1. Artificial damping was not introduced in the time integration method used here.

Figures 3.17 and 3.18 show the effect of shell radius on the time history of the central deflection and the impact force. It is observed from these graphs that the maximum impact force will increase and the central deflection will decrease with increasing curvature of the stiffened shell panel. This stems from the fact that decreasing the shell radius and thus increasing the curvature has a stiffening effect on the shell panel due to membrane actions. This increases the natural frequency and thus reduces the impact duration. The calculated fundamental frequencies of the stiffened shells for various radii of curvature are listed in Table 3.7. In Figure 3.17, the deflection time history of the shallow shell with radius $R = 5a$ is very similar to that of the flat plate.

The maximum deflection of the plate and shallow shell ($R = 5a$) shown in Figure 3.17 is greater than the skin thickness. Therefore large deflection analysis is carried out for these problems and the results are shown in Figure 3.19. It can be seen that the membrane

deformations accounted for in large deflection analysis will make the panel act stiffer and thus decreases the magnitude of the central deflection.

3.4.2.2 Effect of Impact Site

Consider a plate with three stiffeners as shown in Figure 3.20. The material properties and geometric sizes of the plate and stiffeners are the same as in Table 3.6 and Figure 3.15 except that there is an intermediate stiffener added to the plate along the centre line. The projectile mass and velocity are the same as in the above examples.

Two typical impact sites, midbay and middle of the central stiffener, are studied using small deflection analysis. The time histories of transverse deflections at the impact point of the stiffened plates are shown in Figure 3.20 and compared with the deflection history for the case of a plate with two-stiffeners.

Table 3.8 predicts a comparison between the maximum impact force in these three cases. It can be seen that in the case where the impact is on the stiffener, maximum impact force is higher and transverse deflections are lower (see Figure 3.20). Transverse deflections are highest when the projectile impacts the two-stiffener plate at the midbay. The time histories of the impact force on the two-stiffener and three-stiffener plates are shown in Figure 3.21.

3.5 Summary

In this chapter, a numerical analysis procedure using super finite elements has been presented for simulating the nonpenetrating impact response of stiffened and plain laminated composite

plates and cylindrical shells. The non-linearity from large deflections is taken into account in the analysis as well. The present formulation has been verified by comparing with existing experimental data and other theoretical solutions in the literature. Good agreement between the predicted and measured results shows that the present numerical technique based upon coarse finite element mesh is an efficient way to compute nonpenetrating impact response of composite structures. The use of artificial damping in the time integration scheme to filter out the high-frequency oscillations in impact force time history shows a clear picture of dominant vibration mode in impact response.

The success of the present numerical analysis gives us confidence to handle nonpenetrating impact response of composite structures, and furthermore provides a robust framework for computing the structural response under penetrating impact events.

Table 3.1 Properties of the laminated plate used for convergence studies.

Boundary Condition	Simply-Supported		
Size	0.2m × 0.2m × 0.00269m		
Material System	$[0/90/0/90/0]_S$ T300/934 CFRP		
E_{11}	120 Gpa	G_{12}	5.5 GPa
E_{22}	7.9 Gpa	h	2.69 mm
ν_{12}	0.33	ρ	1580 kg/m^3

Table 3.2 Fundamental frequencies of the laminate defined in Table 3.1 obtained from different mesh geometries.

Super-Finite Element Mesh	Fundamental Frequencies (Hz)
1×1 for the whole plate	303.116
1×1 for a quarter plate	303.106
2×2 for a quarter plate	303.083
4×4 for a quarter plate	303.082
5×5 for a quarter plate	303.082
Analytical solution	302.692

Table 3.3 Properties of the laminated plate used in instrumented impact tests.

Boundary Condition	Simply-Supported		
Size	0.127m × 0.0762m × 0.00465m		
Material System	$[45/90/-45/0]_{3S}$ T800H/3900-2 CFRP		
E_{11}	129 GPa	G_{12}	3.5 GPa
E_{22}	7.5 GPa	h	4.65 mm
ν_{12}	0.33	ρ	1540 kg/m^3

Table 3.4 Properties of the cylindrical shell used in the analysis of Christoforou and Swanson (1990).

Target Material System	$[90/\pm22]_{2T}$ IM7/55A CFRP	
Size	L=41.9cm, R=4.91 cm, h=1.52 mm	
Projectile Parameters	Mass m=0.032 kg, Impact velocity V_0=3.0 m/s	
Target Material Constants	E_{11}=169 GPa	ν_{12}=0.266
	E_{22}=6.72 GPa	ρ=1620 kg/m^3
	G_{12}=5.26 GPa	

Table 3.5 Properties of the laminated plate used in Matsuhashi *et al.* (1993).

Boundary Condition	Clamped - Clamped in width Free -Free in length		
Size	0.252m × 0.089m × 0.001608m		
Material System	$[\pm 45_2/0_2]_S$ AS4/3501-6 Graphite/Epoxy		
E_{11}	142.0 GPa	G_{12}	6.0GPa
E_{22}	9.81 GPa	h	1.608 mm
ν_{12}	0.30	ρ	1540 kg/m^3

Table 3.6 Material properties and lay-up of the stiffened plate shown in Figure 3.15.

Material properties	E_1 = 120 GPa, E_2 = 7.65 GPa, G_{12} = 3.44 GPa, ν_{12} = 0.363, ρ = 1540 Kg/m^3	
Lay-up	skin [45/90/-45/0/45/90/-45/0/90/0/90/0]$_s$ stiffener [22.5/90/-22.5/0_2]$_{2s}$	
Stiffener size	shape of cross-section: T web thickness: 6.02 mm flange thickness: 3.0 mm	web spacing: 178.0 mm web height: 28.40 mm flange width: 72.06 mm

Table 3.7 Parametric studies: fundamental frequency and maximum impact force of the stiffened laminated cylindrical shells.

	Fundamental frequency (Hz)	Maximum impact force (KN)
R = infinity	274	5.77
R/arc length = 5	408	10.8
R/arc length = 1	1250	18.2

Table 3.8 Maximum impact force for a stiffened plate impacted at different sites.

Impact sites	Maximum impact force (KN)
Midbay of two-stiffener plate	5.77
Midbay of three-stiffener plate	10.6
Stiffener centre of three-stiffener plate	21.7

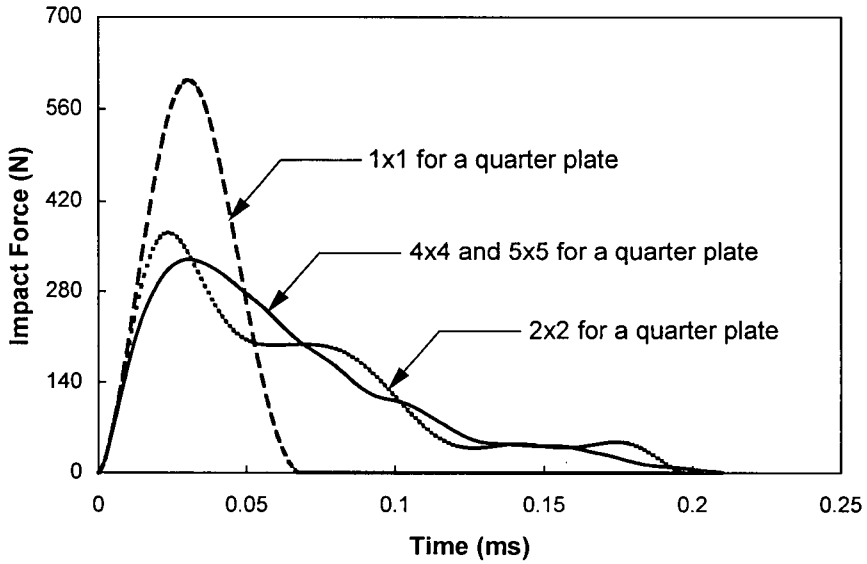

Figure 3.1 Convergence of the transient response of the laminated plate defined in Table 3.1 subjected to a 8.54 g, 3.0 m/s central impact.

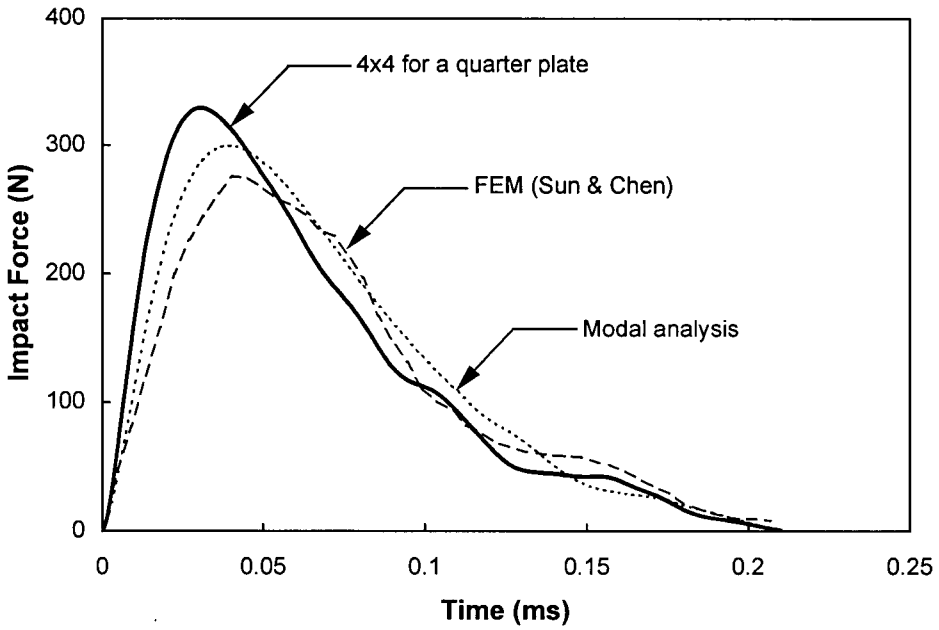

Figure 3.2 Impact force history of the laminated plate defined in Table 3.1; present analysis compared with modal analysis of Pierson and Vaziri (1996) and finite element analysis of Sun and Chen (1985).

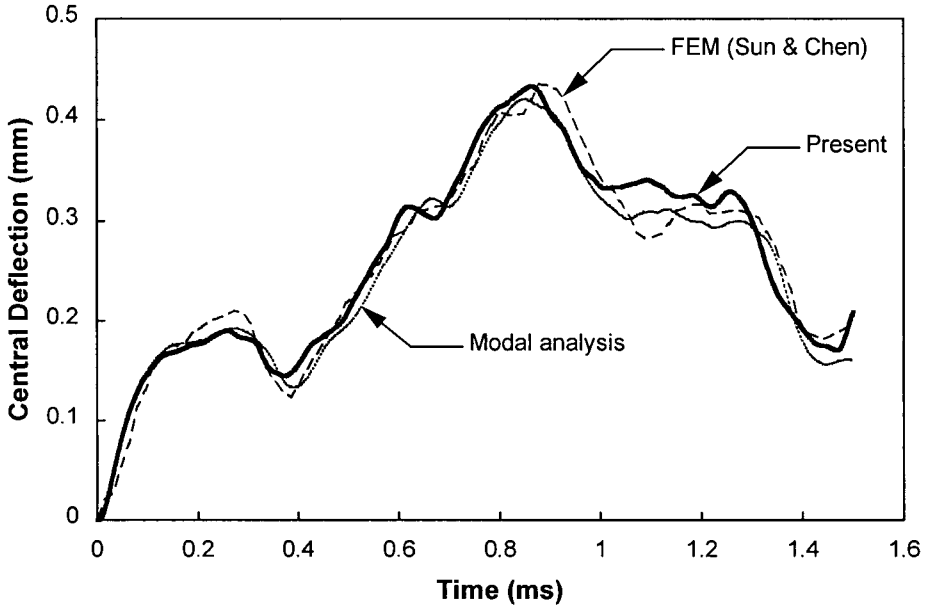

Figure 3.3 Central deflection history of the laminated plate defined in Table 3.1; present analysis compared with modal analysis of Pierson and Vaziri (1996) and finite element analysis of Sun and Chen (1985).

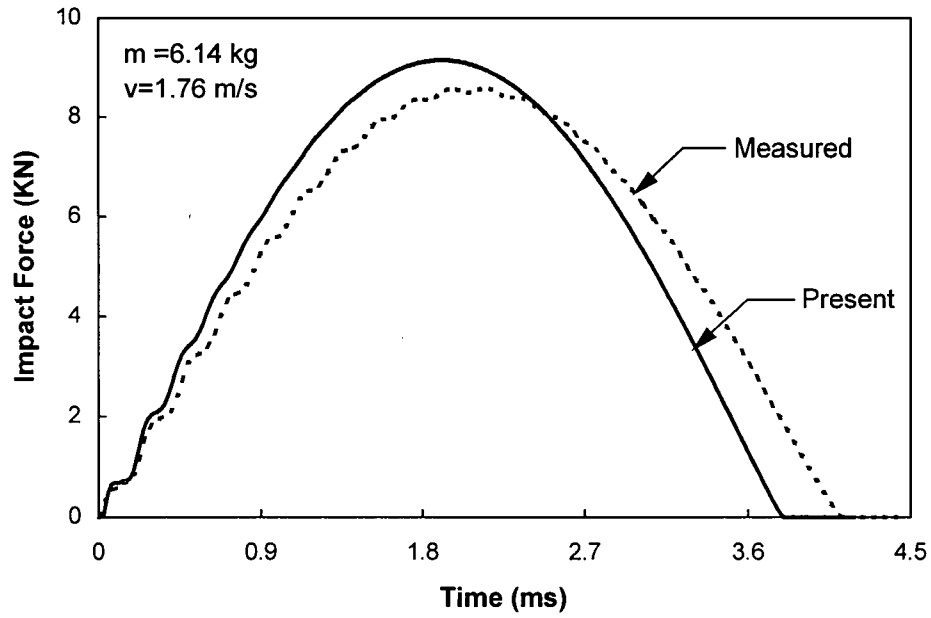

Figure 3.4 Impact force history for 6.14 kg, 1.76 m/s impact on the laminate defined in Table 3.3; present model compared with drop-weight test results (Delfosse *et al.*, 1993b).

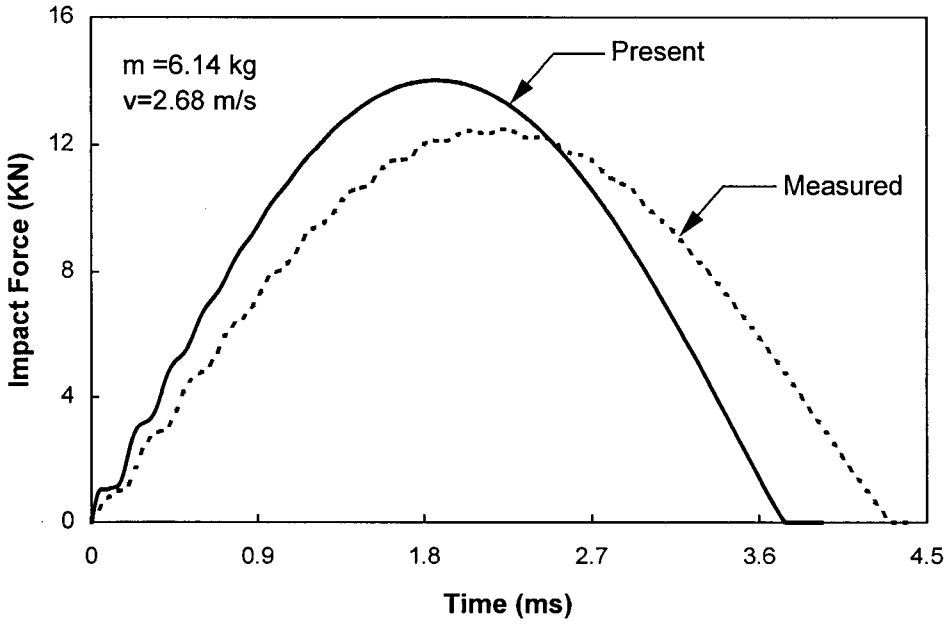

Figure 3.5 Impact force history for 6.14 kg, 2.68 m/s impact on the laminate defined in Table 3.3; present model compared with drop-weight test results (Delfosse *et al.*, 1993b).

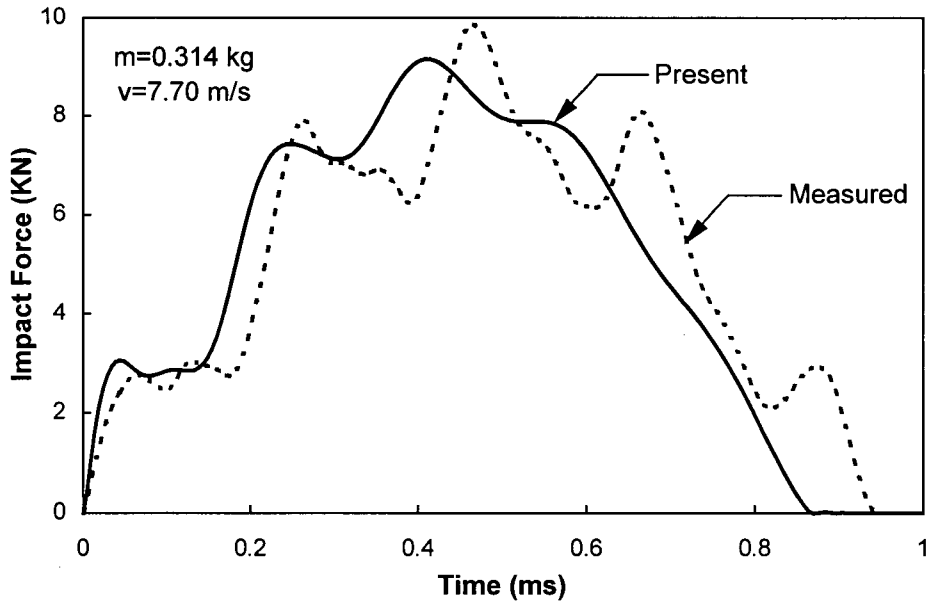

Figure 3.6 Impact force history for 0.314 kg, 7.70 m/s impact on the laminate defined in Table 3.3; present model compared with gas-gun test results (Delfosse *et al.*, 1993b).

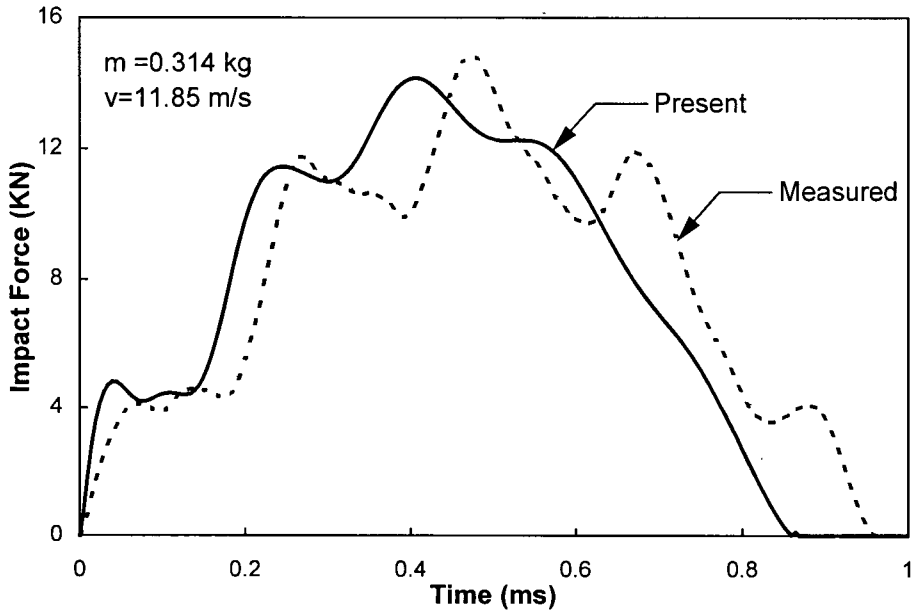

Figure 3.7 Impact force history for 0.314 kg, 11.85 m/s impact on the laminate defined in Table 3.3; present model compared with gas-gun test results (Delfosse *et al.*, 1993b).

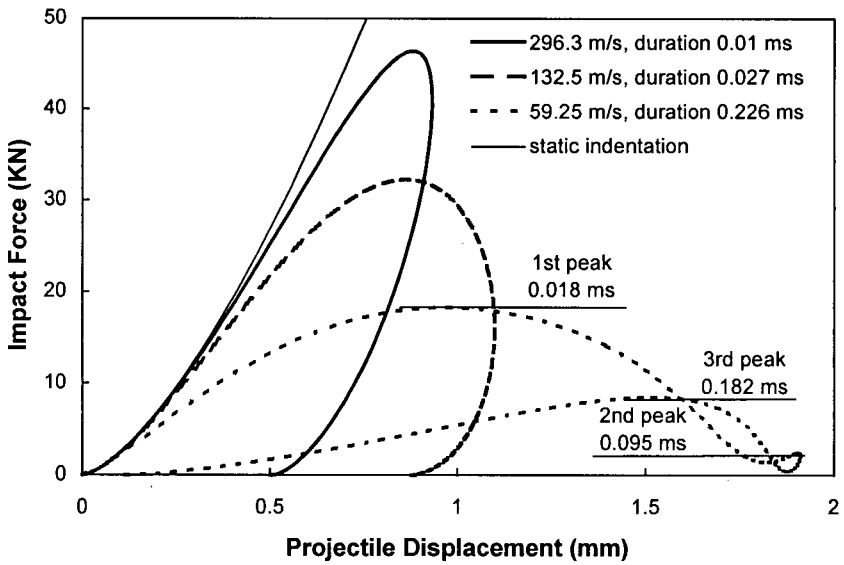

Figure 3.8 Parametric studies: Predicted impact force-displacement curves for impact events with the same incident energy but with different striking velocities on the laminate defined in Table 3.3. Also see Figure 3.9 for a description of the force-displacement curve with a striking velocity of 59.25 m/s.

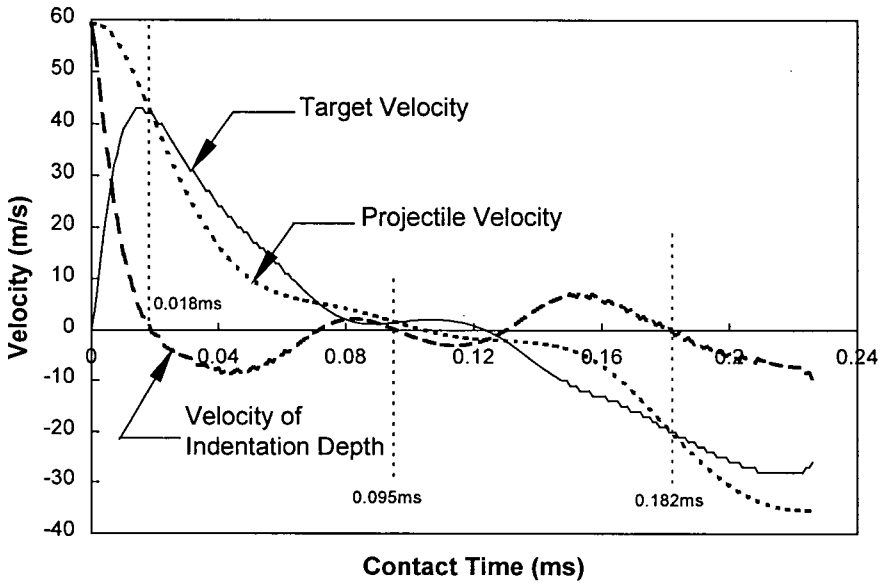

Figure 3.9 Predicted time histories of the projectile velocity, central target velocity, and velocity of indentation depth for the impact event shown in Figure 3.8 with a striking velocity of 59.25 m/s.

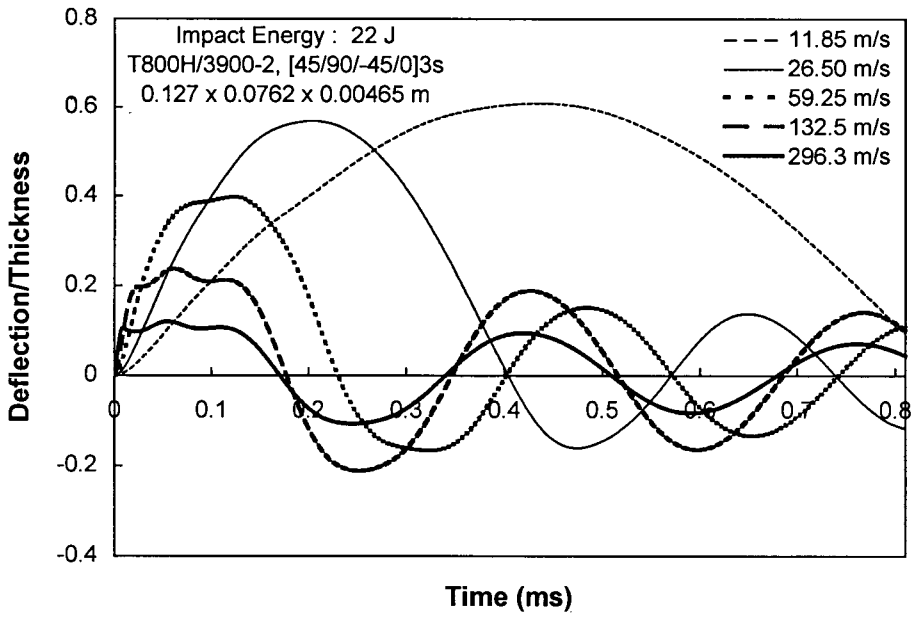

Figure 3.10 Parametric studies: Time histories of central deflection of the target for impact events with the same incident energy but with different striking velocities on the laminate defined in Table 3.3.

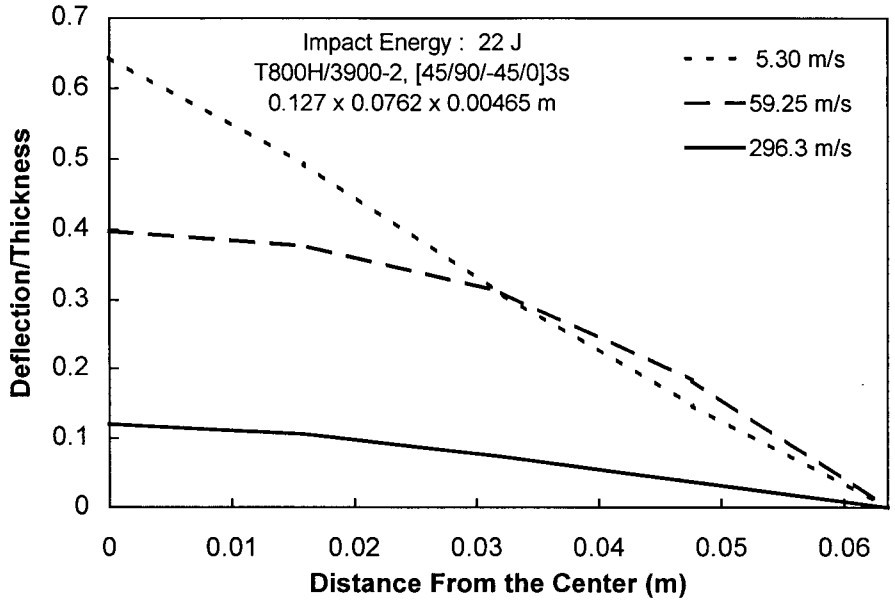

Figure 3.11 Profiles of central deflections under impacts with the same amount of energy but in different velocities on the laminate defined in Table 3.3.

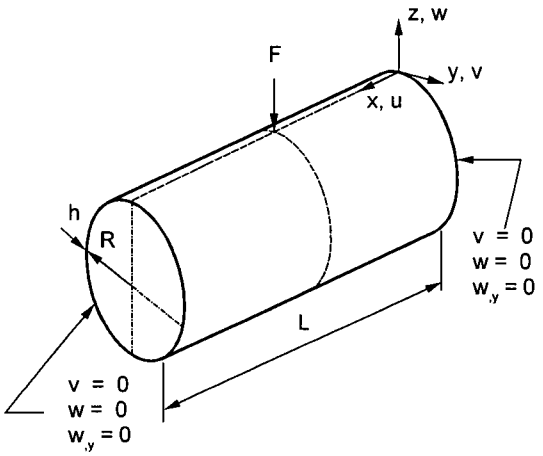

(a)

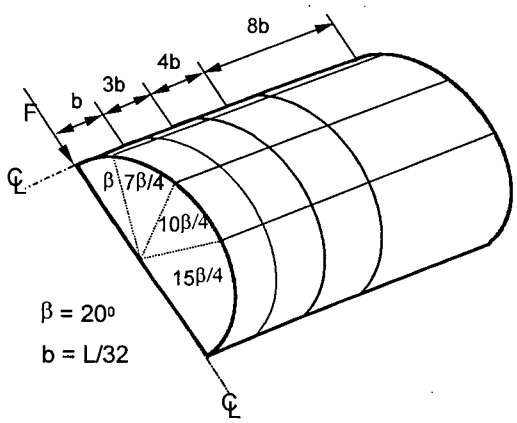

(b)

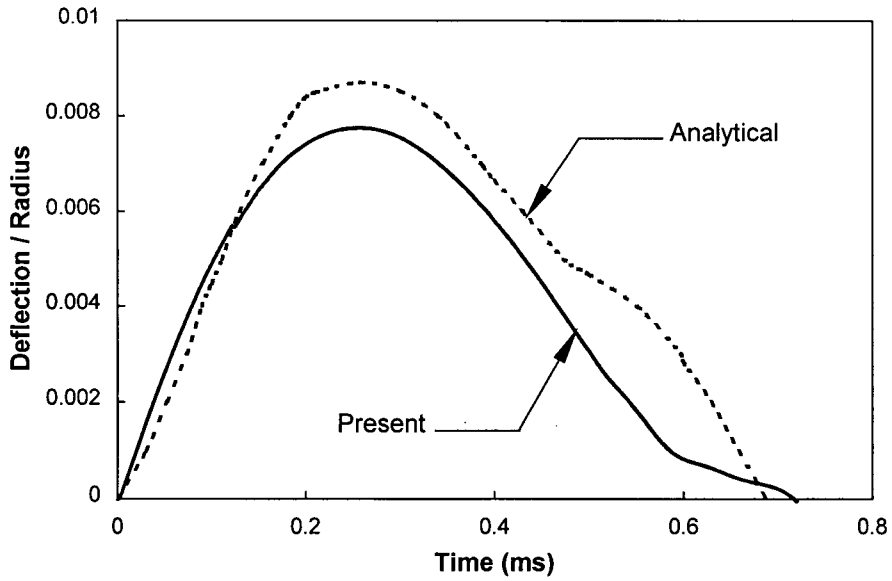

(c)

Figure 3.12 Vertical deflection history at the impact point for the Christoforou and Swanson's cylinder impact problem defined in Table 3.4. (a). Circular cylinder under an impact at the center. (b). Finite element mesh for a quarter cylinder used in present analysis. (c) Present predictions compared with Christoforou and Swanson's analytical results.

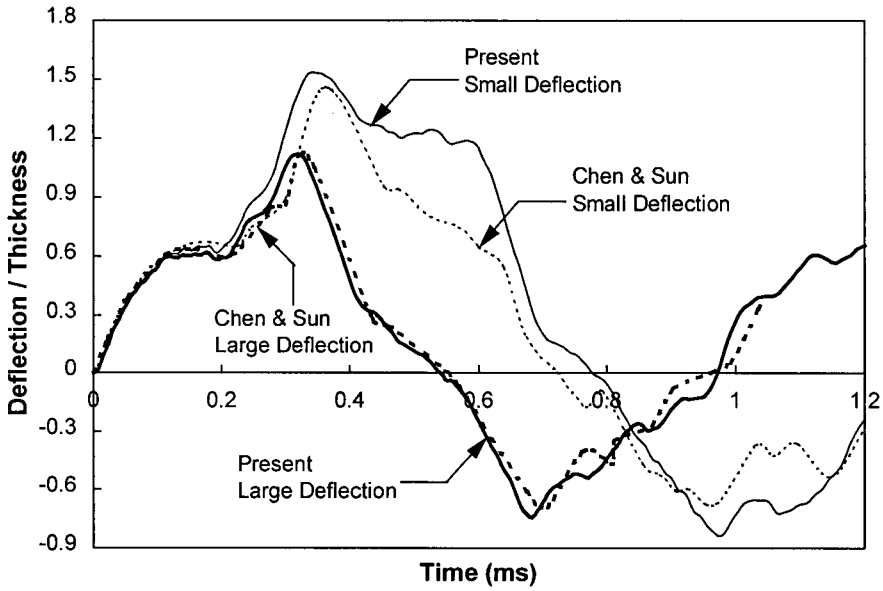

Figure 3.13 Central deflection history for a 8.54 g, 30.0 m/s impact on a simply-supported $[0/45/0/45/0]_{2S}$ CFRP rectangular plate with the layer properties defined in Table 3.1; present results obtained from a small and large deflection analysis compared with the corresponding results of Chen and Sun (1985).

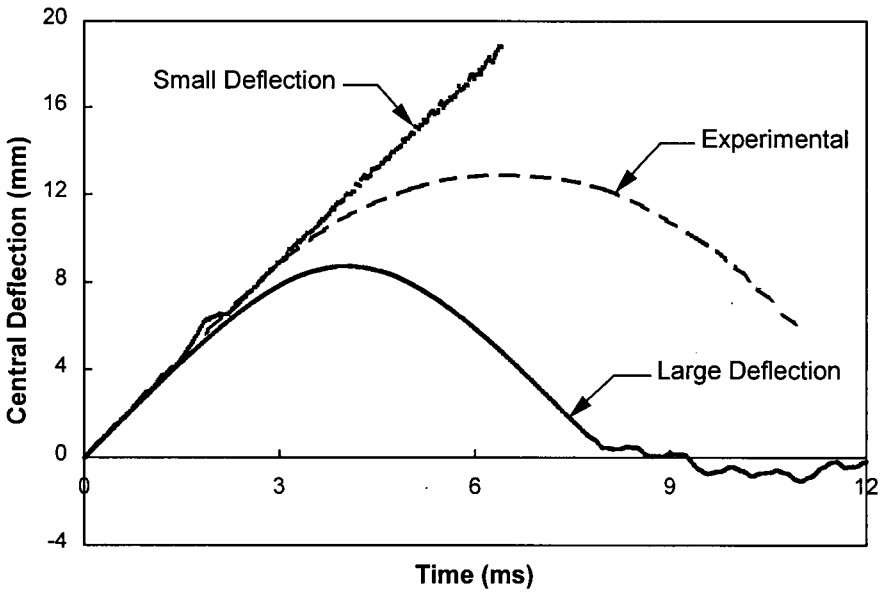

Figure 3.14 Central deflection history for a 1.53 kg, 3.0 m/s impact on a clamped-free $[\pm 45_2/0_2]_{2S}$ CFRP plate with the layer properties defined in Table 3.5; present small and large deflection analysis results compared with experimental data in Matsuhashi *et al.* (1993).

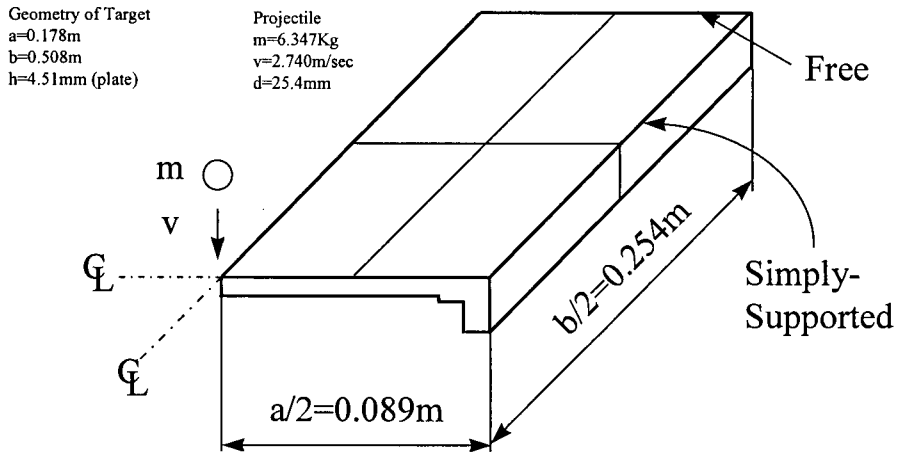

Figure 3.15 Super finite element mesh in nonpenetrating impact analysis of laminated composite stiffened plates (Dost *et al.*, 1991). Material properties and lay-up are shown in Table 3.6.

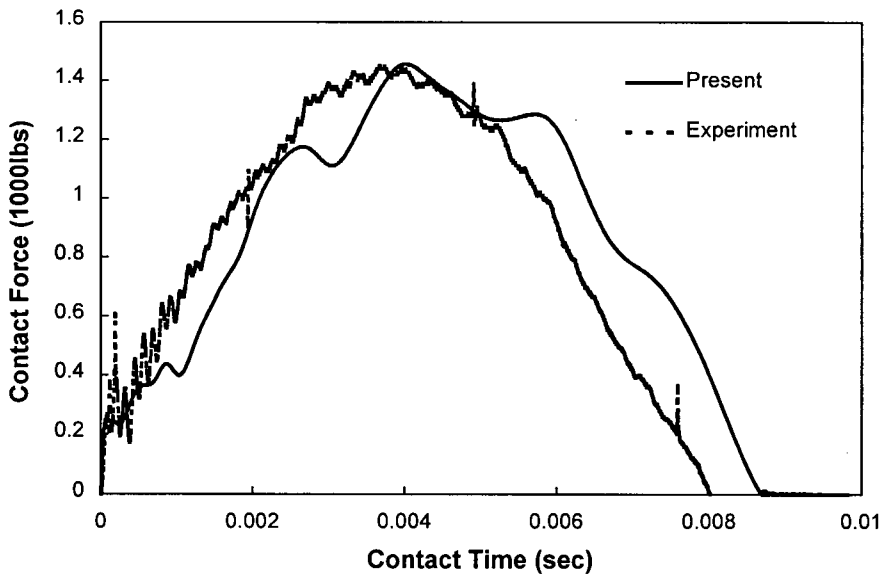

Figure 3.16 The comparison of the predicted contact force time history with the measured data from instrumented impact tests in Dost *et al.* (1991). The material properties and geometric sizes are shown in Figure 3.15 and Table 3.6.

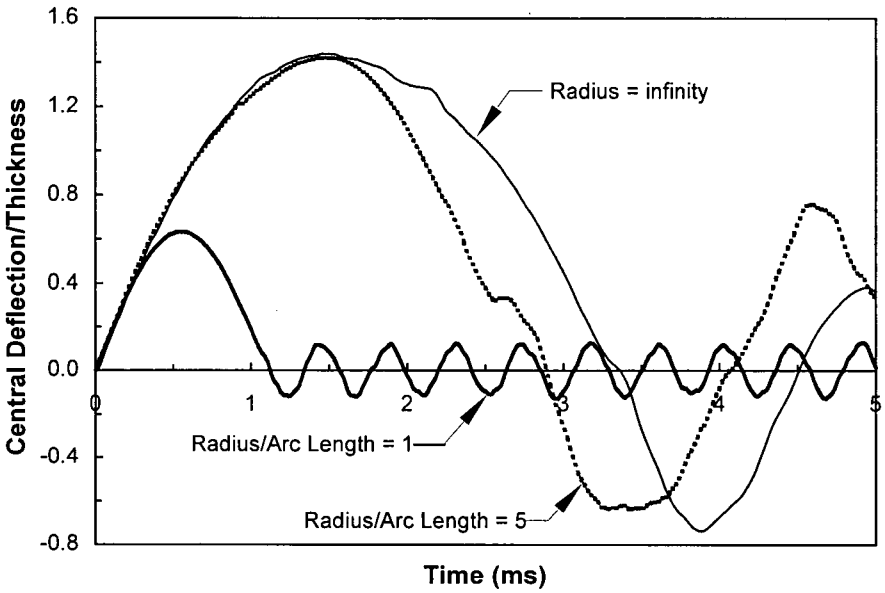

Figure 3.17 Parametric studies: The time history of the central deflection at the impact point for stiffened cylindrical shells with various radii of curvature. The material properties and geometric sizes are shown in Figure 3.15 and Table 3.6 with arc length $b = 0.508\ m$.

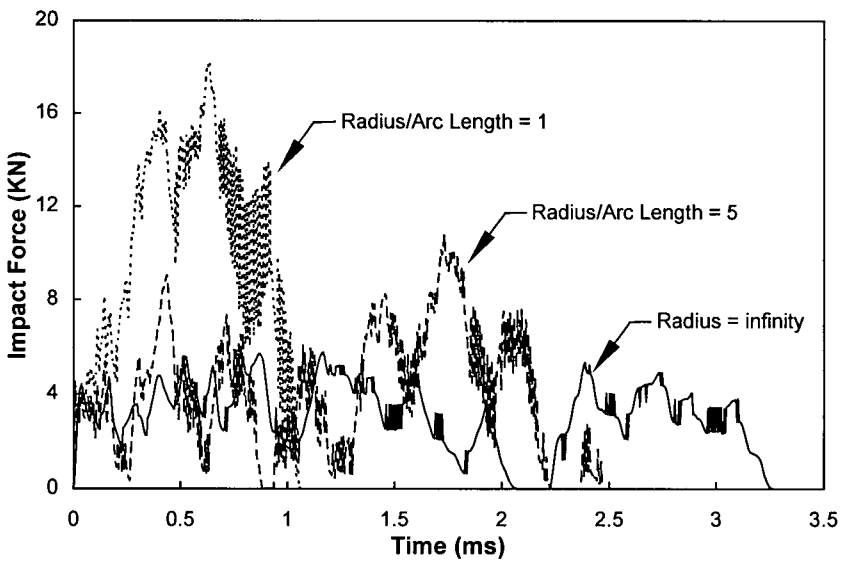

Figure 3.18 Parametric studies: The time history of the impact force for stiffened cylindrical shells with various radii of curvature. The material properties and geometric sizes are shown in Figure 3.15 and Table 3.6 with arc length $b = 0.508\ m$.

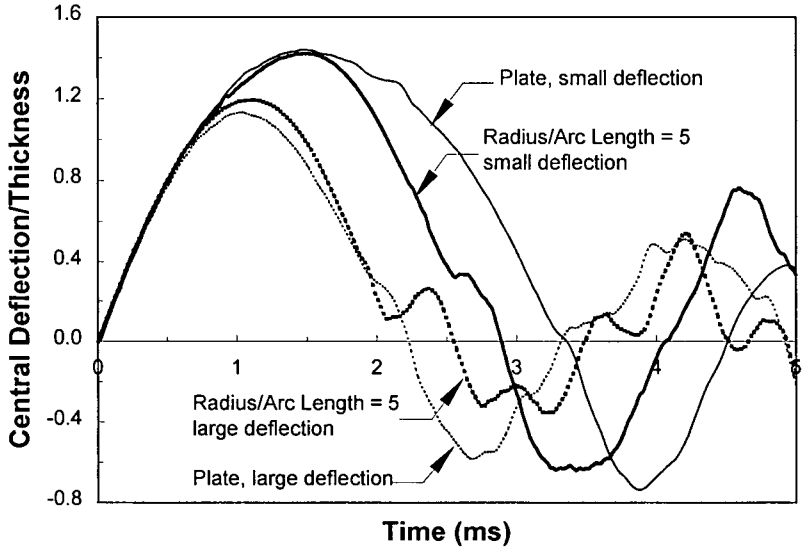

Figure 3.19 Parametric studies: The time history of predicted non-linear central deflection for stiffened cylindrical shells with various radii of curvature. The material properties and geometric sizes are shown in Figure 3.15 and Table 3.6 with arc length $b = 0.508\ m$.

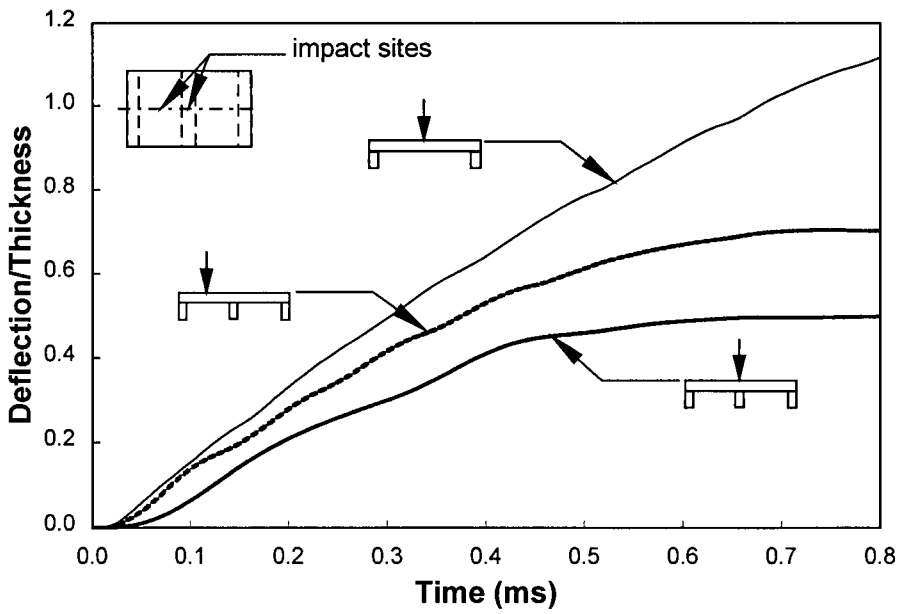

Figure 3.20 Parametric studies: Comparison of deflection at different impact sites. The material properties and geometric sizes are shown in Figure 3.15 and Table 3.6.

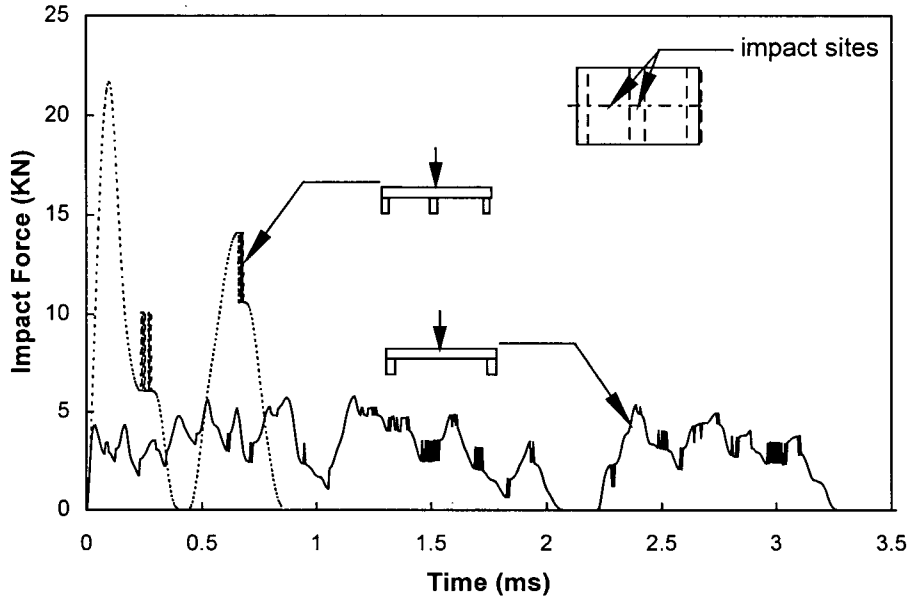

Figure 3.21 Parametric studies: Comparison of the impact force at different impact sites. The material properties and geometric sizes are shown in Figure 3.15 and Table 3.6.

Chapter Four: Literature Review on Penetration Mechanisms and Modelling

There are numerous papers in the literature addressing penetration problems of metallic materials. These have been carefully reviewed by Johnson (1972), Backman and Goldsmith (1978), and Corbett *et al.* (1996). The work on modelling the penetration behaviour of laminated composite materials started in the last decade. Some of the work have been reviewed by Abrate (1991 and 1994).

The present review will concentrate on the major penetration mechanisms and damage patterns found in penetration tests on metallic and composite materials using an indenter (or projectile). The transitions between these penetration mechanisms with changes in geometric sizes of projectiles and targets will also be discussed. The penetration models developed for laminated composite materials are reviewed as well.

Ballistic limit is the critical impact velocity required by the projectile to just perforate (or penetrate through) the target. It is treated as a kind of material property by engineers in their assessment of ballistic performance of materials. The major task of the next four chapters (Chapter Four to Seven) is to predict ballistic limit of a target and evaluate the effects from geometric sizes of a projectile and a target.

4.1 Penetration Mechanisms

The major penetration mechanisms that have been observed in penetration tests of metallic and composite materials by a conical indenter (or projectile) are hole expansion, dishing/petalling, transverse plugging, and delaminations. They are reviewed separately in the following sections.

4.1.1 Hole Expansion

4.1.1.1 Metals

When metallic materials are penetrated by conical projectiles, the projectiles push the material to the side, causing the material to yield and flow plastically. This kind of deformation is called "hole expansion" and was first tackled by Taylor (1948) and Hill (1950). In their models, the hole expansion problems were treated as plastic expansion of a circular hole in radial direction under plane stress condition. The material constitutive relation was assumed to be rigid-plastic, and the resulting stress and strain fields around the expansion hole were obtained by solving the differential equations of equilibrium. The total plastic work done in expanding the hole from zero radius to the projectile or indenter radius is equal to the product of target material yield stress σ_Y and the material volume displaced by the projectile. The plate thickening around the hole, caused by plastic flow and incompressibility of the material, was also taken into account in the calculation of plastic work by Taylor (1948) and Hill (1950).

After measuring the ballistic limits for different thicknesses of metallic plates, Woodward (1978) concluded that the plastic work done in hole expansion was a lower bound on energy absorption provided that the target yield stress value was carefully chosen. The flow stress (*i.e.* yield stress) defined in Woodward (1978) was the stress at a natural compressive strain of 1.0 in static indentation tests on that material. The natural compressive strain was the natural logarithm of the instantaneous thickness of material between the indenter tip and rigid support divided by the original plate thickness. Woodward also pointed out that when the ratio of projectile diameter to target thickness decreased, the plate thickening around the hole would not be as severe as that predicted by Taylor (1948). In this case, because of a relatively large value of target thickness compared to projectile diameter, a transition was occurring from the plane stress state assumed in Taylor (1948) to the state approaching the plane strain deformation where no plate thickening occurred.

4.1.1.2 Composites

Based upon cross-sectional examinations of perforated GFRP laminates (E-glass woven rovings in polyester resin) with a thickness of 15.0 mm, Greaves (1992) indicated that the major penetration mechanism, which was defined as absorbing most of the impact energy, was "compression and displacement of the plate material" by the fragment simulating projectile (FSP). Although Greaves (1992) didn't use the term "hole expansion" to describe this kind of deformation state, it did have the same characteristics of deformation pattern as hole expansion.

In their subsequent penetration tests of GFRP laminates (E-glass/polyster and S2-glass/phenolic), Howlett and Greaves (1995) found that the initial part of the measured force-displacement curves had a parabolic increase in load with indenter displacement. The curves then levelled off and there was no further increase in load once the indenter shaft started to penetrate into the GFRP laminates. The parabolic increase of load meant that the penetration mechanism in the plate material was hole expansion (see Section 5.2.2). The indenters used in their tests had diameters of 7.62 mm and 12.7 mm, and an included cone angle of 90°.

The hole expansion mechanism was also used by Zhu *et al.* (1992b) as the deformation pattern in the first stage of penetration when modelling the ballistic behaviour of woven kevlar composites impacted by a conical projectile with a cone angle of 60°.

4.1.2 Dishing/Petalling

4.1.2.1 Metals

After examining the cross-sections of perforated metallic plates with different thicknesses, Taylor (1948) found that hole expansion deformation was only valid when the projectile diameter was in the same order of or greater than the target thickness. For very thin plates, (*e.g.* plate thickness to projectile diameter ratio less than 0.1), the plates were always bent out of their planes. This type of deformation was called "dishing" by Thomson (1955). The energy absorption during the dishing type of deformation was calculated in Taylor (1948) and Thomson (1955) to be about one quarter of the impact energy absorbed in hole expansion.

When the dishing area around the hole continues to deform, the circumferential strain will exceed the material ductile limit and the dished material will break and form into several petals. This mechanism was called "petalling" by Zaid and Paul (1957).

Johnson *et al.* (1973) conducted a thorough series of penetration tests on metallic plates using conical indenters with included cone angles of 30°, 45°, 60°, 90°, 150°, and 180°. It was shown that the peak contact force increased with the indenter cone angle, while the total indenter movement for a complete perforation decreased. The contact force increased with the indenter movement first and then dropped when the indenter shaft entered into the plates. Johnson *et al.* (1973) proved in their analysis that the dishing or petalling deformation would not occur when the half cone angle $\beta_0 > \tan^{-1}(1/\mu)$, where μ is the coefficient of friction between the indenter and the dishing (or petalling) area in the plates.

The direction of the plate material movement in hole expansion differs from dishing/petalling. In hole expansion, the plate material is assumed to conform to the conical head shape of projectile and be pushed aside. However, in dishing/petalling mechanism, the plate material does not necessarily conform to the conical shape of projectile head and deforms in stretching or out of plane bending. A typical model for petalling deformation was developed by Landkof and Goldsmith (1985), where the crater deformation was determined by bending of the petals with plastic hinge on one end, instead of conforming to the configuration of projectile head.

When the plate thickness decreases, the penetration mechanism changes from hole expansion to dishing/petalling mode. For example, based upon calculated energy absorption during

perforation, Woodward (1978a) showed the transition of energetically favourable penetration mechanism from dishing to hole expansion when the plate thickness increased up to the projectile diameter. This prediction was also verified in his ballistic tests.

Dishing/petalling can also be attained from transverse plugging. Woodward and Cimpoeru (1997) observed the transition of penetration mechanisms from transverse plugging to dishing on the distal side of laminated aluminium plates in their ballistic tests, where blunt-ended and 90° conical projectiles were used. Thick homogeneous plates plugged transversely whereas laminates with the same thickness were indented on the impact side and deformed by a dishing mechanism on the exit side. Thinner laminates favoured more extensive dishing, which mainly involved energy absorption by stretching and bending.

4.1.2.2 Composites

Petalling on the distal side of thin laminates was also observed in ballistic tests of woven carbon fibre laminates in Goldsmith *et al.* (1995) where the ratio of the projectile diameter to target thickness was about 5 and the projectile included cone angle was 60°.

4.1.3 Transverse Plugging

4.1.3.1 Metals

When metallic plates are impacted by blunt-ended projectiles, the target material is geometrically constrained to move forward instead of laterally as impacted by conical projectiles. Thus a shear failure (ductile plugging) occurs. This has been shown clearly in

the ballistic tests by Woodward (1978b), Liss and Goldsmith (1984), and Crouch and Woodward (1988). In the instrumented impact tests of thin metallic plates by blunt projectiles, Langseth and Larsen (1990) found that a transverse plug always occurred at maximum impact force and a sudden drop of the force happened after occurrence of the plug.

In some cases, depending on the geometric sizes of projectiles and targets, transverse plugging also occurs when metallic plates are impacted by conical projectiles. For example, Recht *et al.* (1963) indicated that a transverse shearing plug was formed in the plates if the plate thickness h was less than both the projectile radius R_p and one half of the projectile head length L_c, *i.e.*, $h < R_p$ and $h < \frac{L_c}{2}$, provided that the projectile material was relatively strong and did not deform excessively. In ballistic tests by Woodward (1978b), transverse plugging generally took place in the plates when the projectile cone angle approached 90°.

Johnson *et al.* (1973) conducted static penetration tests on metallic plates by a series of conical indenters. According to their tests and analysis, transverse plugging occurred when the included cone angle $2\beta_0$ was greater than 90° no matter what friction coefficient μ was applied. Plugging always occurred if the values of $2\beta_0$ and μ fell into the area above line AB shown in Figure 4.1 and dishing or petalling for values below line CD. In the region between AB and CD, predicted behaviour was obscure and depended on the precise values of $2\beta_0$ and μ. The ratio of the indenter shaft diameter to the plate thickness was about 4 in their studies, which meant that the plates were still relatively thin.

Similar trends were also seen by Woodward (1984) in his qualitative study based upon observations from many ballistic tests.

4.1.3.2 Composites

In penetration tests of graphite/epoxy laminates by blunt-ended projectiles, Lee and Sun (1993a) found that transverse plugging was a major damage pattern during penetration of composites. Ursenbach *et al.* (1995) also observed the same phenomenon in their penetration tests of T300H/F593 CFRP laminates.

Similar to metals, for conical-tipped projectiles, transverse plugging also occurs when the projectile cone angle is large. For example, Zhu *et al.* (1992a) found transverse plugging on the distal side of a 6.35 mm thick woven Kevlar laminate when penetrated by a 120° cone.

4.1.4 Delamination

Malvern *et al.* (1989) conducted a series of nonpenetrating impact tests on different kinds of laminated composites. They found that delamination was a major damage mechanism in the laminates. The total delamination area was found to be a linear function of the energy absorbed by the plates.

When the impact velocity was increased beyond the ballistic limit, the relationship between the delamination area and the initial impact energy was still linear but with a much smaller slope as shown in Wu and Chang (1995).

Greaves (1992) observed delamination in 15 mm thick E-glass composites which was as large as 160 mm in diameter on the distal surface of the plate, i.e., about 10 times the plate thickness and 20 times the projectile diameter.

Although delamination may not dissipate a major amount of impact energy as shown in Zhu *et al.* (1992a), it will greatly affect the local deformation and subsequent damage patterns. For example, in dynamic penetration tests of laminated aluminium plates conducted by Woodward *et al.* (1997), the penetration mechanism changed from transverse plugging to dishing/petalling due to delaminations in the plates. In the penetration tests of T300H/F593 CFRP laminates conducted by Ursenbach *et al.* (1995), delamination increased the local deformation and greatly reduced the flexural stiffness of the plate.

4.2 Transition of Penetration Mechanisms

Woodward (1984) also observed dishing deformation instead of hole expansion in thick plates when the plate material had a very low toughness in the through-thickness direction. It was found that the target material could bulge rearward (similar to dishing of thin plates) instead of being pushed aside when the projectile penetrated to a certain depth in the target.

Goldsmith and Finnegan (1986) performed a series of dynamic penetration tests on metallic plates by conical (60°) and blunt (180°) projectiles. The plate thicknesses ranged from 1.78 mm to 25.4 mm. The penetration mechanisms such as dishing, petalling, plugging, and shear banding were identified from experimental observations and metallurgical tests. The transition of these penetration mechanisms were also noted, which meant that both the target

thickness and the projectile cone angle played an important role in the transitions from one penetration mechanism to another.

Based upon energy analysis, Woodward (1984) proposed the following transitions of penetration mechanisms for conical projectiles:

- When the thickness of the plate still to be penetrated, h, is less than the projectile diameter $2R_p$, $h < 2R_p$, dishing instead of hole expansion will become the favourable penetration mechanism for metallic materials with low toughness in the through thickness direction.

- When the thickness of the plate still to be penetrated, h, is less than $\sqrt{3}/2$ times the projectile diameter, $h < \sqrt{3}R_p$, ductile plug formation and ejection instead of hole expansion will become the favourable penetration mechanism for metallic materials with high strength, low work-hardening rate, and high thermal softening rate.

4.3 Penetration Modelling of Composites

In this section, the available penetration models for composites are reviewed. However, before discussing the models it is instructive to highlight the similarities between static and dynamic penetration patterns as obtained from experiments.

4.3.1 Static vs. Dynamic Tests

Experimental study conducted by Lee and Sun (1993b) indicated that in static penetration tests of carbon/epoxy laminates the relationship between the contact force and indenter displacement showed approximately the same trends for various laminate planar sizes. It was inferred from the indenter force-displacement curves that the load at the onset of damage and the ultimate load were about the same. Impact test results also showed that the dynamic failure modes were very similar to those obtained under static loading. This close agreement in damage patterns indicated the possibility of using static penetration tests to characterise the dynamic penetration process. Similar conclusions were also drawn by Zhu *et al.* (1992a), Lee and Sun (1993a), Sun and Potti (1996), Jackson (1996), and Potti and Sun (1997).

Sanders (1997) and Delfosse (1994b) examined the micrographs of cross-sections of IM7/8551-7 CFRP laminates in static penetration and dynamic penetration tests. They are shown in Figure 4.2, where the damage area and pattern are very similar in both tests.

Virostek *et al.* (1987) measured the time history of impact force when projectiles with conical or hemispherical head shapes impacted thin plates at different angles of incidence. Different plate materials were studied, ranging from aluminium, steel, lexan, nylon, ceramic, and Kevlar. It was found that the peak impact force obtained for a given plate material under normal incidence was relatively independent of the initial projectile velocity for impacts where perforation occurred (*i.e.*, above ballistic limit). For experiments at velocities below the ballistic limit, the peak impact force was found to be approximately proportional to the initial impact velocity.

Based upon the above work, it appears that static penetration tests can be used to identify the damage patterns and penetration mechanisms of some laminated composites when strain-rate effect is neglected. The closeness of peak impact force for a certain target which completely perforated by projectiles in different velocities (Virostek *et al.*, 1987) means that their force-displacement curves have similar shapes, because for a certain projectile and target the projectile displacement span is almost the same (sum of projectile length plus target thickness and its permanent deflection). This was verified by the measurements in ballistic tests of Sanders (1997) as well. Thus the damage modes and deformation patterns can be assumed to be independent of impact velocity when perforation occurs.

4.3.2 Analytical Models for Projectiles with Spherical Head Shapes

Cantwell and Morton (1990) developed a simple analytical model for perforation of CFRP laminates by a spherical projectile. Using balancing of energy, the projectile kinetic energy was dissipated into the laminate elastic flexure, indentation, delamination, and transverse plugging, represented by E_f , E_c , E_d, and E_p, respectively. E_f, the maximum strain energy absorbed by the laminates subjected to transverse loading, was determined by classical laminate theory in conjunction with a maximum strain failure criterion. E_c, the energy dissipated in indenting the laminates, was determined by a Hertzian contact law. E_d, the energy dissipated in delamination, was determined by measuring the area of delamination after the tests and multiplying this area by the fracture energy of delamination. E_p, the energy dissipated in plugging of the plates, was determined by multiplying the surface area of fracture zone by the transverse fracture energy of the composite. This was a very simple

model and the predicted ballistic limits were in good agreement with experimental results for thin laminated plates.

However, details of the impact event such as the impact force cannot be obtained using this kind of approach. In most cases, the peak impact force governs the damage mode and progression and is thus another important factor that needs to be considered in addition to the energy absorbed by the target.

Cantwell (1988) studied the perforation events in CFRP beams resting on steel supports with different opening sizes and shapes. Test data showed that changing the opening size did not influence the ballistic response of the targets and its energy absorption capability, due to the nature of localised impact loading. However, changing the target thickness could significantly affect the impact energy required to perforate the target.

The penetrating impact response of woven E-glass/epoxy composite laminates by a hemi-spherically-tipped projectile was studied in Wu and Chang (1995). The impact velocity ranged from well below the ballistic limit of the target material to twice its ballistic limit. The relationships between the peak impact force and the extent of damage (delamination area) versus the initial impact energy of the projectile were studied. The details on the experimental set-up and procedures were described in Wu *et al.* (1994).

4.3.3 Analytical Models for Blunt-Ended Projectiles

Lee and Sun (1993a & b) developed an analytical model for the penetration of graphite/epoxy laminates impacted by a blunt projectile. Delaminations and transverse plugging were

identified as the two major mechanisms during penetration. Since the damage patterns in dynamic penetration resembled those observed in static penetration tests, the model used results from the static tests to characterise the dynamic penetration. Finite element analyses were conducted to obtain the detailed distribution of stress components and predict the initiation of delamination in the laminates. The force for plug initiation was a material property determined from the static penetration tests. The validity of the model prediction was restricted to limited laminate thicknesses.

In an attempt to improve their previous model, Sun and Potti (1996), and Potti and Sun (1997) developed a ring model to predict damage progression and energy absorption for thicker laminates. A force-displacement curve from quasi-static penetration tests by a blunt indenter also served as the "structural constitutive model" which captured the highly non-linear behaviour of the laminate during dynamic penetration events. The transverse shear modulus was degraded to model the progressive reduction of plate stiffness appearing in static penetration curves. Four different kinds of initiation criteria for transverse plugging were suggested. They were based on contact force, shear force, plate shear strain, and plate deflection. In the latter, the differential plate deflection between the periphery of the indenter and the boundary of local area was used as an initiation criterion. The local area was defined in the quasi-static penetration tests as a circular area with a diameter three times that of the projectile diameter.

In order to model the behaviour of a partially delaminated plate, Ursenbach *et al.* (1995) assumed an embedded isotropic plate with reduced stiffness to represent the region of delamination. The deformation behaviour of the laminates in the post-delamination stage

was described using the experimental measurements of strains and displacements at the plate centre. The model was capable of estimating the delamination size and the effective bending modulus of the delaminated zone. The predicted delamination sizes for various laminate thicknesses were successfully correlated with those measured using C-scans.

For GFRP composite laminates, a simple analytical model based upon one-dimensional stress wave theory was developed by Howlett and Greaves (1995) to predict the ballistic limit of the targets for blunt-ended projectiles. The authors also conducted static penetration tests on GFRP laminates using conical-tipped indenters.

4.3.4 Analytical Models for Projectiles with Conical Head Shapes

Zhu *et al.* (1992b) developed an analytical model for the penetration of Kevlar 29/polyester laminated plates by a conical projectile with 60° included cone angle. The penetration process was divided into three successive and non-interactive stages: indentation, perforation, and projectile exit. The analysis consisted of both global and local deformation, where the former employed linear-elastic laminate plate theory, while the latter consisted of the indention (hole expansion) on the frontal surface of the target, bulging at the distal surface, fibre breakage, and delamination. Friction, neglected in the first two stages, was the only force acting during the exit phase. Resistance to projectile penetration was used in conjunction with Newton's law to determine the projectile and structural response and a maximum strain criterion was applied in the penetration process to reduce the material strength due to the impact damage. A comparison of predicted ballistic limits with test measurements showed good agreement. In their tests, the ballistic limit was found to vary

linearly with the laminate thickness. The lay-up of the laminates and prior partial delaminations in the laminates did not play a significant role in the energy absorption capability of the laminates.

For thin, woven, carbon fibre/epoxy laminates impacted by 60° conical projectiles, Goldsmith *et al.* (1995) developed a penetration model based upon energy balance, taking account of energy absorption due to global plate deflection, fibre breakage, delamination, formation and bending of petals, and friction between the projectile and the plate. The maximum delamination size was found to be as large as four times the projectile diameter.

A simplifying model based upon one-dimensional wave propagation theory for impacts on fibre-reinforced polymer with fibre architectures of unidirectional fibres and woven fabric composites was developed by Navarro *et al.* (1994). In this model, the kinetic energy of the projectile was assumed to be absorbed in the form of elastic and kinetic energy in the fibres directly in contact with the projectile. The interaction effects between warp and filling fibres at crossovers were considered using an approximate solution. The predictions by the model agreed with the measured projectile displacement and velocity drop. However, the predicted impact force was far from the experimental measurements.

Pierson *et al.* (1993) applied the penetration models in Awerbuch and Bodner (1974) and Zhu *et al.* (1992b) to CFRP laminates and compared the predictions with measurements from ballistic tests. They pointed out that because of the inherent differences between the metallic and composite materials, models initially developed for metals could not capture the

evolution, sequence, and magnitude of the damage growth if such models were directly applied to composite materials.

4.3.5 Analytical Model for FSP (Fragment Simulating Projectiles)

In the ballistic studies of S2-glass laminates conducted by Bless and Hartman (1989), the post-test examination of the perforated target cross-sections revealed that there was a region that had experienced compressive failure and expulsion of cut fibres, followed by a region which appears to be dominated by tensile failure and parting of the cut fibres. The former was in the frontal part of the target, considered by the authors as "compressive flow around the penetrator" and yielded the same equation calculating the force as the hole expansion mechanism in present approach (see section 5.2.2). The latter mechanism was in the distal side of the target, defined as "shear failure around the periphery of the penetration cavity", which is the transverse plugging mechanism. The effective compressive strength and effective transverse strength of the laminates were proposed by the authors to measure the penetration resistance of the laminates. Increasing the fracture strength of the resin matrix resulted in increase in the ballistic limit of the laminated composites. The projectiles used in their tests were FSP (fragment simulating projectiles), which have a chisel shape nose. The ballistic limit was found to be proportional to the square root of the transverse compressive strength of the laminates.

4.3.6 Numerical Modelling

Because experimental methods for dynamic perforation problems can become very expensive when numerous variables are involved in the design of laminated composite structures, numerical analysis has been found to be extremely useful in interpreting experimental results and providing a tool for parametric studies.

A number of existing computer programs suitable for simulating penetration problems have been carefully reviewed in Vaziri *et al.* (1989). The most commonly used codes are DYNA2D, DYNA3D, AUTODYN, and PAMCRASH. DYNA3D, is an explicit three-dimensional finite element code originally developed at Lawrence Livermore National Laboratory, and subsequently enhanced and marketed by Livermore Software Technology Corporation (LSTC).

Many material models are already built in and users can also import their own material models to DYNA3D for penetration analysis. Currently implemented damage models in DYNA for composite materials are the Chang and Chang (1987) model (see Blanas, 1991) and Matzenmiller *et al.* (1991) model (see Williams and Vaziri, 1995). Lu and Vaziri (1994) provided an extensive review of constitutive and failure models for numerical analysis of impact response of composites using DYNA2D and DYNA3D.

Williams (1998) formulated a physically-based damage model based on continuum damage mechanics and implemented it into LS-DYNA3D. This model takes account of stiffness reduction and strain softening in composite laminates. Williams (1998) used his model to simulate the response of thin CFRP laminates impacted by a hemispherical projectile.

4.4 Summary

From the review conducted here, it appears that there has been some limited work on modelling the penetration process in laminated composites. These models provide good estimates of the energy absorption and ballistic limits of composites for certain material systems and certain ranges of geometric sizes of projectiles and targets. However, little or no work has been reported in the literature on prediction of impact force-time history or force-projectile displacement relationship, which are very important when predicting damage initiation, damage progression, and transient response of laminated structures. Also, the effects of projectile cone angle on ballistic performance of composite materials have not been reported yet. The present work aims at fulfilling these gaps. A penetration model will be developed in Chapter Five and Six. This model, which is driven by experimental observations and engineering mechanisms will be used in conjunction with the finite element model developed earlier to simulate the ballistic response of various laminates in Chapter Seven.

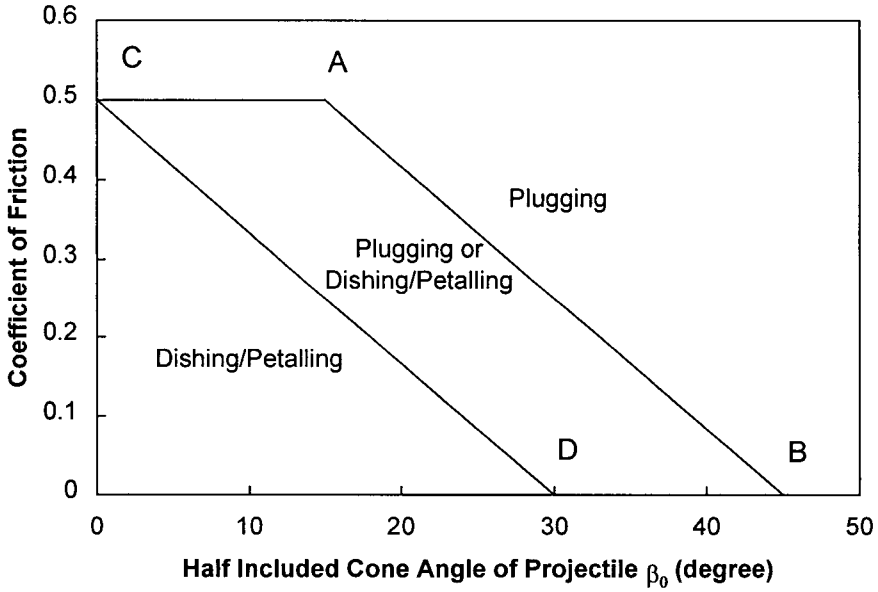

Figure 4.1 Schematic illustration of transition of penetration mechanisms in static penetration tests of thin metallic plates by conical indenters with different cone angles (Johnson *et al.*, 1973).

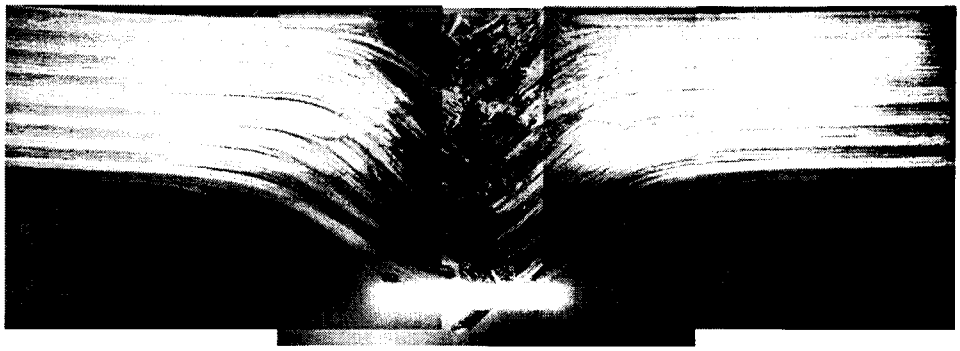

(a) Static Penetration Test

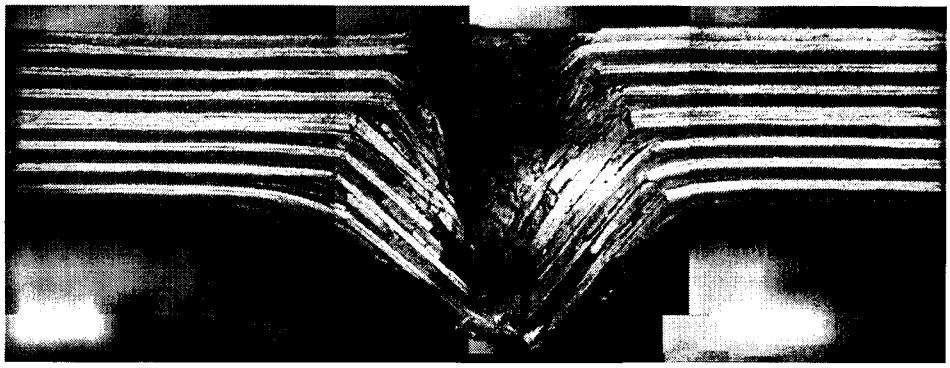

(b) Dynamic Penetration Test

Figure 4.2 Micrographs of cross-sections of IM7/8551-7 CFRP laminates in (a) static penetration tests and (b) in dynamic penetration tests (Delfosse, 1994b and Sanders, 1997).

Chapter Five: Penetration Mechanisms

Guided by the literature review in the previous chapter and the supporting experimental work carried out at UBC, several penetration mechanisms are studied in this chapter. These mechanisms include elastic deformation, hole expansion, delamination and dishing/petalling, transverse plugging, and friction. Before examining these mechanisms, the experimental penetration results of Carbon Fibre-Reinforced Polymer (CFRP) and Glass Fibre-Reinforced Polymer (GFRP) are summarised first.

5.1 Experimental Investigations

Static penetration tests and indentation tests are two types of experiments used to investigate penetration mechanisms of composite materials (Bless *et al.* 1989, Lee *et al.* 1993b, Zhu *et al.* 1992a, and Howlett *et al.* 1995). These tests were conducted at UBC by Delfosse (1994b) and Sanders (1997) on CFRP and GFRP laminates. They provide physical insight into penetration mechanisms outlined in this chapter and the penetration model developed in the next chapter.

5.1.1 Static Penetration Tests

Static penetration tests shown in Figure 5.1 are performed on an Instron Universal Testing Machine for CFRP and GFRP laminated plates. The indenter size and material properties are

listed in Table 5.1. The geometric sizes and material properties of CFRP and GFRP laminates are summarised in Table 5.2 and Table 5.3, respectively. The static penetration tests are conducted under displacement control with the penetration force being measured. A video camera and microphone are also used to record the penetration process as well.

Two types of opening sizes for rigid (steel) support plates are used in the tests. One is called a large-geometry opening, which is rectangular with dimensions of 127 mm × 76.2 mm. The other is called a small-geometry opening, which is circular with a diameter of 25.4 mm. The tests on the small-geometry opening are treated as material characterisation tests in the present work. This is because the small specimen minimises the global bending of the laminate and hence the response is primarily material rather than structural.

The laminated specimens with a rectangular size of 152.4 mm × 101.6 mm are used for the large-geometry testing, while the specimens with a square size of 50.8 mm × 50.8 mm are used in the small-geometry tests.

The specimens are categorised in three groups (Delfosse 1994b and Sanders 1997). The first group of specimens is used to get the whole indenter force-displacement curves up to the complete perforation of the laminates. The second group is also tested up to the complete perforation but during the tests it is loaded, unloaded, and reloaded at various points on the force-displacement curve in order to check the visible damages on the frontal and distal surfaces of the specimens. The third group of specimens is loaded up to the check points and unloaded. Subsequently these specimens are cut along the 0° direction. Micrographic

images of the cross-sections of these specimens and their deformation profiles are then carefully studied.

5.1.2 Static Indentation Tests

A schematic illustration of the static indentation tests is shown in Figure 5.2, where a laminated plate is supported by a rigid (steel) flat plate without any openings, and thus the bending of the laminate is inhibited. Such tests are used to characterise the compressive behaviour of the material for penetration problems, because the compressive strength obtained from traditional uniaxial compression tests is not suitable for penetration problems.

To characterise the penetration behaviour, Woordward *et al.* (1994) carried out a set of constrained compressive tests on various materials (Aluminium, GFRP, Kevlar, Nylon, and Polyethylene) and for aluminium compared the derived stress-strain curves with those under simple compressive loading. They found that there was a substantial difference between these two curves. For a given strain, the stresses in the constrained compressive tests were much larger than those in the simple compressive tests.

Static indentation tests are considered to be a more realistic measure of the penetration resistance of a material. The first application of the static indentation tests in composite materials was by Zhu *et al.* (1992a & b), where a mean indentation pressure for woven Kevlar was obtained from the tests.

In the present approach, the static indentation tests were conducted using the indenters with two different kinds of head shapes, namely 37° and 120° included cone angles. The results

of the tests (such as the force-displacement relationship and the penetrated hole shape) are used to calculate the effective compressive resistance of the material to penetration.

5.1.3 Experimental Force-Displacement Relationships

The results of static penetration tests on CFRP and GFRP laminates are prescribed and discussed in the following sections.

5.1.3.1 CFRP Laminates

The relationship between the measured penetration force and indenter displacement in the static penetration tests on CFRP laminates up to the point when the indenter tip penetrates through the target is shown in Figure 5.3 for indenters with four different included cone angles: 37°, 60°, 120°, and 180° (Delfosse 1994b). The tests on 37° and 180° conical indenters were conducted on the support plate with the large-geometry opening while the tests on 60° and 120° conical indenters were conducted on the plate with the small-geometry opening due to the shortage of material supply. Details of the experimental investigation have been presented in Delfosse (1994b) and Sanders (1997). Some general trends are summarised here:

1. The force-displacement relationship for small cone angle indenters (37° and 60°) are quite different from those corresponding to large cone angle indenters (120° and 180°). Indenters with small cone angles result in force-displacement curves that are more flat at the peak load and extend over a wide range of indenter displacement. However, indenters

with large cone angles result in force-displacement curves that are more steep leading up to the peak load and then drop abruptly.

2. The initial part of the measured load-displacement curves always has a nearly parabolic shape. The rate of increase of the force depends on the included cone angle of the indenter. Larger cone angles lead to higher rates of force increase. The specimen penetrated by a 37° conical indenter was unloaded and cut into two halves (Sanders, 1997). Figure 5.4 shows the cross-sectional micrograph of the specimen, where material around the indenter is seen to be crushed and pushed aside by the indenter. These are the characteristics of hole expansion mechanism reviewed in the previous chapter.

3. There is a load drop in the force-displacement curve when the penetration force reaches its peak value. For penetration by an indenter with a small cone angle, this load drop is caused by a number of fibre breaks as shown in Figure 5.5 (Sanders, 1997); while for an indenter with a large cone angle, it is caused by the initiation and push-out of a transverse plug as shown in Figure 5.6. The former case corresponds to the indenter tip approaching the distal surface of the laminate, while in the latter case the tip stays well inside the laminate.

4. Delaminations are initiated as shown in Figure 5.7 and are well developed by the time the indenter shaft reaches the frontal surface of the laminate as shown in Figure 5.8 (Sanders, 1997). Because of the presence of the delaminations, the whole laminate is separated to several sublaminates in the thickness direction. Each sublaminate behaves like a thin plate and has a significant bending behaviour.

5.1.3.2 GFRP Laminates

Static penetration tests on the GFRP laminates were conducted by Sanders (1997) for three different laminate thicknesses (6.35 mm, 12.7 mm, and 19.05 mm). The relationship between the measured penetration force and the indenter displacement in these tests is shown in Figure 5.9 for the indenter with an included cone angle of 37° and in Figure 5.10 for the indenter with an angle of 120°. The support plate has a large-geometry opening. Details of these tests have been presented in Sanders (1997). The general characteristics of the force-displacement curves are summarised here:

1. Similar to CFRP, the force-displacement relationship for small cone angle indenter (37°) is substantially different from the corresponding curve for large cone angle indenter (120°). The force-displacement curve for the indenter with a small cone angle is triangular in shape, while the force-displacement curve for the indenter with a large cone angle has a plateau regime spanning over a wider displacement range than that corresponding to the small cone angle indenter.

2. The whole penetration curve is quite smooth and continuous. There are no sudden load drops for both the large and small cone angle indenters.

3. The micro-delaminations and matrix cracks start very early during the penetration as shown in Figure 5.11. The delamination pattern in GFRP is quite different from that in CFRP laminates. The massive micro-delaminations are developed around the indenter while in CFRP macro-delaminations are developed only below the indenter. Macro-delamination is observed in the GFRP laminates when penetrated by a 120° conical

indenter as shown in Figure 5.12. A big gap between the sublaminates stemming from the macro-delamination is clearly visible.

4. The indenter with a 120° cone angle does not actually penetrate through the 6.35 mm thick laminate as shown in Figure 5.13. It simply pushes the laminate through the opening of the support plate. For the 12.70 mm and 19.05 mm thick laminates, the indenter penetrates through to a certain depth in the laminates. After that, a macro delamination initiates, which causes the sub-laminate below the indenter to separate from the original laminate. Then, similar to the 6.35 mm thick laminate, the indenter pushes the sub-laminate through the opening of the support plate and never penetrates through it.

5.1.4 Characterised Force-Displacement Relationships

Based on the experimental observation summarised in the previous section, the penetration process can be characterised by the schematic curves shown in Figure 5.14 for CFRP and GFRP laminates when penetrated by an indenter with a general cone angle. The critical points are shown as capital letters on these curves. The penetration mechanism that operates between two adjacent critical points are identified. The whole penetration event is divided into four phases, from phase I to phase IV. The start and end points of these phases are labelled by capital letters A-D.

It should be mentioned here that these are typical force-displacement curves during penetration of CFRP and GFRP laminates. They capture the essence of the force-

displacement relationship but could not represent exactly all the cases of different cone angles, different target thicknesses, and different projectile lengths.

Phase I: Line OA

In this stage, the laminate material around the indenter is crushed and pushed aside by the indenter. Comparing with the severe damage (a penetration hole) on the frontal surface of the laminate, there is just a slight deformation occurring on the laminate distal surface according to the micrographic study in Figure 5.4. The penetration mechanism during this phase is categorised as hole expansion. The local stresses (transverse shear stresses) are built up with increasing indenter penetration depth. When the increasing local shear stresses meet the initiation criterion for delamination or transverse shear plugging, either delaminations are initiated in the laminate below the indenter as shown by curve 1 in Figure 5.14 or transverse plugging is initiated in the laminate below the indenter as shown by curve 2 in the same figure. The initiation point for these penetration mechanisms is labelled as "A_1" for curve 1 and "A_2" for curve 2.

Phase II, Line AB

In this stage, the penetration mechanisms are different for the two characterised force-displacement curves.

On curve 1, the laminate is divided into two deformation zones as shown in Figure 5.15. In zone I, the frontal part of the laminate, the major penetration mechanism is hole expansion (see Figure 5.5). In zone II, the distal part of the laminate, the bending rigidity is reduced due

to the delaminations thus leading to severe bending deformations(see Figure 5.7 and Figure 5.8). The penetration mechanism in zone II is flexural deformation of a delaminated plate with a number of delaminations (splits). We will refer to this as "flexural deformation of a split-plate". There is a large amount of local deformation on the distal surface of the laminate. At point B_1', the indenter tip penetrates through the target if the indenter cone length L_c is greater than the target thickness ($L_c > h$). Thus the target is defined as "partially perforated" at this stage. At point B_1, the indenter shaft reaches the frontal surface of the target.

In curve 2, the penetration force drops from point A_2 to point B_2' on the force-displacement curve. This drop is caused by transverse shear failure of the laminate (see Figure 5.6). The laminate material below the indenter loses its transverse shear capacity and a transverse plug is initiated as shown in Figure 5.16. At point B_2', friction between an indenter-plug system and the adjacent target material initiates. With increasing indenter shaft length in the laminate, the frictional force between the plug and the adjacent laminate material is gradually replaced by the frictional force between the indenter and the laminate material around the indenter. At point B_2, the indenter tip penetrates through the target and the target is partially perforated. It should be noted that a horizontal curve is used here to represent the penetration stage between points B_2' and B_2. However, both the experimental measurement and model prediction show that the curve between B_2' and B_2 may not be horizontal.

Phase III, Line BC

In this phase, the target has been partially perforated for both curves. The friction becomes the major penetration mechanism when the indenter shaft reaches the laminate frontal surface. The length of the shaft in the laminate becomes larger and larger with the indenter penetration. For curve 1, the penetration force resulting from hole expansion and flexural deformation of the split-plate both decrease with increasing shaft length in the laminate. However, for both curves the friction force between the indenter and the adjacent laminate material increases with the advancing indenter displacement.

At point C, for both curves, the indenter shaft reaches the distal surface of the laminate (*i.e.*, the indenter's conical head exits the laminate). Thus only the indenter shaft stays in the laminate after point C.

Phase IV, Line CD

In this stage, the force is purely frictional and energy is absorbed through friction only.

5.2 Identification of Penetration Mechanisms

Based on the literature review in the previous chapter and experimental studies on penetration behaviour of CFRP and GFRP laminates, one deformation mechanism and four penetration mechanisms have been identified. They are elastic deformation, hole expansion, flexural deflection of a split-plate (delamination and dishing/petalling), transverse shear plugging, and friction. Each mechanism is discussed here in separate sub-sections.

5.2.1 Elastic Deformation

When the penetration force is very low, the global deformation of the laminate at the impact site is linear-elastic. If the penetration depth is very small, the indenter displacement is almost the same as the laminate deflection at the impact site. Thus the relationship between the penetration force and the indenter displacement is linear until appreciable penetration depth sets in or the penetration force becomes high.

When either the penetration depth or the penetration force becomes large, the material around the projectile or indenter undergoes severe non-linear deformations and a large amount of damage occurs under or around the projectile. However, the material far away from the indenter continues to deform elastically, and its deflection can be calculated using the super finite element computer program developed in Chapters Two and Three.

The equivalent laminate elastic modulus and Poisson's ratio of the CFRP laminates are calculated using the classical lamination plate theory (*e.g.* Whitney, 1987), yielding $E = 62.5\ GPa$ and $\nu = 0.32$.

The equivalent laminate elastic modulus of the GFRP laminates is back-calculated from three-point flexural tests on 6.35 mm, 12.70 mm, and 19.05 mm thick specimens resulting in a mean elastic modulus, $E = 16.2\ GPa$. This value is close to the one measured by Woodward *et al.* (1994) as 18.1 GPa for plain woven S2-glass laminates with nominal fibre-volume fraction of 60%. The Poisson's ratio is taken to be $\nu = 0.2$ (Greaves, 1993).

5.2.2 Hole Expansion

In the hole expansion mechanism, the material is cut at the apex of the cone and pushed away from the conical indenter as shown in Figures 5.17 and 5.18. This mechanism initiates when the contact pressure under the cone reaches a certain mean indentation pressure value.

From Figure 5.17 and equilibrium of force in the vertical direction, the penetration force F can be written as

$$F = \sigma_0(1+\frac{\mu}{\tan\beta_0})A_p = \sigma_m \pi(\alpha + b_0)^2 \tan^2\beta_0 \tag{5.1}$$

where α is the penetration depth defined in Figure 5.18 and σ_m is the mean indentation pressure defined as

$$\sigma_m = \sigma_0(1+\frac{\mu}{\tan\beta_0}) \tag{5.2}$$

In Equations (5.1) and (5.2), β_0 is the half included cone angle of the indenter, σ_0 is the hole expansion pressure, A_p is the projected area of the indenter, b_0 is the bluntness of the indenter as shown in Figure 5.19 which is assumed to be very small, and μ is the coefficient of friction.

When Equation (5.1) is used to calculate a penetration force at a certain depth of penetration, σ_0 and μ have to be known first. σ_0 is a measure of the compressive resistance of the laminate material, while μ measures its interfacial or frictional resistance.

In the present approach, the static indentation tests are conducted using indenters with two different kinds of head shapes, 37° and 120° cone angles. From the measured force-

displacement curves in these tests, the mean indentation pressure σ_m in each case can be calculated by rearranging Equation (5.1):

$$\sigma_m = \frac{F}{\pi(\alpha + b_0)^2 \tan^2 \beta_0} \tag{5.3}$$

The hole expansion pressure σ_0, which is treated as the compressive strength of the material, and coefficient of friction μ, can then be obtained by using Equation (5.2) and the two known values of mean indentation pressure σ_m. Thus σ_0 and μ are empirical parameters that best fit the current experimental measurements.

With the knowledge of σ_0 and μ, the indentation pressure for an indenter with a general included cone angle can be readily calculated from Equation (5.2).

This kind of approach will provide a realistic estimation of the effective compressive resistance of the material to projectile (or indenter) penetration.

5.2.2.1 Material Characterisation

Material characterisation tests (static indentation tests) are conducted for CFRP and GFRP laminates. The characterisation for CFRP and GFRP is discussed in the following sections.

5.2.2.1.1 CFRP Laminates

The indentation force and indenter displacement in the static indentation tests of CFRP laminates are shown in Figure 5.20 where the indenter has an included cone angle of 37°. The thickness of the specimen is 6.15 mm. The indentation depth in the target is equal to the

indenter displacement because the distal surface of the laminate is supported by a rigid block. The bluntness of the indenter (see Figure 5.19) is $b_0 = 0.5\ mm$. The relationship between the indentation pressure and indenter displacement is also shown in Figure 5.20 and its mean value is calculated as $\sigma_m = 1585\ MPa$.

The indentation force versus the indenter displacement of a 120° indenter penetrating the same specimen is shown in Figure 5.21. The calculation of the indentation pressure ends when the indenter shaft reaches the frontal surface of the laminate, *i. e.*, after 2.2 mm of indenter displacement. Careful examination of the specimen cross-section revealed the so-called "sinking-in" phenomenon on the frontal surface around the indenter as shown in Figure 5.22. This was not observed in the indentation tests by the 37° indenter.

"Sinking-in" was first identified in the indentation tests on metals by Tabor (1951). When the indenter material is harder than the specimen material, the specimen material is depressed around the indentation and left at a lower level than the material farther away from the indenter. This is only observed close to the rim of the indentation and is referred to as "sinking-in" by Tabor (1951).

Because of the "sinking in" phenomenon, the indentation depth will be over-predicted if we simply take the indenter displacement to be the indentation depth. Measuring Δ and α in Figure 5.22 will provide a relationship between the indentation depth and indenter displacement as $\alpha \approx 0.7\Delta$. Based on the above penetration depth, the indentation pressure is calculated using Equation (5.3). The mean pressure turns out to be $\sigma_m = 697\ MPa$ as shown in Figure 5.21. The indenter is assumed to have no bluntness in this calculation.

5.2.2.1.2 GFRP laminates

For GFRP (G-glass) laminates, Delfosse (1994b) measured the elastic modulus in the through-thickness direction to be $E_z = 14.0\ GPa$, a value close to the elastic modulus in the in-plane direction $E_x = 19.0\ GPa$. Because of its relatively high elastic modulus in the transverse direction, the deformation of this material around the indentation is in the form of "piling-up" instead of "sinking-in" (Tabor 1951), especially for an indenter with a small included cone angle. This phenomenon was observed by Sanders (1997) in indentation tests on GFRP (S2-glass) laminates as well.

In the material "piling-up", there is an upward extrusion of displaced material to form a raised crater in the specimen. Thus if we simply use the indenter displacement Δ as the indentation depth in the specimen, the actual indentation α will be under-predicted as shown in Figure 5.24. The under-prediction of the indentation depth will result in under-prediction of contact area and therefore over-prediction of indentation pressure.

Following the same approach as that for the CFRP laminate, the relationship between the indentation depth and the indenter displacement is estimated from the examination of the cross-section of GFRP specimen shown in Figure 5.24 as $\alpha \approx 1.3\Delta$. The indentation pressures are calculated from Equation (5.3) as shown in Figures 5.23 and 5.25 and their mean values are $\sigma_m = 860\ MPa$ for the 37° indenter and $\sigma_m = 368\ MPa$ for the 120° indenter.

Based on the measured mean indentation pressure values corresponding to the two included cone angles of 37° and 120°, the hole expansion pressure σ_0 and the coefficient of friction μ for CFRP and GFRP laminates are calculated using Equation (5.2) as

$$\sigma_0 = 485\ MPa \text{ and } \mu = 0.75 \text{ for CFRP}$$

$$\sigma_0 = 250\ MPa \text{ and } \mu = 0.81 \text{ for GFRP}$$

Figure 5.26 shows the comparison between the measured and predicted force-displacement relationships of a 6.15 mm CFRP specimen when statically penetrated by an indenter with an included cone angle of 60°. The predicted curve is calculated using the above values of σ_0 and μ. The good agreement between the measured and predicted curves serves as a verification of the empirical parameters σ_0 and μ.

Having the knowledge of the hole expansion pressure σ_0 and the coefficient of friction μ, mean indentation pressure σ_m for a general conical indenter can be calculated using Equation (5.2). The mean indentation pressure σ_m is plotted against the included cone angle of the indenter $2\beta_0$ in Figure 5.27. The mean indentation pressure decreases with increasing cone angle. For angles greater than 40°, the mean indentation pressure reaches a relatively constant value for both materials.

5.2.2.2 Calculation of Penetration Force

Before the onset of delaminations, the penetration force due to hole expansion is calculated using Equation (5.1). Then, at a certain penetration depth α_0, delaminations are initiated in the laminate below the indenter. After the delaminations are initiated, deformations due to

hole expansion continues to increase, but at a rate less than that before the initiation of the delamination. Figure 5.28 shows the forces that come into play for calculation of the hole expansion force in the delaminated laminates.

It needs to be emphasised that the mean indentation pressure σ_m is obtained from the static indentation tests, where the specimens are backed-up by a rigid support without any openings. Therefore, there are no lateral deformations on the distal surface of the specimen, only compressive deformation.

When the specimens are backed-up by a rigid support with an opening, experimental work conducted by Sanders (1997) indicated that there was very little lateral deformation on the distal surface of the specimens before delaminations were initiated (see Figure 5.4). So σ_m from the static indentation tests can still be applied to this case.

However, when delaminations occur below or around the indenter (or projectile), the flexural rigidity of the specimen is reduced. The mean indentation pressure σ_m is not applicable in this case anymore. However, for simplicity in modelling, σ_m is still used but multiplied by a reduction parameter D in the following form

$$D = 1 - \frac{\alpha - \alpha_0}{\max(L_c, h) - \alpha_0} \tag{5.4}$$

where L_c is the indenter's cone height and h is the laminate thickness. Thus, the mean indentation pressure σ_m' after the onset of delaminations can be written in the following form

$$\sigma'_m = \sigma_m D = \sigma_m \left(1 - \frac{\alpha - \alpha_0}{\max(L_c, h) - \alpha_0}\right) \tag{5.5}$$

The hole expansion force is then calculated as

$$F = \sigma'_m A_p = \sigma'_m \pi \tan^2 \beta_0 \left[(\alpha + b_0)^2 - (\alpha - \alpha_0)^2 \right] \tag{5.6}$$

instead of using the Equation (5.1).

5.2.3 Flexural Deflection of a Split-Plate

As mentioned before, flexural deformation of a split-plate includes the initiation of delamination followed by bending of the delaminated laminate (*i.e.,* dishing/petalling). A simple application of the split-plate theory (presented in Quan *et al.*, 1996) has proven that it is quite an effective tool for modelling the delamination and post-delamination behaviour in laminated composites during penetration process. This gives us confidence in applying the split-plate theory to other cases involving delaminated layers.

5.2.3.1 Delamination Initiation and Progression

Hole expansion causes the material around the indenter to crush and form a damage zone. This is denoted as zone I in Figure 5.15, which is the projected area underneath the indenter or the projectile. The laminate material inside zone I loses its shear strength and transfers the indentation pressure to the neighbouring material and the lower part of the laminate.

The calculation of the transverse shear force and stress follows the schematic diagram shown in Figure 5.29. On the cylindrical surface of radius $(\alpha + b_0)\tan\beta$, we have the following equilibrium condition

$$Q = \frac{F}{2\pi(\alpha + b_0)\tan\beta_0} \tag{5.7}$$

where Q is transverse shear force per unit circumferential length acting on the boundary surface. It is assumed that when the shear stress τ at the corner edge as shown in Figure 5.29 reaches a critical value, delamination occurs. This shear stress τ is calculated from the average shear stress through the thickness $\frac{Q}{h-\alpha}$ multiplying a geometric factor $\frac{\alpha}{h}$

$$\tau = \frac{Q}{h-\alpha}\frac{\alpha}{h} \tag{5.8}$$

The critical value of τ, τ_s can be obtained from the static penetration tests on the specimen.

Based on the cross-sectional examination of the CFRP specimens penetrated by an indenter (with 37° cone angle) and unloaded at different points along the force-displacement curve, the delamination initiation point can be detected as shown in Figure 5.7. The delamination initiation stress τ_s is then calculated based on the contact force and the penetration depth measured at that point as shown in Figure 5.7 by applying Equations (5.7) and (5.8). Thus, the calculations lead to $\tau_s = 100\ MPa$.

For GFRP laminates, $\tau_s = 13.7\ MPa$, taken from the three-point flexural tests on GFRP specimens as the transverse interlaminar shear strength (Lau, 1997).

Delamination initiates when

$$\tau \geq \tau_s \tag{5.9}$$

When Equation (5.9) is satisfied at a certain depth of indenter penetration, delaminations are assumed to initiate below the indenter. Subsequently, the flexural deformation of the split-plate starts.

Experimental study conducted by Sanders (1997) showed that many of the matrix cracks that occured in the CFRP laminate formed an angle of 45° with the fibre direction. This meant that the matrix cracks were likely caused by transverse shear stresses. When matrix cracks grow and finally reach an interface between two plies delamination occurs. Therefore, our assumption that delaminations occur when a critical shear stress is reached is justified.

Intensive C-scan and pulse-echo ultrasound (PEUS) studies revealed that delaminations generally form in pie-shaped sectors in a staircase helical pattern through the whole sublaminate thickness, as shown in Figure 5.31 (Delfosse *et al.*, 1994b). It was also found that for quasi-isotropic lay-ups, one full revolution (circle) of the helical delamination pattern will occur in each sublaminate (Delfosse *et al.*, 1994b). Therefore, to simplify the analysis in the present approach, one full circular delamination is assumed to occur at the interface between two adjacent sublaminates.

Based on micrographic examinations and to enable theoretical developments, the delamination size is assumed to be bounded by the normal to the cone surface and shown as zone II in Figure 5.15. When the penetration depth increases, the delamination size also expands in a self-similar shape. The inner and outer radii of the delamination zone will increase until the indenter shaft reaches the frontal surface of the specimen. The increase in

the inner radius is due to the continuous crushing of the material as the indenter advances in the target.

It is worth noting that the delamination pattern in CFRP and GFRP are quite different. There are obvious (visible) macro-delaminations that initiate in the CFRP laminates, while in the GFRP laminates, there are individually invisible micro-delaminations that start very early in the penetration process. This explains why the delamination initiation stress in the GFRP laminates is much smaller than that in the CFRP. The micro-delaminations in the GFRP are also approximated as circular macro-delaminations in the present analysis.

5.2.3.2 Calculation of Compliance of a Single Split

Because each split is assumed to be a circular plate, compliance of a single split can be calculated from a circular plate or ring using classical flexural theory of plates. Let a_j and b_j denote the outer and inner radii of the j'th split clamped along its boundary as shown in Figure 5.32. The total number of splits is n_s.

5.2.3.2.1 Compliance of a Circular Plate without a Central Hole

In this case, $b_j = 0$. From flexural theory of circular plates presented in Timoshenko and Woinowsky-Krieger (1959), the compliance of this plate is given by

$$f_j = \frac{a_j^2}{16\pi D_{dj}}, \quad j = 1,2,\ldots\ldots,n_s \tag{5.10}$$

where D_{dj} is the bending rigidity of the j'th split. Let h_j denote the distance in thickness direction between two adjacent delaminations the j'th and $(j+1)$'th, then $D_{dj} = \frac{Eh_j^3}{12(1-\nu^2)}$, where ν is the Poisson's ratio of the material.

5.2.3.2.2 Compliance of a Circular Plate with a Central Hole

The compliance of the j'th split can be calculated as (Timoshenko and Woinowsky-Krieger, 1959)

$$f_j = \frac{b_j^2}{8\pi D_{dj}}(\ln\frac{b_j}{a_j} - 1) + \frac{1}{16\pi D_{dj}}(b_j^2 + a_j^2) - \frac{1}{8\pi D_{dj}} \frac{\ln\frac{b_j}{a_j} + \frac{1}{1+\nu}}{1 + \frac{a_j^2}{b_j^2}\frac{1-\nu}{1+\nu}} \quad (5.11)$$

$$(b_j^2 - a_j^2 - 2a_j^2 \ln\frac{b_j}{a_j})$$

Details of derivations of this equation are given in Appendix E.

From Figure 5.33, we can write a_j and b_j as

$$a_j = (\alpha + b_0)\tan\beta_0 + [\alpha_0 + (j-1)\, h_j]/\tan\beta_0 \quad (5.12)$$

$$b_j = [\alpha + b_0 - \alpha_0 - (j-1)\, h_j]\tan\beta_0 \quad (5.13)$$

where h_j is the distance between two delaminated interfaces. For the quasi-isotropic CFRP laminates, h_j is equal to a sublaminate thickness. The development pattern of delaminations is shown in Figure 5.34.

5.2.3.3 Total Compliance of a Split-Plate

Total compliance is calculated for two different cases of interaction between the splits. In the first case, it is assumed that all the splits have the same lateral deflections. In the second case, all the splits are assumed to have the same force acting on them.

5.2.3.3.1 Splits Having the Same Deflections

If we assume that the splits satisfy the compatibility condition that all of them have the same deflection shape at any time, then the total force F_s on the split-plate is the sum of the forces on the each split, *i.e.*,

$$F_s = F_1 + F_2 + \ldots\ldots + F_{n_s} \tag{5.14}$$

Rewriting Equation (5.14) in terms of deflections

$$\frac{w_s}{f} = \frac{w_1}{f_1} + \frac{w_2}{f_2} + \ldots\ldots + \frac{w_{n_s}}{f_{n_s}} \tag{5.15}$$

Because all of the splits have the same transverse deflection, i.e., $w_s = w_1 = w_2 = \ldots\ldots = w_{n_s}$, the total compliance f of this split-plate, can be written in terms of compliance of each split f_j as

$$\frac{1}{f} = \sum_{j=1}^{n_s} \frac{1}{f_j} \tag{5.16}$$

If the split-plate deflection is denoted by w_s, then the penetrating force according to this deflection is

$$F_s = \frac{w_s}{f} \tag{5.17}$$

5.2.3.3.2 Splits Subjected to the Same Force

If we assume that all the splits are subjected to the same amount of force and do not necessarily have the same deflections as shown in Figure 5.31, then the total deflection of the split-plate can be approximated as the sum of the deflection of each split, *i.e.*,

$$w_s = w_1 + w_2 + \ldots\ldots + w_{n_s} \tag{5.18}$$

This approximation will underestimate the total deflection of the split-plate. But if the deflection of each split is small compared with the split thickness, and the planar size of the new generated split is smaller than the splits already there, which is the same situation as in the current case, the error caused by this approximation is small.

Rewriting Equation (5.18) in terms of the force on the splits

$$fF_s = f_1F_1 + f_2F_2 + \ldots\ldots + f_{n_s}F_{n_s} \tag{5.19}$$

Because the forces acting on the each split are the same, i.e., $F_1 = F_2 = \ldots\ldots = F_{n_s} = F_s$, the total compliance from Equation (5.19) is given by

$$f = \sum_{j=1}^{n_s} f_j \tag{5.20}$$

If the total split-plate deflection is w_s, then the corresponding penetration force is

$$F_s = \frac{w_s}{\sum_{j=1}^{n_s} f_j} \tag{5.21}$$

Equations (5.16) and (5.20) are two ways of calculating the total compliance of the split-plate. Which one is used in the analysis depends on the pattern of delamination during the penetration process in that material system.

5.2.3.4 Local Deflection of a Delaminated Plate

Based on the experimental observations in Delfosse (1994b) and Sanders (1997), for the CFRP laminates, all delaminations are assumed to occur simultaneously and their shapes are taken to be one full circle for each single sublaminate. For the GFRP laminates as shown in Figure 5.11 (a-e) (Sanders, 1997), delaminations initiate and develop around the projectile. As the projectile penetrates the target deeper, more delaminations occur through the thickness. Thus the circular delaminations in GFRP laminates are assumed to be initiated sequentially, one by one.

When delamination occurs in the laminate, the delaminated region of the laminate will behave like a split-plate as shown in Figure 5.32 and deflects more than the remainder of the plate due to its reduced bending rigidity. The plate will be more compliant (flexural) in the region with the delaminations, especially when the laminate has been penetrated through at the centre by the indenter or projectile tip.

The local plate deflection w_s, or the so-called deflection of the split-plate, is calculated at each increment of the penetration depth. The laminate material in the local deformation region, zone II shown in Figure 5.15, undergoes flexural deformations as shown in Figure 5.36.

Let's consider a line element *OA*, which is the outer radius of the current split. It is horizontal before the indenter tip penetrates through it. The line OA bends and moves to a new position, *OB,* after it is perforated by the indenter tip. Assuming that there is no tensile or compressive deformation in this line, $\overline{OA} = \overline{OB}$. The local deflection is $w_{sj}^0 = \overline{BC}$.

In ΔOBD, $\overline{OB} = a_j$, the angle between the lines $\overline{OD}$ and $\overline{BD}$ is equal to

$$\angle ODB = \pi - \angle CDB .$$

In ΔAED, the angle between line $\overline{AD}$ and $\overline{ED}$ is equal to

$$\angle ADE = \frac{\pi}{2} - \angle AED = \frac{\pi}{2} - \beta_0 .$$

Since $\angle CDB = \angle ADE$, we have

$$\angle ODB = \frac{\pi}{2} + \beta_0 . \tag{5.22}$$

Also, the length of $\overline{OD}$ is calculated by

$$\overline{OD} = \overline{OA} - \overline{DA} = a_j - \Delta\alpha \tan\beta_0 \tag{5.23}$$

In ΔOBD, we have

$$\frac{\sin\angle DBO}{\overline{OD}} = \frac{\sin\angle ODB}{a_j} \tag{5.24}$$

Substituting Equations (5.22) and (5.23) into Equation (5.24),

$$\sin\angle DBO = \overline{OD}\frac{\sin\angle ODB}{a_j} = (1 - \frac{\Delta\alpha}{a_j}\tan\beta_0)\cos\beta_0 \tag{5.25}$$

In ΔOBC, we have

$$\angle COB + \angle OBC = \frac{\pi}{2} \tag{5.26}$$

i. e.,

$$\angle COB + \angle DBO + \beta_0 = \frac{\pi}{2}$$

Thus,

$$\angle COB = \frac{\pi}{2} - \beta_0 - \sin^{-1}[(1 - \frac{\Delta\alpha}{a_j}\tan\beta_0)\cos\beta_0] \tag{5.27}$$

Therefore, the local deflection of the split is equal to

$$w_{sj}^0 = \overline{OB}\sin\angle COB = a_j \sin\{\frac{\pi}{2} - \beta_0 - \sin^{-1}[(1 - \frac{\Delta\alpha}{a_j}\tan\beta_0)\cos\beta_0]\} \tag{5.28}$$

The above derivations imply that point O is a pin and line OA rotates as a rigid body about point O to line OB. This is not true in contradiction to our assumption of a split-plate, where a split is assumed to be clamped along its boundary. Therefore, Equation (5.28) needs to be modified in order to consider the effect of clamped boundary.

The displacement function of a simply-supported circular ring with an outer radius a_j and loaded by a uniformly distributed load (of total magnitude F_j) along the perimeter of the hole is given by Timoshenko and Woinowsky (1959)

$$w_{sj} = \frac{F_j}{8\pi D_{dj}}[\frac{3+\nu}{2(1+\nu)}(a_j^2 - r^2) + r^2 \ln\frac{r}{a_j}] \tag{5.29}$$

The rotation on the support edge is

$$_j = \left.\frac{dw_{sj}}{dr}\right|_{r=a_j} = -\frac{F_j}{4\pi D_{dj}}\frac{a_j}{1+\nu} \tag{5.30}$$

Therefore, the local deflection when edges are clamped is

$$w_{sj} = w_{sj}^0 + \theta_j a_j \tag{5.31}$$

5.2.3.5 *Lateral Force on the Split-Plate*

At the instant when delamination occurs, since no central hole exists for the delaminations under the indenter, the compliance of the split-plate is calculated using Equation (5.10), where the inner radius of the split-plate $b_j = 0$.

As the indenter continues to penetrate into the target, a central hole begins to appear in the splits. Depending on the penetration depth in the laminate, some splits will have a central hole while others won't. Accordingly, the compliance of each split is calculated using either Equations (5.10) or (5.11). The total compliance of the split-plate is then calculated using Equations (5.16) or (5.20).

The force is calculated from Equation (5.17) or (5.21). After substituting Equations (5.30) and (5.31) into Equations (5.17) or (5.21),

$$F_s = \frac{w_s}{f} = \frac{w_{s1}}{f} = \frac{w_{s1}^0}{f} - \frac{1}{f}\frac{F_1}{4\pi D_{d1}}\frac{a_1^2}{1+\nu}; \qquad \text{for CFRP} \tag{5.32a}$$

$$F_s = \frac{\sum_{j=1}^{n_s} w_{sj}}{\sum_{j=1}^{n_s} f_j} = \frac{\sum_{j=1}^{n_s} w_{sj}^0 + \sum_{j=1}^{n_s} \theta_j a_j}{f} = \frac{w_s^0}{f} - \frac{1}{f}\sum_{j=1}^{n_s}\frac{F_j}{4\pi D_{dj}}\frac{a_j^2}{1+\nu}; \text{for GFRP} \tag{5.32b}$$

For CFRP laminates, we assume that all the splits have the same deflection, $f_1 F_1 = f F_s$, so that $\frac{F_1}{f} = \frac{F_s}{f_1}$ in Equation (5.32a). Rearranging the terms in Equation (5.32a), then

$$F_s = w_{s1}^0 \frac{4\pi D_{d1}(1+\nu)}{4\pi D_{d1}(1+\nu)f + a_1^2 \frac{f}{f_1}}; \qquad \text{for CFRP} \quad (5.33a)$$

For GFRP laminates, we assume that all the splits are under the same force, $F_s = F_j$, and therefore rearrangement of the terms in Equation (5.32b) will lead to

$$F_s = \frac{w_s^0}{f} \frac{1}{[1 + \frac{1}{4\pi f(1+\nu)} \sum_{j=1}^{n_s} \frac{a_j^2}{D_{dj}}]}; \qquad \text{for GFRP} \quad (5.33b)$$

Because the outer and inner radii of the circular split-plate change with increasing penetration depth, compliance is a function of the penetration depth and therefore has to be recalculated at each increment of the indenter or projectile displacement.

The bending deformation of the split-plate terminates when the indenter shaft reaches the frontal surface of the specimen.

5.2.4 Transverse Plugging

Transverse plugging is a penetration mechanism that usually arises in transverse indentation by blunt or obtuse indenters. Static penetration tests with the blunt indenter are therefore used to find the transverse shear strength of laminates. The penetration force and indenter displacement are recorded until the laminate is perforated. A typical force-displacement relationship in a small-geometry test is shown in Figure 5.37 (Delfosse 1994b). The transverse shear strength τ_0 is calculated based on the maximum shear force required to form a transverse plug through the laminate thickness.

For CFRP laminates, the transverse shear strength τ_0 is calculated to be 142 MPa, corresponding to a maximum contact force of 20.8 kN (Figure 5.37) for a specimen with 6.15 mm thickness penetrated by a blunt-ended cylinder of diameter 7.62 mm. The friction force F_{pf} between the plug and the adjacent material can be calculated from the measured force-displacement curve. At point *f* in Figure 5.37, the contact force drops and a transverse plug initiates. At point *g*, the indenter travels a distance equal to the target thickness, which means that the plug has been pushed out from the target at this time. The trapezoidal area represents this plug push-out stage. By extrapolating the line CD to the point E, the friction force between the plug and the rest of the target material is estimated as $F_{pf} = 11.4\ kN$.

The initiation criterion for transverse plugging mechanism is in the following form

$$\tau \geq \tau_0 \tag{5.34}$$

For a given penetration depth α, the transverse shear stress τ can be calculated as $\tau = \dfrac{F}{2\pi(\alpha + b_0)h\tan\beta_0}$ and compared with the plugging strength τ_0. If the initiation condition in Equation (5.34) is met, then a transverse shear plug is deemed to form.

In the case of GFRP laminates, the blunt-ended indenter did not perforate the specimens. Instead, for 6.35 mm thick specimen the laminate deflected and was pushed out from the opening of the rigid support plate. For thicker laminates (12.7 mm and 19.05 mm), the indenter yielded.

It can also be inferred that the transverse shear strength for the GFRP laminates considered in this study is large enough such that the transverse plugging mechanism will likely not occur in such laminates.

If transverse plugging occurs (*i.e.*, $\tau \geq \tau_0$), the contact force will drop to a value of

$$F = F_{pf} \frac{h - \alpha}{h} \tag{5.35}$$

5.2.5 Friction

Friction starts when the indenter shaft reaches the frontal surface of the specimen. It is assumed that the penetration force arising from hole expansion and flexural deformation of the delaminated plate (split-plate) or from push-out of a transverse plug decreases linearly in this phase, while the frictional force increases linearly with increasing indenter or projectile shaft length in the laminate. When the projectile shaft penetrates through the laminate, the penetration force reaches a value denoted by F_f. This value is measured from static penetration tests of the same material penetrated by an indenter of the same diameter. It is the magnitude of the force corresponding to post-perforation plateau in the force-displacement curves.

It should be noted that the coefficient of friction μ discussed in Section 5.2.2 couldn't be used here to calculate the friction force F_f. μ is merely the empirical parameter derived from static indentation tests. It may not really reflect the physical nature of friction between the projectile and target.

For the 6.15 mm thick CFRP laminates considered here, this frictional force is found to be $F_f = 2000\frac{h}{6.15}$ (N) (see Figure 5.37), while for GFRP laminates, it is $F_f = 4270\frac{h}{12.7}$ (N). h is the laminate thickness in millimetre, and 2000 N and 4270 N are the friction force corresponding to the 6.15 mm CFRP and 12.7 mm GFRP laminates, respectively.

5.2.5.1 Effects of Geometric Sizes of Projectiles and Targets

In static penetration tests, the indenter shaft is still in the laminate at the end of the penetration process when the indenter cone completely penetrates through the laminate thickness. The effects of the projectile length on the penetration process is only brought up in dynamic penetration tests, where the long projectiles will absorb more impact energy in friction than the short projectiles.

The frictional force is assumed to start when the projectile shaft reaches the frontal surface of the laminate. If the projectile cone length is greater than the laminate thickness, the projectile cone will stick out from the distal surface of the laminate when friction starts. Frictional force changes for different relative positions of the projectile and the target. Therefore, calculation of the penetration force depends on the geometric sizes of the projectile and target thickness, and the position of the projectile in the target.

There are four different cases depending on the projectile cone length L_c, projectile shaft length $L_p - L_c$, and target thickness h:

1. L_c is smaller than the local thickness of the target which is the sum of the target thickness h and the local bending deflection w_s, while the projectile shaft length is greater than the

local thickness of the target, i.e., $L_c \le h + w_s$ and $L_p - L_c > h + w_s$ as shown in Figure 5.38 (1);

2. L_c is greater than the local thickness of the target $h + w_s$, while the projectile shaft length is still greater than the local thickness of the target, i.e., $L_c > h + w_s$ and $L_p - L_c > h + w_s$ as shown in Figure 5.39 (1);

3. Projectile shaft length $L_p - L_c$ is smaller than the local thickness of the target $h + w_s$, while the projectile cone length L_c is smaller than the local thickness of the target, *i.e.*, $L_p - L_c \le h + w_s$ and $L_c \le h + w_s$ as shown in Figure 5.38 (2);

4. Projectile shaft length $L_p - L_c$ is still smaller than the local thickness of the target $h + w_s$, while the projectile cone length L_c is greater than the local thickness of the target, i.e., $L_p - L_c \le h + w_s$ and $L_c > h + w_s$ as shown in Figure 5.39 (2).

The maximum frictional length in the target as shown in Figures 5.39 and 5.40, can be written as

$$L_{f1} = \min(h + w_s, L_p - L_c) \tag{5.36}$$

L_{f1} defines the maximum length in the target over which friction is operative.

For a thin target ($L_c > h + w_s$) penetrated by a long projectile ($L_p - L_c > h + w_s$), the total frictional length at that time is the target thickness plus the local bending deflection, i.e., $L_{f1} = h + w_s$ as shown in Figure 5.39(c) and Figure 5.39(b1). For a thick target ($L_c \le h + w_s$) penetrated by a short projectile ($L_p - L_c \le h + w_s$), when the back end of the projectile has

penetrated into the target, the projectile tip may not have completely penetrated through the target yet, so that the total frictional length at that time is the projectile shaft length, i.e., $L_{f1} = L_p - L_c$ as shown in Figure 5.38 (b2) and Figure 5.39 (b2).

5.2.5.2 Calculation of Penetration Force for Different Positions of Projectile during the Friction Phase

Let us set four typical checking points:

$$\alpha = h + w_s,\ \alpha = L_c + h + w_s,\ \alpha = L_c + L_{f2}, \text{ and } \alpha = L_p + h + w_s.$$

where L_{f2} denotes the distance,

$$L_{f2} = \max(h + w_s, L_p - L_c) \tag{5.37}$$

Figures 5.39 and 5.40 show how we can use L_{f1} and L_{f2} to check the start of friction and perforation of the target.

The equations used to calculate the penetration force are shown in this section, which depend on the positions of the projectile within two checking points.

1. $L_c < \alpha \le h + w_s$ as shown in Figure 5.39(a),

$$F = F_{s0} + F_f \frac{\alpha - L_c}{h + w_s}, \text{ if } \alpha - L_c \le L_{f1}, \text{ or} \tag{5.38}$$

$$F = F_{s0} + F_f \frac{L_{f1}}{h + w_s}, \text{ if } \alpha - L_c > L_{f1}; \tag{5.39}$$

where F_{s0} is the penetration force at $\alpha = L_c$ and F_f is the penetration force in static penetration tests when only the indenter shaft is penetrating the target.

2. $h + w_s < \alpha \leq L_c + h + w_s$, in the case when the projectile cone length L_c is smaller than the local target thickness $h + w_s$, as shown in Figure 5.38(b);

$$F = F_{s0}\frac{L_c + L_{f1} - \alpha}{L_c} + F_f\frac{\alpha - L_c}{L_{f1}}, \text{ if } \alpha - L_c \leq L_{f1}, \text{ and } L_c \leq h + w_s \text{ or} \tag{5.40}$$

$$F = F_{s0}\frac{L_c + L_{f2} - \alpha}{L_c} + F_f\frac{L_{f1}}{L_{f2}}, \text{ if } \alpha - L_c > L_{f1} \text{ and } L_c \leq h + w_s; \tag{5.41}$$

and in the case where the projectile cone length L_c is greater than the local target thickness $h + w_s$ as shown in Figure 5.39(a),

$$F = F_{s0}\frac{L_c + L_{f1} - \alpha}{L_{f1}} + F_f\frac{\alpha - L_c}{L_{f1}}, \text{ if } \alpha - L_c \leq L_{f1}, \text{ and } L_c > h + w_s \text{ or} \tag{5.42}$$

$$F = F_{s0}\frac{L_c + L_{f2} - \alpha}{L_{f1}} + F_f\frac{L_{f1}}{L_{f2}}, \text{ if } \alpha - L_c > L_{f1} \text{ and } L_c > h + w_s; \tag{5.43}$$

3. $L_c + h + w_s < \alpha \leq L_c + L_{f2}$ as shown in Figure 5.39(c) and Figure 5.38(b),

$$F = F_f\frac{L_{f1}}{h + w_s}; \tag{5.44}$$

4. $L_c + L_{f2} < \alpha \leq L_p + h + w_s$ as shown in Figure 5.39(d) and Figure 5.38(c),

$$F = F_f\frac{L_c + L_{f1} + L_{f2} - \alpha}{h + w_s}; \tag{5.45}$$

5. $\alpha > L_p + h + w_s$ as shown in Figure 5.38(e) and Figure 5.39(d),

$$F = 0. \tag{5.46}$$

5.3 Summary

Based on the literature review and experimental work done in our research group, hole expansion, delaminations and associated flexural deformations of a split-plate, transverse plugging, and friction are identified as dominant mechanisms during penetration of laminated composites. For each penetration mechanism, analytical models for their initiation criteria and subsequent development patterns are developed in this chapter.

A summary of the equations used to calculate the contact force is provided in Table 5.4. These developments are based on experimental studies and thus have a solid physical background.

Table 5.1 Geometric sizes and material properties of the indenters used in static penetration and indentation tests.

Material		hardened steel, R_c 30
Diameter $2R_p$		7.62 mm
Included cone angle $2\beta_0$		37°, 60°, 120°, 180°
Bluntness b_0	37°	0.5 mm
	60°	0.2 mm
	120°	0.0 mm
	180°	0.0 mm

Table 5.2 Geometric sizes and material properties of the CFRP laminated plates used in static indentation and penetration tests.

Material	IM7 carbon fibres with 8551-7 epoxy matrix
Lay-up	$[-45/90/45/0_2]_{4s}$
Properties*	E_{11} = 142 GPa, E_{22} = 7.9 GPa, G_{12} = 4.1 GPa, $G_{13} = G_{23}$ = 3.0 GPa, ν_{12} =0.34
Equivalent isotropic properties**	E = 62.5 GPa, ν = 0.32
Thickness h	6.15 mm

* Delfosse (1994b).
** Calculated using lamination plate theory (Whitney, 1987).

Table 5.3 Geometric sizes and material properties of the GFRP laminated plates used in static indentation and penetration tests.

Material	S2-glass plain weave rovings with phenolic resin matrix
Elastic properties	E = 16.2 GPa*, ν = 0.2**
Density	$\rho = 1.9$ g/cm^3
Thickness h	6.35 mm, 12.7 mm, and 19.05 mm.

* Lau (1997).
** Greaves (1992).

Table 5.4 Summary of the equations used to calculate the contact force during penetration of a laminate.

Mechanism	Equations	Equation Number
hole expansion	no delaminations: $F = \sigma_m \pi(\alpha + b_0)^2 \tan^2 \beta_0$;	(5.1)
	with delaminations:	
	$F = \sigma'_m A_p = \sigma'_m \pi \tan^2 \beta_0 \left[(\alpha + b_0)^2 - (\alpha - \alpha_0)^2\right]$,	(5.6)
	$\sigma'_m = \sigma_m D = \sigma_m (1 - \frac{\alpha - \alpha_0}{\max(L_c, h) - \alpha_0})$.	(5.5)
flexural deflection of a split-plate	all the splits have the same deflection: $F_s = w_{s1}^0 \frac{4\pi D_{d1}(1+\nu)}{4\pi D_{d1}(1+\nu) f + a_1^2 \frac{f}{f_1}}$;	(5.33a)
	all the splits have the same force: $F_s = \frac{w_s^0}{f} \frac{1}{[1 + \frac{1}{4\pi f(1+\nu)} \sum_{j=1}^{n} \frac{a_j^2}{D_{dj}}]}$.	(5.33b)
transverse plugging	$F = F_{pf} \frac{h - \alpha}{h}$	(5.35)
friction	see pages 118-120	(5.38)-(5.46)

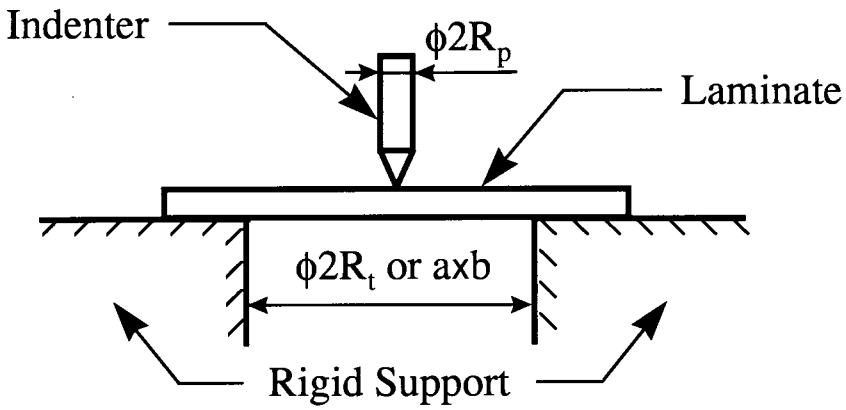

Figure 5.1 Schematic illustration of static penetration tests. The specimen sits on a rigid support with a circular or rectangular opening. R_t denotes the radius of a circular opening, while a and b denote the length and width of a rectangular opening. The indenter diameter is $2R_p$= 7.62 mm.

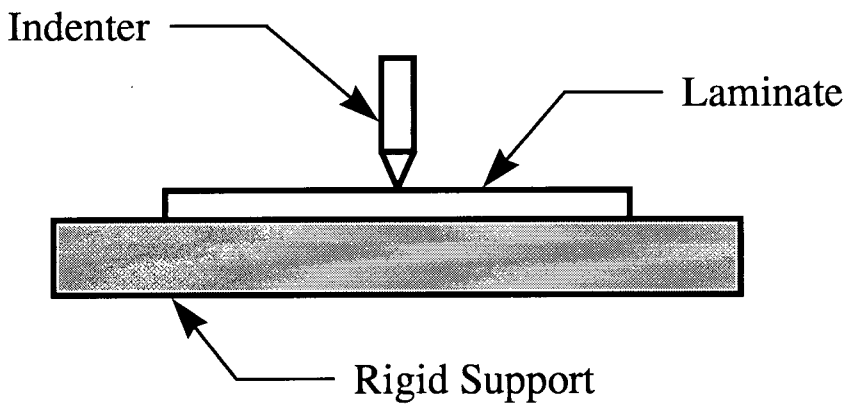

Figure 5.2 Schematic illustration of static indentation tests.

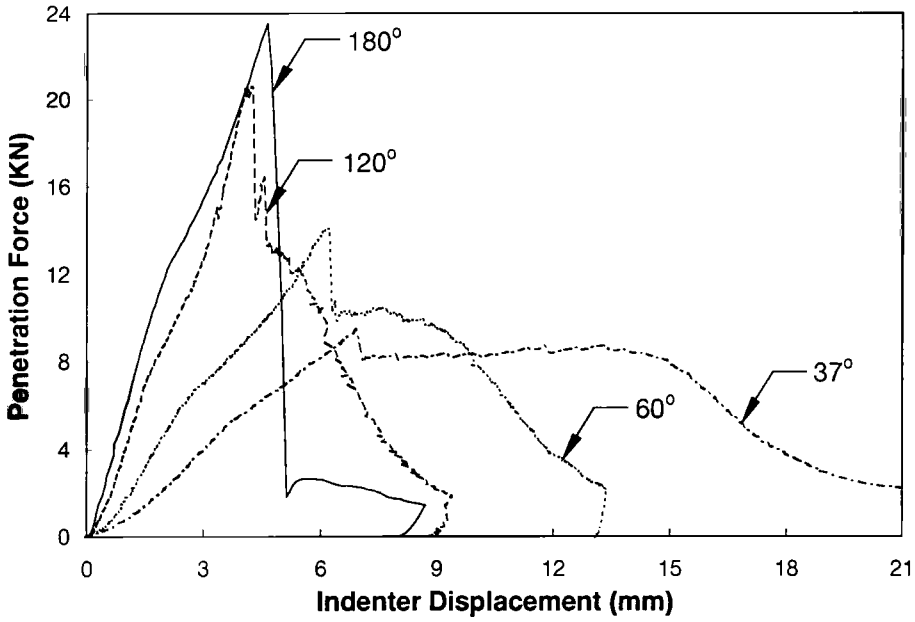

Figure 5.3 Penetration force versus indenter displacement in static penetration tests on the CFRP laminates defined in Table 5.2 penetrated by indenters with included cone angles of 37°, 60°, 120°, and 180° (Delfosse, 1994b).

Figure 5.4 Micrographic illustration of the initial penetration stage in a 6.15 mm thick CFRP laminate penetrated by an indenter with 37° cone angle (Sanders, 1997). The material around the indenter is crushed and is pushed aside by the indenter.

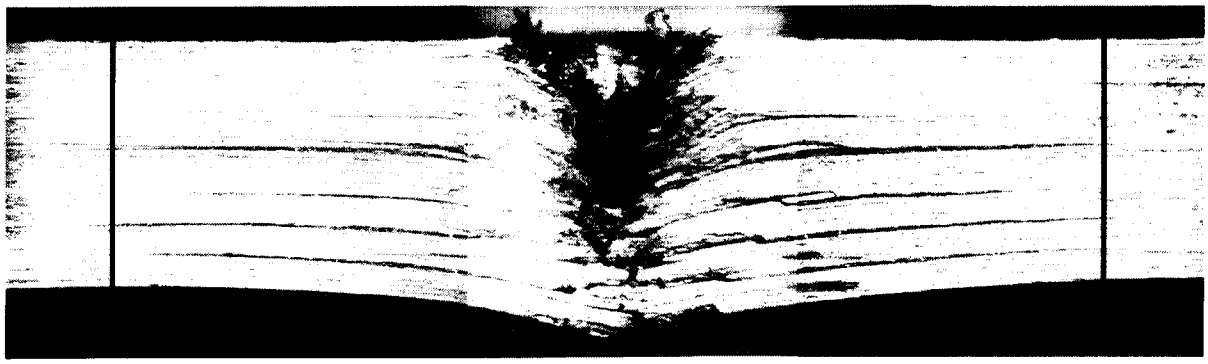

Figure 5.5 Micrographic illustration of failure in a 6.15 mm thick CFRP specimen penetrated by an indenter with a cone angle of 37° (Sanders, 1997). The material below the indenter is broken and bent away from the indenter.

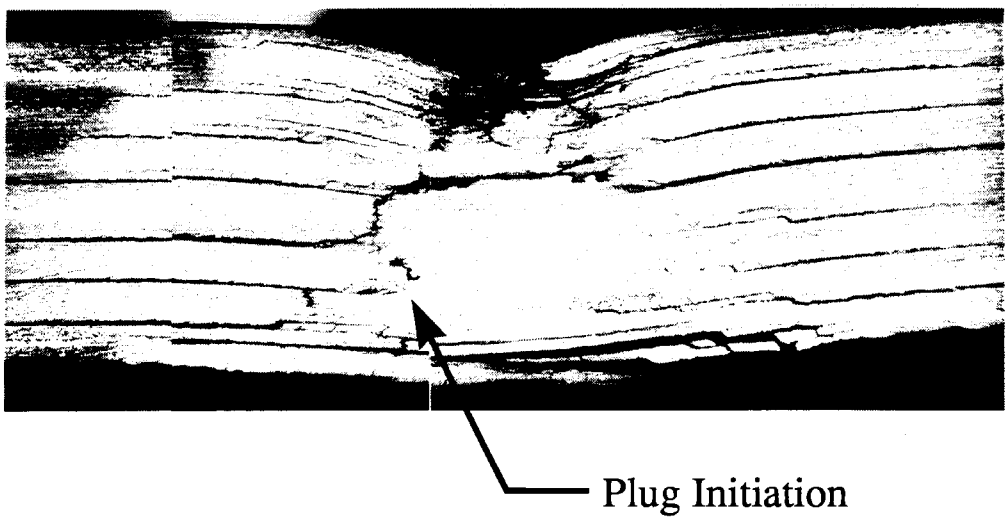

Figure 5.6 Cross-sectional micrograph of a 6.15 mm thick CFRP laminate penetrated by the indenter with an included cone angle of 120°. The plug initiation site can be seen very clearly.

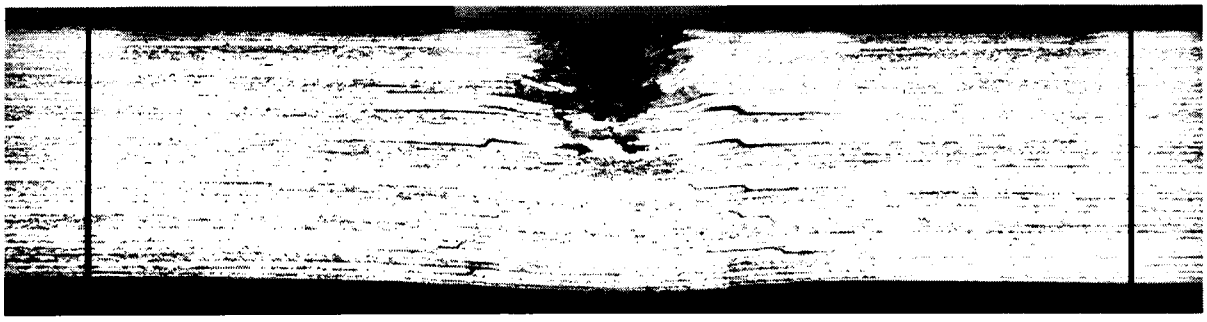

Figure 5.7 Micrographic illustration of delamination initiation in a 6.15 mm thick CFRP specimen when penetrated by an indenter with 37° cone angle (Sanders, 1997). The delaminations are located below the indenter and matrix cracks nearby.

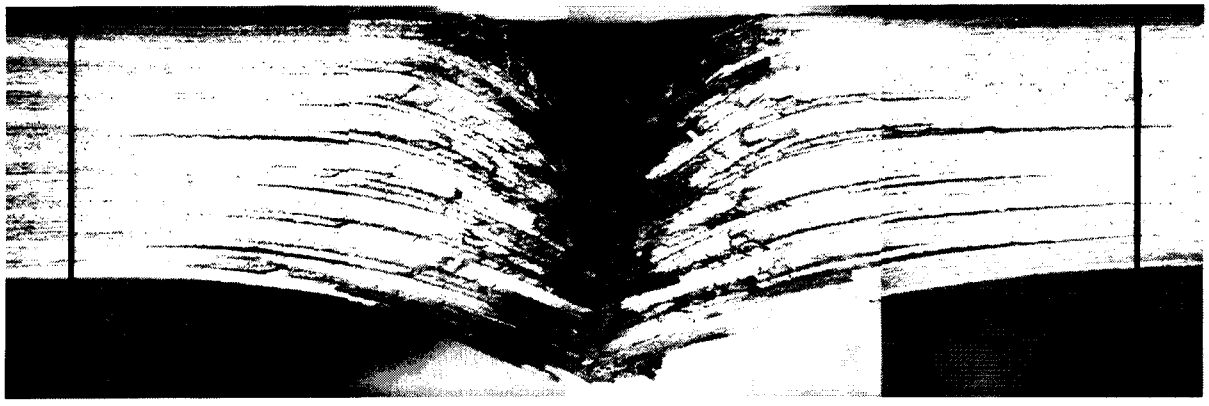

Figure 5.8 Micrographic illustration of delamination development in a 6.15 mm thick CFRP specimen penetrated by an indenter with 37° cone angle (Sanders, 1997). The delaminations are well developed by the time the indenter shaft reaches the frontal surface of the specimen as shown in the figure.

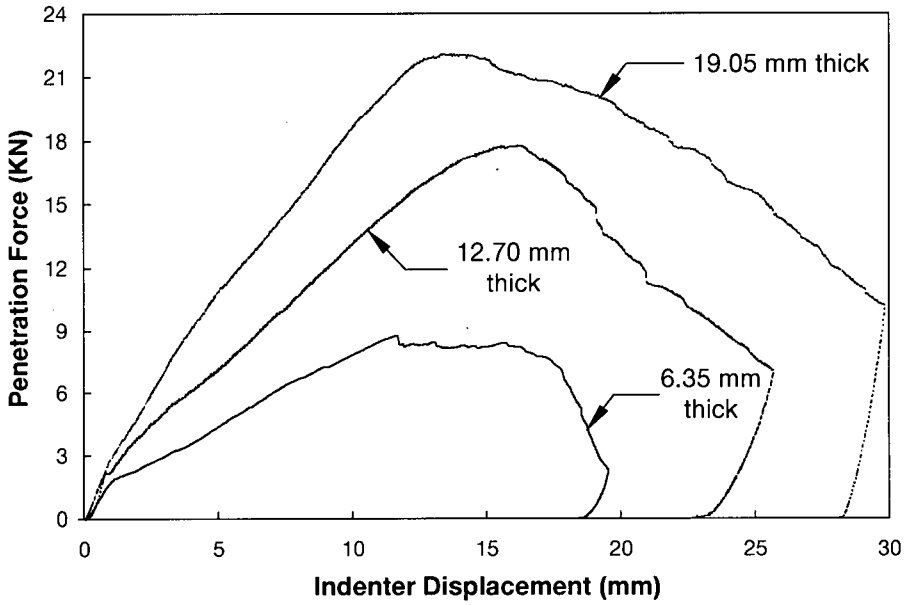

Figure 5.9 Experimental force versus indenter displacement curves for 6.35 mm, 12.70 mm, and 19.05 mm thick GFRP laminates penetrated by an indenter with 37° included cone angle (Sanders, 1997).

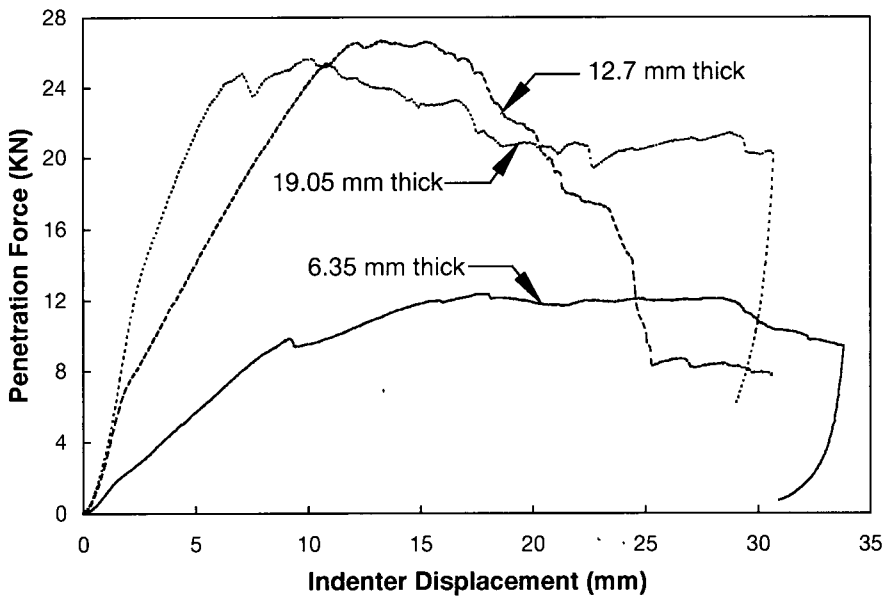

Figure 5.10 Experimental force versus indenter displacement curves for 6.35 mm, 12.70 mm, and 19.05 mm thick GFRP laminates penetrated by an indenter with 120° included cone angle (Sanders, 1997).

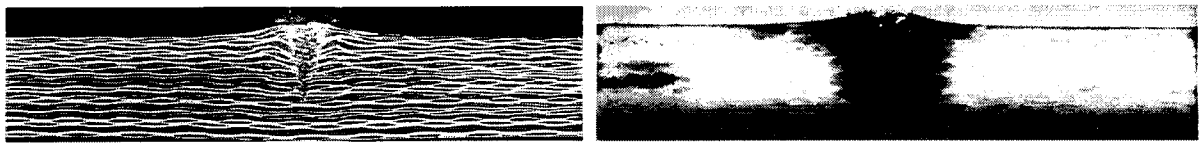

(a) projectile striking energy $E_s = 154\ J$, $V_s = 153\ m/s$

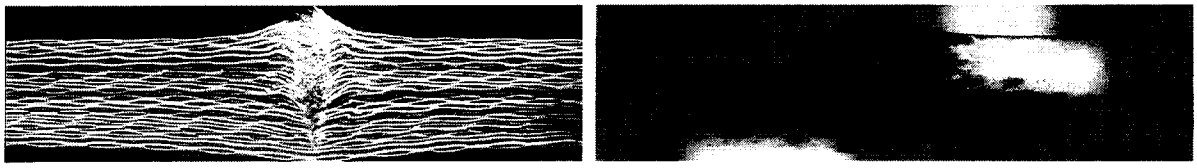

(b) projectile striking energy $E_s = 284\ J$, $V_s = 207\ m/s$

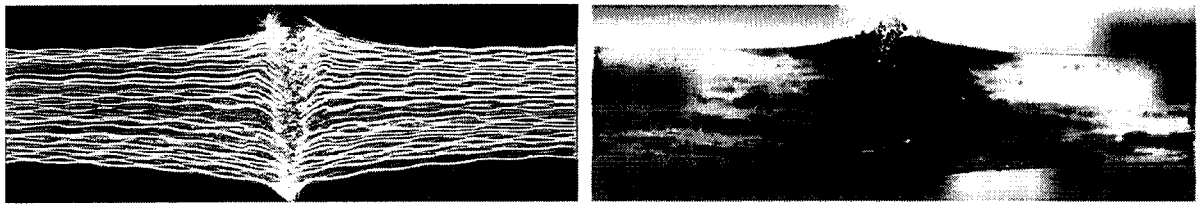

(c) projectile striking energy $E_s = 365\ J$, $V_s = 235\ m/s$

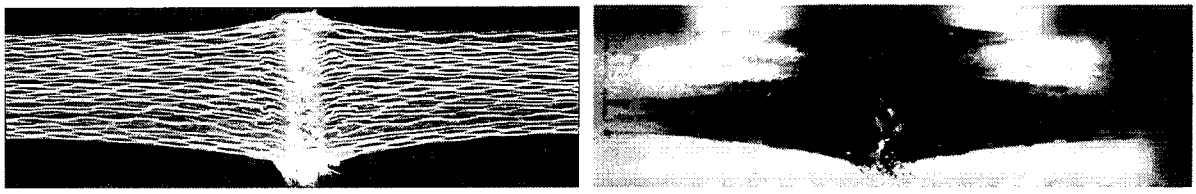

(d) projectile striking energy $E_s = 469\ J$, $V_s = 267\ m/s$

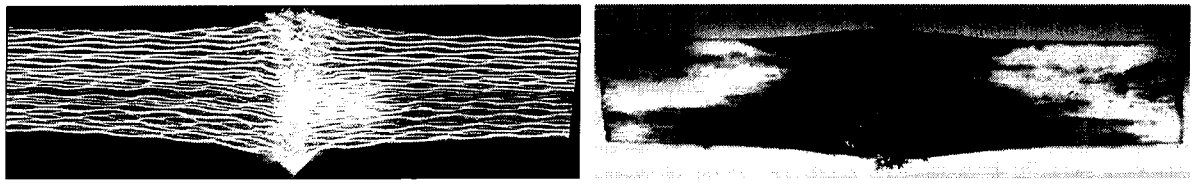

(e) projectile striking energy $E_s = 763\ J$, $V_s = 340\ m/s$

Figure 5.11 Cross-sectional micrographs of the penetrated and the perforated specimens and corresponding sections with dye penetrant for a 19.05 mm thick GFRP laminate impacted by a projectile with 37° cone angle at different striking energies (Sanders, 1997). The micro-delamination sites are shown as the black areas in the sections with dye penetrant.

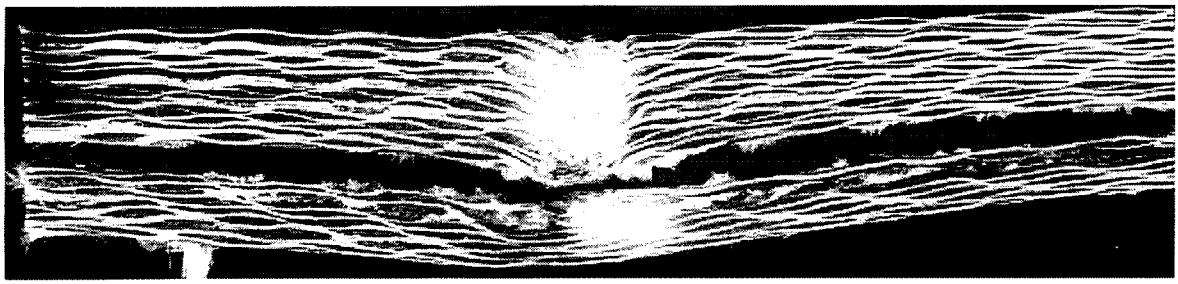

Figure 5.12 Micrographic illustration of macro-delamination for a 12.7 mm thick GFRP specimen impacted by an indenter with 120° cone angle (Sanders, 1997). The development of macro-delamination is clearly visible.

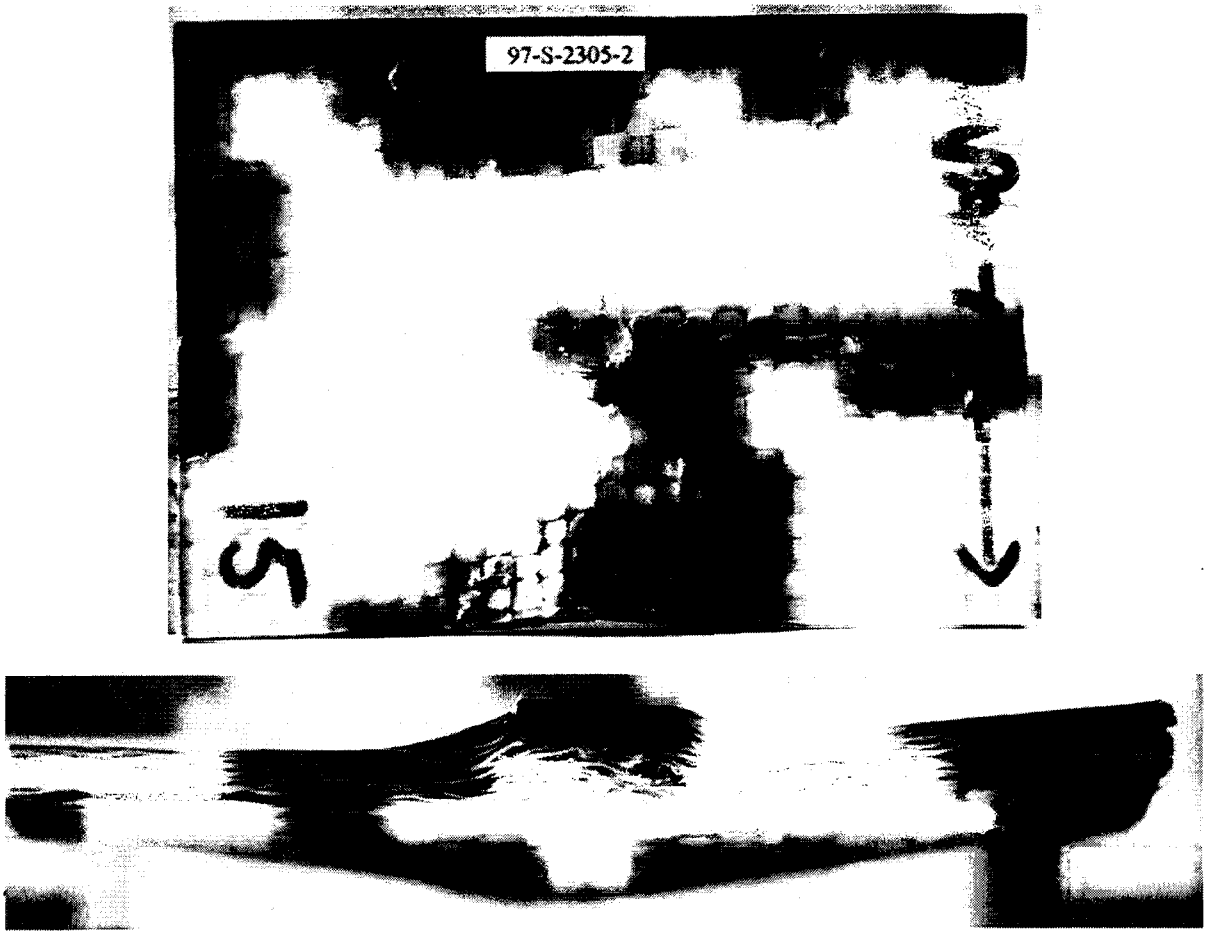

Figure 5.13 Top and side view of a 6.35 mm thick GFRP specimen penetrated by a 120° indenter (Sanders, 1997). The indenter simply pushes the laminate through the opening of the support plate and does not actually penetrate it.

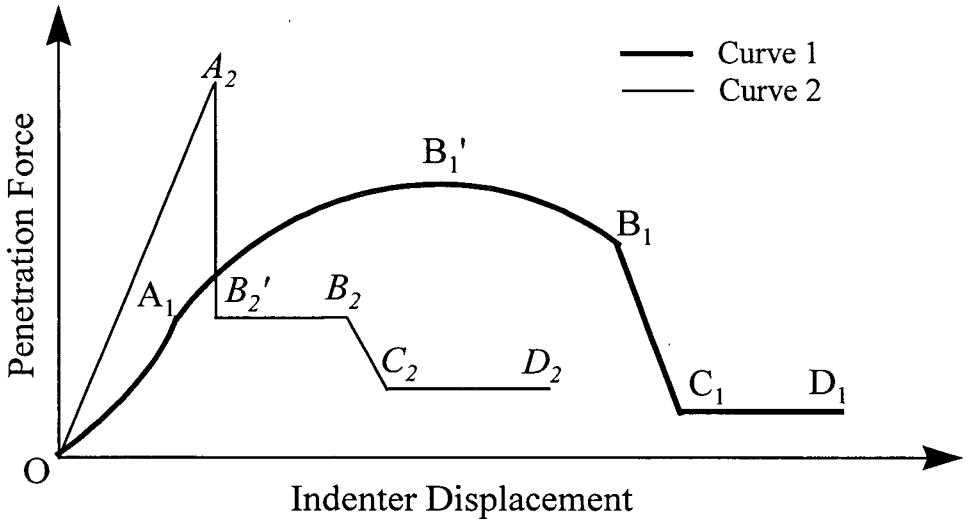

A_1 ⟶ delamination initiation on curve 1

A_2 ⟶ transverse shear plugging initiation on curve 2

B_1, B_2' ⟶ friction initiation

B_1', B_2 ⟶ projectile tip penetrates through the target

C_1, C_2
D_1, D_2 ⟶ friction plateau

Figure 5.14 Schematic illustration of the force-displacement curves of CFRP and GFRP laminates when penetrated by an indenter with a general cone angle. The penetration mechanisms follow the initial hole expansion mechanism (OA_1 or OA_2) are hole expansion and flexural deformation of a delaminated plate (split-plate) in curve 1 (A_1B_1) and transverse plugging in curve 2 (A_2B_2). Friction force initiates and gradually dominates the penetration process after B_1 in curve 1 and B_2 in curve 2.

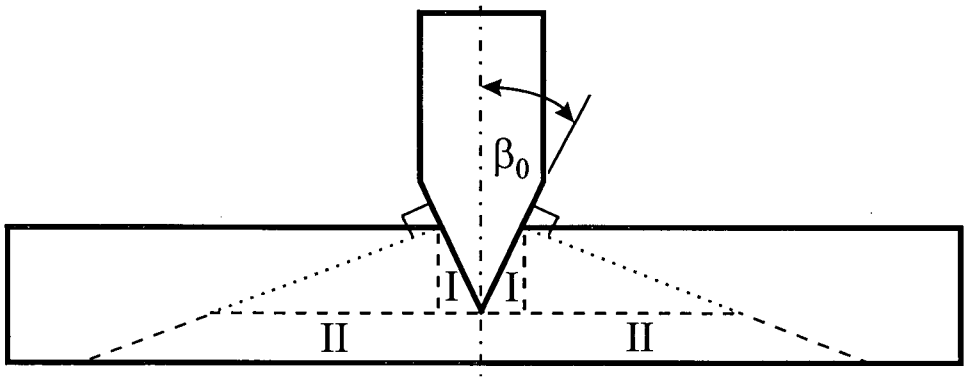

Figure 5.15 Local deformation zones: zone I, hole expansion; zone II, flexural deformation of the delaminated plate (split-plate).

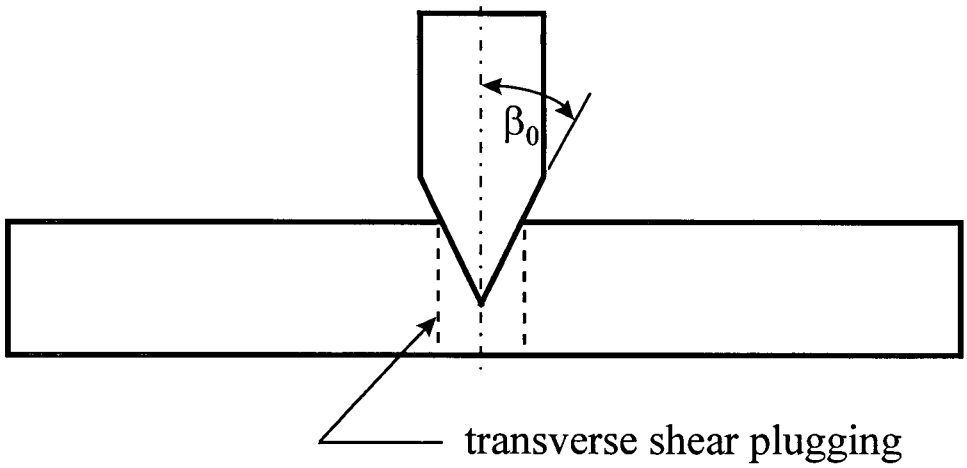

Figure 5.16 Schematic illustration of transverse shear plugging initiation.

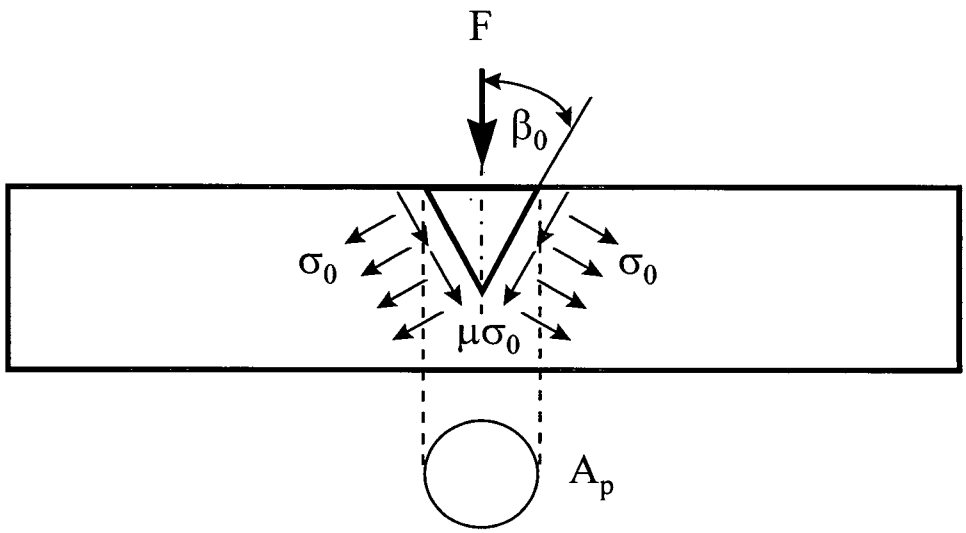

Figure 5.17 Schematic illustration of hole expansion mechanism. A_p is the projected area of a projectile or indenter, σ_0 is the hole expansion pressure of the laminate, and μ is the coefficient of friction of the laminate material.

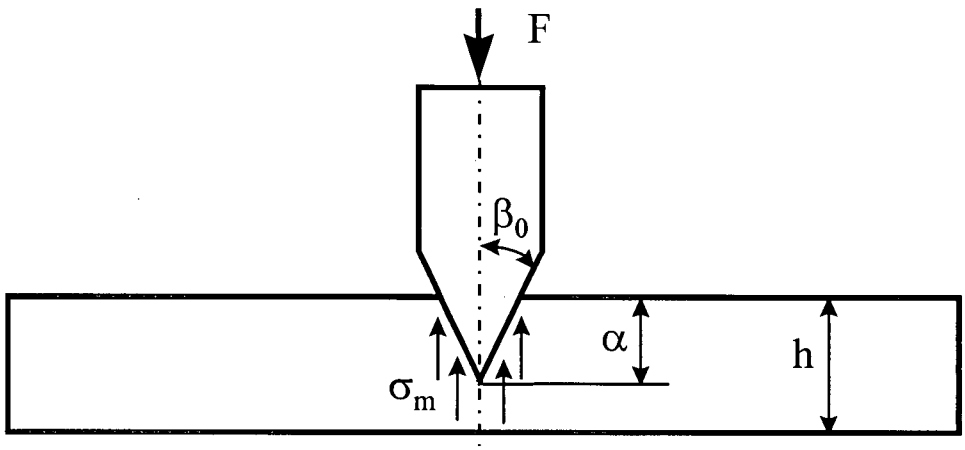

Figure 5.18 Schematic illustration of indentation pressure σ_m in static penetration tests. The relationship between σ_m and σ_0 in Figure 5.17 is shown in Equation (5.2).

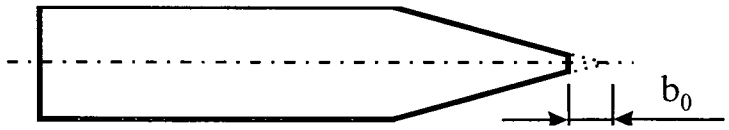

Figure 5.19 Schematic illustration of bluntness b_0 on the tip of a conical projectile or indenter.

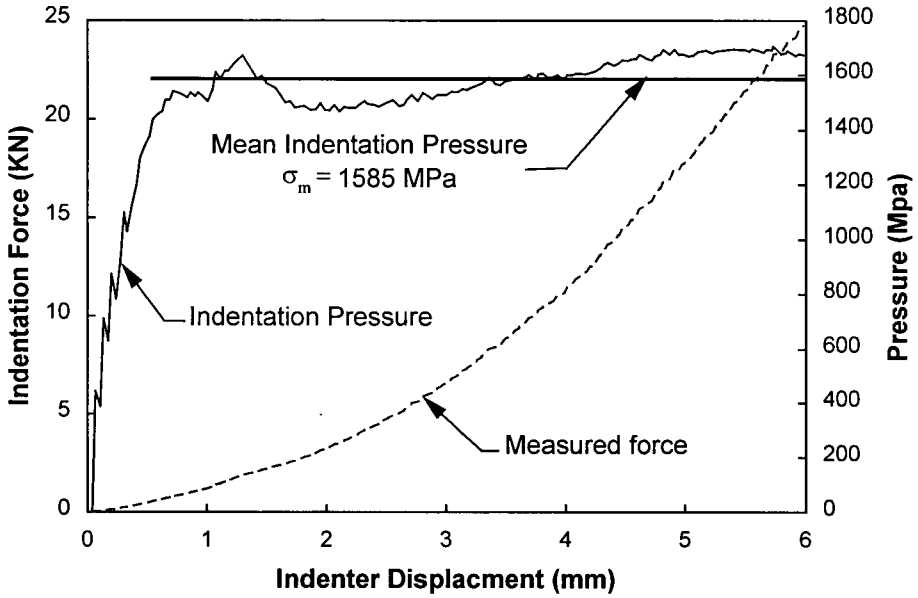

Figure 5.20 Calculation of mean indentation pressure based on measured force-displacement curve for the CFRP laminate. The conical indenter has an included cone angle of 37°. The specimen thickness is 6.15 mm.

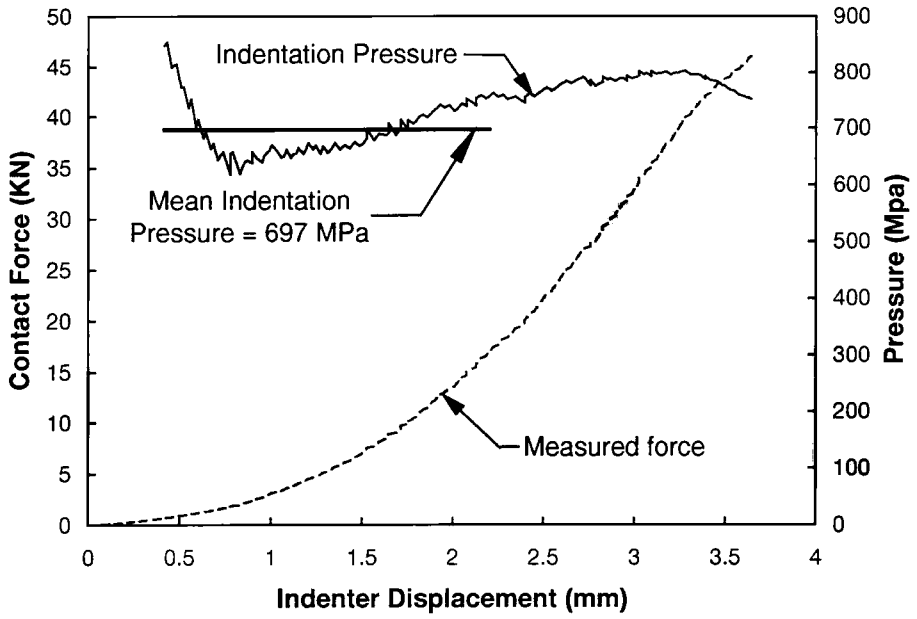

Figure 5.21 Calculation of mean indentation pressure based on the measured force-displacement curve for a CFRP laminate. The conical indenter has an included cone angle of 120°. The specimen thickness is 6.15 mm. The calculation of indentation pressure ends when the indenter shaft reaches the frontal surface of the laminate, *i. e.*, 2.2 mm of indenter displacement.

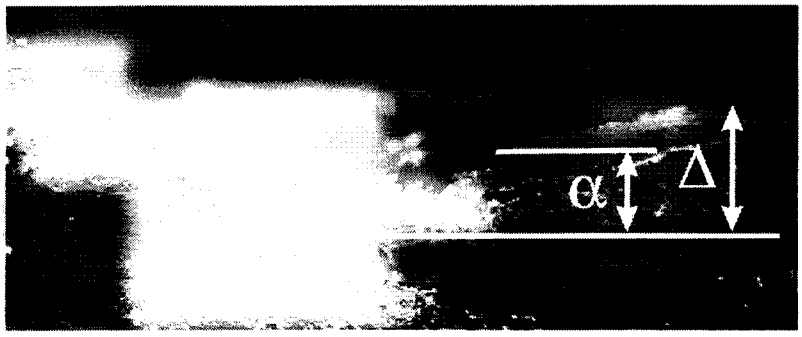

Figure 5.22 Micrograph examination of cross-section of the CFRP specimen in static indentation tests by a 120° indenter. "Sinking-in" ($\alpha<\Delta$) is clearly observed. The measured relationship between α and Δ is $\alpha \approx 0.7\Delta$.

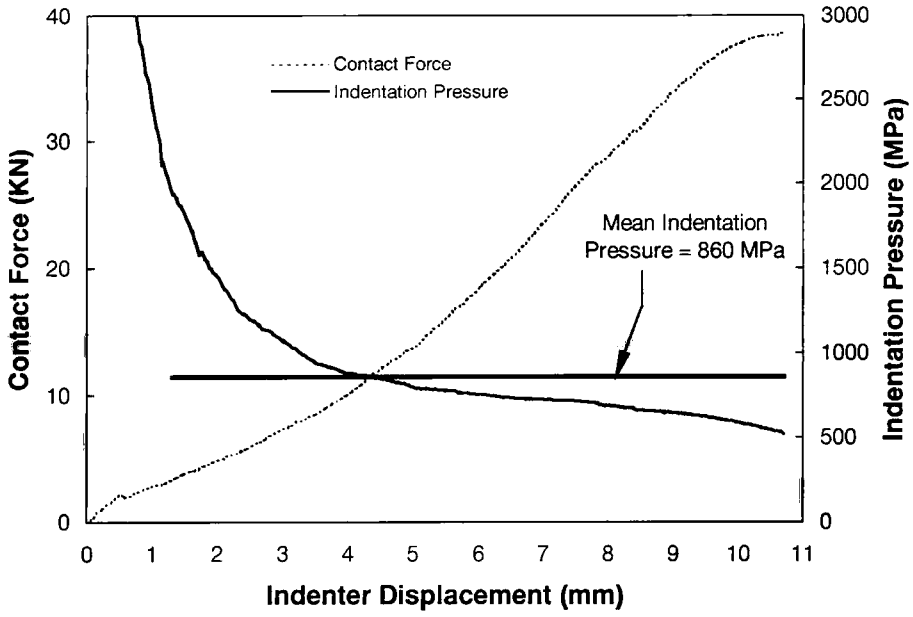

Figure 5.23 Calculation of mean indentation pressure based on the measured force-displacement curve for a S2-glass laminate where the conical indenter has an included cone angle of 37° and a diameter of 7.62 mm. The specimen thickness is 19.0 mm.

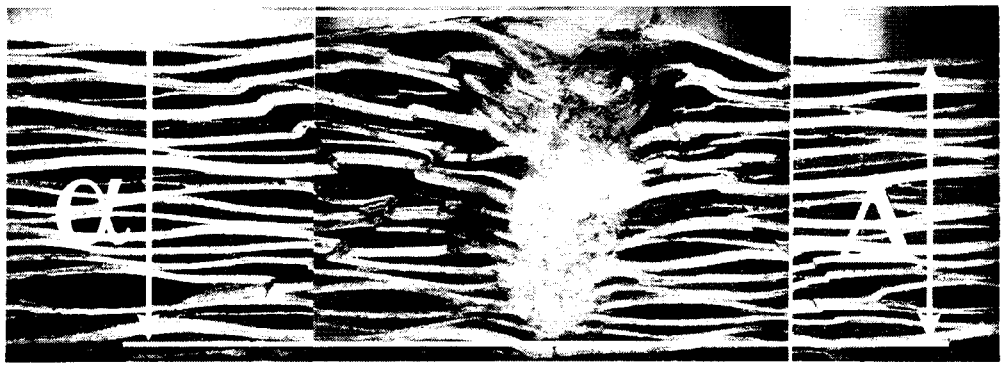

Figure 5.24 Cross-sectional micragragh showing "piling-up" in the 19.05 mm thick GFRP specimen when penetrated by an indenter with an included cone angle of 37° and a diameter of 7.62 mm, $\alpha \approx 1.3\Delta$.

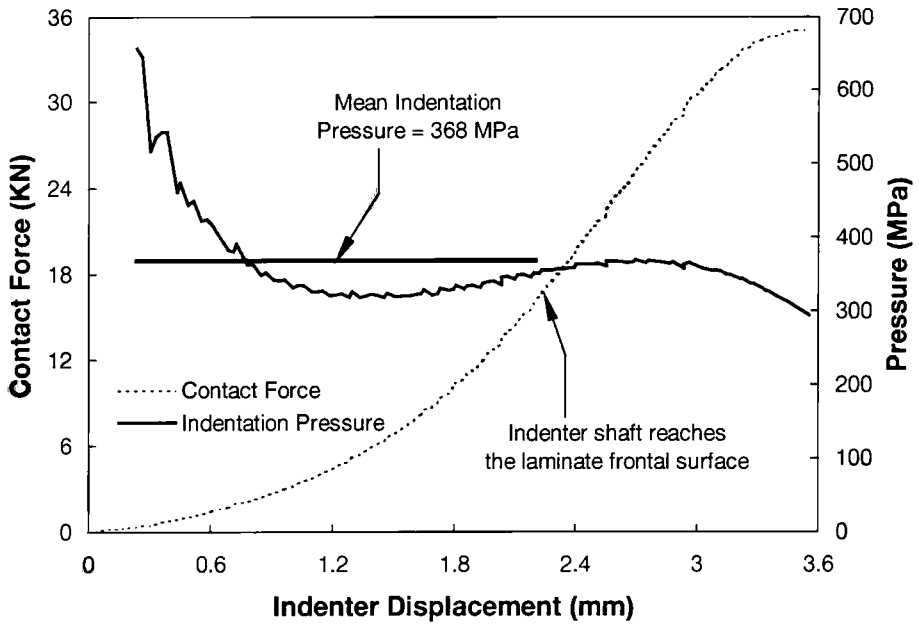

Figure 5.25 Calculation of mean indentation pressure based on the measured force-displacement curve for a S2-glass laminate penetrated by a conical indenter with an included cone angle of 120° and a diameter of 7.62 mm. The specimen thickness is 19.05 mm.

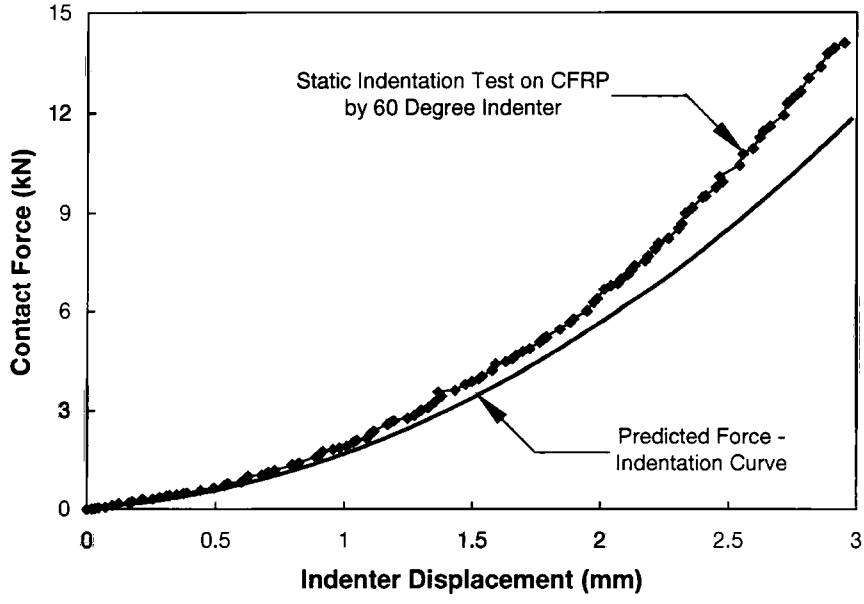

Figure 5.26 Comparison between the predicted and the measured contact force-indenter displacement curve in static indentation tests on a 6.15 mm thick CFRP specimen by an indenter with an included cone angle of 60°.

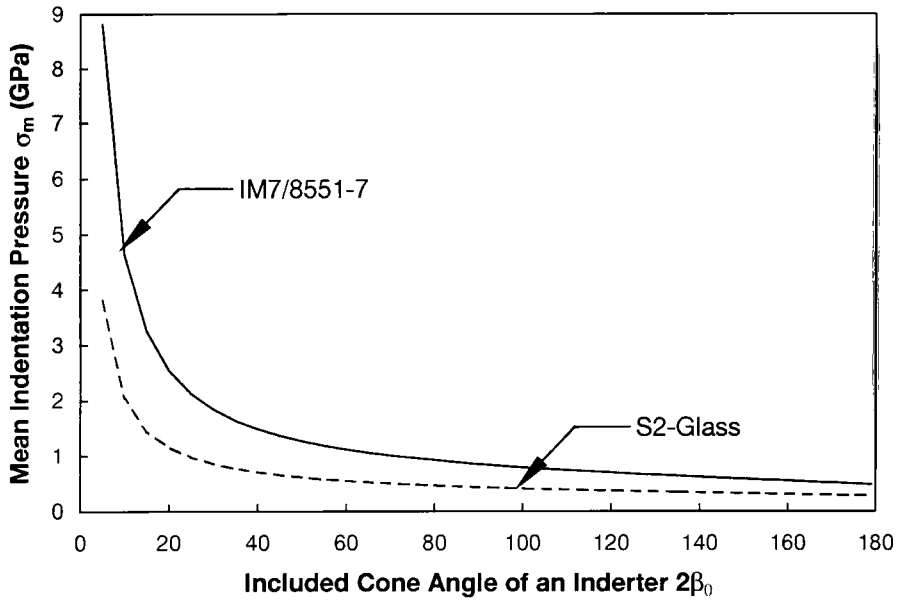

Figure 5.27 Relationship between the mean indentation pressure and the included cone angle of an indenter for CFRP and GFRP laminates.

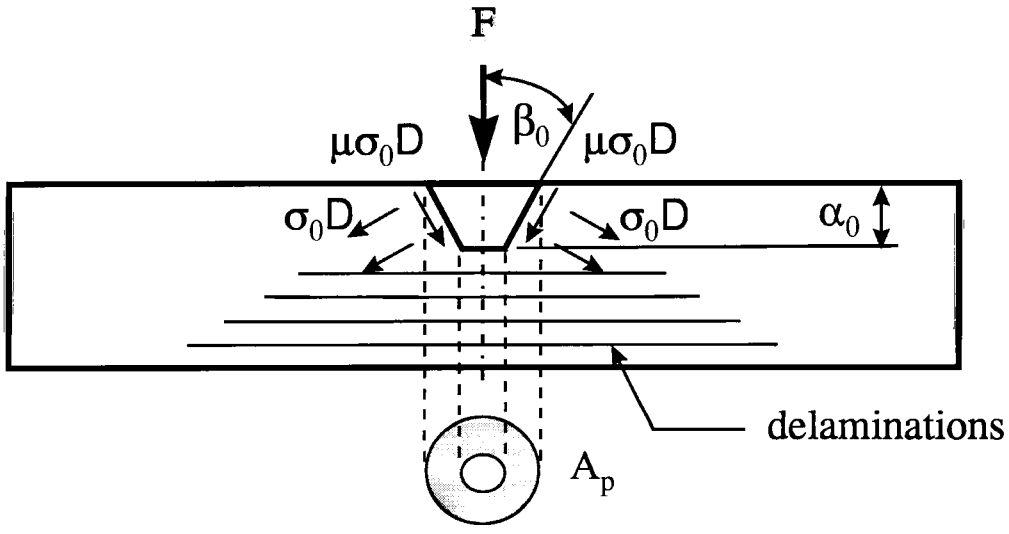

Figure 5.28 Schematic illustration of hole expansion mechanism after delamination is initiated in the laminate. A_p is the projected area undergoing hole expansion. D is a reduction factor accounting for lateral deformation on the distal surface of the laminate.

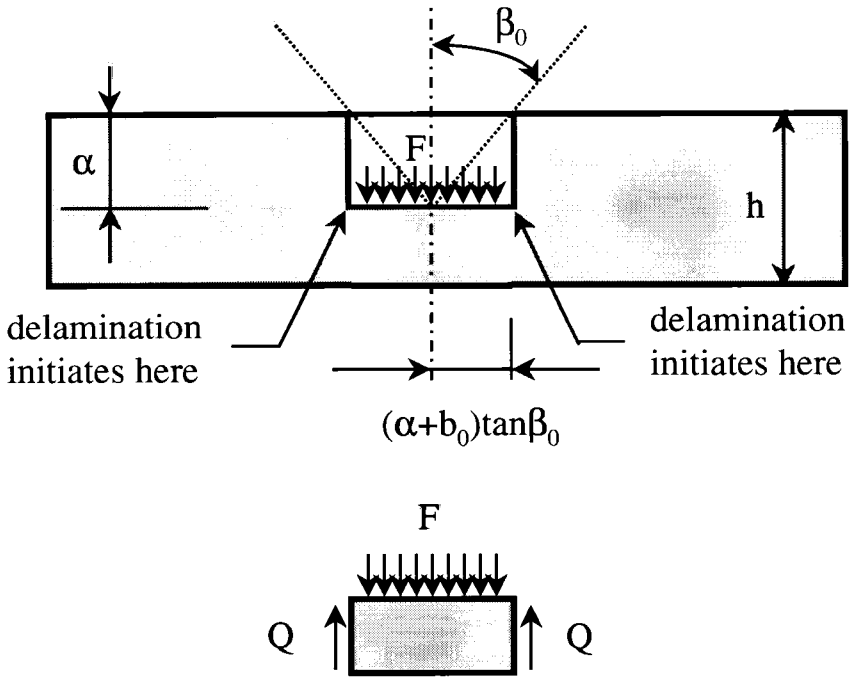

Figure 5.29 Free body diagrams used in calculation of shear stresses for delamination criterion.

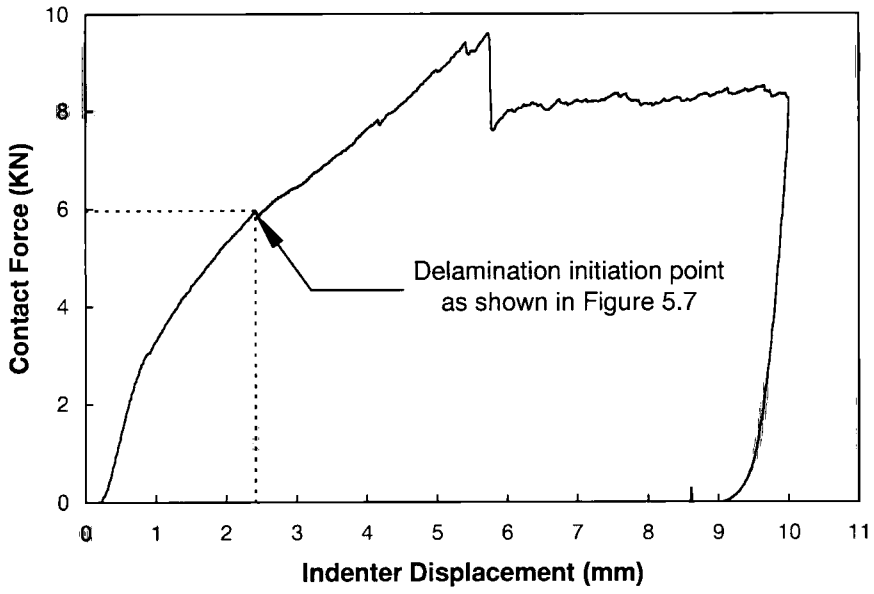

Figure 5.30 The experimental force-displacement curve for a 6.15 mm thick CFRP laminate statically penetrated by a 37° indenter. The support plate has a small-geometry opening.

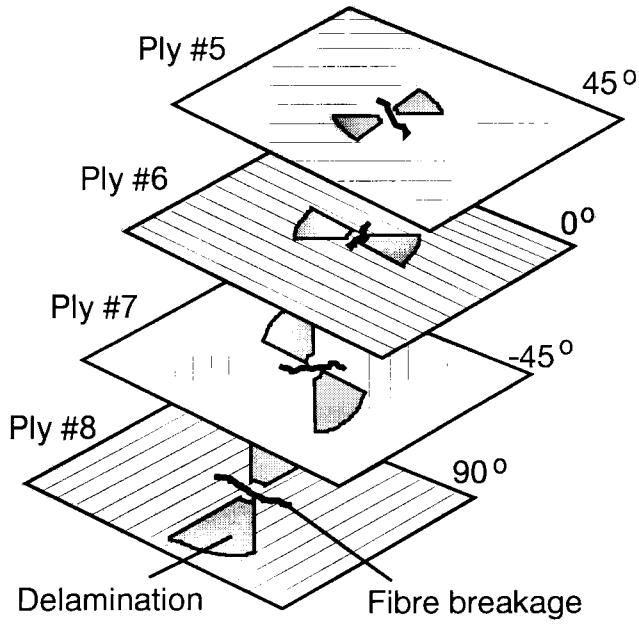

Figure 5.31 Schematic illustration of delamination patterns in a T300H/F593 CFRP laminate with a stacking sequence of $[45/0/-45/90]_{ns}$ under static loading by a flat indenter (Delfosse *et al.*, 1994b).

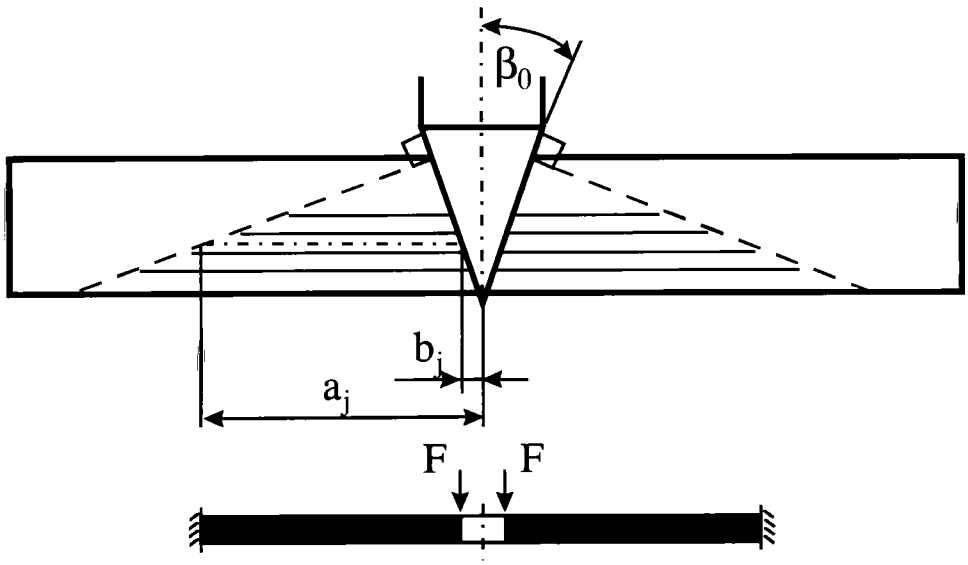

Figure 5.32 Schematic illustration of the geometry and loading condition of a typical split in the multi-split plate.

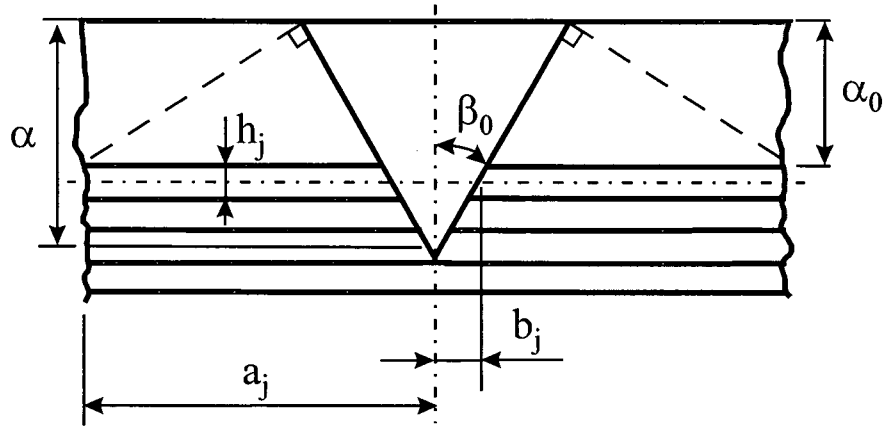

Figure 5.33 Schematic illustration for calculation of the inner and outer radii of each split in the split-plate.

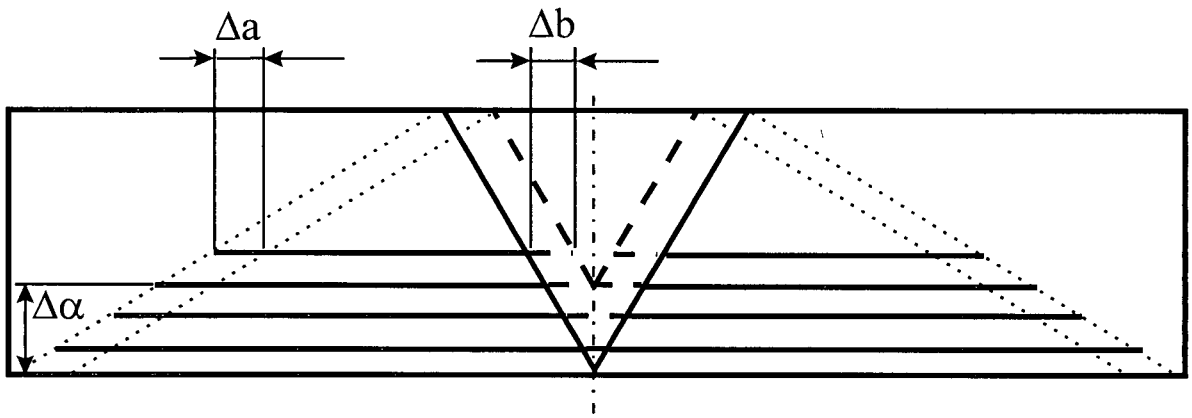

Figure 5.34 Schematic illustration of growth of the outer and inner radii of delaminations.

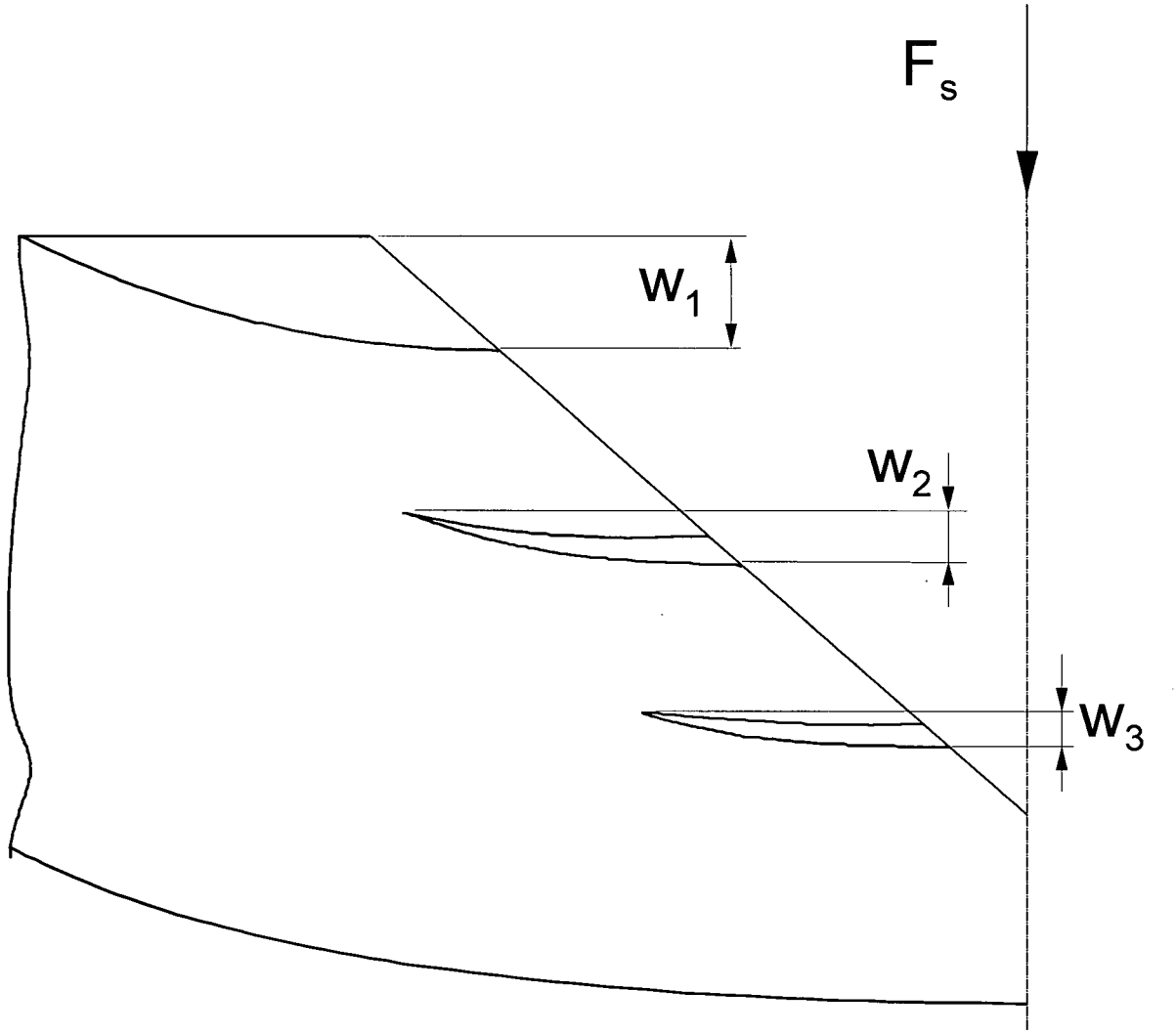

Figure 5.35 Schematic illustration of flexural deformation of a split-plate in section 5.2.3.3.2.

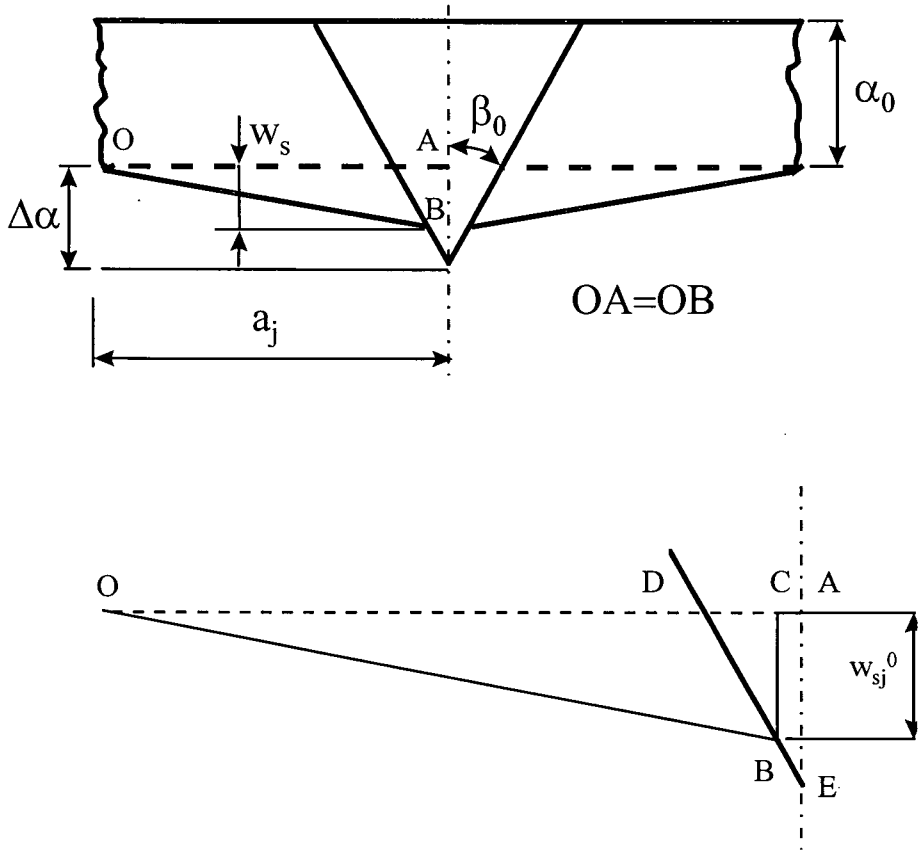

Figure 5.36 Nomenclature for the split-plate deflection after the projectile tip penetrates a certain layer of the laminate. α_0 is the penetration depth just when delaminations have initiated.

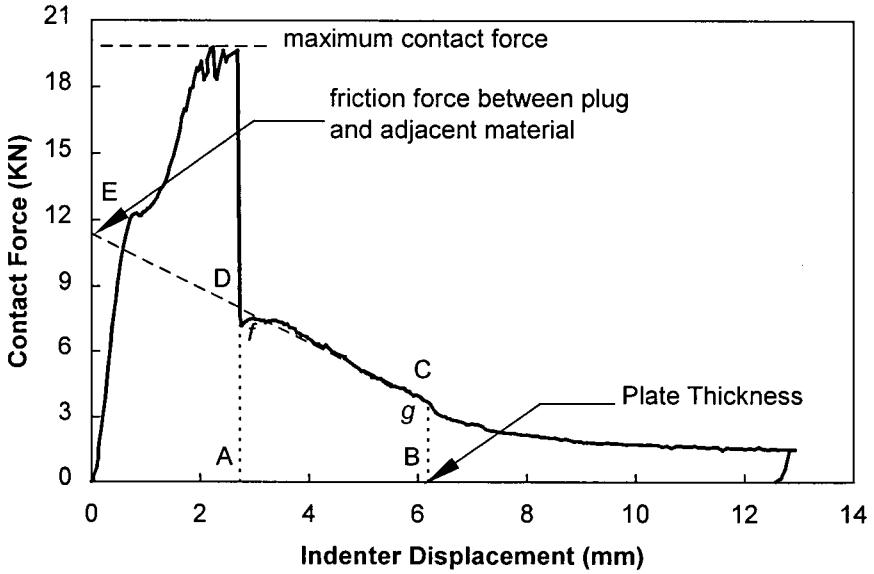

Figure 5.37 Estimation of the transverse shear strength and friction force between the plug and adjacent material for CFRP laminates.

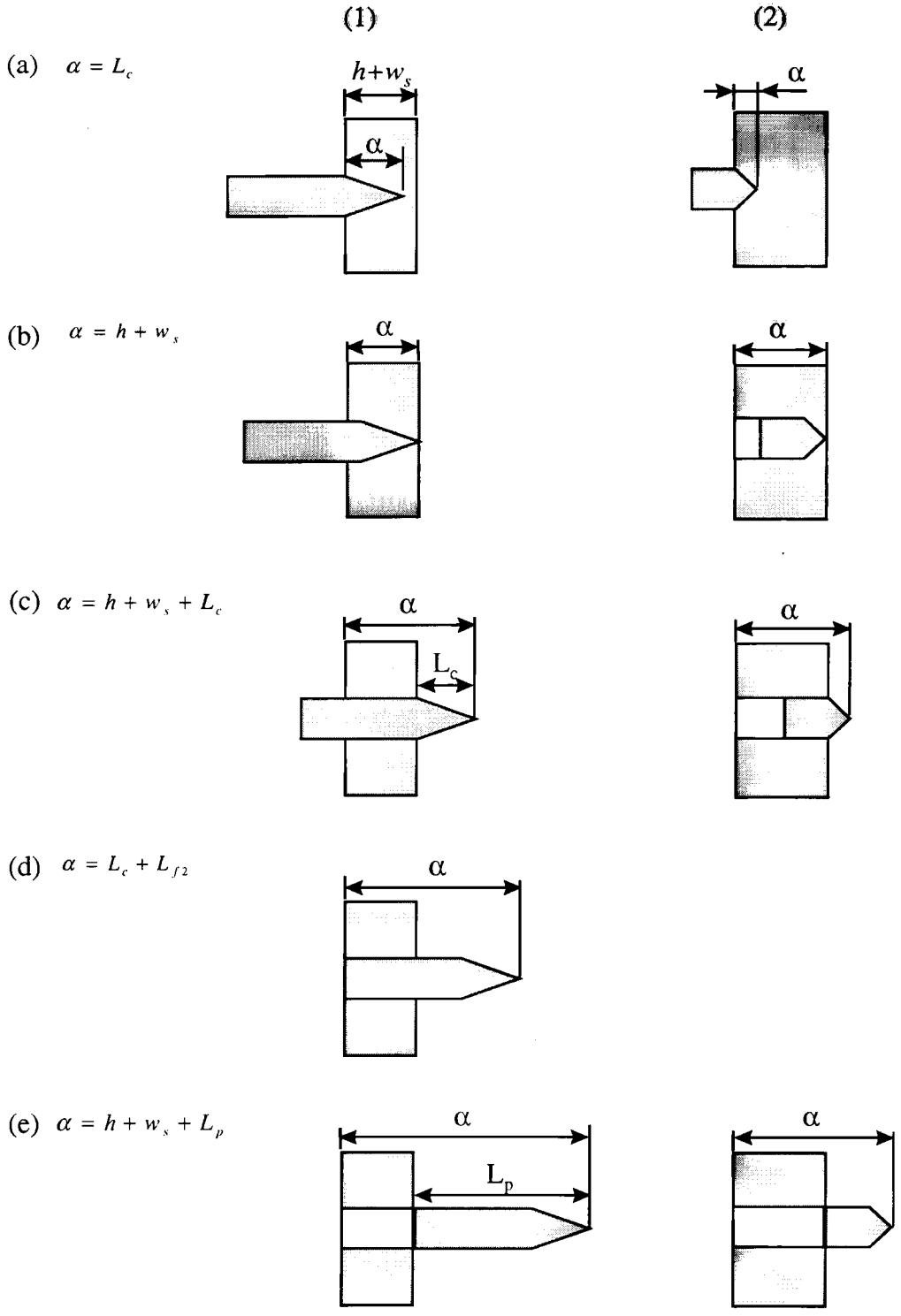

Figure 5.38 Calculation of penetration force at different positions of the projectile in the target when the projectile cone length is smaller than the local target thickness for (1) long projectiles ($L_p - L_c > h+w_s$) and (2) short projectiles ($L_p - L_c \leq h+w_s$).

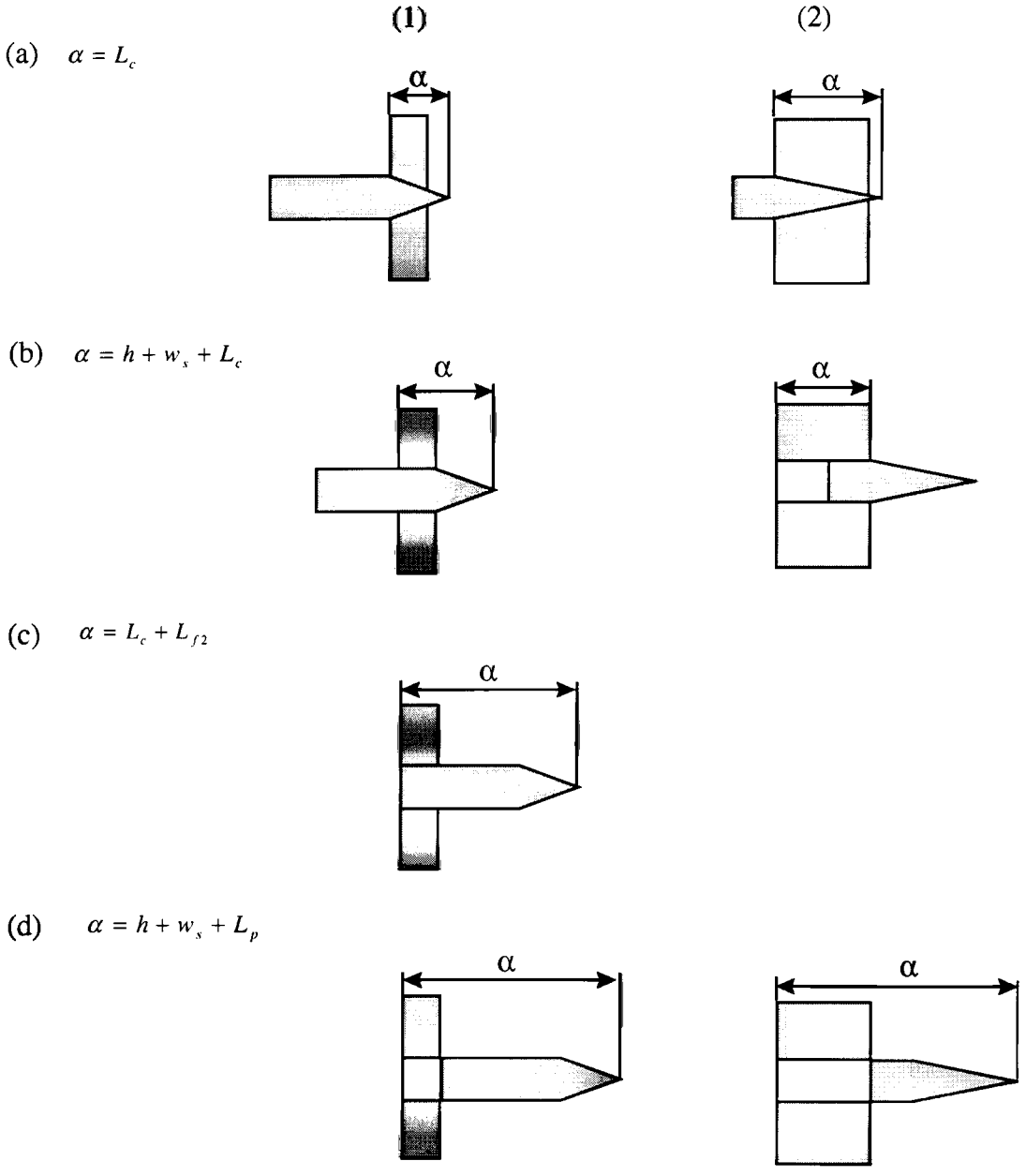

Figure 5.39 Calculation of penetration force at different positions of the projectile in the target when the projectile cone length is greater than the local target thickness for (1) long projectiles ($L_p - L_c > h + w_s$) and (2) short projectiles ($L_p - L_c \leq h + w_s$).

Chapter Six: Static Penetration Model and Applications

Based on the penetration mechanisms identified in the previous chapter, a penetration model is developed here. This model predicts the resistive force in addition to the energy absorbed by the composite target during projectile penetration. The model accounts for the penetration mechanisms and their transitions for different cone angles of projectiles. Two different material systems, CFRP and GFRP which are considered before (see Table 5.2 and Table 5.3), will be studied for the purposes of verifying the present model.

6.1 Model Development

The penetration depth is the difference between the projectile (or indenter) displacement and target deflection at the impact point. This can be written as

$$\alpha = \Delta - w = \Delta - (w_0 + w_s) \tag{6.1}$$

where Δ is the projectile (or indenter) displacement, w, w_0, and w_s are the total, global, and local target deflections at the impact site, respectively.

The assumptions used in developing the penetration model are:

1. The projectile is nondeformable (rigid) during penetration. Because a certain part of the kinetic energy of the deformable projectile is removed by elastic and/or permanent deformations, the deformable projectile needs more initial kinetic energy to perforate the

target than rigid projectiles. So this assumption will give a conservative estimate of the perforation energy.

2. The energy dissipated in heat, sound, and other sources not identified in the previous chapter is ignored in the penetration model.

3. Dynamic material characterisation tests (Delfosse, 1994b) showed that the CFRP is a strain rate insensitive material. GFRP is more sensitive to strain rate than CFRP. However, the force-displacement curves obtained from static penetration tests and dynamic tests on GFRP have been shown by Sanders (1997) to be very similar. Thus for simplifying the problems, material strain rate effects are ignored here.

Based on the penetration mechanisms discussed in the previous section, a flow chart of the proposed penetration model and its description will be presented first.

6.1.1 Description and Flow Chart of the Penetration Model

A flow chart of the proposed penetration model is illustrated in Figure 6.1. The initial penetration mechanism is hole expansion. The material around the projectile is pushed aside from the impact point and the deformation on the distal surface of the specimen is assumed to be negligible. In this phase, delamination has not initiated in the laminate and thus the local plate deflection $w_s = 0$.

The penetration force is calculated using

$$F = \sigma_m \pi (\alpha + b_0)^2 \tan^2 \beta_0 \tag{5.1}$$

At each increment of penetration depth, initiation of delamination and transverse plugging are checked using the following conditions:

$$\tau \geq \tau_s \qquad \text{for delamination initiation} \qquad (5.9)$$

$$\tau \geq \tau_0 \qquad \text{for transverse plugging initiation} \qquad (5.34)$$

If delaminations occur, the flexural deflection of the split-plate combines with hole expansion to affect the penetration response of the laminate. At this time, we need to calculate the local plate deflection w_{sj}^0 in the laminate due to the split-plate bending deformation

$$w_{sj} = w_{sj}^0 + \theta_j a_j \qquad (5.31)$$

The total resistive force is calculated as

$$F = F_h + F_s \qquad (6.2)$$

where

$$F_h = \sigma_m [1 - \frac{\alpha - \alpha_0}{\max(L_c, h) - \alpha_0}] \pi \tan^2 \beta_0 \left[(\alpha + b_0)^2 - (\alpha - \alpha_0)^2 \right] \qquad (5.6)$$

$$F_s = w_{s1}^0 \frac{4\pi D_{d1}(1+\nu)}{4\pi D_{d1}(1+\nu) f + a_j^2 \frac{f}{f_1}} \qquad \text{for CFRP} \qquad (5.33a)$$

$$F_s = \frac{w_s^0}{f} \frac{1}{[1 + \frac{1}{4\pi f(1+\nu)} \sum_{j=1}^{n} \frac{a_j^2}{D_{dj}}]} \qquad \text{for GFRP} \qquad (5.33b)$$

If transverse plugging occurs, the force drops to a value of

$$F = F_{pf} \frac{h - \alpha}{h} \qquad (5.35)$$

When the projectile (indenter) shaft reaches the frontal surface of the target, friction starts. The equations to calculate the penetration force after initiation of the friction phase presented in the previous chapter [Equations (5.38) - (5.46)].

The penetration model can also be illustrated using the spring system shown in Figure 6.2, where k_h, k_s, k_p denote the spring stiffnesses due to hole expansion, flexural deformation of the split-plate, and transverse plugging, respectively.

The spring corresponding to the hole expansion is continually active from the beginning of the penetration event to the time when the projectile (or indenter) shaft reaches the frontal surface of the target, while the other two springs k_h and k_p do not trigger until a certain criterion has been met.

Experimental observations have shown that in the GFRP laminates delaminations have a "thickening" effect. Part of the "thickening" is due to the local bending of the laminates and can be modelled as split-plates as in CFRP laminates. The other reason for "thickening" is the gap between the micro-delaminations in the laminates (see Figure 5.12). Therefore, when the split-plate model is applied, the total compliance of the split-plate is calculated using Equation (5.20) because in this case the splits do not have the same deflection.

Furthermore, the increasing gap between delaminations will cause changes in applying the hole expansion mechanism. The penetration force F in hole expansion deformation before any delamination initiate is calculated from Equiation (5.1). When $\tau \geq \tau_s$, new delamination initiates in the target material around the projectile tip. Let α_0 denote the penetration depth when a new delamination initiates. Then in subsequent penetration the projectile penetrates a

new surface from very beginning until new delamination initiates, which is schematically shown in Figure 6.3. The calculation of hole expansion force becomes

$$F = F_h + \sigma_m \pi(\alpha + b_0 - \alpha_0)^2 \tan^2 \beta_0; \qquad \text{for GFRP} \qquad (6.3)$$

where F_h is calculated from Equation (5.6).

For CFRP laminates, all the delaminations initiate at the same time while for GFRP laminates, delaminations initiate sequentially, one by one. Therefore, there is a penetration stage in GFRP laminates which CFRP laminates do not have, *i.e.*, the stage from the initiation of the first delamination to the last delamination. Equation (6.3) is used to calculate the penetration force during this stage.

The new delamination interface is then generated using the criterion of

$$\tau = \frac{Q}{h-\alpha}\frac{\alpha-\alpha_0}{h-\alpha_0} \geq \tau_s; \qquad \text{for GFRP} \qquad (6.4)$$

where Q is calculated using Equation (5.7). Then α_0 are updated until next delamination initiates.

When all the delamiantions have been initiated in the laminate, the combined flexural deformation of the split-plate and hole expansion acts as the second penetration mechanism. The penetration force is still calculated in the same way as CFRP except that the calculation of the compliance of the split-plate follows Equation (5.20) instead of Equation (5.16).

In SENACS, a flag is used in the input file load definition to direct the computational procedure for a CFRP and GFRP laminate.

6.1.2 Sensitivity Analysis

In this section, a sensitivity analysis is conducted on the present penetration model for CFRP laminates. The objective is to better understand the initiation criteria for delamination and transverse plugging, and to know how definitive these material constants obtained from static penetration and indentation tests are.

6.1.2.1 Initiation of Delamination

From Equations (5.7), (5.8), and (5.9), we have

$$\frac{F}{2\pi(\alpha+b_0)\tan\beta_0}\frac{\alpha}{h(h-\alpha)}=\tau_s \tag{6.5a}$$

Because b_0 is very small, $\alpha+b_0\approx\alpha$. While the projectile (indenter) shaft has not reached the target frontal surface $[(\alpha+b_0)\tan\beta_0\le L_c]$, Equation (6.5a) can be written as

$$\alpha=h-\frac{F}{2\pi h\tan\beta_0\tau_s} \tag{6.6a}$$

When the projectile (indenter) shaft reaches the target frontal surface $[(\alpha+b_0)\tan\beta_0 > L_c]$, Equations (6.5a) and (6.6a) become

$$\frac{F}{2\pi R_p}\frac{\alpha}{h(h-\alpha)}=\tau_s \tag{6.5b}$$

or after rearranging terms

$$F=2\pi R_p h\tau_s\left(\frac{h}{\alpha}-1\right) \tag{6.6b}$$

Thus, a series of curves of delamination initiation corresponding to different included cone angles are shown in Figure 6.4 for CFRP laminates. When a pair of contact force and penetration depth locates above the curve corresponding to that indenter cone angle, delamination initiates.

As the cone angle increases, higher forces are required to initiate delamination. In other words, according to the present model, penetration by an indenter with a small cone angle is more likely to cause delamination.

6.1.2.2 Initiation of Transverse Shear Plugging

From Equations (5.34), while the projectile (indenter) shaft has not reached the target frontal surface $[(\alpha + b_0)\tan\beta_0 \le L_c]$, we have

$$\frac{F}{2\pi(\alpha + b_0)h\tan\beta_0} = \tau_0 \tag{6.7a}$$

Thus

$$F = 2\pi(\alpha + b_0)h\tau_0\tan\beta_0 \tag{6.8a}$$

When the projectile (indenter) shaft reaches the target frontal surface $[(\alpha + b_0)\tan\beta_0 > L_c]$, Equations (6.7a) and (6.8a) turn to be

$$\frac{F}{2\pi R_p} = \tau_0 \tag{6.7b}$$

and

$$F = 2\pi R_p\tau_0 \tag{6.8b}$$

In Figure 6.5, a series of curves of transverse shear plugging initiation corresponding to an indenter with different included cone angles are shown for CFRP. The plateau on the curves for large cone angles (90°, 120°, and 150°) means that the indenter shaft has penetrated into the laminate and there is no more increase in the indenter projected area A_p. The indenter bluntness causes the different start points of the curves of 15°, 37°, and 60°. When a point falls above the curve corresponding to a given indenter cone angle, plugging mechanism dominates. Each curve is the locus of forces and penetration depths that correspond to initiation of plugging.

For a given penetration depth, an indenter with a large cone angle needs higher force to initiate transverse plugging than an indenter with a small cone angle. For a given contact force, an indenter with a large cone angle is more easily to initiate the plugging than that with a small cone angle.

6.1.2.3 Sensitivity of Hole Expansion Pressure σ_0 on Initiation of Penetration Mechanism

The relationship between hole expansion force and penetration depth, delamination initiation curve, and transverse plugging initiation curve are shown in Figure 6.6 for the CFRP laminate penetrated by an indenter with 37° cone angle. It can be seen that the delamination initiation curve meets the force curve earlier than the plugging initiation curve. Therefore, delamination initiates instead of plugging. If the value of current hole expansion pressure σ_0 is increased by 35%, plugging initiation curve would meet the force curve first instead of delamination initiation curve. Then, transverse plugging rather than delamination would initiate.

The same curves are also plotted for an indenter with an included cone angle of 120° as shown in Figure 6.7. It can be seen that the plugging initiation curve meets the force curve first and thus causes transverse shear plugging. If the value of the current hole expansion pressure σ_0 is decreased by 32%, delamination rather than transverse plugging would initiate.

6.2 *Results and Discussion*

We apply the penetration model developed in the previous sections to predict the CFRP and GFRP penetration responses and compare the model predictions with experimental measurements.

6.2.1 CFRP Laminates

The foregoing model is used to simulate the static penetration responses of large-geometry or small-geometry specimens of CFRP laminates. The material properties and geometric sizes are listed in Table 5.2. Specimens with dimensions of 152 mm × 102 mm or 50.4 mm × 50.4 mm are placed on a steel support with a 127.0 mm × 75.4 mm rectangular opening or circular opening of diameter 25.4 mm.

The predicted force-displacement curves and energy-displacement curves for indenters with included angles of 37°, 60°, 120°, and 180° are compared with the corresponding experimental results in Figures 6.8 to 6.15, respectively. The static penetration tests on 60° and 120° conical indenters were conducted on the small-geometry specimen due to the shortage of material supply. The labels A_1, B_1 or B_1', C_1, A_2, B_2 or B_2', and C_2 on the curves

correspond to the critical points shown on the characterised force-displacement curves shown in Figure 5.14.

6.2.1.1 Penetration by 37° and 60° Conical Indenters

A comparison between the predicted and measured results are shown in Figures 6.8 and 6.9 for 37° conical indenter, and Figures 6.10 and 6.11 for 60° conical indenter.

It can be seen that the current model compares fairly well with the experimental force-displacement and energy-displacement curves for both the 37° and 60° conical indenters. The parabolic increase in the force at the early stage of penetration, delamination initiation, and friction plateau that are characteristics of the experimental curves are reasonably well predicted by the model. The predicted potential energy (*i.e.*, integration of the force-displacement curve) versus indenter displacement compares well with the experimental results for the 37° and 60° conical indenters.

6.2.1.2 Penetration by 120° and 180° Conical Indenters

A comparison between the predicted and measured results are shown in Figures 6.12 and 6.13 for the 120° conical indenter, and Figures 6.14 and 6.15 for the 180° conical indenter.

The model is seen to capture very well the essence rather than details of the force-displacement curves, such as the load drop and friction plateau. The model predicts that a transverse plug forms in the laminate and this is supported by examining the cross-sectional micrograph of the specimen as shown in Figure 5.6. The peak force in a 180° conical

indenter is very close to that in the experiment. However, the comparison between the predicted and measured peak force is rather poor for the 120° indenter.

One reason for this discrepancy is that the model does not predict the delaminations that have been observed in the static penetration tests with 120° and 180° conical indenters. Delaminations will reduce the flexural rigidity of the laminate and cause larger bending deflection and hence lead to an increase in the indenter displacement. A major deficiency of the current model is that it does not account for both delamination and transverse plugging. As shown in the flow chart (see Figure 6.1), either delamination or plugging can occur but not both.

6.2.1.3 Penetration by an Indenter with a General Cone Angle

Figure 6.16 shows the comparison among the predicted force-displacement curves for a range of included cone angles of indenters. These curves have all been generated for large-geometry specimens. With increasing cone angle, the peak penetration force increases while the span of the indenter displacement decreases. This trend is similar to the experimental force-displacement curves for Kevlar penetrated statically by a range of cone angles (60°, 90° , and 120°) presented in Zhu *et al.* (1992). For small indenter cone angles, such as 15°, 37°, and 60°, the material around the indenter undergoes hole expansion as well as flexural deformation of delaminated plate (split-plate). For large cone angles, such as 90°, 120°, and 150°, the plate material undergoes hole expansion and then formation and push-out of a transverse plug. A similar trend was also observed by Woodward (1984) for metallic materials.

Johnson *et al.* (1973) found that plug formation occurred when the included cone angle of the indenter was greater than 90° in the plates when there were no friction between the indenter and the plate. If the coefficient of friction were to increase, plug formation would occur at included cone angles less than 90°.

The predicted initiation force of delamination and transverse plugging, and peak penetration force are also shown in Figure 6.17 and Figure 6.18, respectively.

6.2.2 GFRP Laminates

The present model is also applied to static penetration tests of GFRP laminates defined in Table 5.3. The indenters are specified in Table 5.1, where only those with 37° and 120° included cone angles are used in the tests.

6.2.2.1 Penetration by 37° Conical Indenter

The calculated force-displacement curves are compared with experimental ones in Figure 6.19 to Figure 6.24.

The results of penetration tests on 6.35 mm laminate are shown in Figures 6.19 and 6.20. The label A_1' represents the initiation of the first delamination in the laminate. With the advancement of the indenter, more delaminations occur. After all the delaminations have been initiated, the hole expansion and flexural deformation of the split-plate commences. This is marked as A_1. At point B_1, the indenter shaft reaches the frontal surface of the laminate and the friction phase starts. Finally, at point C_1, the indenter shaft reaches the

distal surface of the laminate. The comparison between the predicted force-displacement and energy-displacement curve is reasonably good.

Point A_1 does not appear on the predicted force-displacement and energy-displacement curves corresponding to penetration tests on 12.70 mm and 19.05 mm thick laminates. According to the model, before all the delaminations are initiated, the indenter shaft has already reached the frontal surface of the laminate and the friction phase starts.

For the penetration tests on all the three laminate thicknesses, the predicted maximum indenter displacements are very close to the measurements.

6.2.2.2 Penetration by 120° Conical Indenter

The predicted and measured force-displacement and energy-displacement curves are compared in Figure 6.25 to Figure 6.30. In the experiments, the indenter did not penetrate through the laminate. It merely pushed the laminate through the opening on the support plate.

The predicted contact force is higher than the measured one while the predicted maximum indenter displacement is smaller than the measurement value as shown in Figures 6.25 and 6.26 for penetration test on the 6.35 mm thick laminate. In the cases of 12.70 mm thick and 19.05 mm thick laminates, both the peak contact forces and the maximum indenter displacements are smaller than the measured values. It is difficult to assess the performance of the model in this case since penetration was not achieved in the experiments.

6.3 Summary

Based on the mechanisms identified in the previous chapter, analytical models for penetration of CFRP and GFRP laminates have been developed in this chapter.

The predicted and measured penetration force and energy absorption versus indenter displacement curves agree well in most cases for different indenter included cone angles (37° , 60°, 120°, and 180°), different target thicknesses (6.35 mm, 12.7 mm, and 19.05 mm), and different material systems (IM7/8551-7 CFRP, S2-glass/phenolic resin GFRP).

The penetration model developed here has been implemented into the super finite element code, SENACS, to enable analysis of dynamic penetration problems. The results of application of the code to ballistic impact of laminated composite structures are presented and discussed in the next chapter.

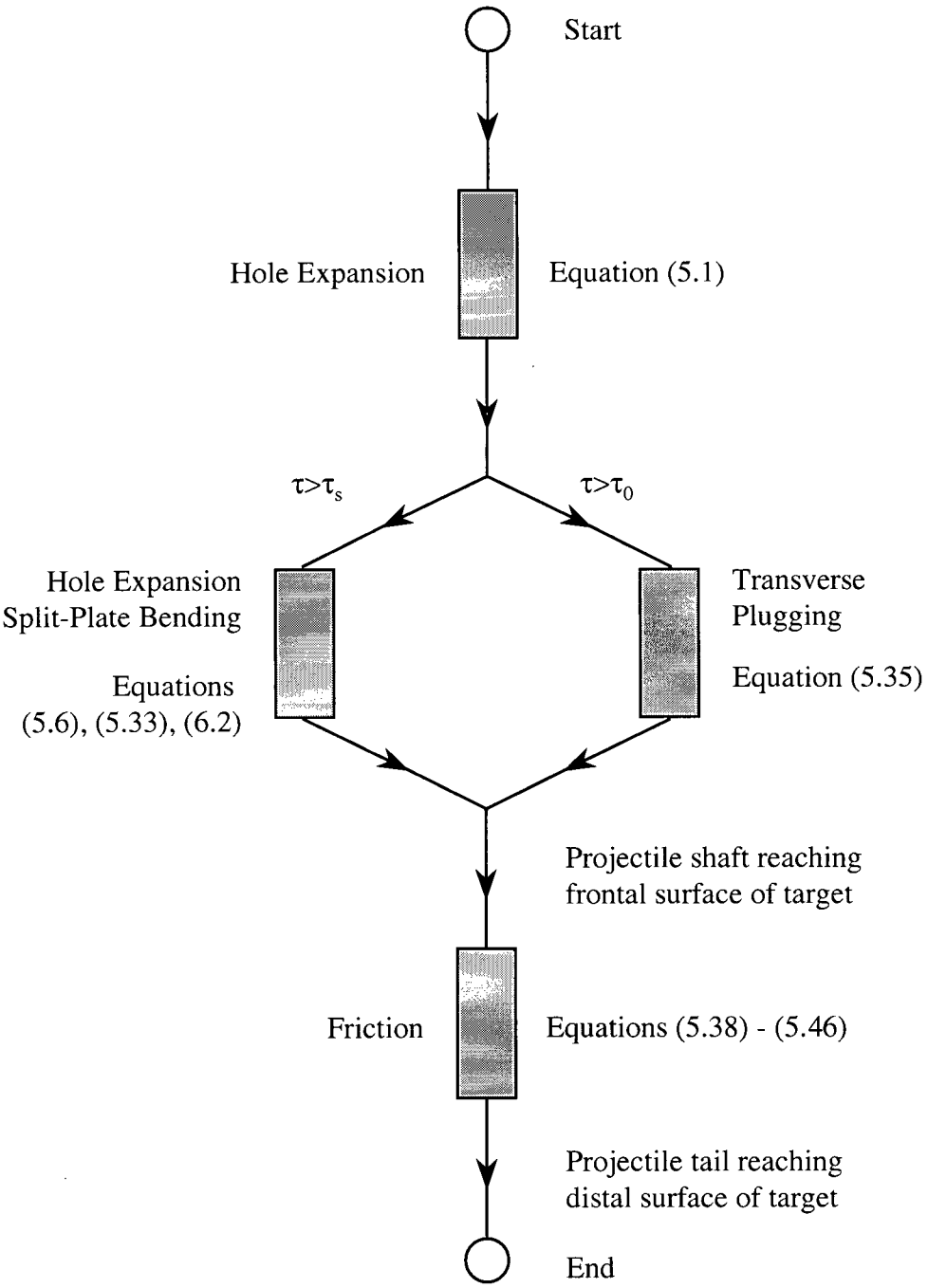

Figure 6.1 Flow chart of the penetration model.

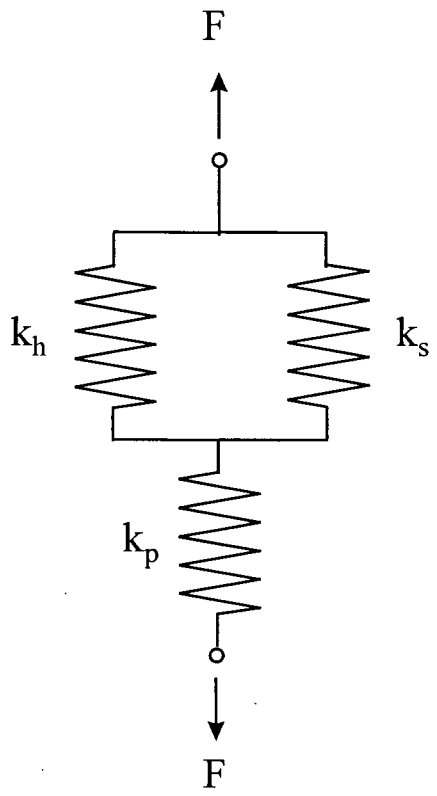

Figure 6.2 Illustration of the penetration model as a spring system. F denotes the penetration force, k_h, k_s, k_p denote the spring stiffnesses due to hole expansion, flexural deformation of a split-plate, and transverse plugging, respectively.

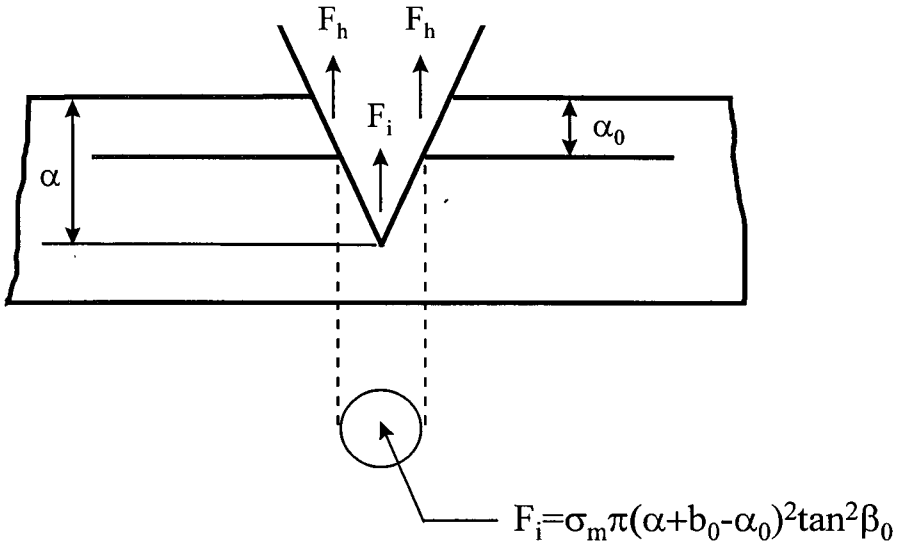

Figure 6.3 Schematic illustration of the penetration behaviour in GFRP laminates when one delamination has already been initiated and developed. Total force is the sum of F_h and F_i.

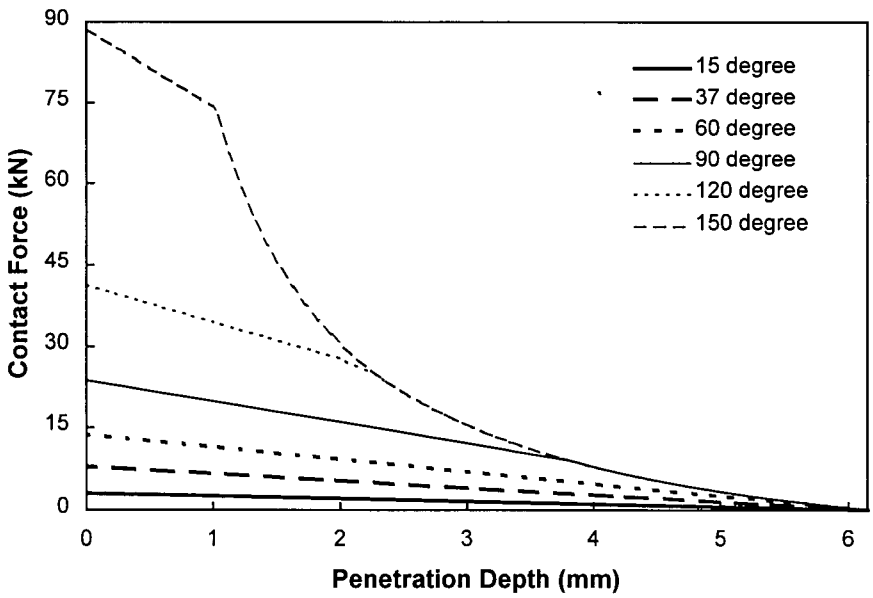

Figure 6.4 Curves of delamination initiation force versus penetration depth for a CFRP laminate.

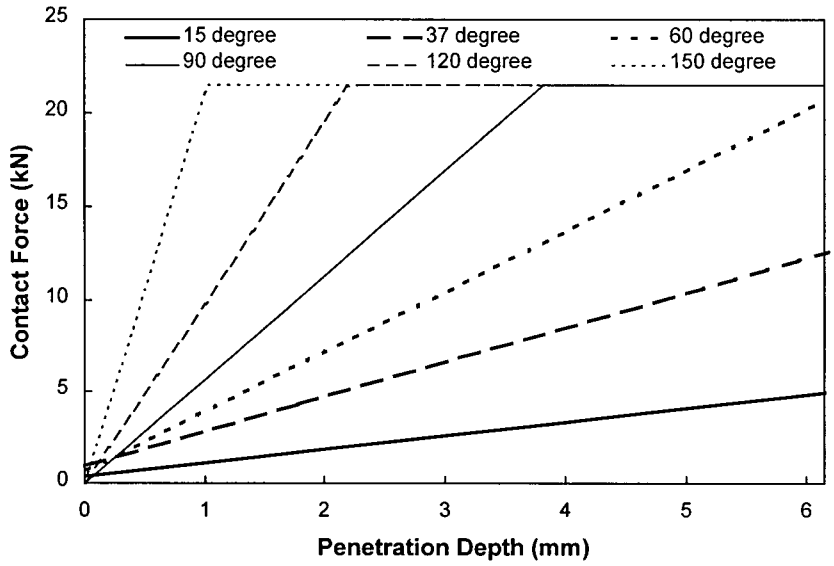

Figure 6.5 Curves of transverse shear plugging initiation force for CFRP laminates versus the penetration depth. When a pair of contact force and penetration depth falls above the curve corresponding to a given indenter cone angle, plugging mechanism dominates.

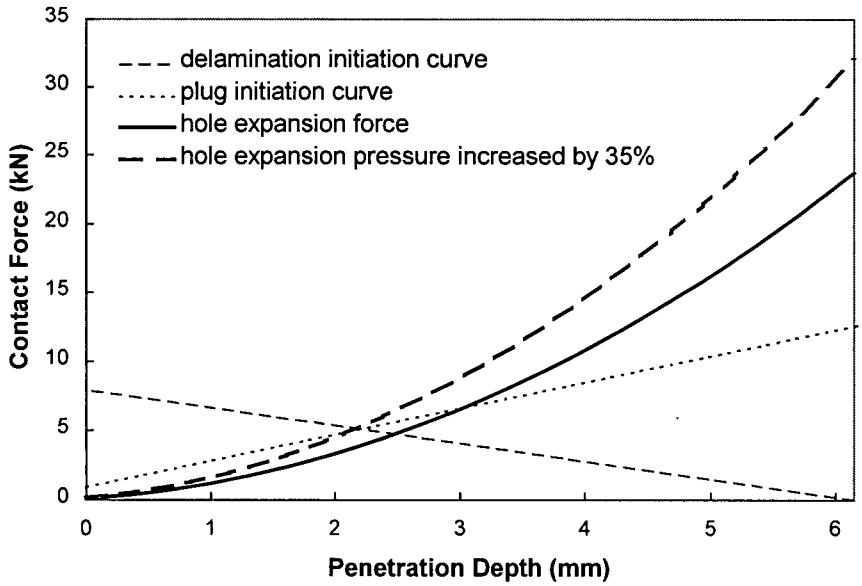

Figure 6.6 Hole expansion force, delamination initiation, and plugging initiation curves of CFRP laminates when penetrated by an indenter with a cone angle of 37°.

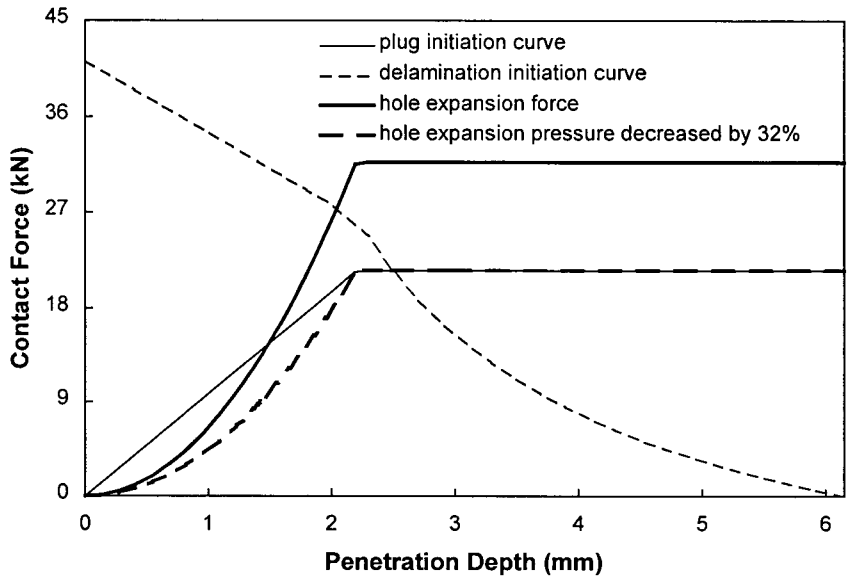

Figure 6.7 Hole expansion force, delamination initiation curve, and plugging initiation curve of CFRP laminates when penetrated by an indenter with a cone angle of 120°.

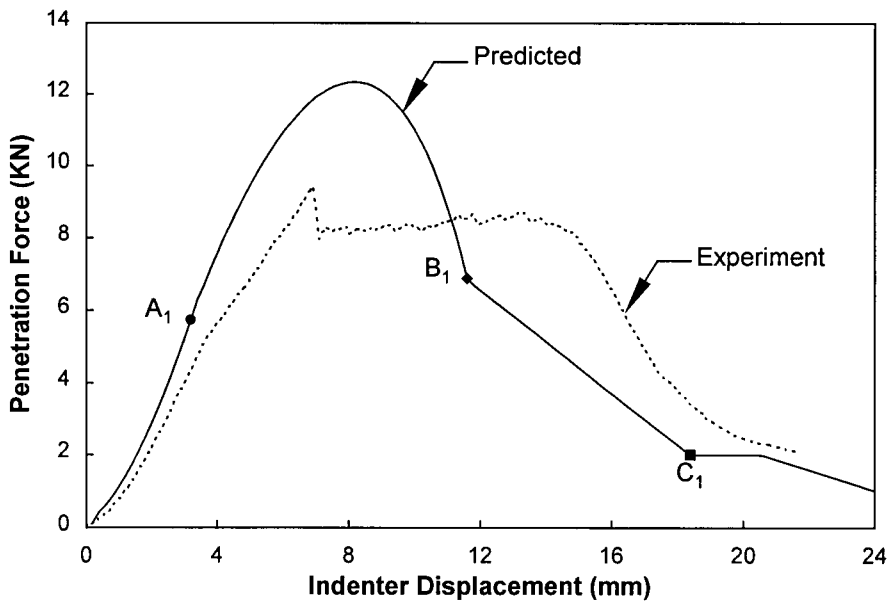

Figure 6.8 Comparison between the predicted and measured static force-displacement curves for the CFRP laminate defined in Table 5.2 penetrated by an indenter with an included cone angle of 37°.

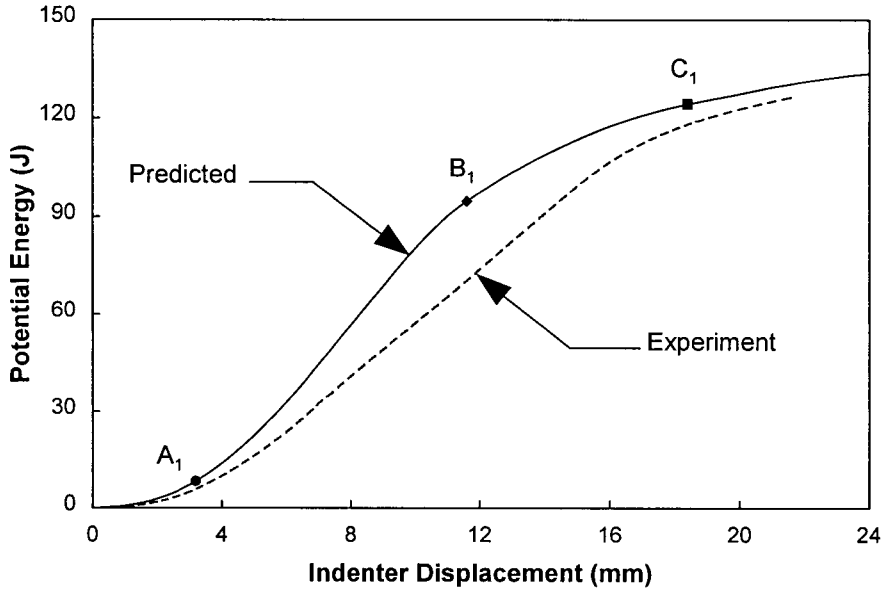

Figure 6.9 Comparison between the predicted and measured energy-displacement curves for the CFRP laminate defined in Table 5.2 penetrated by an indenter with an included cone angle of 37°.

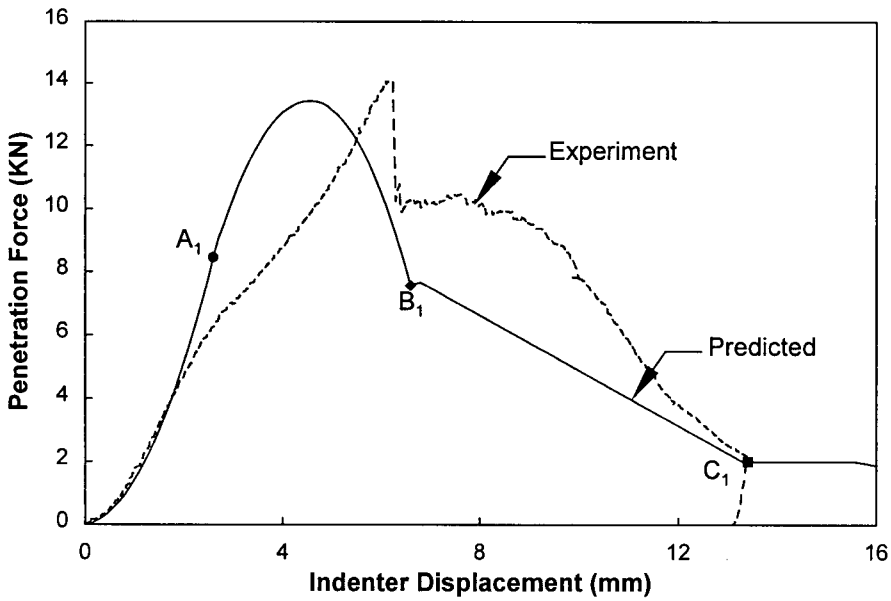

Figure 6.10 Comparison between the predicted and measured static force-displacement curves for the CFRP laminate defined in Table 5.2 penetrated by an indenter with an included cone angle of 60°.

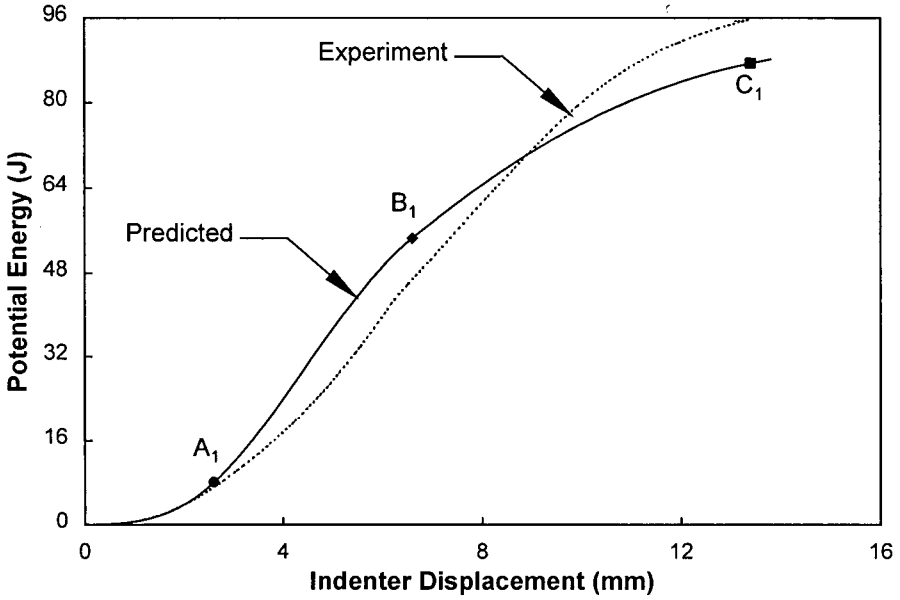

Figure 6.11 Comparison between the predicted and measured energy-displacement curves for the CFRP laminate defined in Table 5.2 penetrated by an indenter with an included cone angle of 60°.

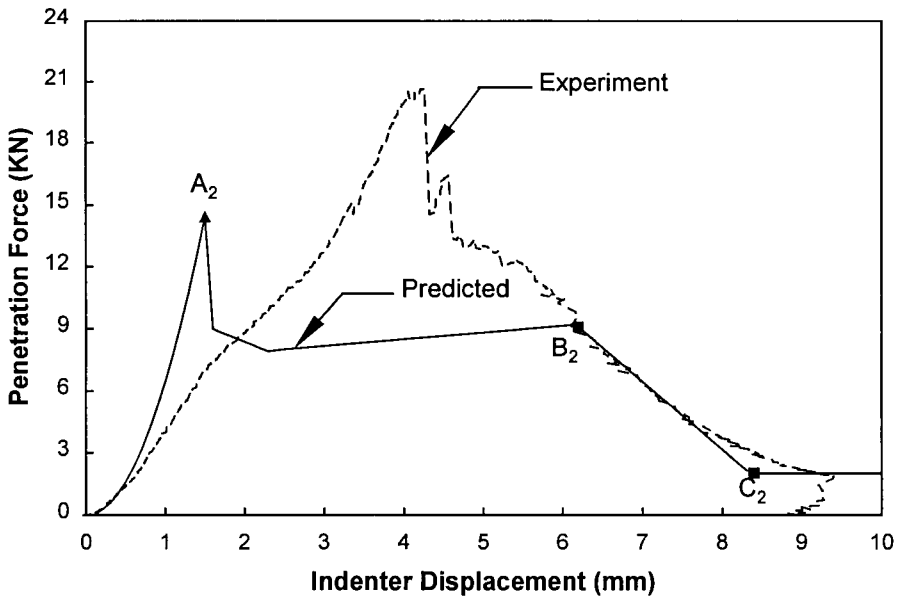

Figure 6.12 Comparison between the predicted and measured static force-displacement curves for the CFRP laminate defined in Table 5.2 penetrated by an indenter with an included cone angle of 120°.

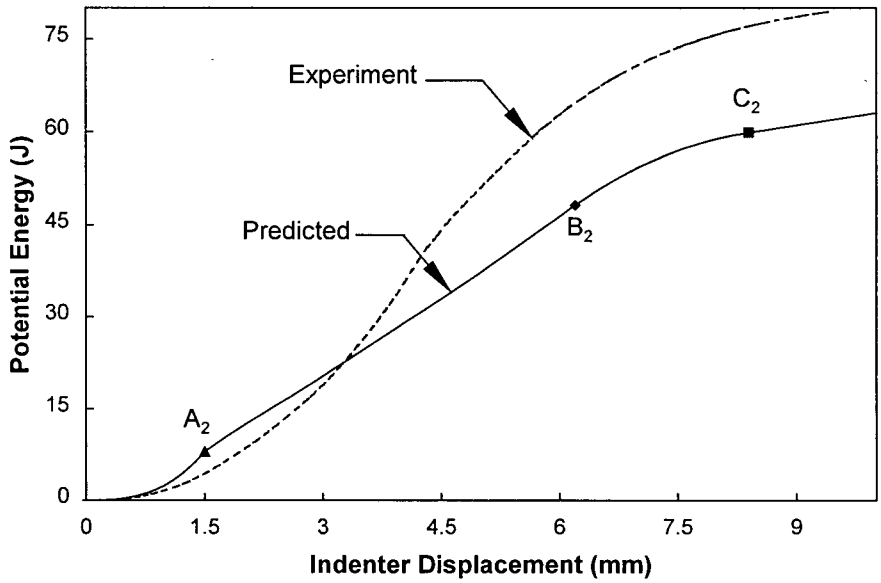

Figure 6.13 Comparison between the predicted and measured energy-displacement curves for the CFRP laminate defined in Table 5.2 penetrated by an indenter with an included cone angle of 120°.

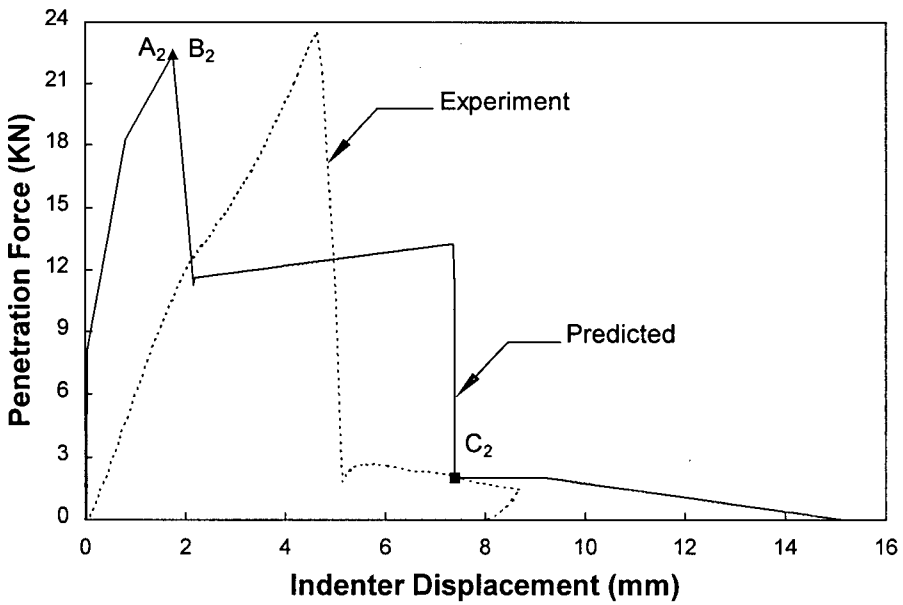

Figure 6.14 Comparison between the predicted and measured static force-displacement curves for the CFRP laminate defined in Table 5.2 penetrated by an indenter with an included cone angle of 180°.

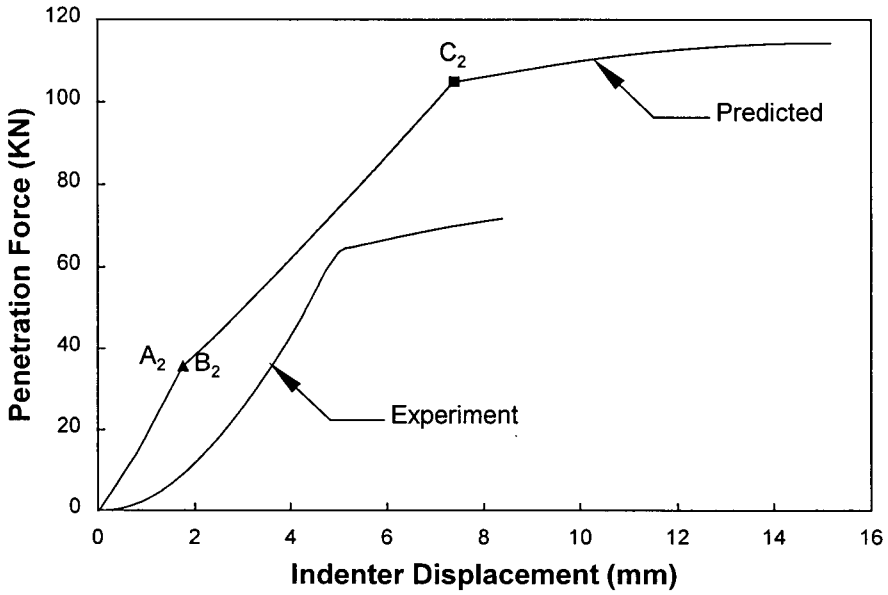

Figure 6.15 Comparison between the predicted and measured energy-displacement curves for the CFRP laminate defined in Table 5.2 penetrated by an indenter with an included cone angle of 180°.

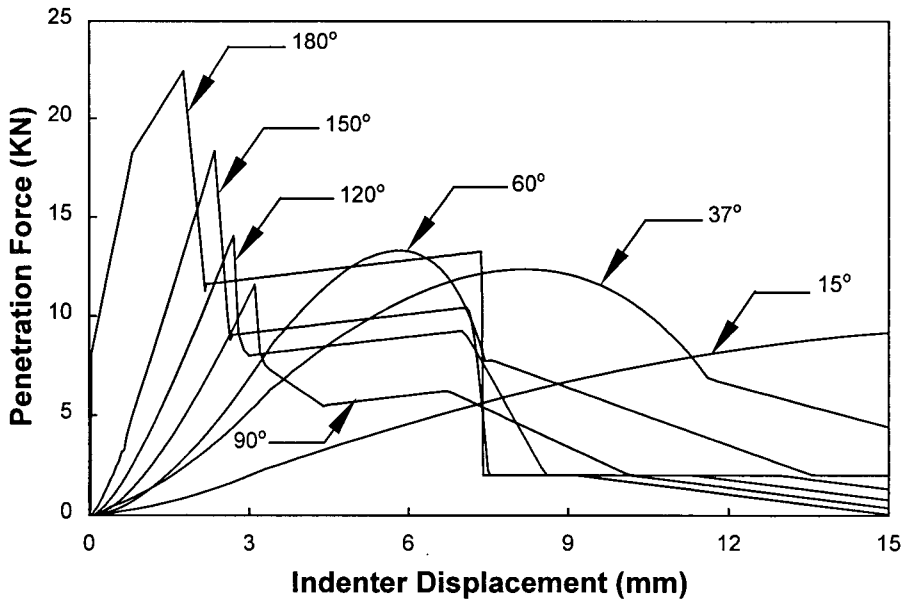

Figure 6.16 Comparison between the predicted and measured static force-displacement curves for the CFRP laminate defined in Table 5.2 penetrated by indenters with included cone angles of 15°, 37°, 60°, 90°, 120°, 150°, and 180°.

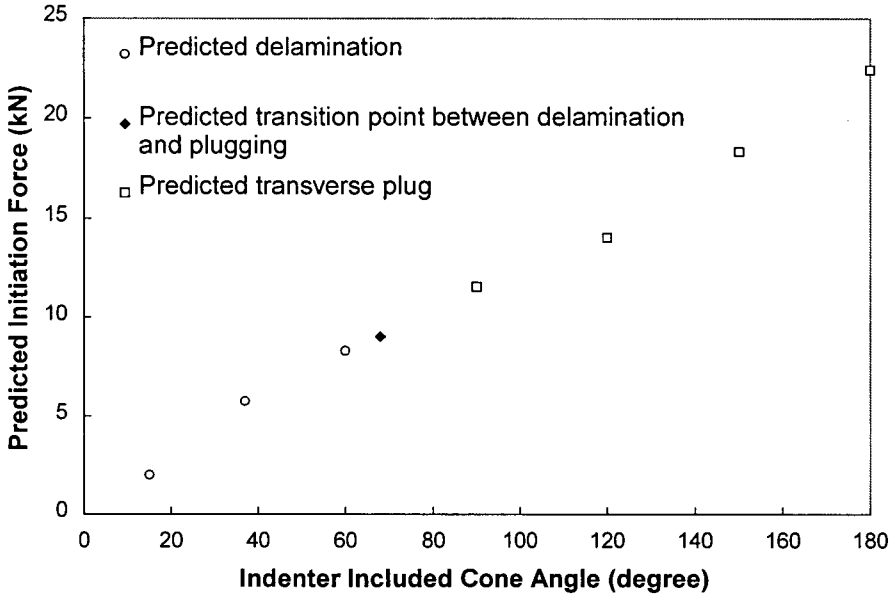

Figure 6.17 Predicted forces at the onset of delamination and transverse plugging for IM7/8551-7 CFRP laminates.

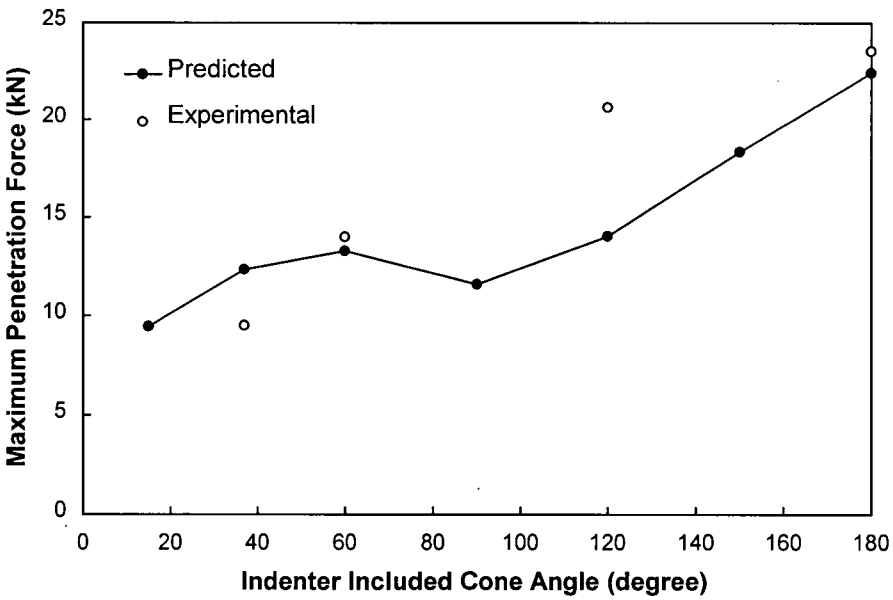

Figure 6.18 Comparison between the predicted and measured maximum penetration force as a function of the indenter included cone angle.

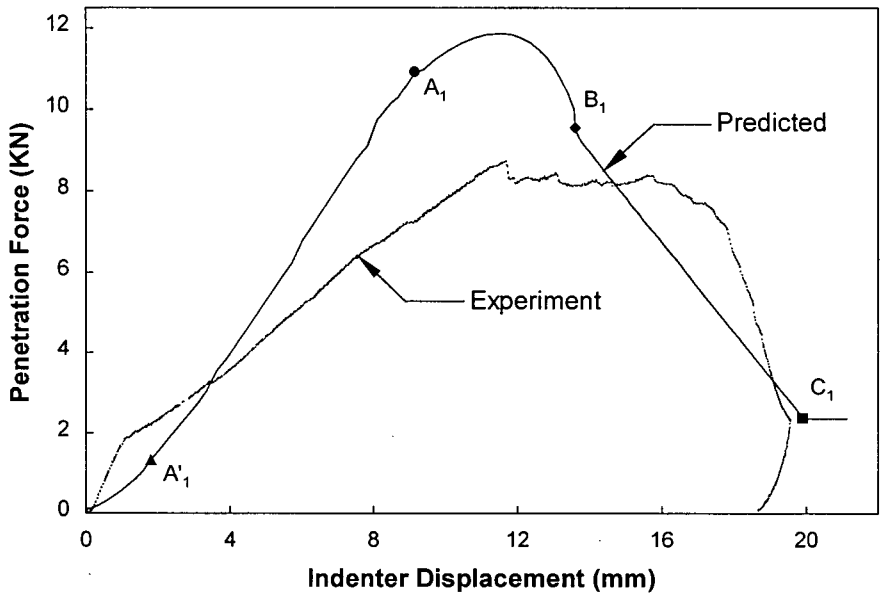

Figure 6.19 Comparison between the predicted and measured static force-displacement curves for 6.35 mm thick GFRP laminate penetrated by an indenter with cone angle of 37°.

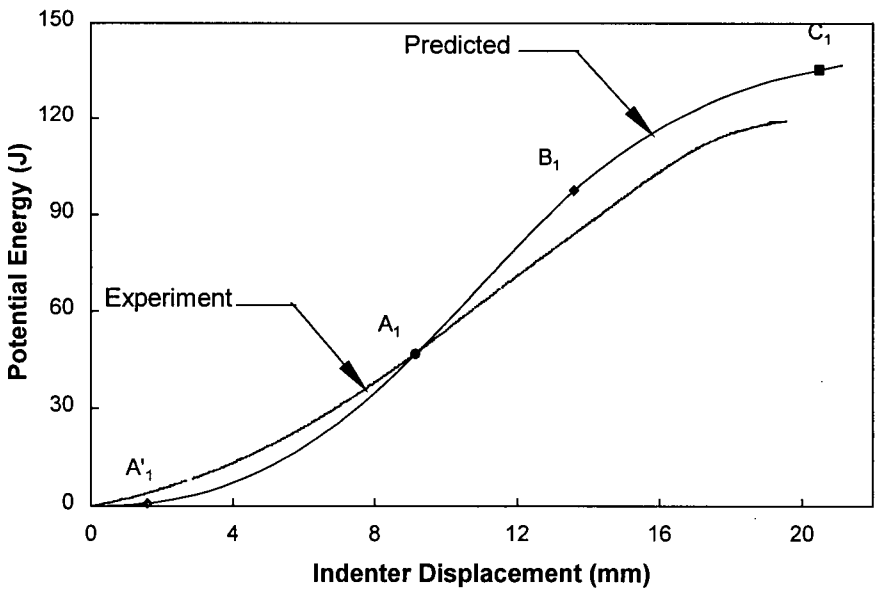

Figure 6.20 Comparison between the predicted and measured energy-displacement curves for 6.35 mm thick GFRP laminate penetrated by an indenter with cone angle of 37°.

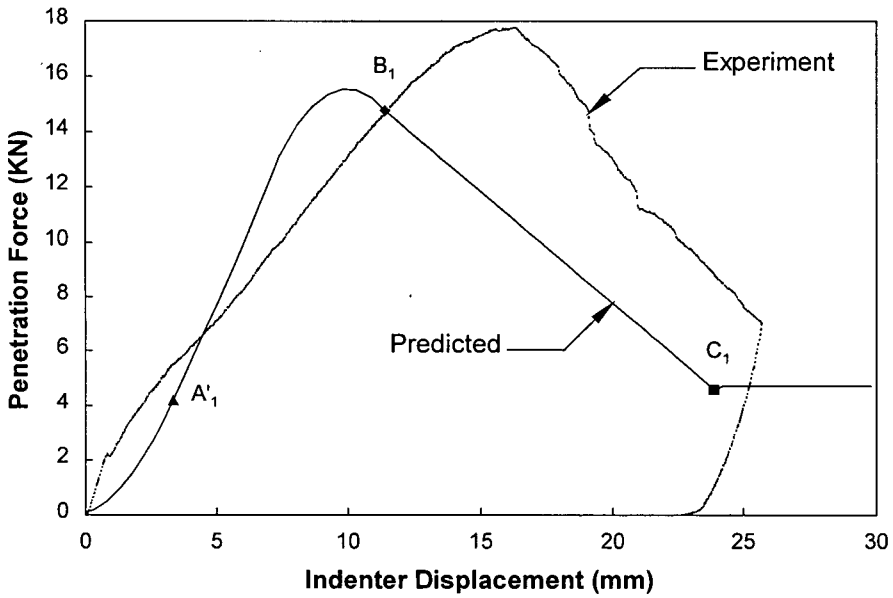

Figure 6.21 Comparison between the predicted and measured static force-displacement curves for 12.7 mm thick GFRP laminate penetrated by an indenter with cone angle of 37°.

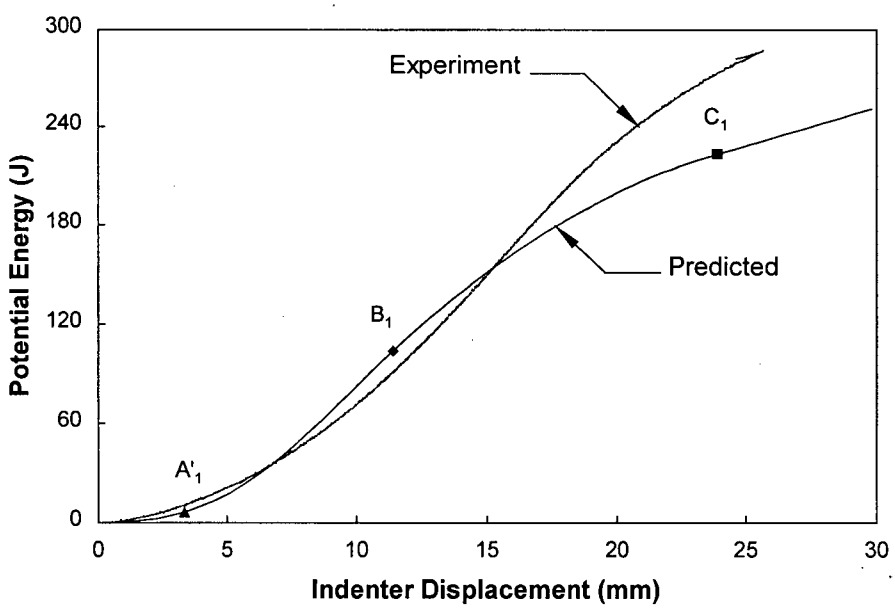

Figure 6.22 Comparison between the predicted and measured energy-displacement curves for 12.7 mm thick GFRP laminate penetrated by an indenter with cone angle of 37°.

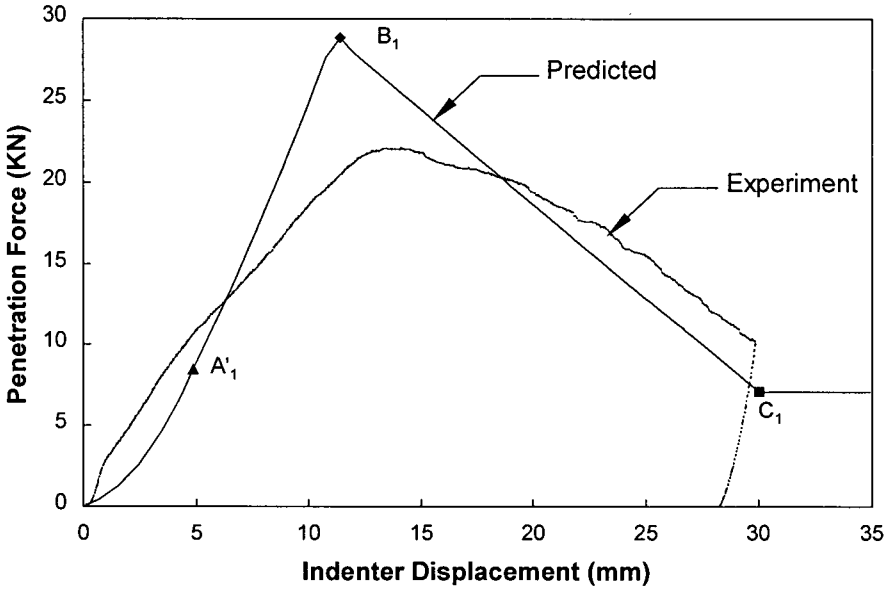

Figure 6.23 Comparison between the predicted and measured static force-displacement curves for 19.05 mm thick GFRP laminate penetrated by an indenter with cone angle of 37°.

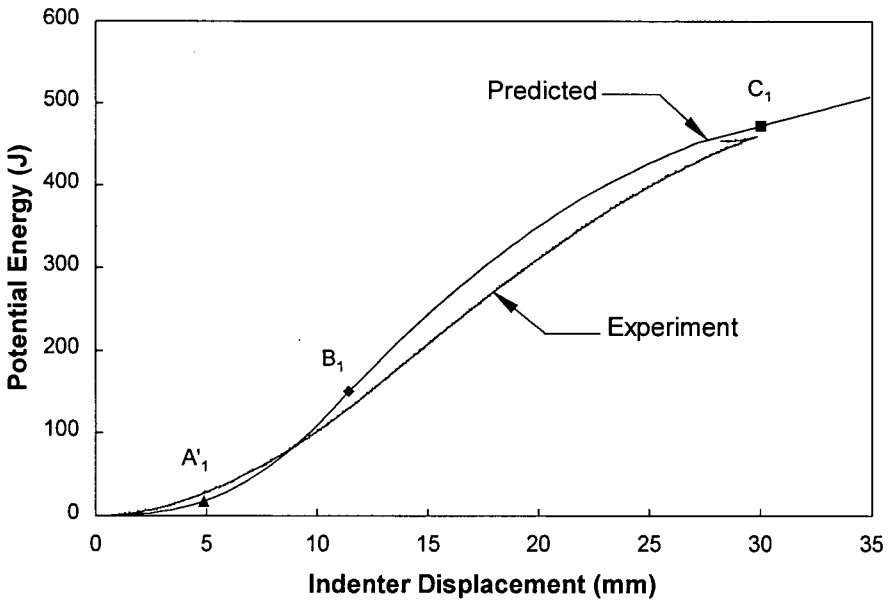

Figure 6.24 Comparison between the predicted and measured energy-displacement curves for 19.05 mm thick GFRP laminate penetrated by an indenter with cone angle of 37°.

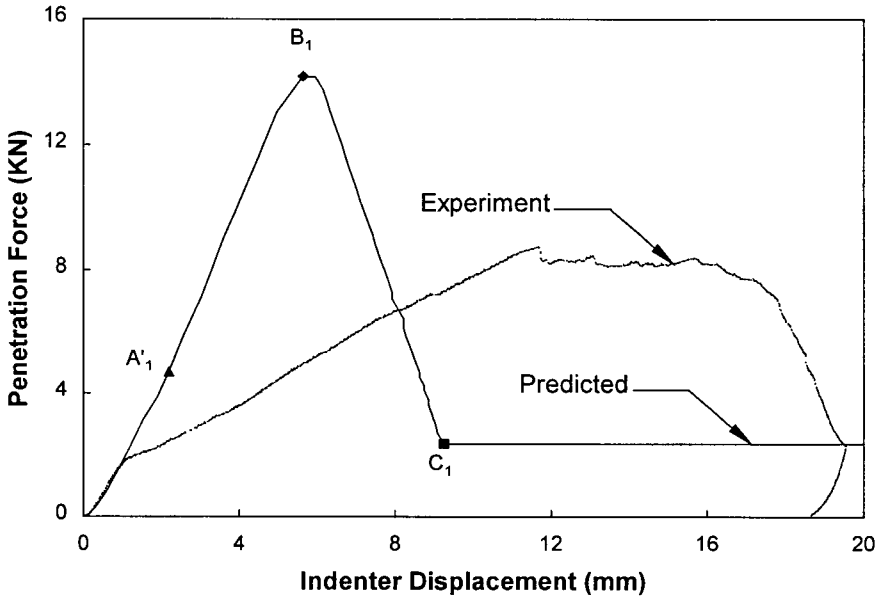

Figure 6.25 Comparison between the predicted and measured static force-displacement curves for a 6.35 mm thick GFRP laminate penetrated by an indenter with a cone angle of 120°.

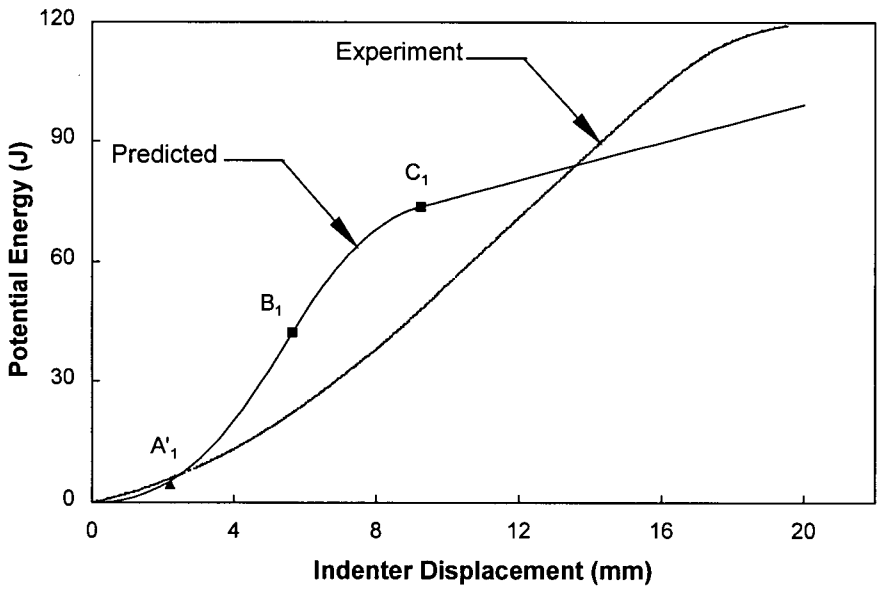

Figure 6.26 Comparison between the predicted and measured energy-displacement curves for a 6.35 mm thick GFRP laminate penetrated by an indenter with a cone angle of 120°.

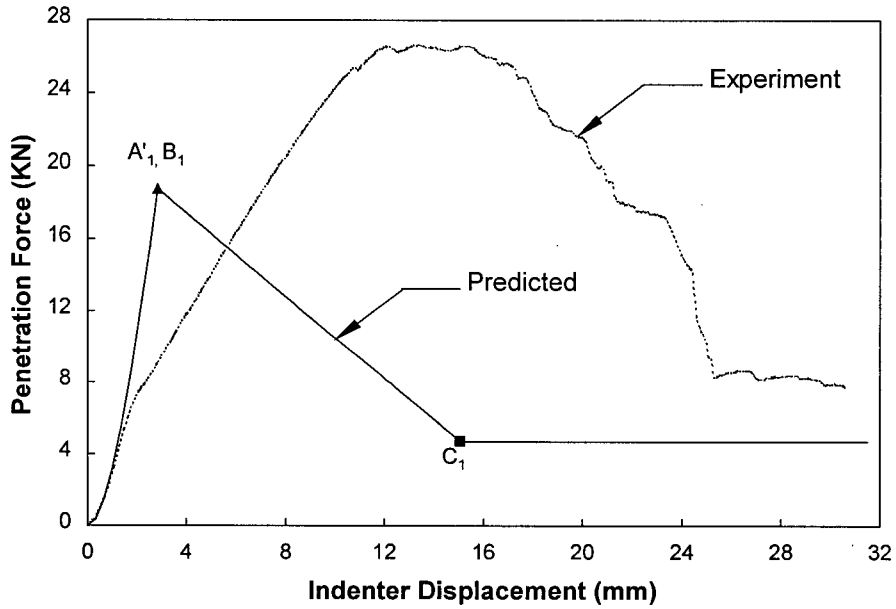

Figure 6.27 Comparison between the predicted and measured static force-displacement curves for a 12.7 mm thick GFRP laminate penetrated by an indenter with a cone angle of 120°.

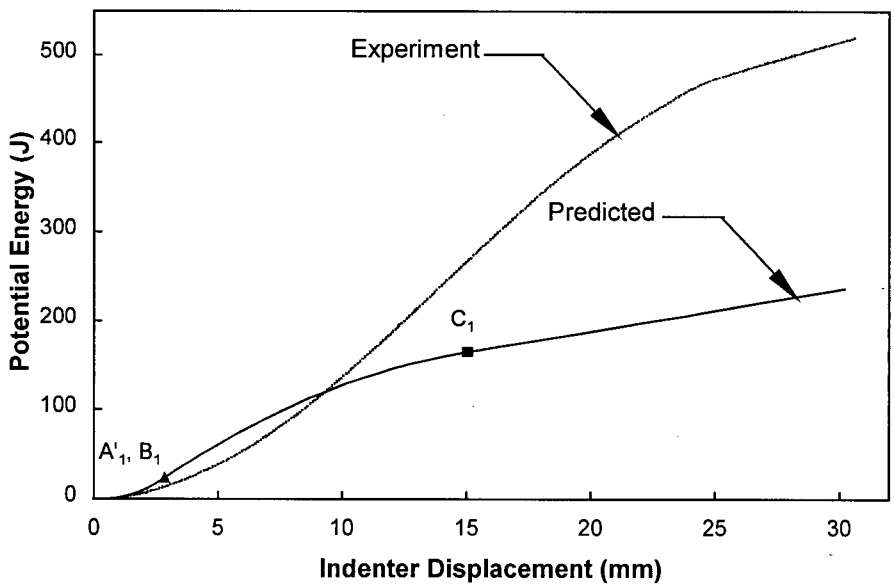

Figure 6.28 Comparison between the predicted and measured energy-displacement curves for a 12.7 mm thick GFRP laminate penetrated by an indenter with a cone angle of 120°.

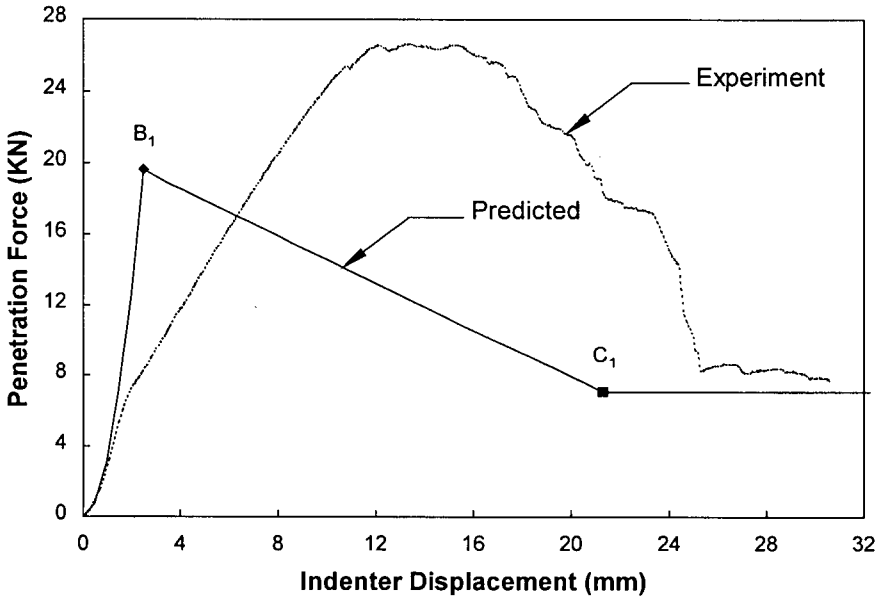

Figure 6.29 Comparison between the predicted and measured static force-displacement curves for a 19.05 thick GFRP laminate penetrated by an indenter with a cone angle of 120°.

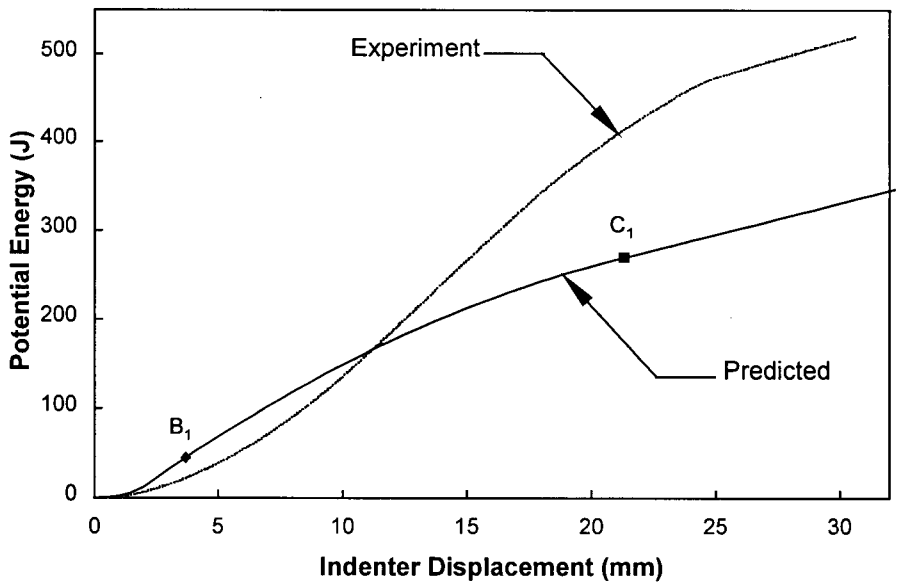

Figure 6.30 Comparison between the predicted and measured energy-displacement curves for a 19.05 mm thick GFRP laminate penetrated by an indenter with a cone angle of 120°.

Chapter Seven: Ballistic Applications

In this chapter, the penetration model developed in the previous chapter is adapted to dynamic analysis and implemented in the super finite element code SENACS described in Chapters Two and Three. Using this code, the transient response of a laminated composite structure under projectile impact causing penetration and perforation can be predicted. The effects of projectile cone angle, projectile velocity, target thickness, target planar size, and target boundary condition on the penetration event are investigated in this chapter. In the global (structural) analysis of the laminates, the material behaviour is assumed to be linear elastic with no damage.

The target inertia consists of two parts. The first part originates from the global deformation and has been considered in the global (structural) analysis. The second part originates from the local deformation. The inertial force resulting from this is ignored in the local analysis due to its relatively small value compared with the other resisting forces.

7.1 Solution Scheme

The dynamic solution algorithm for the penetration model is illustrated in Figure 7.1. The time integration method follows the Newmark-β method with $\beta = 0.25$ and $\gamma = 0.5$ as used in Chapter Two. The finite element formulation is the same as that in Chapter Three for nonpenetrating impact problems, except that the impact force is now calculated using the

Equations developed in Chapter Six instead of the Hertzian contact law given by Equation (3.1).

Let n represent the time step number, $n = 1,2,\ldots\ldots,N_0$, where N_0 is the total number of time steps and Δt is the time increment. Also, let the solution at time station t_n be known. Then sequence of calculation for a dynamic penetration problem is as follows:

1. Increase the time t_n by one time step:

$$t_{n+1} = t_n + \Delta t \tag{7.1}$$

2. Calculate the increment of the projectile displacement using Newton's 2nd Law of Motion:

$$\Delta(\Delta)_{n+1} = V_n \Delta t - \frac{1}{2}\frac{F_n}{m}(\Delta t)^2 \tag{7.2}$$

where V_n and F_n are the projectile velocity and impact force at the n'th time step, respectively, and m is the projectile mass.

3. Calculate the increment of penetration depth:

$$\Delta\alpha_{n+1} = \Delta(\Delta)_{n+1} - (w_{0n} - w_{0n-1}) - (w_{sn} - w_{sn-1}) \tag{7.3}$$

where w_0 is the global elastic bending deflection of the target at the impact site and w_s is the local bending deflection at the impact site due to damage mechanisms induced by projectile penetration. This equation comes from the subtraction of the following two displacement compatibility conditions:

$$\alpha_{n+1} = \Delta_{n+1} - (w_{0n} + w_{sn}) \tag{7.3a}$$

$$\alpha_n = \Delta_n - (w_{0n-1} + w_{sn-1}) \tag{7.3b}$$

The reason for using Equation (7.3) instead of Equations (7.3a) or (7.3b) is that the former can be easily used to check the sign of $\Delta\alpha_{n+1}$.

4. If $\Delta\alpha_{n+1} > 0$, update the penetration depth α as

$$\alpha_{n+1} = \alpha_n + \Delta\alpha_{n+1} \tag{7.4}$$

and then calculate the penetration force F_{n+1} using the equations developed in the previous Chapter, which can generally be expressed in the following form

$$F_{n+1} = f_F(\alpha, \zeta) \tag{7.5}$$

In Equation (7.5), α represents the penetration depth, and ζ represents the other geometric and material parameters. Depending on which penetration mechanism is initiated, α can be either the penetration depth at the current time step, α_{n+1}, or the increment of penetration depth at that time step, $\Delta\alpha_{n+1}$. The explicit form of the parameter ζ in Equation (7.5) is provided in Table 5.4.

5. If $\Delta\alpha_{n+1} \leq 0$, the increment of projectile displacement is not sufficiently large to cause further penetration in the target. Thus skip updating of F and α, because in the present work decreasing penetration depth (rebounding) which has been considered in non-penetrating impact problems, is not considered for penetrating type of problems.

In nonpenetrating impact events, decreasing indentation depth and impact force are caused by projectile rebounding from the target. However, in penetrating impact problems, the penetration force decreases due to perforation (*i.e.*, when the projectile completely

penetrates through the target), and not necessary due to rebounding. Therefore, the penetration depth always increases until the projectile completely loses its kinetic energy and causes to a halt.

It is conceivable that when the projectile comes to a halt the stored energy in the target results in oscillations which could induce relative motion between the projectile and the target. However, this effect is ignored here.

6. Calculate the global deformation and update the global bending deflection at the impact site, w_{0n+1}, using global structural analysis described in Chapter Two. This deflection can be generally expressed as

$$w_{0n+1} = f_w(F_{n+1}) \tag{7.6}$$

7. If the projectile displacement is greater than the sum of the projectile length, the target thickness, and the global and local deflections of the target, then the projectile has completely penetrated through the target, or "completely perforated" the target. If the projectile velocity is equal to or less than zero while the projectile has not caused complete perforation of the target, the projectile stops within the target. The target is referred to as "partially perforated" if the projectile tip penetrates through the target as the projectile stops. Program will stop if any of the above two cases occurs. Otherwise, go back to step 1 and repeat steps 1 to 6. This is summarised as the following expression of

$$\text{Program stops when } \begin{cases} \text{either } \Delta_{n+1} > L_p + h + w_{0n} + w_{sn}, \text{ completely perforated;} \\ \text{or } V_{n+1} \le 0, \begin{cases} \Delta_{n+1} \ge h, \text{ partially perforated;} \\ \Delta_{n+1} < h, \text{ embedded.} \end{cases} \end{cases} \tag{7.7}$$

7.2 Comparison with Experiments

The predicted impact force and impact energy absorption are compared with the experimental measurements on CFRP and GFRP laminates to verify the present penetration model and its implementation in SENACS.

There are three types of instrumented dynamic impact experiments that have been conducted at UBC: drop weight (DW), gas gun (GG), and power gun (PG) tests. In the DW tests, the projectile has a mass of 6.14 kg and the impact velocity is of the order of 10 m/s depending on the drop height.

In GG tests, a force transducer is attached to the projectile tail which records the impact force as a function of time during impact. The projectile velocity and displacement are then obtained by integrating the force-time curve. The projectile mass is 0.32 kg and depending on the gas pressure, the impact velocity can easily reach 50 m/s (Delfosse *et al.*, 1993a).

The PG tests are ballistic type of tests where the projectile mass is low (4.2 g or 13.2 g) and depending on the amount of powder used the velocity can reach 1000 m/s. The projectiles are fired from a .308 calibre standard rifle barrel.

The projectile motion (displacement) in PG tests is recorded using the ELVS (Enhanced Laser Velocity Sensor). The projectile velocity and acceleration are then calculated by appropriate time differentiations. The impact force in turn is calculated by multiplying the projectile acceleration by the projectile mass. The impact energy absorption at a certain time is calculated as the difference between the initial and current projectile kinetic energy. The

details of the experimental set-up and calibration of ELVS are provided in Starratt *et al.* (1998).

It should be noted that once the projectile passes through the entire width of the laser sheet (*i. e.*, projectile leaves the measurement window), the ELVS can no longer detect the projectile motion. The measured results from ELVS will therefore not cover the whole range of penetration process as the penetration model does.

Perforation energy in this chapter is the projectile impact energy that is consumed in completely perforating the target. In dynamic penetration tests and numerical calculations, it is the difference between the measured (or calculated) initial and residual kinetic energies of the projectile. In static penetration tests, it is the sum of the area under the force-displacement curve when the indenter cone completely perforates the target and the friction energy resulting from the motion of the indenter shaft.

7.2.1 CFRP Laminates

Specimens of the CFRP laminate shown in Table 5.2 were penetrated by instrumented projectiles with either a conical tip (37° cone angle) or a blunt tip (180° cone angle), fired from a gas gun (Delfosse 1994b). The projectile mass and length are given in Table 7.1.

The tests were conducted on a large-geometry opening, where a 101.6 × 152.4 mm (4 × 6 inch) specimen was placed on a steel support with a 76.2 × 127 mm (3 × 5 inch) opening.

7.2.1.1 37° Cone Angle

The predicted and measured impact force versus projectile displacement curves are shown in Figure 7.2. The predicted maximum projectile displacement agrees very well with the measurements. The initial slope of the predicted force-displacement curve is in good agreement with the measured slope. However, the peak impact force is over-predicted. It is also interesting to see that the peak contact force in the static penetration test is higher than that in the dynamic penetration test. The physical reason for this is not known at present.

For clarity, the predicted position of the projectile in the target is also shown schematically in the graph. The labels *A, B,* and *C* denote the initiation of delamination and subsequent flexural deformation of the delaminated plate (split-plate), the initiation of friction phase, and the completion of projectile cone penetration, respectively. Subscript 1 on the labels in the figure indicates that delamination rather than transverse plugging initiates in the penetrated target and thus the penetration response is characterised by Curve 1 in Figure 5.14.

Due to the over-predicted impact force, the predicted impact energy absorption (*i. e.*, the difference between the current and initial projectile kinetic energy) will be greater than the measured loss of projectile kinetic energy, as shown in Figure 7.3.

The time histories of impact force, energy absorption, projectile velocity, projectile displacement, and target deflection (at the impact site) during the penetration event are shown in Figure 7.4 to Figure 7.6. When the projectile cone has penetrated through the target, the impact force reaches a friction plateau and the target starts to oscillate flexurally with an almost constant frequency (see point C_1 in Figure 7.6). The time period of the oscillation is

253 μs as shown in Figure 7.6, which is very close to the natural period of the laminate, 248 μs (corresponding to a natural frequency of 4.032 kHz).

7.2.1.2 180° Cone Angle (Blunt)

The GG test by a blunt-ended projectile (180° cone angle) with a velocity of 30.2 m/s was conducted on the same specimen and support condition as the 37° projectile (Delfosse, 1994b). Due to the singularity of $\tan\beta_0$ when $\beta_0 = 90^0$, the cone angle used in the analysis is $2\beta_0 = 179^0$. The comparison between the model prediction and experimental measurements for the impact force and energy absorption versus the projectile displacement are shown in Figures 7.7 and 7.8. The predicted peak impact force and peak projectile displacement agree very well with the experimental results.

The labels A_2, B_2, and C_2 denote the initiation of transverse plugging, the initiation of friction phase, and the completion of projectile cone penetration. Before transverse plugging initiates at point A_2, penetration force increases with the projectile displacement very rapidly due to the large cone angle of the projectile. Point B_2 represents the instant when the projectile head reaches the distal surface of the laminate. For a projectile with a finite cone length (cone angle $2\beta_0 < 180^0$), the impact force decreases gradually from B_2 to C_2; while in Figure 7.7, the force drops from B_2 to C_2 abruptly due to a very small length of projectile cone when the cone angle $2\beta_0 = 179^0$. The predicted results show that the projectile completely penetrates through and exits the target with a residual velocity of 18.9 m/s.

In the experimental impact force-displacement curve shown in Figure 7.7, the projectile has perforated the target when the impact force reaches a zero value. Because of onboard instrumentation that is attached to the tail end of the projectile in GG tests, the projectile remains in the target and vibrates with it. That is why we see the oscillations in the measured impact force and energy absorption shown in Figures 7.7 and 7.8.

The penetration force and energy absorption obtained from the static test of the same specimen under the same support condition are also superposed on the dynamic penetration results in Figures 7.7 and 7.8. It can be seen that the peak force in the static test is higher than that in the dynamic test. A similar trend was observed for the 37° projectile penetration tests.

7.2.2 GFRP Laminates

Instrumented ballistic tests were performed by Sanders (1997) on GFRP laminates defined in Table 5.3 for three different laminate thicknesses (6.35 mm, 12.7 mm, and 19.05 mm). The steel projectiles used which were hardened to HRc30 are defined in Table 7.2. In all these tests, the GFRP specimens were supported by a steel plate with a large-geometry opening (a rectangular opening of 76.2 × 127 mm, or 3 × 5 inch).

7.2.2.1 6.35 mm Thick Plate

Figure 7.9 (a-e) and Figure 7.10 (a-e) show the comparisons between the predicted and experimental time histories of projectile displacement, projectile velocity, and impact force when the projectile impacts a 6.35 mm thick GFRP specimen. The impact energy absorption

in the target and impact force as a function of the projectile displacement are also shown in the figures. The 37° projectile has an initial impact velocity of 104 m/s, while the initial impact velocity of the 120° projectile is 211 m/s.

For the 37° projectile test, the predicted and measured impact force agree very well from the start of penetration to the point where the projectile displacement reaches 3.0 mm [Figure 7.9 (e)]. After that point, the measured force starts to oscillate while the predicted force continues to increase until the critical point A_1 which is the point at which the projectile tip reaches the distal surface of the target (partial perforation). Four delaminations occur between the points A'_1 and A_1. The delaminated target bends like a split-plate in the subsequent penetration.

The model predicts that the projectile stops inside the target, with a 0.3 mm length sticking out from the distal surface of the target, *i.e.*, partially perforated. This agrees quite well with the experiment. In the test, the projectile did not completely perforate the target (Sanders, 1997) and there was a small hole observed on the distal surface of the target after the projectile was removed, which means that the projectile tip had indeed pierced from the target distal surface.

The projectile displacement and velocity are under-predicted, and impact energy absorption is over-predicted, relative to the experimental results. The oscillations on the measured force-displacement curve which cause the discrepancy between the prediction and measurement need to be further studied.

The same comparison is conducted for 120° projectile penetrating the same GFRP specimen which is shown in Figure 7.10 (a-e). The experiment showed that the projectile had penetrated through the target with an exit velocity less than 85 m/s (Sanders, 1997). The model predicts that the projectile completely perforates the target with a residual velocity of 123 m/s. Both the model prediction and experimental measurements conclude that the projectile completely perforates the target in this case.

As shown in Figure 7.10 (e) and Figure 7.10 (c), the predicted initial slopes of the curves agree with the experiment very well. In the force-displacement curve, A_1' denotes the initiation of the first delamination in the target, while B_1 denotes that the projectile shaft reaches the target frontal surface and the friction phase starts. The 2nd and 3rd delaminations are initiated between points A_1' and B_1. At the point B_1', the projectile tip exits from the distal surface of the target. The target at this stage is partially perforated. After this point, the experimental force starts to oscillate while the predicted force decreases until the point C_1, where the whole projectile cone tip penetrates through the target leaving the shaft still inside the target.

The predicted time histories of the projectile displacement and velocity, and the impact force as well as the energy absorption as a function of the projectile displacement, are in good agreement with the experiment until the point B_1. The reasons for the increase and subsequent oscillations of the measured impact force (when the projectile displacement is larger than 8.0 mm) is not clear at this moment and needs to be further studied.

7.2.2.2 12.7 mm Thick Plate

The 12.7 mm GFRP specimens were impacted and penetrated by a 37° projectile with impact velocities of 304 m/s and 170 m/s, and a 120° projectile with impact velocity of 278 m/s. The comparisons between the predicted and experimental results for these cases are shown in Figure 7.11 (a-e), Figure 7.12 (a-e), and Figure 7.13 (a-e), respectively.

For the GFRP specimen penetrated by a 37° projectile with a striking velocity of 304 m/s, the experiment showed that the projectile had perforated the target with an exit velocity of 200 m/s (Sanders, 1997). The model predicts that the projectile completely perforates the target with an exit velocity of 196 m/s. The agreement between the predicted and measured time histories of projectile displacement and velocity is good. The predicted impact force and energy absorption are close to the measured ones with the predicted value falling somewhat below the measurements. The labels A_1', B_1, B_1', and C_1 in Figure 7.11 (e) have the same meaning as those in Figure 7.10 (e) discussed before.

Figure 7.12 (a-e) shows the comparisons between the predicted and experimental results when the same target is penetrated by a projectile with the same cone angle but with a lower incident velocity of 170 m/s. According to the experiment the projectile did partially perforated the target but not perforate it completely. The cross-sectional examination of the specimen indicated that there was about 2.0 mm of the target thickness which was not penetrated through by the projectile. The model predicts that there is a 5.8 mm length of the projectile sticking out from the target distal surface.

The predicted and experimental peak impact force shown in Figure 7.12 (a-e) agree quite well. Again, the labels on the prediction curve in Figure 7.12 (e) have the same meaning as those defined before. The target is being partially perforated.

For the GFRP target penetrated by a 120° projectile with a striking velocity of 278 m/s, the experiment showed that the projectile completely perforated and exited the target. Unfortunately, the exit velocity of the projectile could not be measured by the ELVS system. The model predicts that the projectile completely perforates the target with a residual velocity of 134 m/s. Therefore, the model prediction and experimental observation both conclude that the projectile perforates the target, which is encouraging from the modelling viewpoint.

The overall agreement between the predicted and measured results is reasonable as shown in Figure 7.13 (a-e). The peak impact force and energy absorption are under-predicted.

7.2.2.3 19.05 mm Thick Plate

The 19.05 mm GFRP specimens were impacted by projectiles with a 37° cone angle and striking velocities of 318 m/s and 211 m/s, and by projectile with a 120° cone angle and striking velocity of 384 m/s. The comparisons between the predicted and experimental results for these cases are shown in Figure 7.14 (a-e), Figure 7.15 (a-e), and Figure 7.16 (a-e), respectively.

For the 37° projectile with striking velocity of 318 m/s, the experiment showed that the projectile did not completely perforate the target and finally came to rest in it (Sanders, 1997). Cross-sectional examination of the target revealed that the penetration hole was close

to the target distal surface and had a conical shape, suggesting that the projectile cone had not perforated the target. According to the model, the projectile also fails to completely perforate the target in this case.

For the same projectile but with a striking velocity of 211 m/s, the model seems to capture the essence of the ballistic response. Cross-sectional observation of the target revealed that there was about 2.0 mm of the target thickness that had not been penetrated, while the model predicts that there is a 2.8 mm of un-penetrated target thickness. Again, the model and experiment are in agreement.

The impact force as well as impact energy absorption are over-predicted by the model as shown in Figure 7.15 (c) and (e) while the projectile displacement and velocity are under-predicted as shown in Figure 7.15 (a) and (b).

For the GFRP target penetrated by a 120° projectile with a striking velocity of 384 m/s, experimental observation showed that the projectile completely perforated the specimen and exited from it with a velocity of 160 m/s. The model predicts that the projectile completely perforates the target with an exit velocity of 243 m/s. Therefore, both the model and experiment arrive at the same conclusion.

The overall agreement between the predicted and measured results is reasonable as shown in Figure 7.16 (a-e). The model under-predicts the impact force and energy absorption and over-predicts the projectile displacement and velocity.

7.3 Effect of Projectile Cone Angle

Experimental results (Figure 5.3, Figure 5.9, and Figure 5.10) showed that penetration response of the target is highly dependent on the projectile cone angle. In this section we conduct a series of numerical experiments to gain insight into the effect of cone angle on the ballistic response of composite materials. While keeping all other parameters constant, we carry out the analysis by systematically changing the cone angle. We will consider both the CFRP and GFRP systems. Where available, experimental results conducted by Delfosse (1994b) and Sanders (1997) will be shown on the graphs for references.

7.3.1 CFRP Laminates

The ballistic tests on CFRP laminates were conducted on a small-geometry opening, where a 50.8 × 50.8 mm (2 × 2 inch) specimen was placed on a steel support with a circular opening with a diameter of 25.4 mm (1 inch). The projectile mass and length used in the analysis are given in Table 7.1. The projectile shaft length is always assumed to be a constant ($L_p - L_c = 9.0\ mm$) for all projectile cone angles.

Figure 7.17 shows the relationship between the predicted impact force and the projectile displacement for a range of projectile cone angles. It can be seen that the force-displacement curves become shallower with decreasing projectile cone angle. With increasing cone angle, on the other hand, the force-displacement curves exhibit a sharper peak force followed by a sudden drop. When the included cone angle reaches 90°, the deformation mechanism following the initial hole expansion phase changes from delamination initiation and

progression to plug initiation and ejection. When the projectile cone angle is greater than 90°, there is always a distinct load drop in the force-displacement curves.

Figure 7.18 shows the prediction of the impact energy absorbed by the target for dynamic penetration of projectiles with various cone angles. Impact energy absorption is calculated as the difference between the projectile incident and residual kinetic energy. The relationship between the peak impact force and the projectile cone angle is shown in Figure 7.19.

Projectiles with larger cone angles will generate higher peak impact forces, while the target absorbs more impact energy when it is penetrated by projectiles with smaller cone angles. Thus based upon energy absorption, a projectile with a small cone angle will encounter a higher penetration resistance than a projectile with a large cone angle. When the projectile cone angle approaches 90°, the penetration resistance reaches its minimum. Then it will increase again at a small rate when the cone angle continues to increase. Therefore, energy-wise projectiles with obtuse cone angles will penetrate through the CFRP targets more easily than the projectiles with acute cone angles.

7.3.2 GFRP Laminates

A comparison of predicted force-displacement relationships for 37°, 45°, 55°, 60°, 75°, 120°, and 180° projectile is shown in Figure 7.20. The 6.35 mm thick GFRP specimen rests on a rigid support with the large-geometry opening (127 mm × 76.2 mm, or 5″ × 3″). The projectile mass is 4.2 g and its length is given in Table 7.1 for various cone angles. For all of the cases studied, the projectile striking velocity is 600 m/s. The difference among the

character of these force-displacement curves is not as severe as that seen in the CFRP laminates.

The 60° projectile has a smaller peak impact force than the other projectiles, similar to the 90° projectile for CFRP laminates. The relationship between the perforation energy (impact energy absorption) and the projectile cone angle is shown in Figure 7.21. The perforation energy for the projectile with a very small cone angle (15°) is the largest. The perforation energy decreases with increasing projectile cone angle until the cone angle reaches 60°. The perforation energy of 60° projectile is the smallest. When the projectile angle continues to increase, the perforation energy increases slightly and reaches a constant for projectile angles greater than 120°. The relationship between the peak force and the projectile cone angle is shown in Figure 7.22.

7.4 Effect of Impact Velocity

The study on the effect of the projectile impact velocity on the ballistic response of the target is very important, because it results in the "ballistic limit" of the target material. It is characterised by V_{cr} in the present thesis. The ballistic limit or V_{cr} is considered to be the impact velocity at which the projectile just completely perforates the target with a zero residual velocity.

7.4.1 CFRP Laminates

Figures 7.23 to 7.27 show the relationships between the projectile initial striking velocity (V_s) and the residual (exit) velocity (V_r) after penetrating through a 6.15 mm thick CFRP laminate at various striking velocities. The V_s-V_r curves have the classical initial parabolic shape followed by a linear rise. The projectile in Figure 7.23 has a 37° cone angle with a mass of 0.32 kg; while the projectile in Figure 7.24 has a mass of 4.2 g with 37° and 180° cone angles.

The ballistic limits for 37° projectiles are 29.1 m/s for a 0.32 kg projectile and 261.6 m/s for a 4.2 g projectile. The ballistic limit for a 180° projectile with a mass of 4.2 g is 206.3 m/s. The laminate is not completely perforated until the projectile velocity reaches these critical values. After that, the projectile exit velocity increases sharply with increasing striking velocity. After the sharp increase, the projectile exit velocity increases at almost the same rate as the striking velocity.

In Figure 7.25, two more V_s-V_r curves from 15° and 120° projectiles with a mass of 4.2 g have been added to the figure. The curves on the right absorb more impact energy than those on the left.

The relationship between the projectile residual kinetic energy E_r and initial kinetic energy E_s for 15°, 37°, 120°, and 180° projectiles is shown in Figures 7.26 and 7.27. The model prediction is very close to the test measurements for the 180° projectile. The perforation energy is $E_{perf} = 261\ J$ for the 15° projectile, $E_{perf} = 144\ J$ for the 37° projectile, $E_{perf} = 77\ J$ for the 120° projectile, and $E_{perf} = 89\ J$ for the 180° projectile.

Figure 7.23 to Figure 7.27 show the capability of a 6.15 mm thick CFRP laminate to absorb the impact energy when perforated by projectiles with various cone angles, which is very useful for design engineers. Another important information is the knowledge of how these absorbed impact energies distribute among the different penetration phases.

The impact energy absorption consists of three parts on the force-displacement curves as shown in Figure 7.28 (a) and (b). For both curves (a) and (b), a major energy absorption mechanism in phase I is hole expansion. In phase II, major energy absorption mechanisms are either hole expansion and flexural deformation of a split-plate [curve (a)], or transverse plug initiation and push-out [curve (b)]. The friction is a major energy absorption mechanism in phase III for both curves. Energy absorption by the target global deformation and motion coexists with all these three phases.

The global energy absorption is calculated as the integration of the impact force over the target central deflection w_0, while the local energy absorption is the integration of the force over the sum of the penetration depth α and local target deflection w_s.

The partitioning of the impact energy absorption is shown in Figure 7.29 (a-d) for projectiles with 15°, 37°, 120°, and 180° cone angles where the CFRP laminate is placed on a rigid support with a small-geometry opening. The impact energy absorbed in the form of global deformation and motion is very small compared with the other three types of energy absorption mechanisms and thus is not shown in the figures. The projectile residual kinetic energy after perforating the target is also shown in the figures. The energy absorbed in phase II contributes the most to the total energy absorption for all four cases (about 247 J for 15°,

128 J for 37°, 52 J for 120°, and 76 J for 180°). Because of the same shaft length L_p-L_c and target thickness h, and small local deflection w_s for these projectiles, the energy dissipated in Phase III is very similar for all four cone angle (15°, 37°, 120°, and 180°), about 12 J. The energy absorbed in phase I is very small for very sharp (15°) projectile and non-existent for blunt-ended projectile (180°).

Therefore, phase II plays a very important role in energy absorption and ballistic resistance of the CFRP laminates.

7.4.2 GFRP Laminates

The effect of impact velocity on energy absorption capability of GFRP laminates with three thicknesses (6.15 mm, 12.7 mm, and 19.05 mm) is studied in this section.

7.4.2.1 6.35 mm Thick

The predicted relationship between the exit velocity V_r and the initial striking velocity V_s for 15°, 37°, 120°, and 180° projectiles is shown in Figure 7.30. The projectile mass is 4.2 g and the length is given in Table 7.1 for various cone angles. The 6.35 mm thick GFRP specimen rests on a rigid support with a large-geometry opening (127 mm × 76.2 mm, or 5″ × 3″).

The right-most V_s-V_r curves correspond to more impact energy absorption than those to the left. So the target absorbs the most impact energy when it is impacted by a 15° projectile and the least impact energy when impacted by a 180° projectile. The ballistic limit V_{cr} for these different projectiles is tabulated in Table 7.3.

The relationship between the projectile residual kinetic energy E_r and its initial kinetic energy E_s for different conical projectiles is shown in Figure 7.31. The perforation energies are listed in Table 7.3.

The composition of impact energy absorption is shown in Figure 7.32 (a-d) for projectiles with 15°, 37°, 120°, and 180° cone angles. The energy absorbed in phase II constitutes the most to the total energy absorption for all four cases (see Table 7.3). The energy absorbed in phase I is small compared with the energy absorption in the other phases.

The impact energy dissipated in the global deformation and motion of the target increases with the projectile striking energy up to the complete perforation of the target, and then decreases. This confirms the widely accepted notion that the global energy absorption plays more important role in low velocity impact events than in high velocity impact events. The high velocity impact can be treated as a local event. Due to the decreasing global energy absorption, the target perforation energy also decreases with the striking energy when the impact velocity is above the ballistic limit.

7.4.2.2 12.7 mm Thick

Consider the GFRP laminate with a thickness of 12.7 mm, supported on a rigid plate with the large-geometry opening (127 mm × 76.2 mm) and impacted by projectiles with 37° and 120° cone angles. The projectile mass is 13.2 g and length are listed in Table 7.2. The predicted relationship between the projectile exit velocity V_r and its initial striking velocity V_s is shown in Figure 7.33. The solid points are the experimental data.

The 120° projectile absorbs more impact energy than the 37° projectile does. Further ballistic tests are needed to obtain the perforation energy in both cases and to verify this prediction. The predicted ballistic limit V_{cr} for both projectiles are $V_{cr} = 234\ m/s$ (37° projectile), and $V_{cr} = 245\ m/s$ (120° projectile).

The relationship between the projectile residual kinetic energy E_r and initial kinetic energy E_s is shown in Figure 7.34. The perforation energy is $E_{perf} = 362\ J$ for the 37° projectile and $E_{perf} = 397\ J$ for the 120° projectile.

The composition of impact energy absorption is shown in Figure 7.35 (a-b), where as in the previous case, the energy absorbed in phase II contributes the most to the total energy absorption (see Table 7.4). The energy dissipated in phase III is also large because the target thickness in this case is longer than in the previous examples. The energy absorbed in phase I is also small compared with the energy absorption in the other phases.

7.4.2.3 19.05 mm Thick

Finally, consider the GFRP laminate with a thickness of 19.05 mm on a rigid support with a large-geometry opening (127 mm × 76.2 mm), impacted by the same projectile as for the 12.7 mm thick laminate. The predicted relationship between the projectile exit velocity V_r and initial striking velocity V_s is shown in Figure 7.36.

The 37° projectile dissipates more impact energy than the 120° projectile. The ballistic limit V_{cr} for both projectiles are given in Table 7.5.

The E_s-E_r curves for the two conical projectiles are shown in Figure 7.37. The perforation energy and the composition of impact energy absorption are shown in Figure 7.38 (a-b) and Table 7.5. Once again the energy absorbed in phase II still accounts for the most part of the total energy absorption. The energy dissipated in phase III is also large because the target is thicker than in the previous examples.

In general, the model prediction suggest that phase II always plays a very important role in energy absorption and ballistic resistance of the GFRP laminates.

7.4.3 Comparison Between the Ballistic Resistance of CFRP and GFRP Laminates

A comparison between the predicted ballistic resistance (perforation energy) of a CFRP laminate (6.15 mm thick) and a GFRP laminate (6.35 mm thick) is shown in Figure 7.39. It is seen that GFRP laminates have higher ballistic resistance than CFRP laminates for all four projectile cone angles (15°, 37°, 120°, and 180°). For large cone angles, the perforation energy of the GFRP and CFRP laminates is about the same. However, for small cone angles the difference between the perforation energy of two laminates is very large.

7.5 Effect of Target Thickness

The predicted relationship between the impact force and projectile displacement for the three different thicknesses (6.35mm, 12.7mm, 19.05mm) of GFRP specimen is shown in Figure 7.40 for a 37° projectile and Figure 7.41 for a 120° projectile. The specimen in each case is supported on a rigid plate with a large-geometry opening and the projectile mass is 13.2 g.

The 37° and 120° projectiles have a velocity of 384 m/s for all three GFRP laminates (6.35 mm, 12.7 mm, and 19.05 mm thick). The greater the thickness, generally the higher the peak impact force and projectile displacement.

7.6 Effect of Boundary Conditions

In all the calculations so far, the laminates were taken to be simply-supported along their edges. In this section, the laminates are assumed to be clamped on all edges in order to demonstrate the effect of boundary conditions on their ballistic response.

A comparison between the predicted impact force versus projectile displacement curve for simply-supported and clamped targets is shown in Figure 7.42, where the projectile mass is 0.32 kg and its cone angle is 37° or 120°. The projectile velocity is 30.2 m/s.

7.7 Effect of Planar Size

The effect of laminate planar size on its ballistic response is shown in Figure 7.43 for a CFRP laminate with a thickness of 6.15 mm. The projectile has a mass of 0.32 kg, a cone angle of 37°, and a striking velocity of 30.2 m/s. The planar size of the laminate (*i.e.*, opening size of the rigid support plate) is seen to affect the maximum projectile displacement. A large opening size will increase the maximum projectile displacement. The perforation energy will increase as well due to more energy being absorbed in the form of global deformation and

motion energy. However, the effect on the peak impact force remains fairly constant with increasing size.

When the projectile velocity increases, the global deformation and motion energy decreases rapidly for the target sitting on a support plate with a large opening and increases slightly for the target sitting on a support plate with a small opening as shown in Figure 7.44. Thus for a large target, penetrating impact acts like a local event when the projectile velocity is very high.

7.8 Effect of Projectile Mass

The predicted time history of the impact force for the 6.35 mm thick GFRP laminate impacted and penetrated by a 37° projectile with three different masses is shown in Figure 7.45. The projectiles all have the same impact energy of 343 J. The projectile with high mass causes a larger impact duration. However, the peak impact force is almost the same for all cases. The relationship between the target deflection at the impact site and the projectile displacement is shown in Figure 7.46. For a given projectile displacement the target deflection is larger for the high mass projectile. Oscillations in the target deflection appear in the curves for the high mass (6.14 kg) and intermediate mass (0.42 kg) projectiles. There are no oscillations in the curve for the low mass projectile. The relationship between the energy absorption and projectile displacement is shown in Figure 7.47.

7.9 Summary

In this chapter, the penetrating impact model in SENACS have been used to perform numerical analyses of the ballistic response of various laminates.

Based on comparisons with experiments conducted by Delfosse (1994b) and Sanders (1997), the present model proves to be a useful tool for predicting the nature and essence of penetration events in composite structures. The accuracy of ballistic limit V_{cr} prediction is very good as shown in Table 7.6 with an error generally less than 10%. Observation of the impacted specimen cross-sections showed that there are often big gaps between delaminated sections in GFRP laminates which the current model does not consider.

After extensive parametric studies, it has been found that the projectile cone angle and target thickness play a very important role in the penetration response of laminates.

The projectile cone angle determines which penetration mechanism will initiate in the target. Generally, a large cone angle projectile causes higher peak impact force, while a small cone angle projectile leads to longer projectile displacement. Although the impact force in penetration by a small cone angle is lower, the projectile impact energy used to perforate the target is higher.

Target thickness will affect the development of the penetration mechanisms initiated by a projectile cone in the target. For a given projectile, the impact force is higher in thicker targets. A thick target also increases the distance that a projectile travels through to perforate. Therefore, the projectile consumes more energy to perforate thicker targets.

The target boundary condition and planar size will also affect the penetration response only when the target flexural deformation is significant, *e.g.*, when the target is thin or the planar size is large. Flexible target will absorb more projectile impact energy in the form of strain energy.

The ballistic limit, V_{cr}, varies significantly with the target thickness and projectile cone angle. V_{cr} is generally higher for sharp projectiles and thick targets.

For a given level of impact energy, the mass of the projectile launched at different velocities will affect the time history of the target deflection, and thus affect the perforation energy and V_{cr}. The target deflection does not affect the penetration response very much for a high impact velocity.

It should be noted that the present penetration model which describes the local target behaviour, can be used separately from the global finite element analysis program. The local model is simple and can be run on a spreadsheet. So for a simple structure, this simplifies and improves the efficiency of the analysis.

The present penetration model includes the penetration mechanism of flexural deflection of a split-plate. The relationship between force and deflection in this mechanism is derived from lateral bending theory of a thin plate. So the present model may cause some error when predicting ballistic resistance of a very thick plate as shown in Table 7.6 (the error of prediction of V_{cr} for a 19.05 mm thick GFRP laminate is larger than that in the other cases).

Table 7.1 Mass and length of projectiles with different cone angles in gas gun and powder gun tests on CFRP laminates. The projectile length is chosen in such a way that all the projectiles have the same shaft length (L_p–L_c) regardless of their cone angles.

Length	15°	37°	45°	60°	90°	120°	150°	180°
L_c (mm)	28.93	11.38	9.19	6.60	3.81	2.20	1.02	0.0
L_p (mm)	37.90	20.35	18.16	15.57	12.78	11.17	9.99	9.0
b_0 (mm)	0.5	0.5	0.5	0.2	0.0	0.0	0.0	0.0

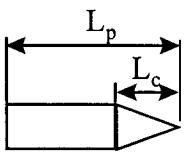

Diameter: 7.62 mm

Mass: 0.32 kg in gas gun tests

4.2 g in powder gun tests

Table 7.2 Mass and length of projectiles with two different cone angles used in powder gun tests on GFRP laminates.

Cone Angle	37°	120°
Diameter (mm)	7.62	7.62
Mass (g)	13.2	13.2
Length, L_p (mm)	46.1	40.0

Table 7.3 Partition of the predicted perforation energy for a 6.35 mm thick GFRP laminate impacted by 4.2 g projectiles with various cone angles.

Projectile Cone Angle	Ballistic Limit V_{cr} (m/s)	Perforation Energy E_{perf} (J)	E_{global} (J)	$E_{phase\ I}$ (J)	$E_{phase\ II}$ (J)	$E_{phase\ III}$ (J)
15°	452	676	52	0.5	586	37.5
37°	302.5	320	34	1	267	18
120°	249	131	19	2.5	96	13.5
180°	229.5	110	17	0	80	13

Table 7.4 Partition of the predicted perforation energy for a 12.7 mm thick GFRP laminate impacted by 13.2 g projectiles with 37° and 120° cone angles.

Projectile Cone Angle	Ballistic Limit V_{cr} (m/s)	Perforation Energy E_{perf} (J)	E_{global} (J)	$E_{phase\ I}$ (J)	$E_{phase\ II}$ (J)	$E_{phase\ III}$ (J)
37°	234	362	8	5	213	136
120°	245	397	12	14	223	148

Table 7.5 Partition of the predicted perforation energy for a 19.05 mm thick GFRP laminate impacted by 13.2 g projectiles with 37° and 120° cone angles.

Projectile Cone Angle	Ballistic Limit V_{cr} (m/s)	Perforation Energy E_{perf} (J)	E_{global} (J)	$E_{phase\ I}$ (J)	$E_{phase\ II}$ (J)	$E_{phase\ III}$ (J)
37°	343	778	9	15	563	191
120°	299	591	5	14	367	205

Table 7.6 Comparison of the predicted and measured ballistic limit V_{cr} for CFRP and GFRP laminates. The projectile mass is 4.2 g for CFRP and 13.2 g for GFRP.

Target	thickness(mm) /cone angle	V_s (m/s)	V_r (m/s) measured	V_r (m/s) predicted	V_{cr}^* (m/s) measured	V_{cr}^* (m/s) predicted	error (V_{cr})
CFRP	6.15/37°	311	203	168	236	261	10%
	6.15/180°	293	180	208	231	206	10%
	6.15/180°	261	143	159	218	205	6%
GFRP	12.7/37°	304	200	196	229	232	1%
	19.05/120°	384	160	243	349	297	15%

* Calculated as $V_{cr} = \sqrt{V_s^2 - V_r^2}$.

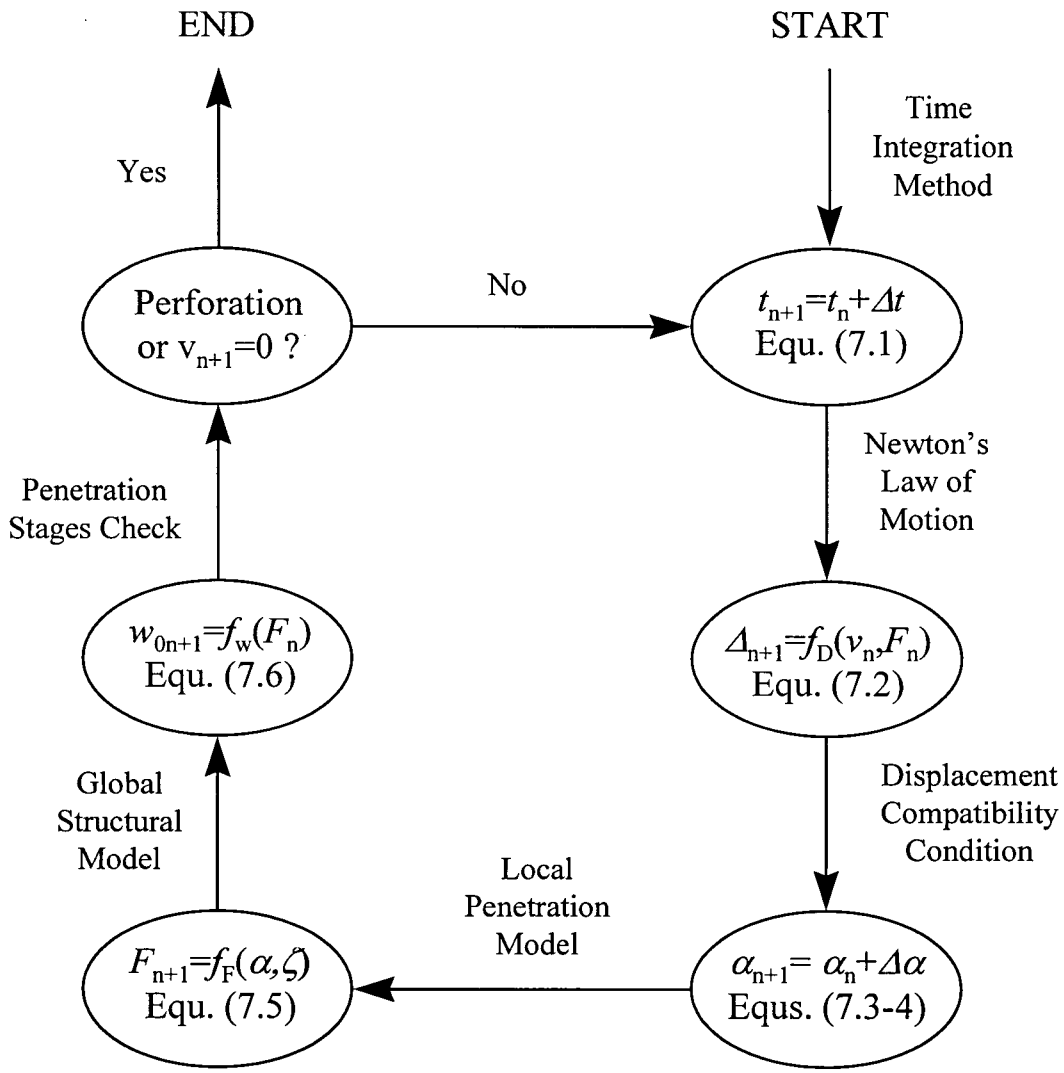

Figure 7.1 Flow chart of the solution scheme for the dynamic penetration model in SENACS.

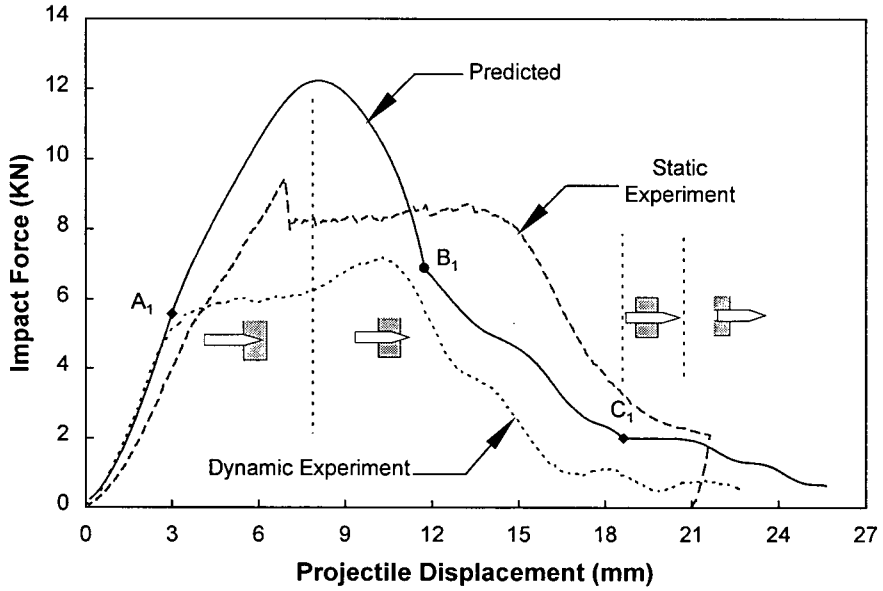

Figure 7.2 Comparison of the predicted and experimental impact force versus projectile displacement when a 0.32 kg steel projectile with a 37° cone angle penetrates through a 6.15 mm thick CFRP laminate with a striking velocity of 30.2 m/s.

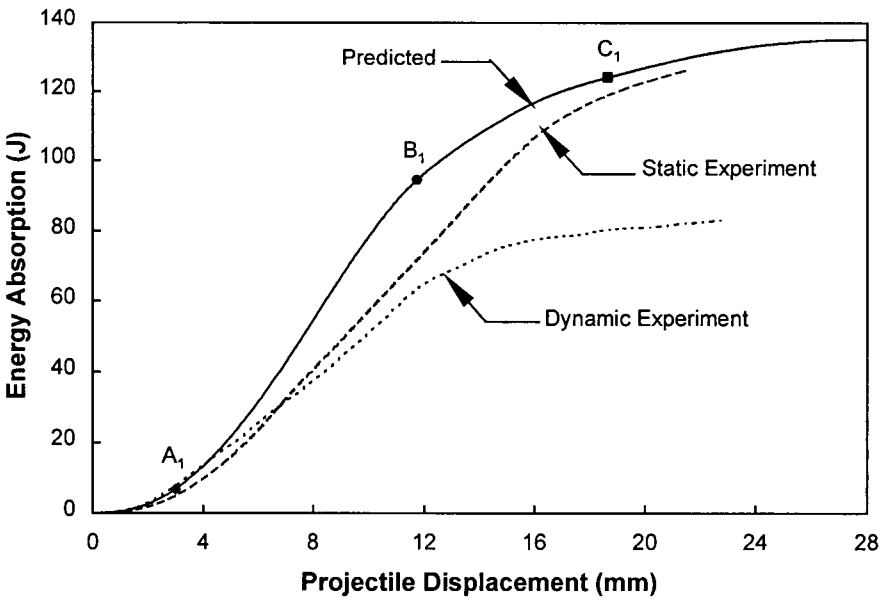

Figure 7.3 Comparison of the predicted and experimental impact energy absorption of the target versus projectile displacement curves when a 0.32 kg steel projectile with a 37° cone angle penetrates through a 6.15 mm thick CFRP laminate with a striking velocity of 30.2 m/s.

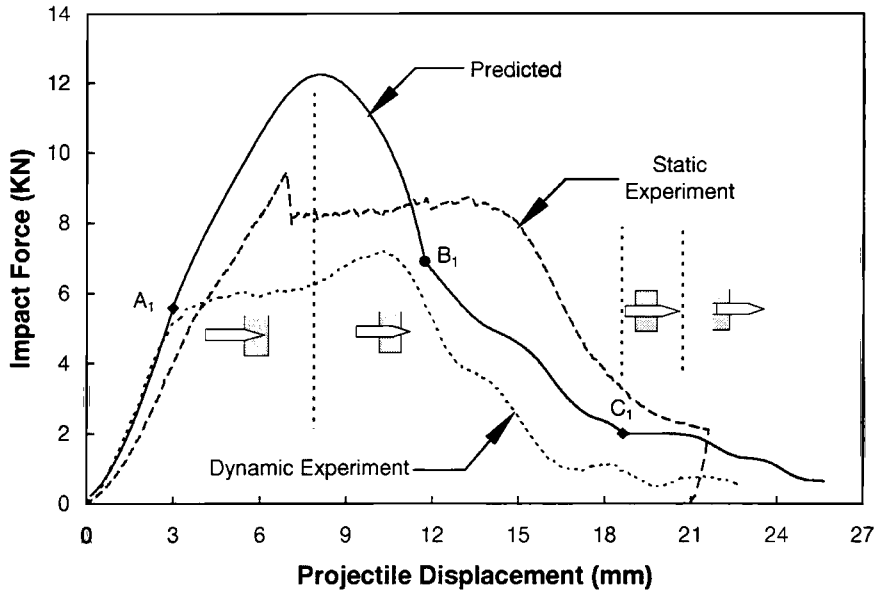

Figure 7.2 Comparison of the predicted and experimental impact force versus projectile displacement when a 0.32 kg steel projectile with a 37° cone angle penetrates through a 6.15 mm thick CFRP laminate with a striking velocity of 30.2 m/s.

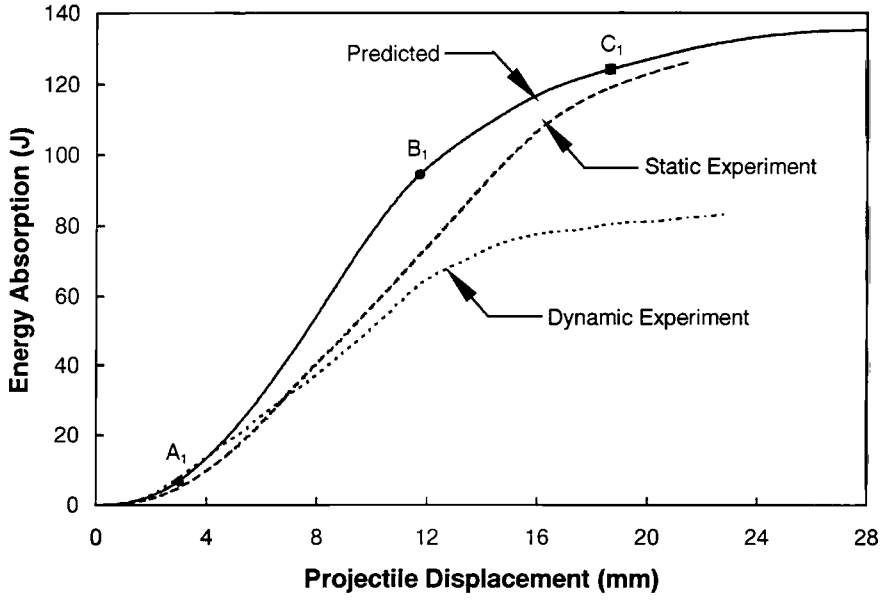

Figure 7.3 Comparison of the predicted and experimental impact energy absorption of the target versus projectile displacement curves when a 0.32 kg steel projectile with a 37° cone angle penetrates through a 6.15 mm thick CFRP laminate with a striking velocity of 30.2 m/s.

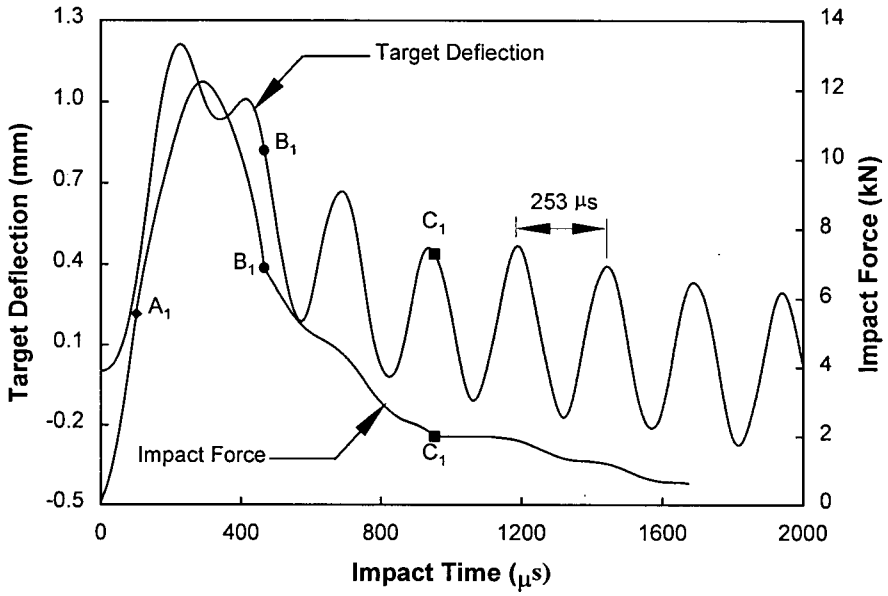

Figure 7.6 Time histories of the predicted target deflection during penetration of a 6.15 mm thick CFRP laminate by a 0.32 kg steel projectile with a 37° cone angle and a striking velocity of 30.2 m/s. The impact force is also plotted here as a reference.

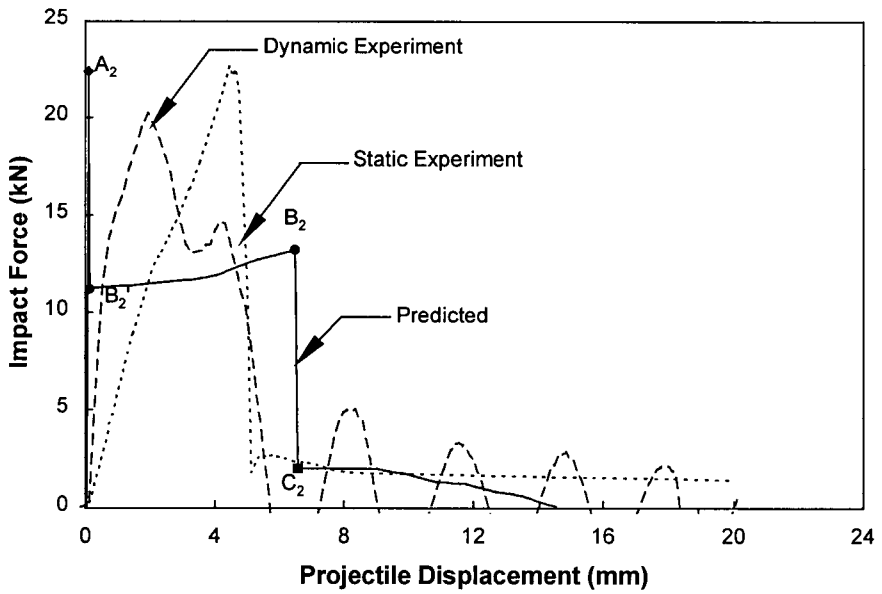

Figure 7.7 Comparison of the predicted and experimental impact force versus projectile displacement curves when a 0.32 kg steel projectile with a blunt-ended head penetrates through a 6.15 mm thick CFRP laminate with a striking velocity of 30.2 m/s.

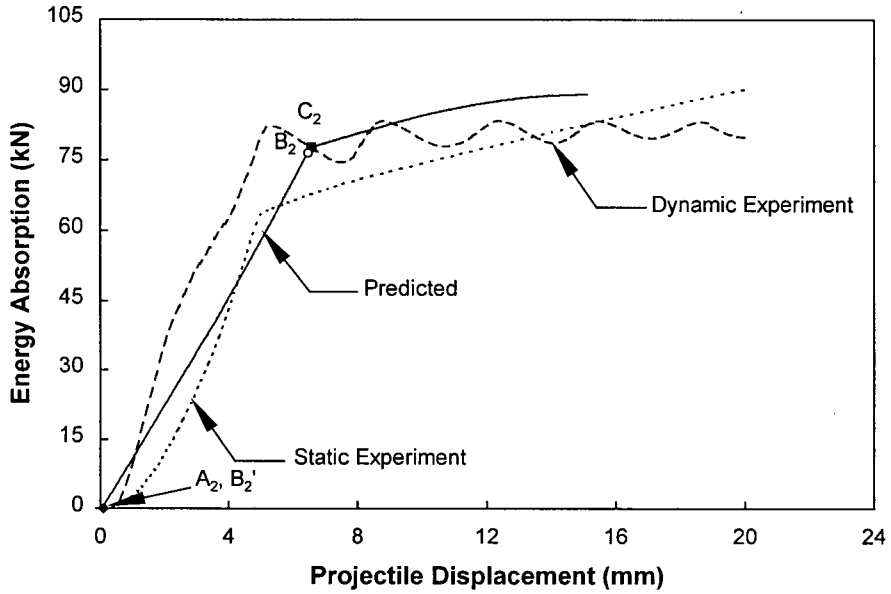

Figure 7.8 Comparison of the predicted and experimental impact energy absorption versus projectile displacement curves when a 0.32 kg steel projectile with a blunt-ended head penetrates through a 6.15 mm thick CFRP laminate with a striking velocity of 30.2 m/s.

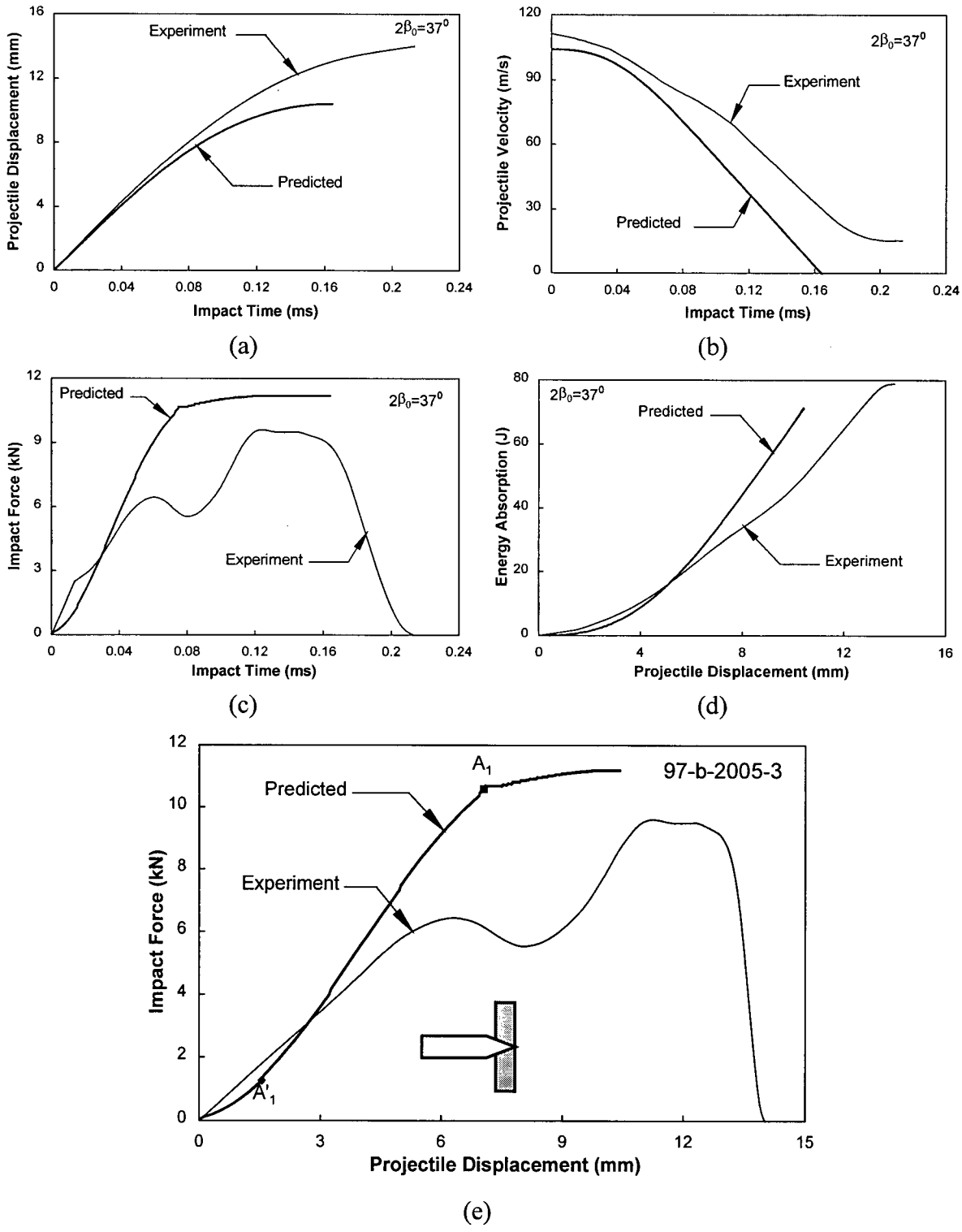

Figure 7.9 Comparison of the predicted and experimental results when a steel projectile with a 37° included cone angle impacts a 6.35mm thick GFRP laminate with a striking velocity of 104 m/s. Both the predicted data and experimental observation show that the projectile stops in the target.

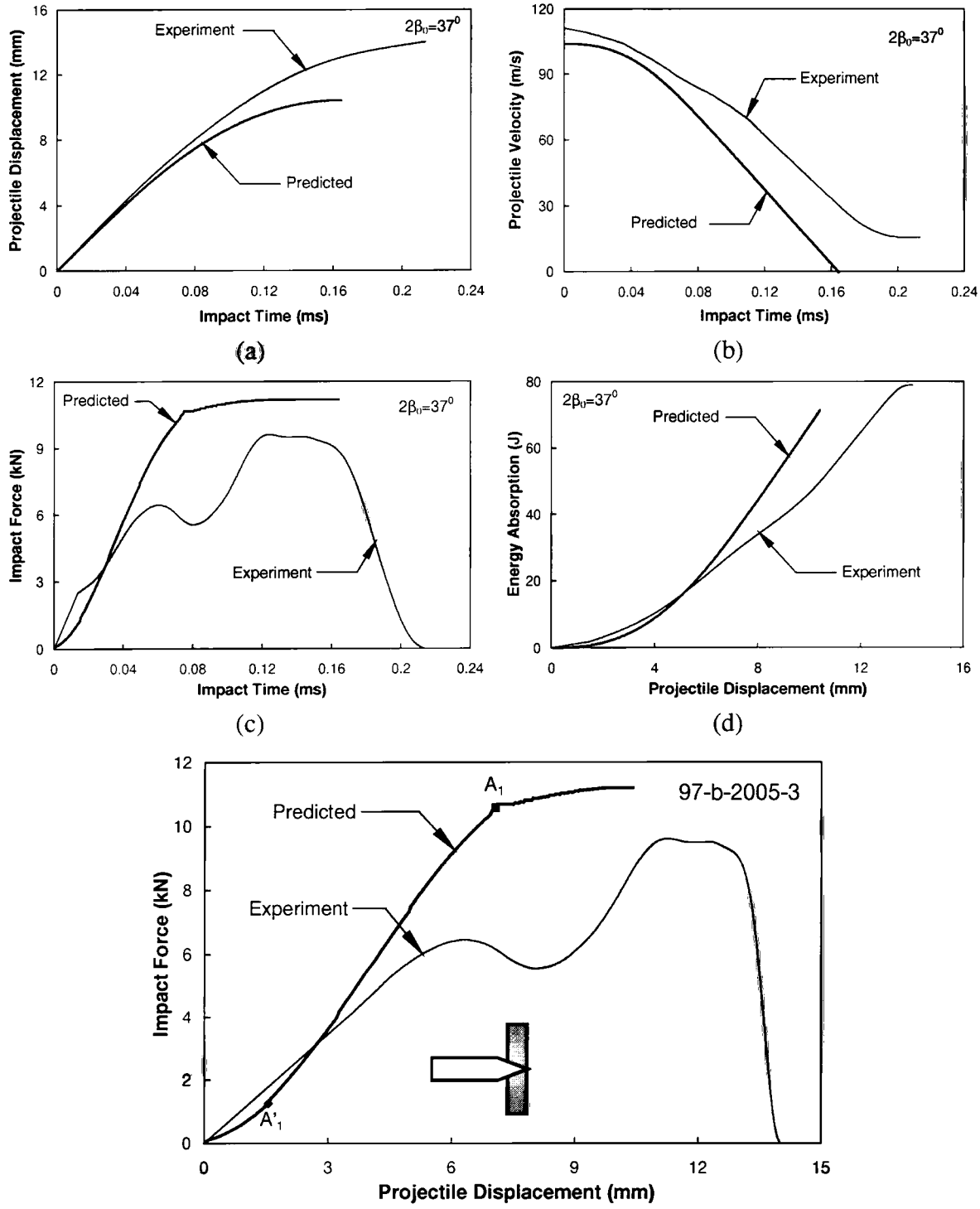

Figure 7.9 Comparison of the predicted and experimental results when a steel projectile with a 37° included cone angle impacts a 6.35mm thick GFRP laminate with a striking velocity of 104 m/s. Both the predicted data and experimental observation show that the projectile stops in the target.

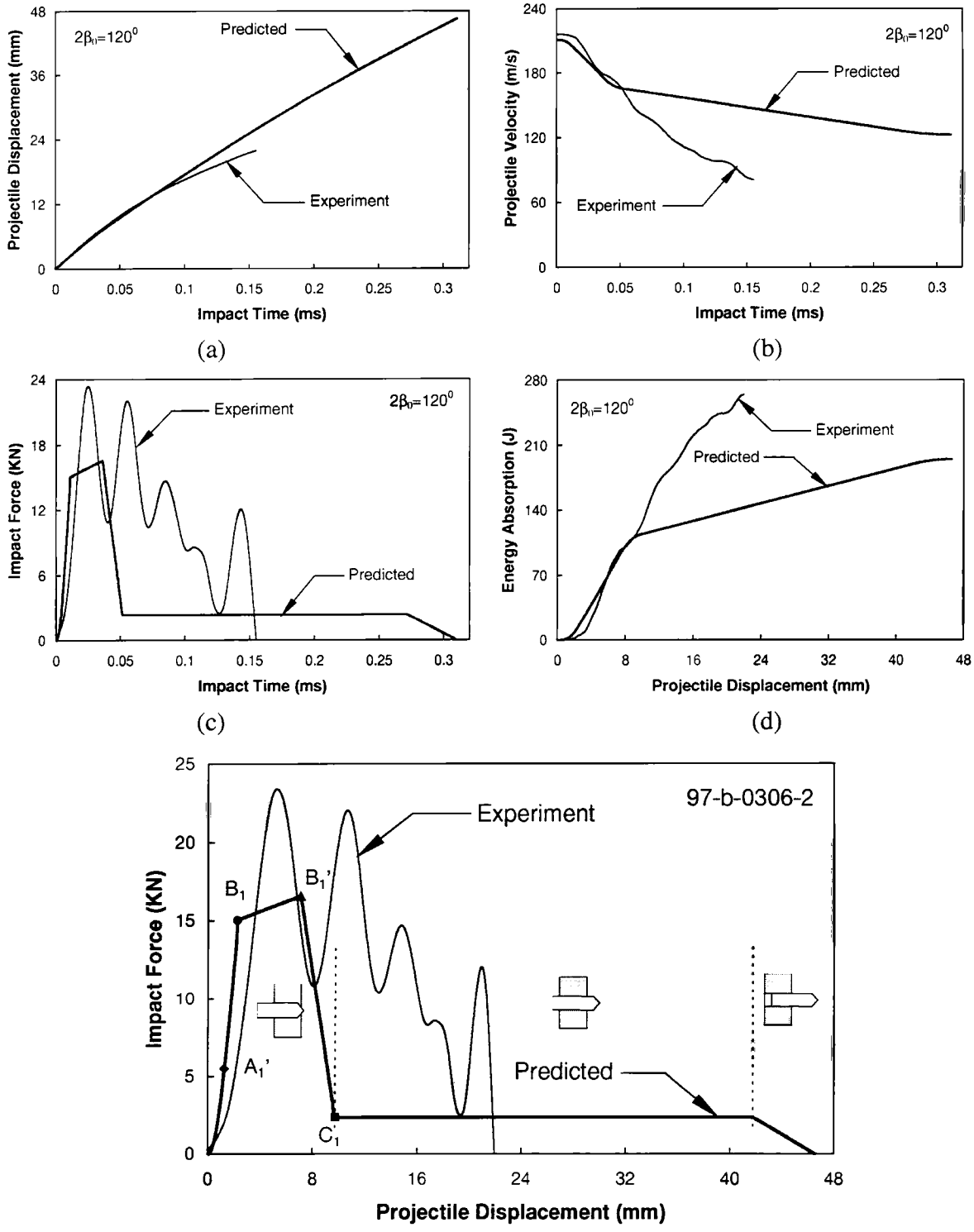

Figure 7.10 Comparison of the predicted and experimental results when a steel projectile with a 120° included cone angle penetrates through a 6.35mm thick GFRP laminate with a striking velocity of 211 m/s. Both the predicted data and experimental measurement show the non-zero projectile exit velocity.

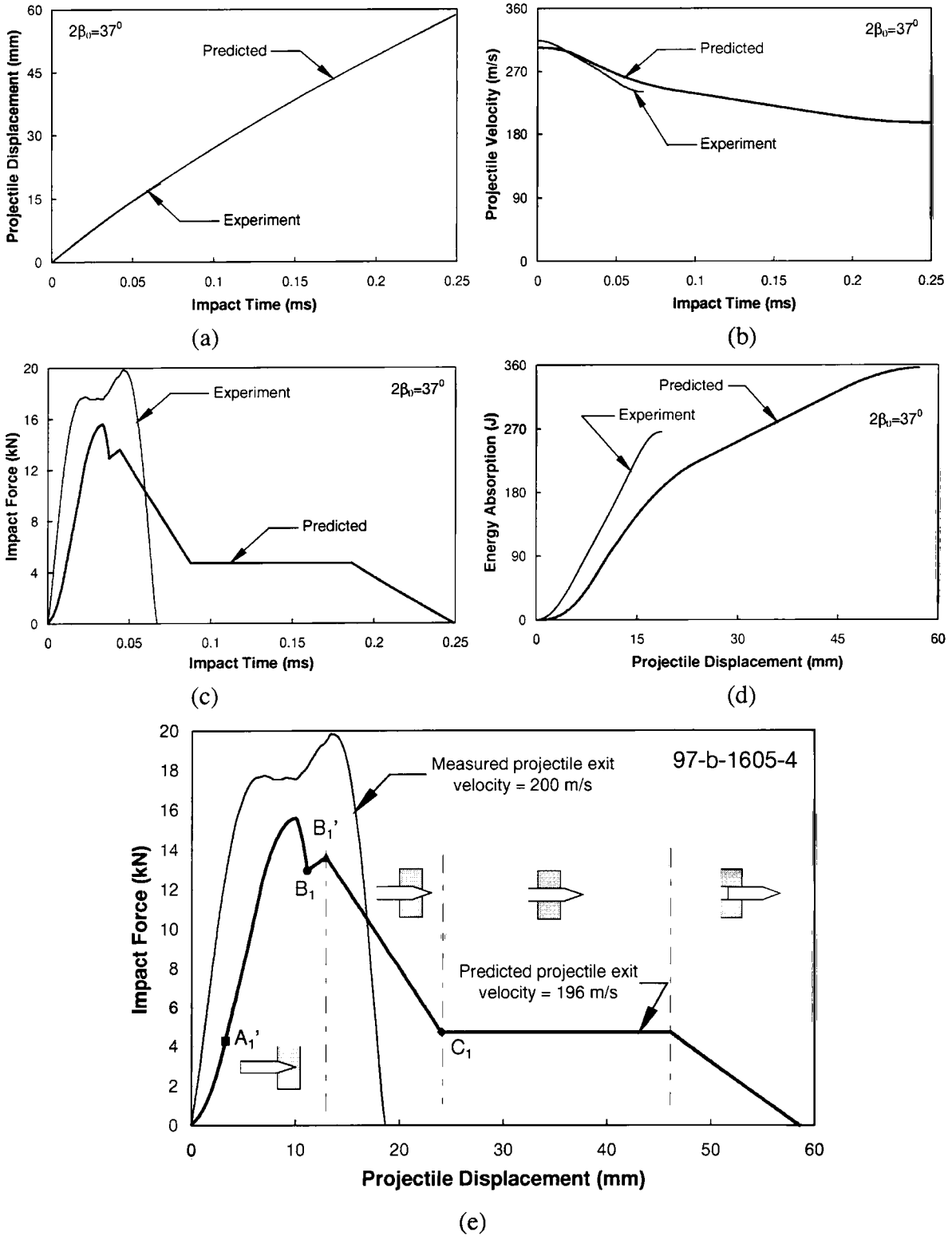

Figure 7.11 Comparison of the predicted and experimental results when a steel projectile with a 37° included cone angle completely perforates a 12.7 mm thick GFRP laminate with a striking velocity of 304 m/s. Predicted projectile exit velocity is very close to the measured one.

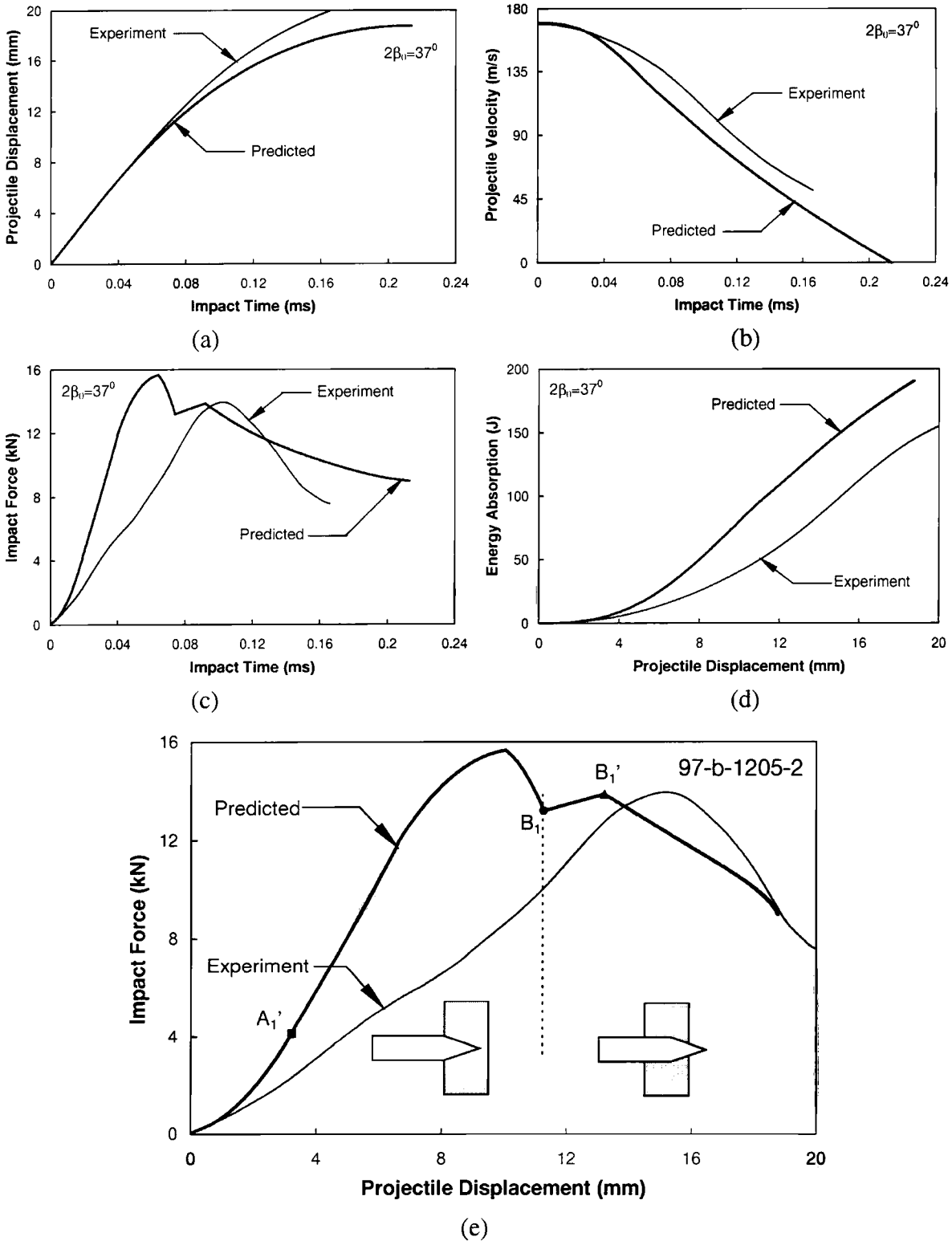

Figure 7.12 Comparison of the predicted and experimental results when a steel projectile with a 37° included cone angle impacts a 12.7 mm thick GFRP laminate with a striking velocity of 170 m/s. Both the predicted data and experimental observation show that the projectile finally rests in the target.

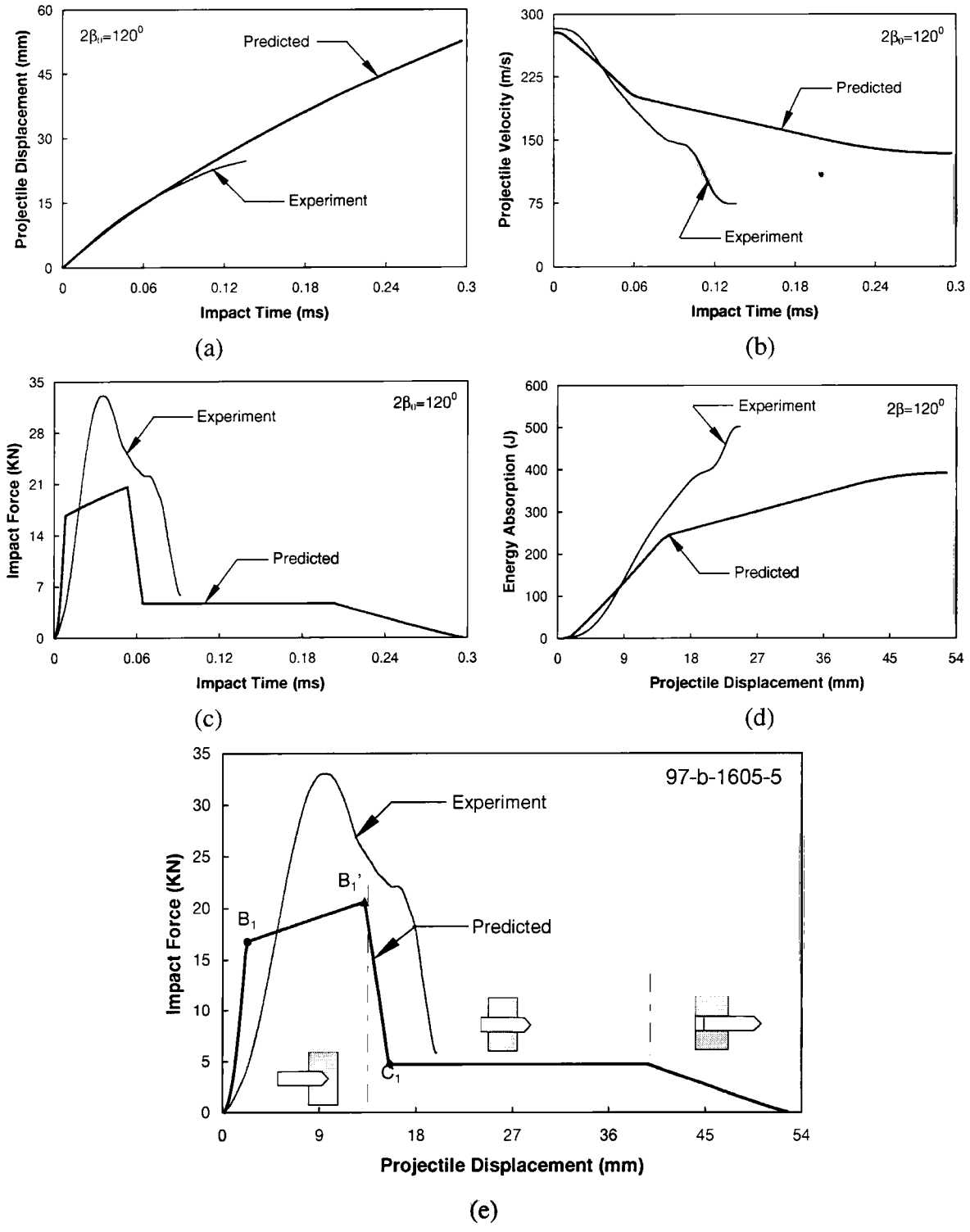

Figure 7.13 Comparison of the predicted and experimental results when a 120° steel projectile penetrates through a 12.7 mm thick GFRP laminate with a velocity of 278 m/s. The predicted projectile residual velocity is 134 m/s. Experimental observation shows the projectile has penetrated through the target but fails to catch its exit velocity.

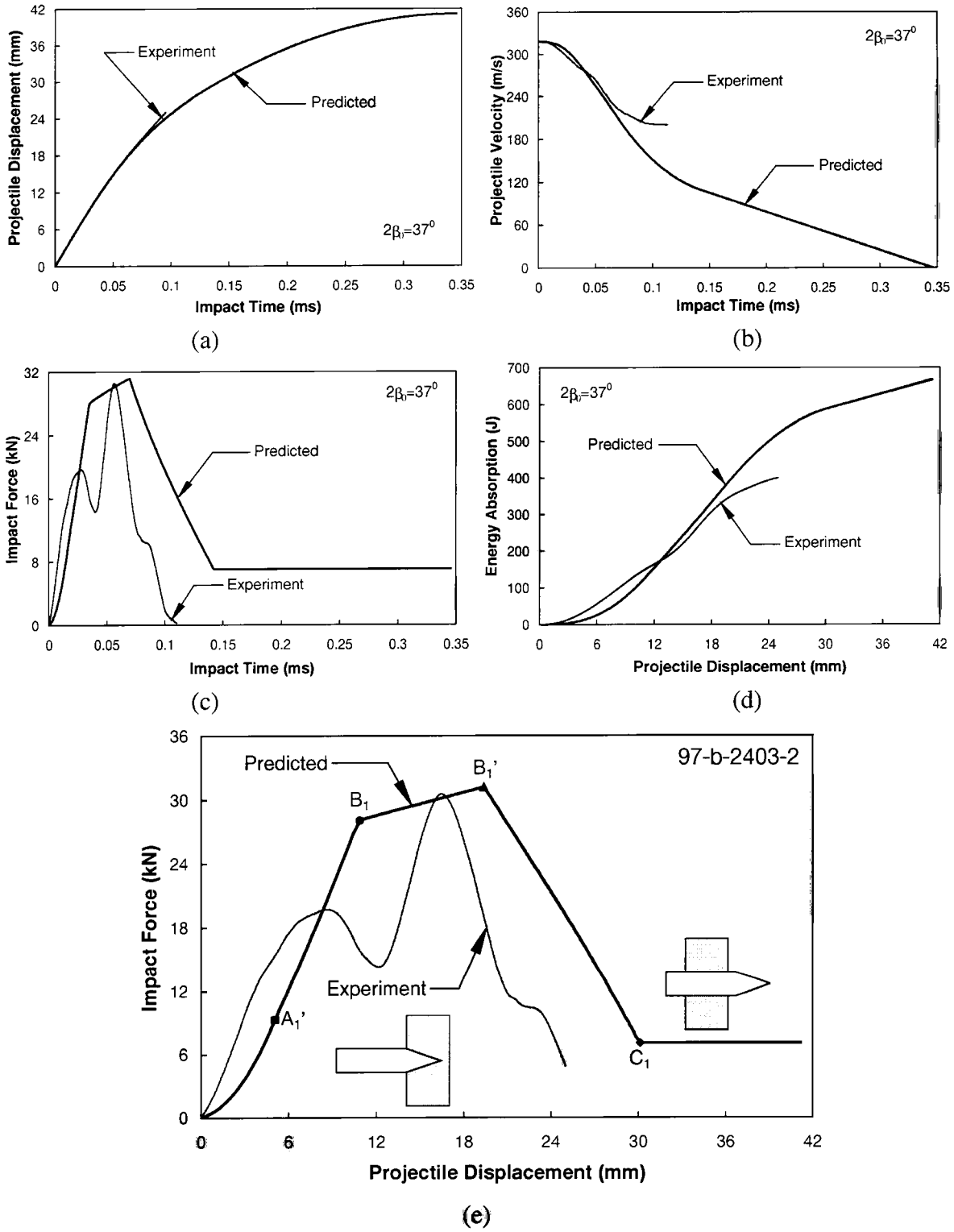

Figure 7.14 Comparison of the predicted and experimental results when a steel projectile with a 37° included cone angle impacts a 19.05 mm thick GFRP laminate with a striking velocity of 318 m/s. Both the predicted data and experimental observation show the partially perforation in the target.

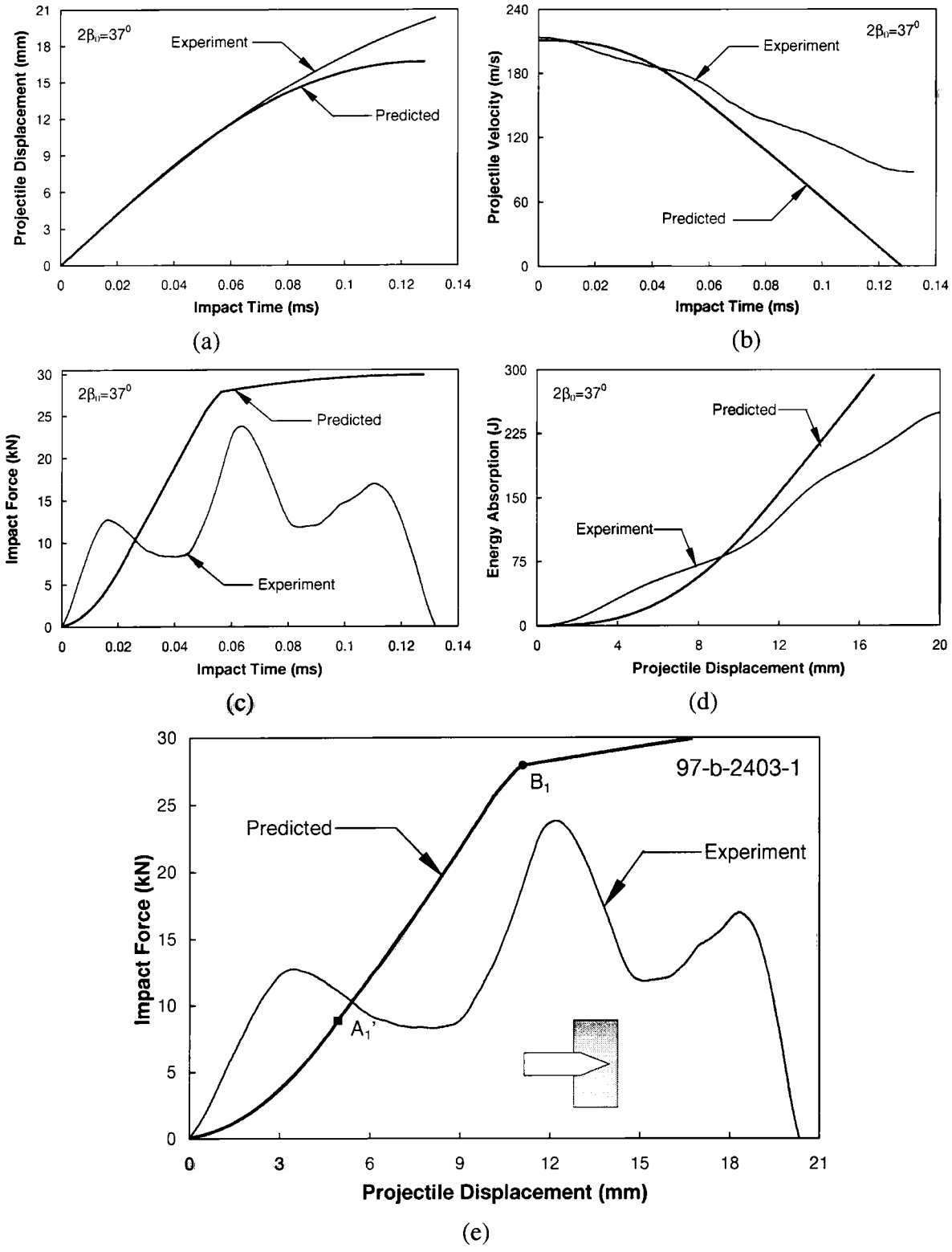

Figure 7.15 Comparison of the predicted and experimental results when a steel projectile with a 37° included cone angle impacts a 19.05 mm thick GFRP laminate with a striking velocity of 211 m/s. Both the predicted data and experimental observation indicate that the projectile finally rests in the target.

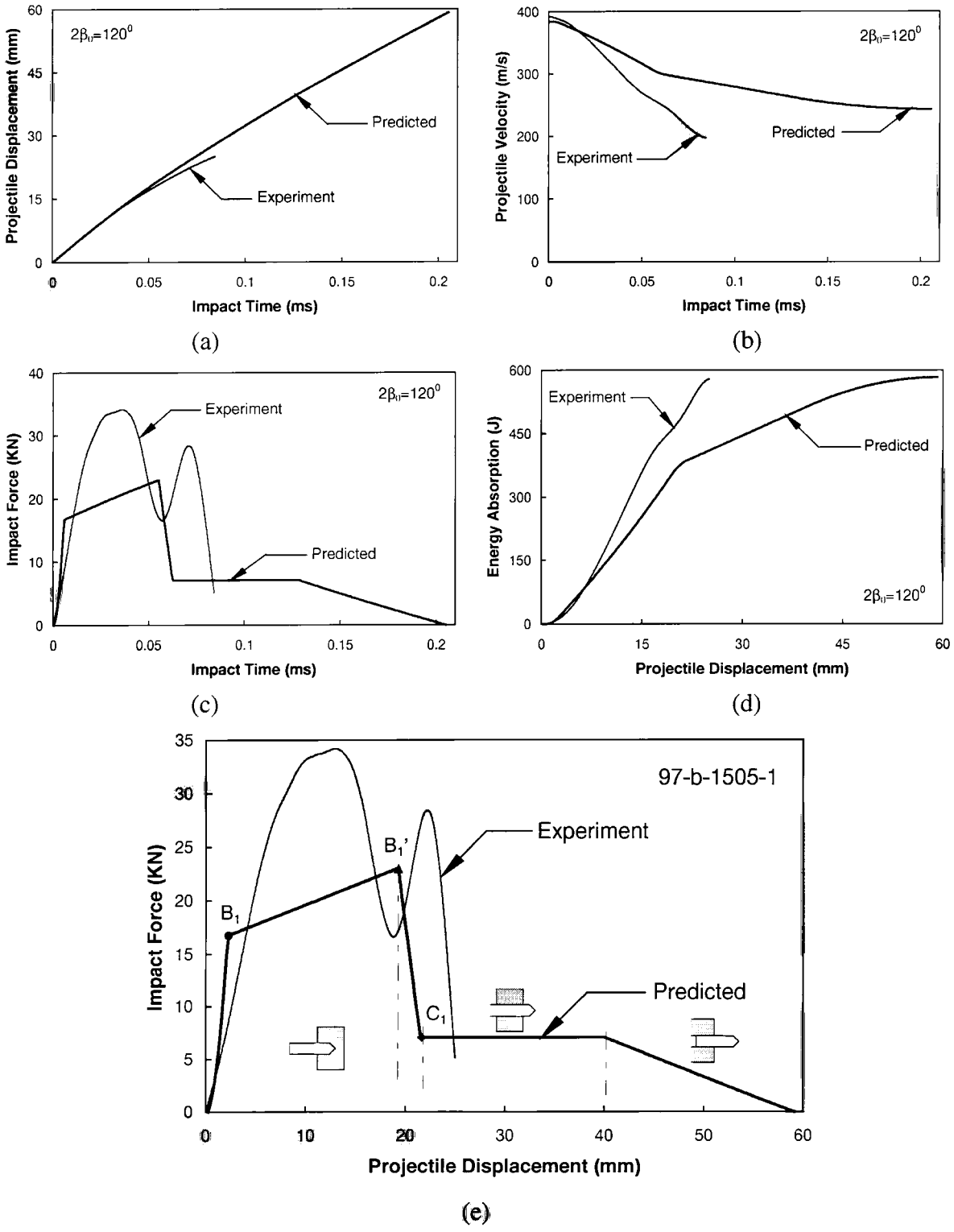

Figure 7.16 Comparison of the predicted and experimental results when a 120° steel projectile penetrates through a 19.05 mm thick GFRP laminate with a velocity of 384 m/s. The predicted projectile residual velocity is 243 m/s, comparing with the measured residual velocity of 160 m/s.

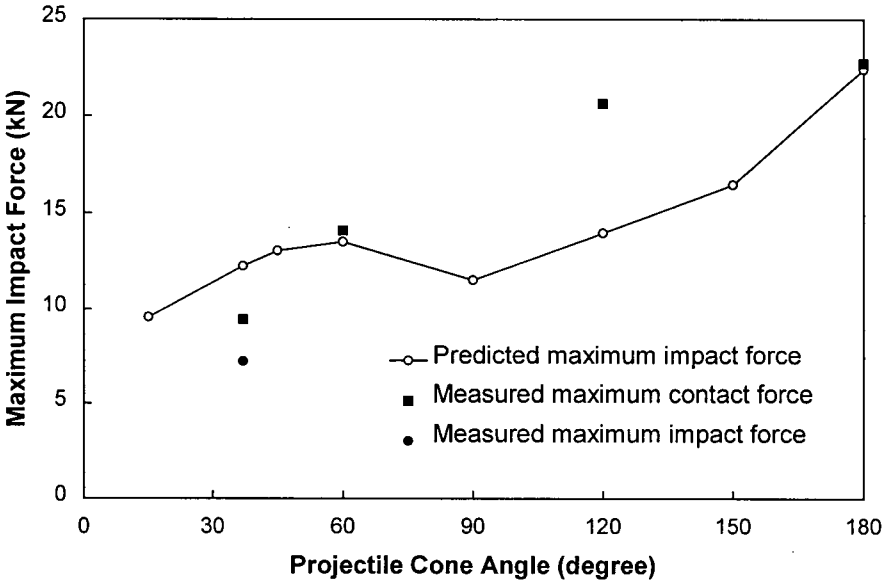

Figure 7.19 Predicted peak impact force when 0.32 kg steel projectiles with various included cone angles penetrate through a 6.15 mm thick CFRP laminate with a striking velocity of 30.2 m/s.

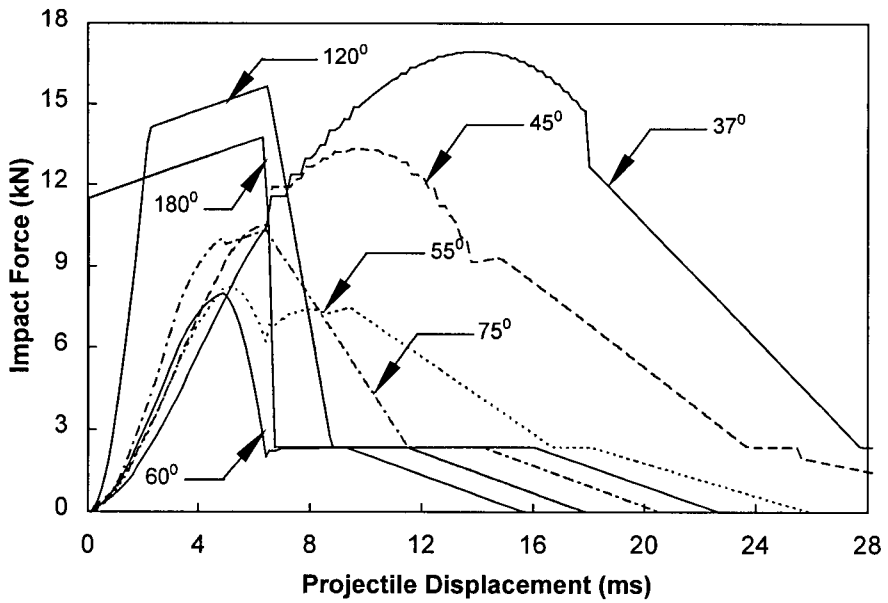

Figure 7.20 Predicted family of impact force versus projectile displacement curves when 4.2 g steel projectiles with various included cone angles penetrate through a 6.35 mm thick GFRP laminate with a striking velocity of 600 m/s.

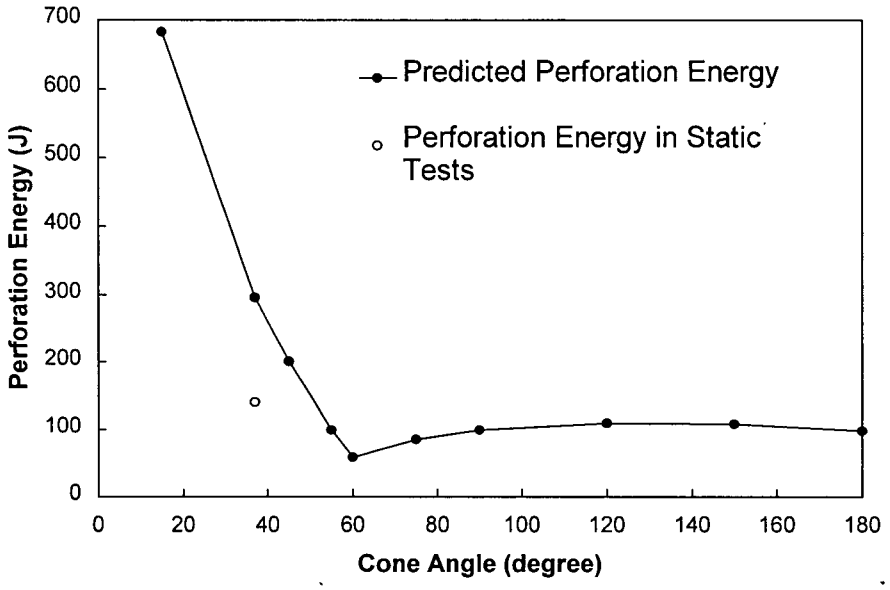

Figure 7.21 Predicted impact energy absorption (perforation energy) when 4.2 g steel projectiles with various included cone angles penetrate through a 6.35 mm thick GFRP laminate with a striking velocity of 600 m/s.

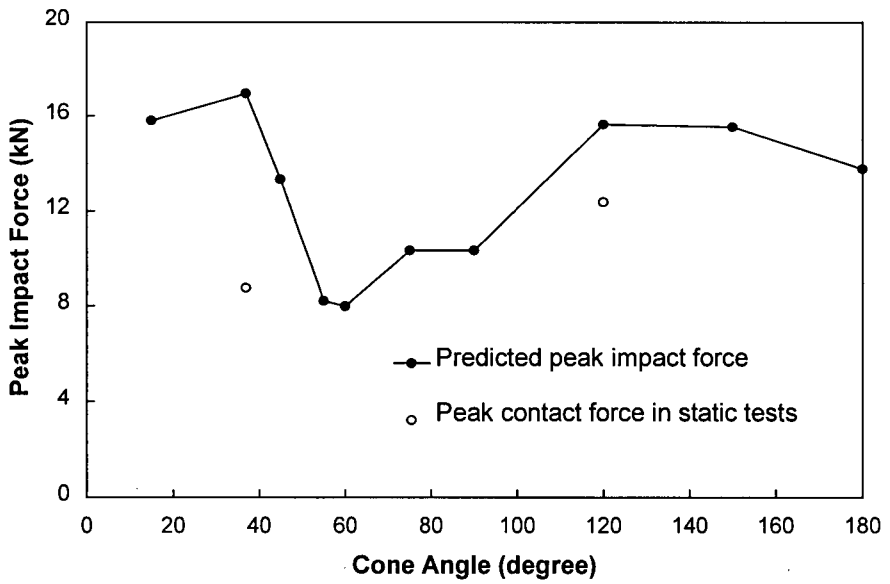

Figure 7.22 Predicted peak impact force when 4.2 g steel projectiles with various included cone angles penetrate through a 6.35 mm thick GFRP laminate with a striking velocity of 600 m/s.

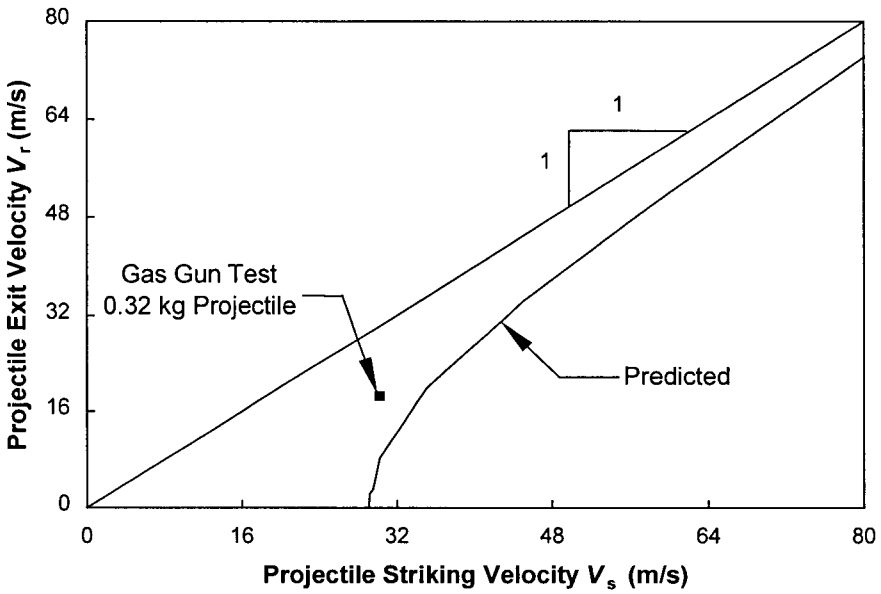

Figure 7.23 Predicted projectile residual versus striking velocity curve for a 0.32 kg projectile with a 37° cone angle penetrating through a 6.15 mm thick CFRP laminate. The experiment data from a gas gun test is also shown here.

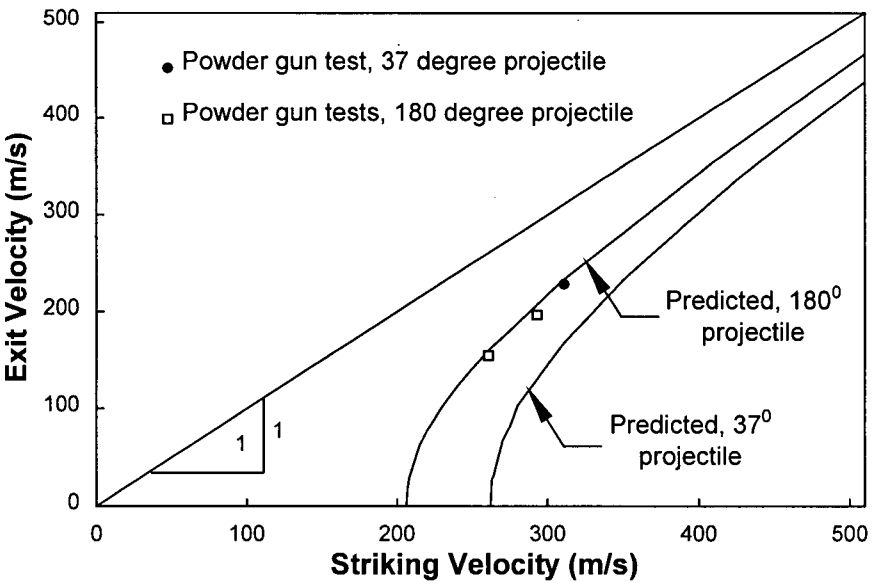

Figure 7.24 Predicted projectile residual versus striking velocity curves for 4.2 g projectiles with 37° and 180° cone angles penetrating through a 6.15mm thick CFRP laminate. The experiment data from gas gun tests are also shown here.

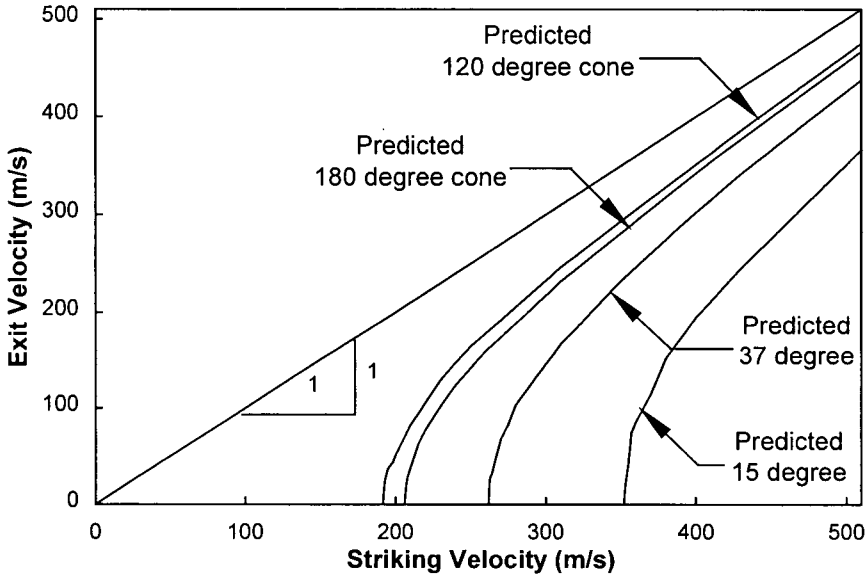

Figure 7.25 Predicted projectile residual versus striking velocity curves for 4.2 g projectiles with 15°, 37°, 120°, and 180° cone angles penetrating through a 6.15mm thick CFRP laminate.

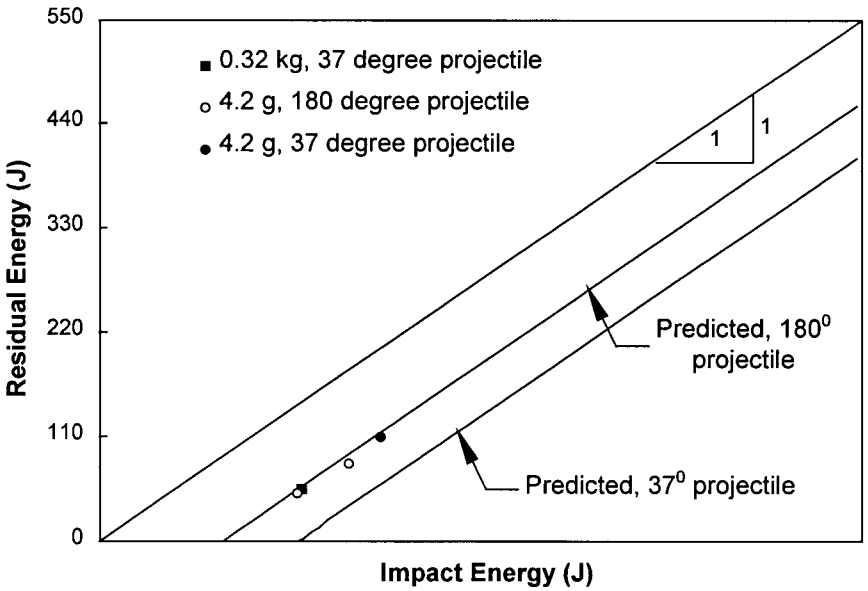

Figure 7.26 Predicted projectile residual versus striking energy for 4.2 g projectiles with 37° and 180° cone angles penetrating through a 6.15 mm thick CFRP laminate. The experimental data are also shown in the graph.

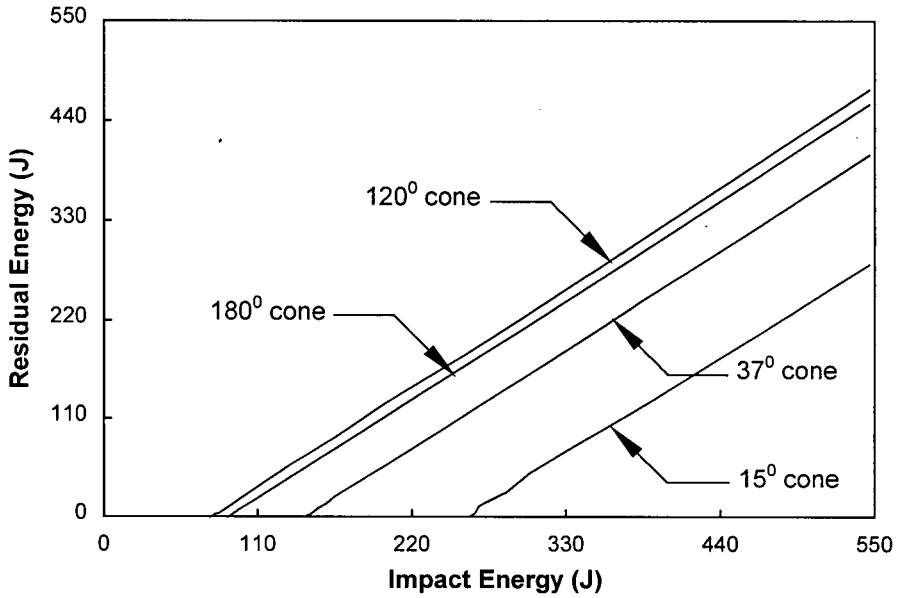

Figure 7.27 Predicted projectile residual versus striking energy curves for 4.2 g projectiles with 15°, 37°, 120°, and 180° cone angles penetrating through a 6.15mm thick CFRP laminate.

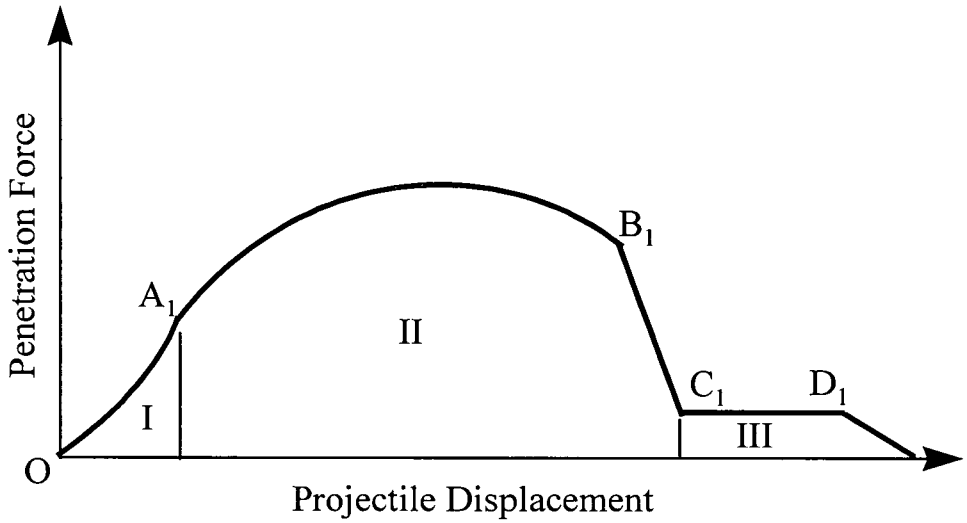

(a)

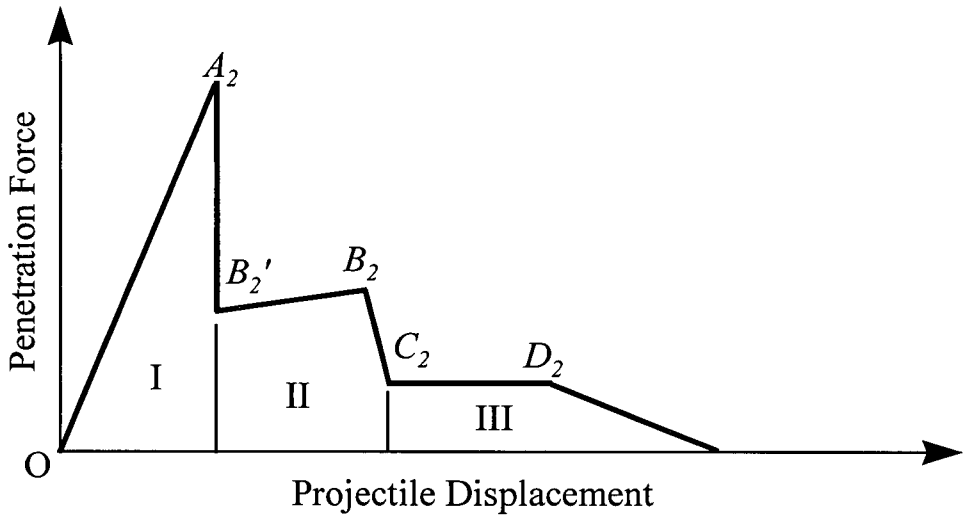

(b)

Figure 7.28 Schematic illustration of three parts of impact energy absorption on force-displacement curves: in phase I, energy dissipates in the form of hole expansion; in phase II, energy dissipates in the form of: (a) hole expansion and flexural deformation of a split-plate or (b) transverse plug initiation an push-out; in phase III, energy dissipates in the form of friction.

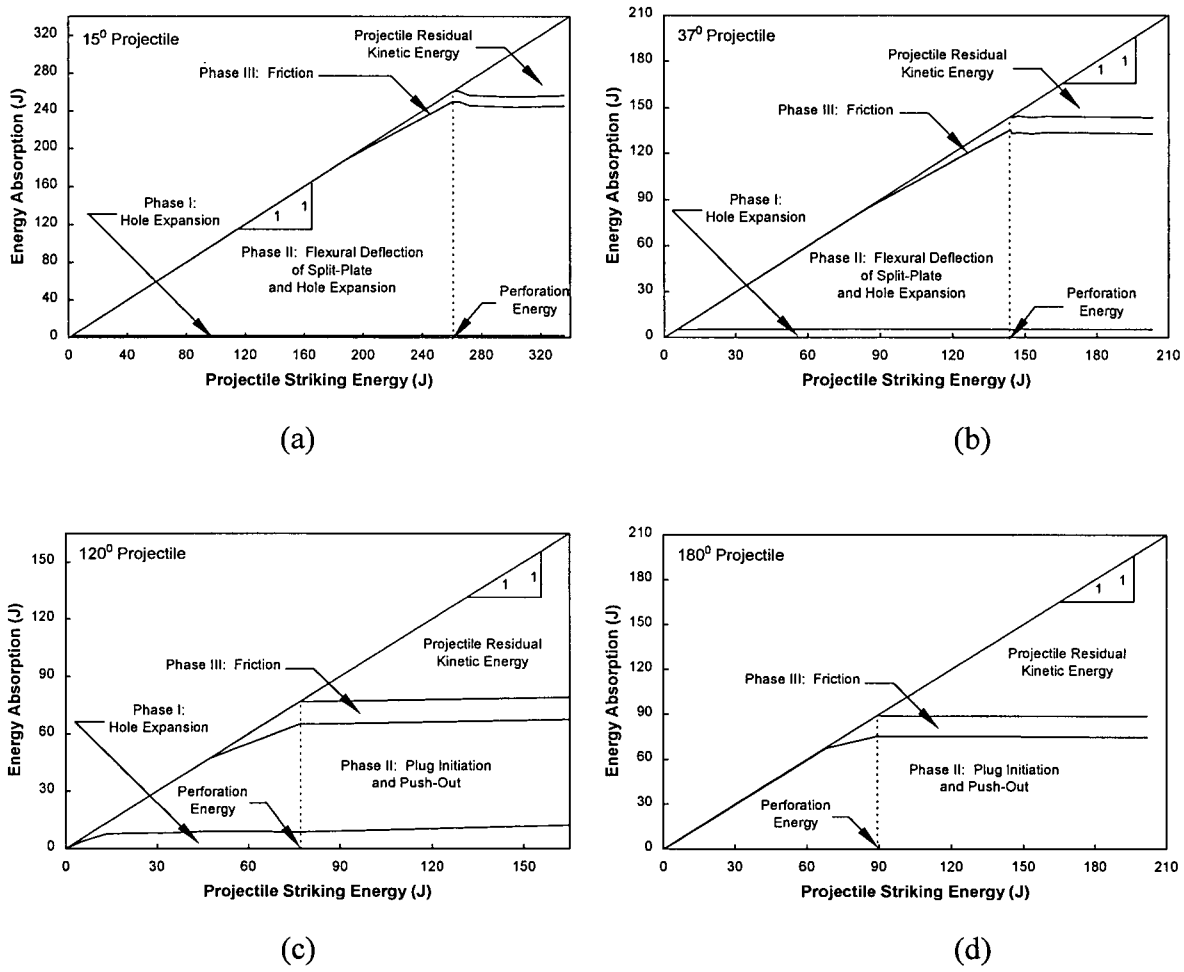

Figure 7.29 Composition of impact energy absorption of a 6.15 mm thick CFRP laminate perforated by a 4.2 g projectile with various cone angles: (a) 15°, (b) 37°, (c) 120°, (d) 180°.

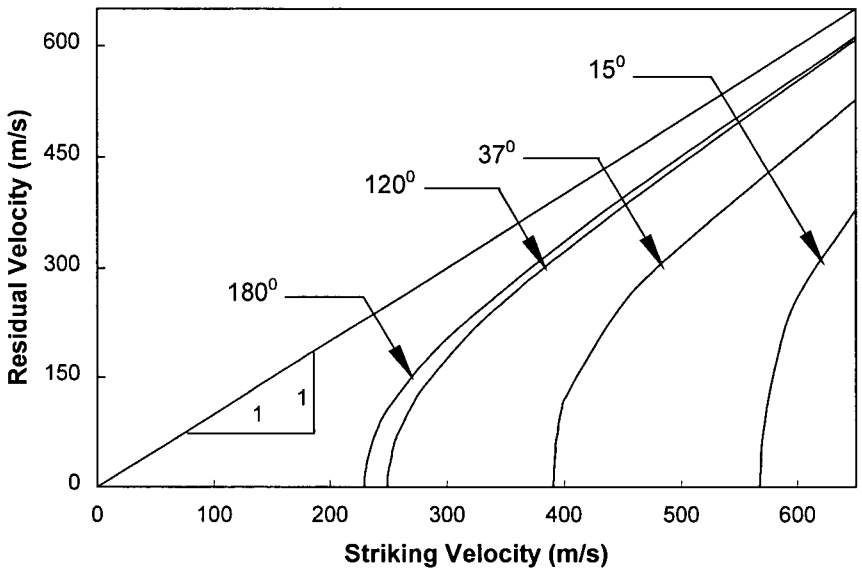

Figure 7.30 Predicted projectile residual versus striking velocity curves for 4.2 g projectiles with 15°, 37°, 120°, and 180° cone angles penetrating through a 6.35 mm thick GFRP laminate.

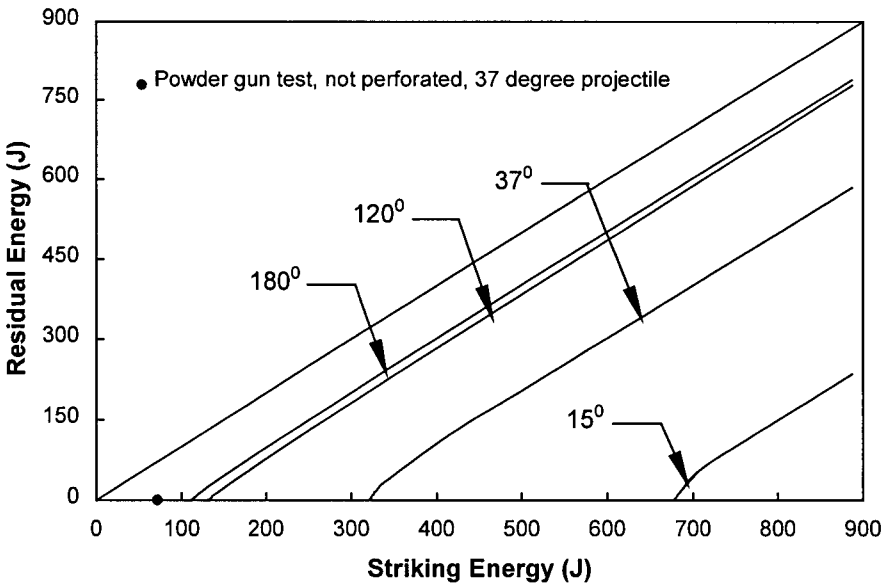

Figure 7.31 Predicted projectile residual versus striking energy for 4.2 g projectiles with 15°, 37°, 120°, and 180° cone angles penetrating through a 6.35 mm thick GFRP laminate. The results of powder gun tests are also shown in the figure.

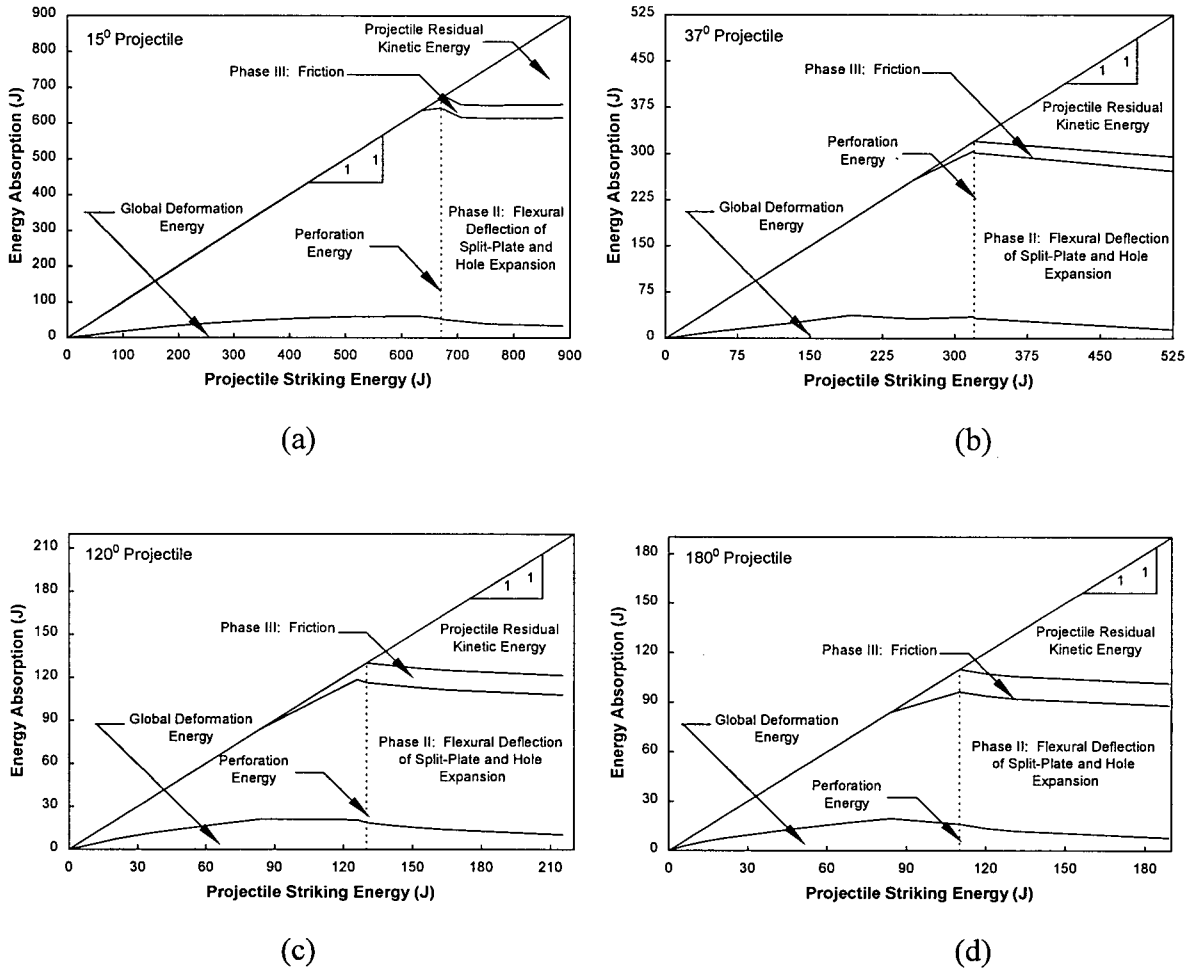

Figure 7.32 Composition of impact energy absorption of a 6.35 mm thick GFRP laminate perforated by a projectile with various cone angles: (a) 15°, (b) 37°, (c) 120°, (d) 180°.

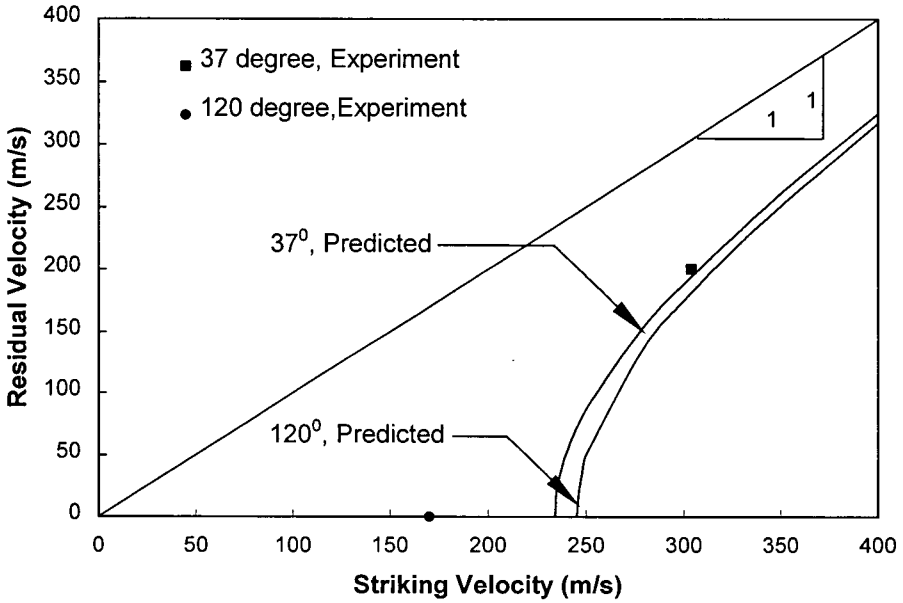

Figure 7.33 Predicted projectile residual versus striking velocity curves for 13.2 g projectiles with 37° and 120° cone angles penetrating through a 12.7 mm thick GFRP laminate. The experimental result in the powder gun test is also shown in the graph.

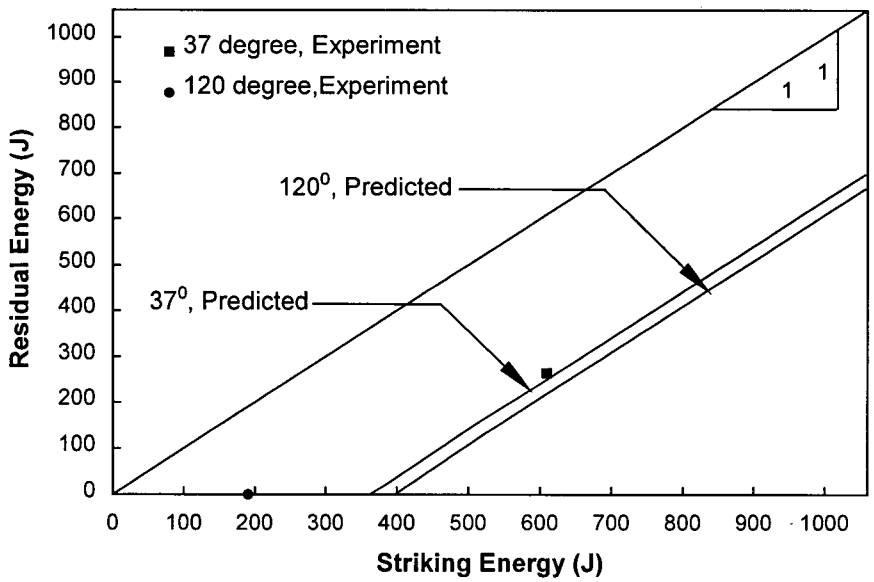

Figure 7.34 Predicted projectile residual versus striking energy for 13.2 g projectiles with 37° and 120° cone angles penetrating through a 12.7 mm thick GFRP laminate. The experimental results in powder gun test are also shown in the figure.

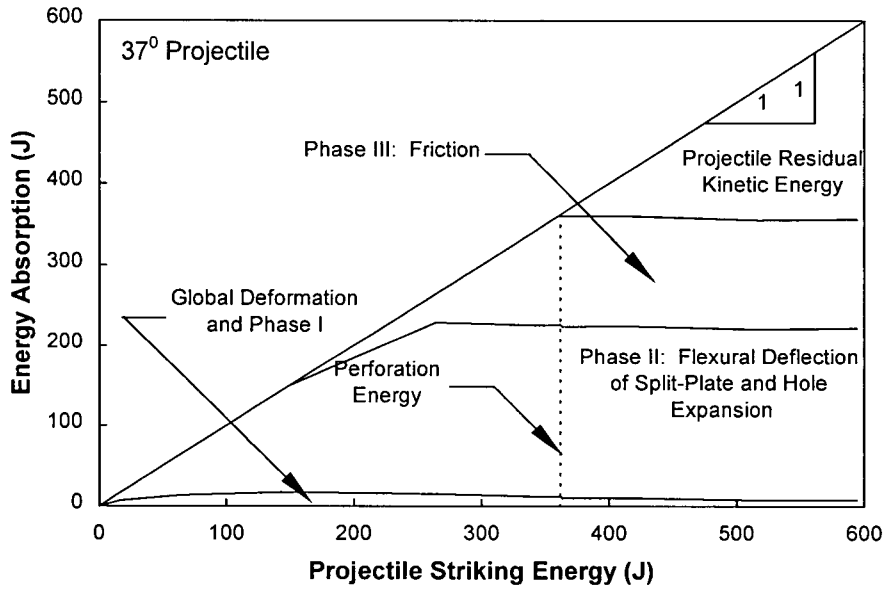

(a)

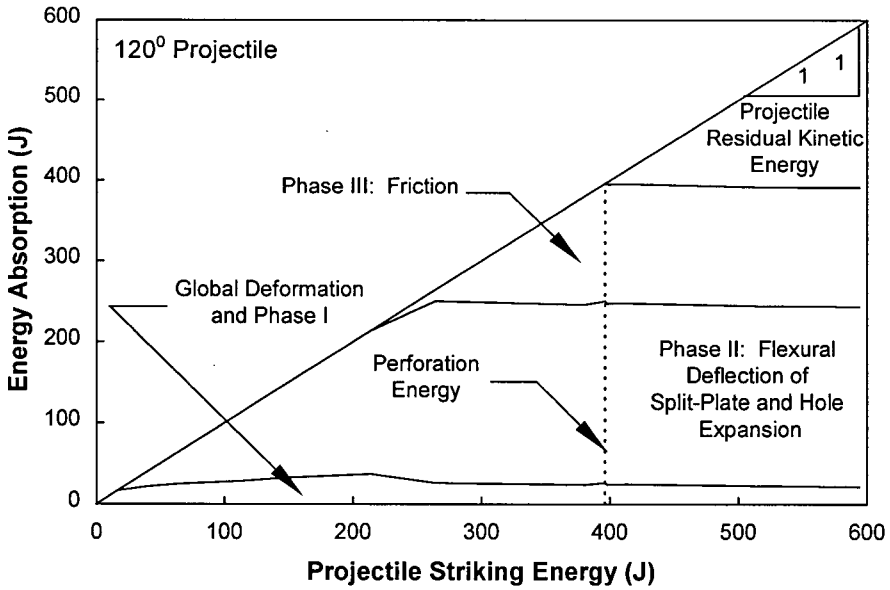

(b)

Figure 7.35 Composition of impact energy absorption of a 12.7 mm thick GFRP laminate perforated by a 13.2 g projectile with various cone angles: (a) 37°; (b) 120°.

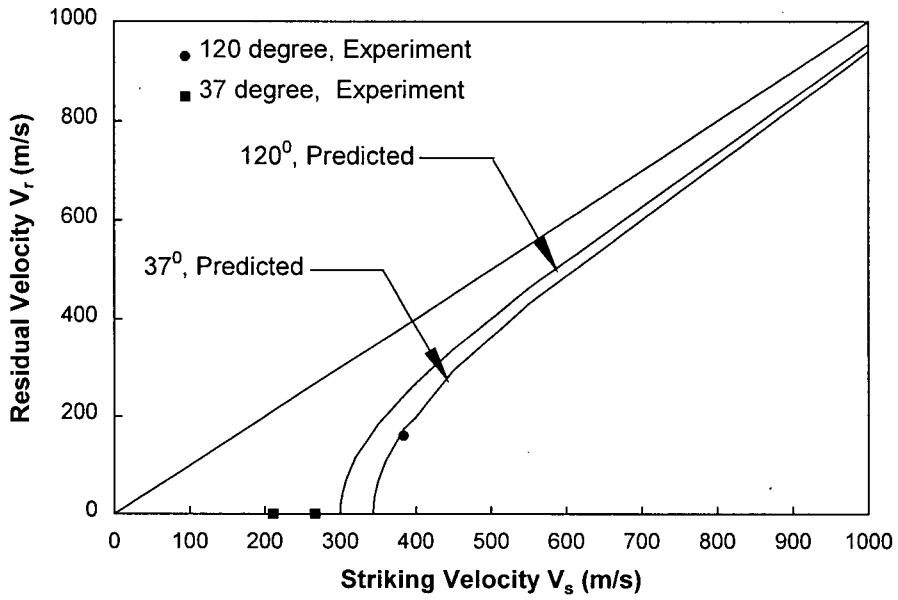

Figure 7.36 Predicted projectile residual versus striking velocity curves for 13.2 g projectiles with 37° and 120° cone angles penetrating through a 19.05 mm thick GFRP laminate. The experimental results in the powder gun test are also shown in the graph.

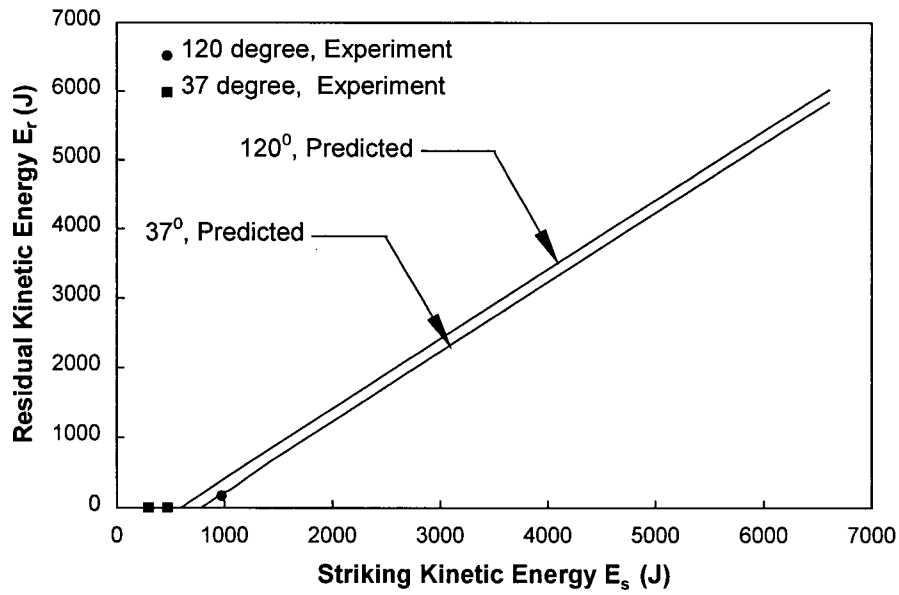

Figure 7.37 Predicted projectile residual versus striking energy for 13.2 g projectiles with 37° and 120° cone angles penetrating through a 19.05 mm thick GFRP laminate. The experimental results in powder gun test are also shown in the figure.

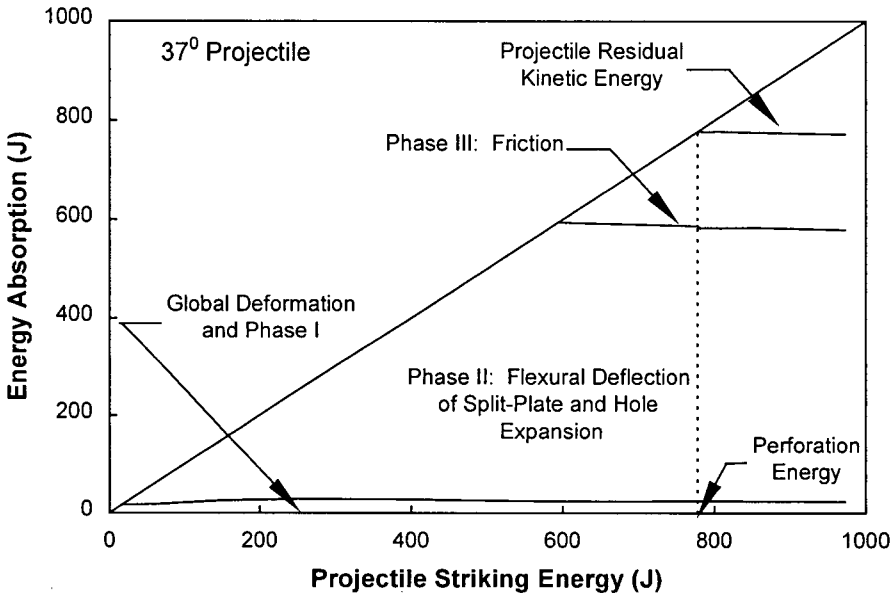

(a)

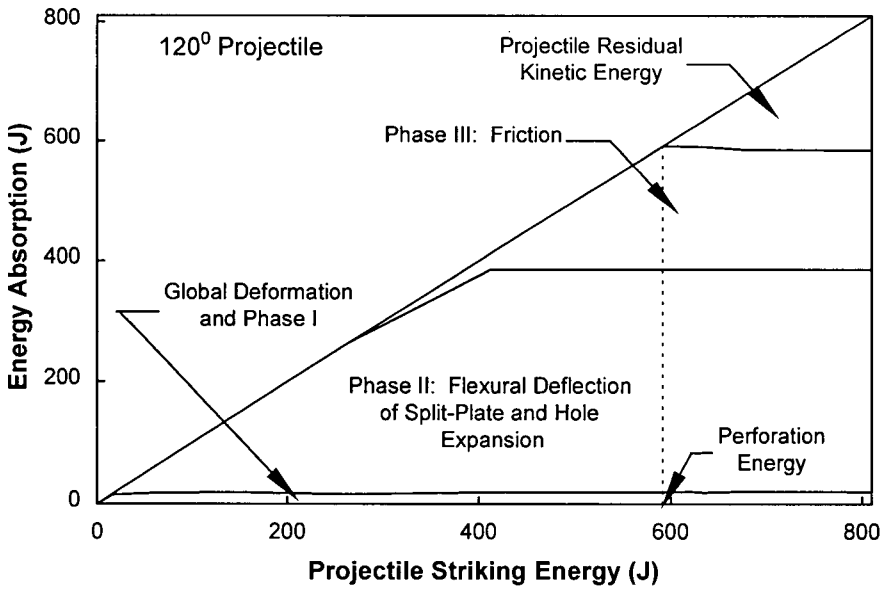

(b)

Figure 7.38 Composition of impact energy absorption of a 19.05 mm thick GFRP laminate perforated by a 13.2 g projectile with various cone angles: (a) 37°; (b) 120°.

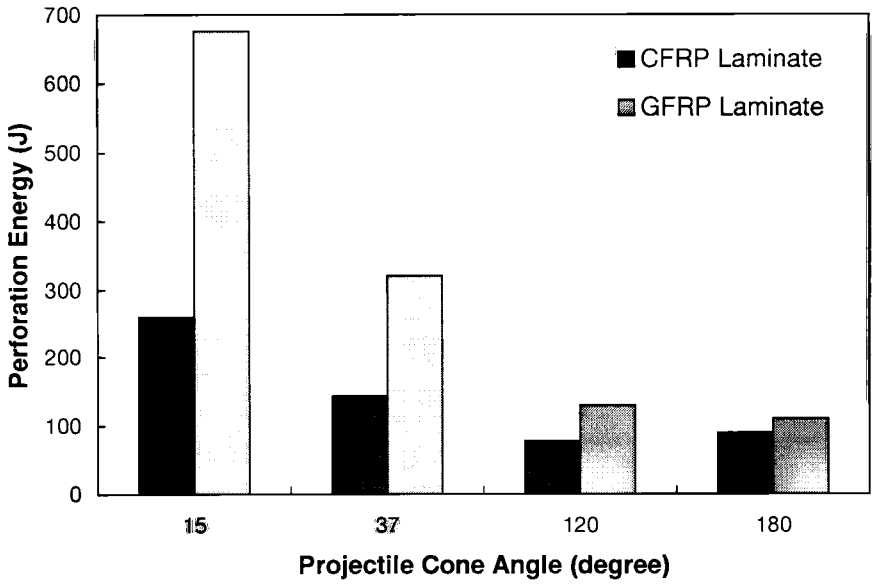

Figure 7.39 Comparison between the predicted ballistic resistance (perforation energy) of a CFRP laminate (6.15 mm thick) and a GFRP laminate (6.35 mm thick). The projectiles used are defined in Table 7.1.

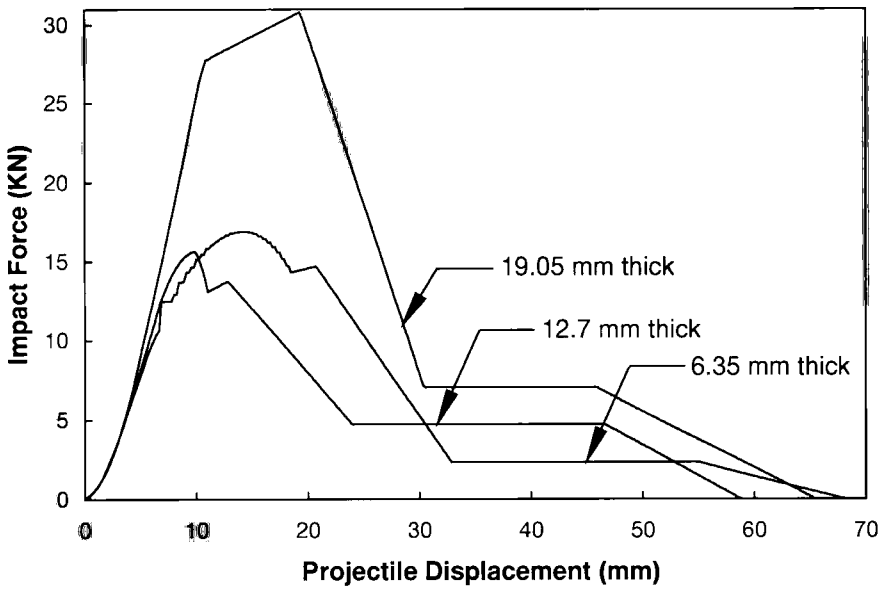

Figure 7.40 Predicted force-displacement curves for a 13.2 g projectile with a 37° cone angle penetrating through 6.35 mm, 12.7 mm, and 19.05 mm thick GFRP laminates with a velocity of 384 m/s.

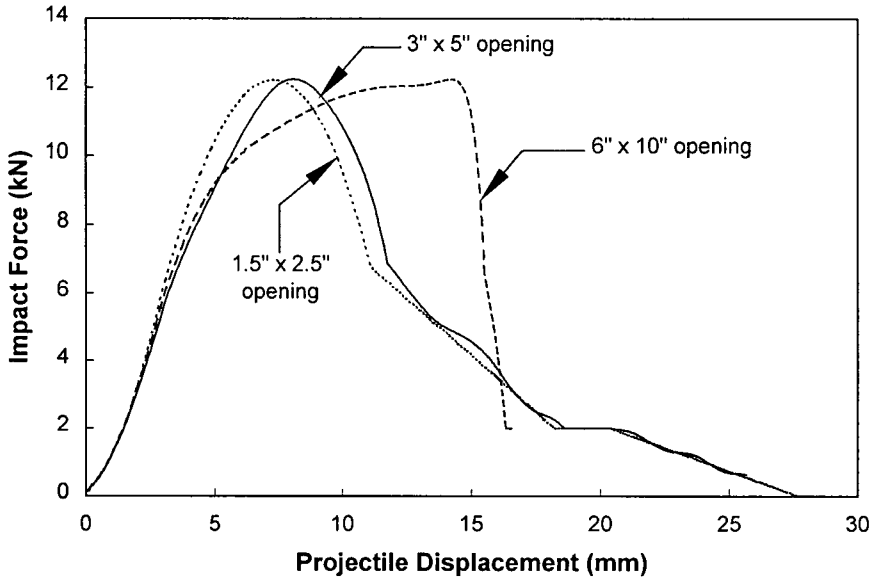

Figure 7.43 Predicted force-displacement curves for a 0.32 kg projectile with a 37° cone angle penetrating a 6.15 mm thick CFRP laminate with different planar dimensions. The projectile velocity is 30.2 m/s.

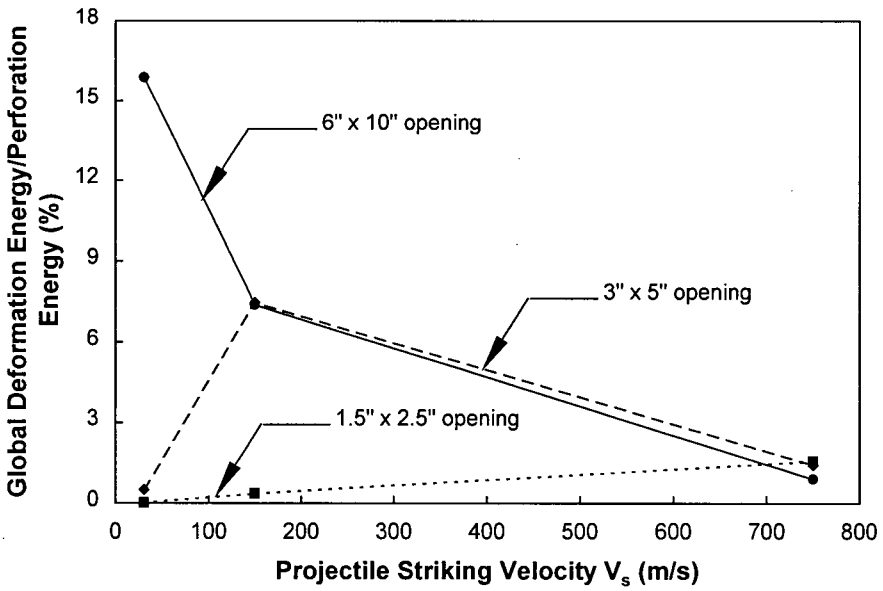

Figure 7.44 Predicted ratio of global deformation and motion energy to target perforation energy versus the projectile striking velocity for a 0.32 kg projectile with a 37° cone angle penetrating a 6.15 mm thick CFRP laminate with different planar dimensions.

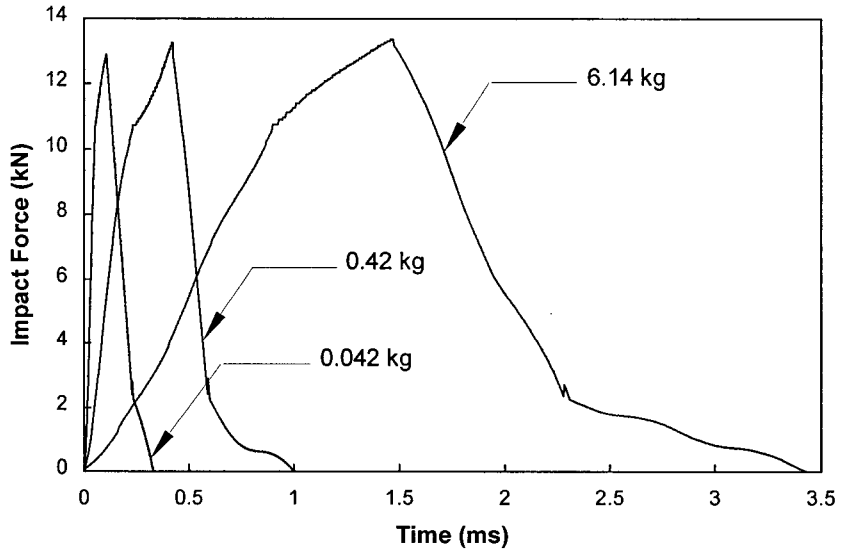

Figure 7.45 Predicted force-time histories for projectiles with three different masses penetrating a 6.35 mm thick GFRP laminate. All projectiles have the same cone angle of 37° and the same striking energy of 343 J.

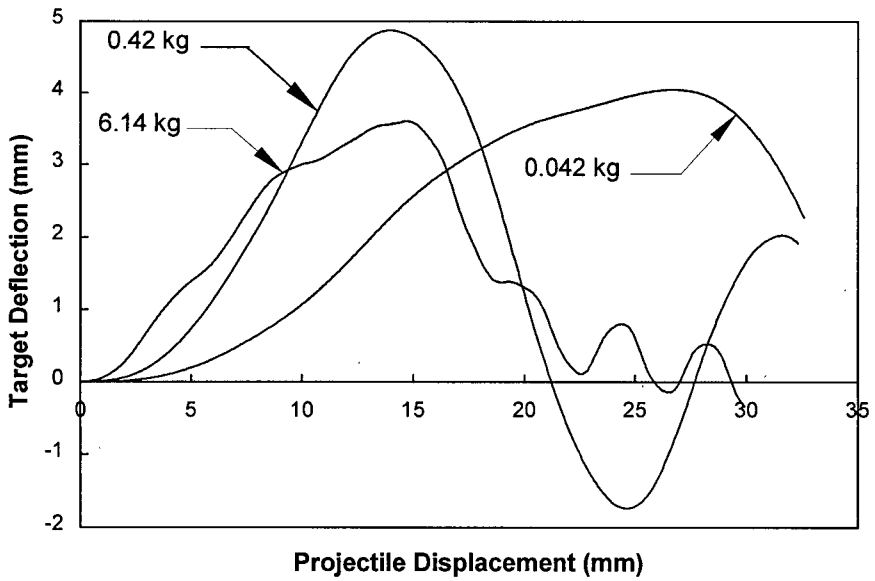

Figure 7.46 Predicted family of target deflection versus projectile displacement at the impact site for projectiles with different masses penetrating a 6.35 mm thick GFRP laminate. All projectiles have the same cone angle of 37° and the same striking energy of 343 J.

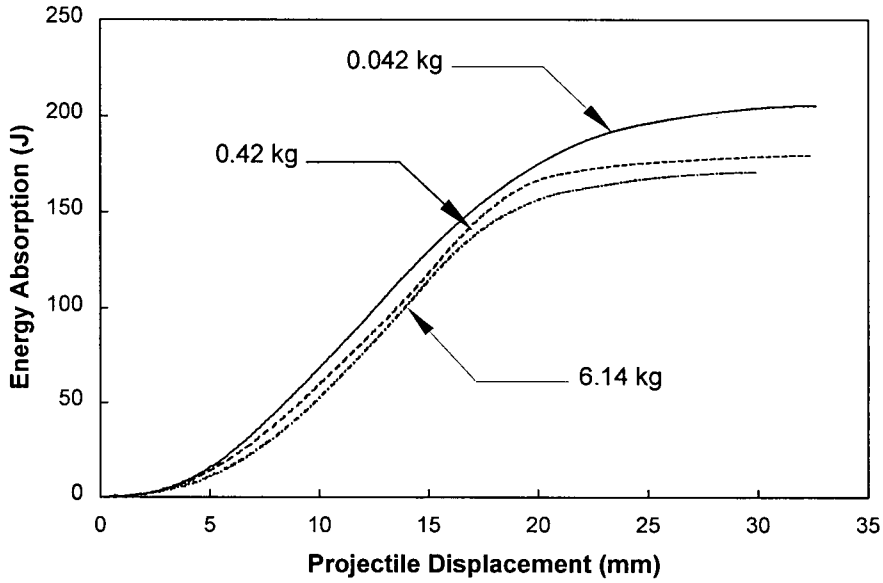

Figure 7.47 Predicted family of impact energy absorption versus projectile displacement at the impact site for projectiles with different masses penetrating a 6.35 mm thick GFRP laminate. All projectiles have the same cone angle of 37° and the same striking energy of 343 J.

Chapter Eight: Summary, Conclusions, and Future Work

8.1. Summary

A numerical model has been developed in the present thesis for non-linear structural and impact analyses of plain and stiffened laminated composite structures.

A super finite element program, SENACS, that was previously developed for transient non-linear analysis of isotropic structures, has been modified to handle the response of layered (laminated) composite materials. Material non-linearity is accounted for through implementation of an existing anisotropic yield condition and associated hardening rule. The von-Karman large deflection assumptions have been incorporated to model the geometric non-linearities. The structural analysis capabilities of the code have been demonstrated by successfully comparing the predictions with other experimental, analytical, and numerical results in the literature.

Impact problems have been subdivided into two groups: nonpenetrating and penetrating. In each case, appropriate contact laws are introduced to evaluate the local impact load on the structure. In nonpenetrating impact events, where there is only indentation in the targets, the Hertzian contact law has been employed to establish the impact force as a function of the local indentation. Predictions of the nonpenetrating impact response of plain and stiffened laminated composite plate and shell structures have been found to be in good agreement with

the experimental measurements previously reported from the literature. No other damage modes except indentation are considered in the nonpenetrating impact problems.

For penetrating impact events, typical of low mass projectile with high impact velocities, a contact law based on an engineering model of the local penetration mechanism has been developed and implemented in SENACS. The target deflection consists of two components. One is contributed by the global response and is calculated using the structural analysis part of the code. The other is contributed by the local response of the target and is calculated using the engineering-based penetration model developed in the thesis. The penetration model considers the following static penetration mechanisms: hole expansion, flexural deformation of a delaminated plate (split-plate), transverse plugging, and friction. It also accounts for the transitions between these mechanisms for varying geometric quantities such as size of the target and the included cone angle of projectiles with conical nose shapes. Two different material systems, IM7/8551-7 Carbon Fibre-Reinforced Polymer (CFRP) and S2-glass/phenolic resin Glass Fibre-Reinforced Polymer (GFRP) laminates provide the physical background and experimental verifications for the present model. For both GFRP and CFRP, the predicted impact energy absorption agrees fairly well with the experimental measurements.

The discrepancies in the penetration force between the model prediction and experimental measurement in some cases results from two sources.

- First, the present model does not account for coexistence of transverse plugging and delaminations (split-plate). Experimental observations show that projectiles (indenters)

with large cone angles will trigger delaminations in the laminates prior to transverse plugging. The present model predicts the delamination initiation in the laminates for small cone angle projectiles but fails to predict delaminations for large cone angle (120° and 180°) projectiles (see Figure 6.12, Figure 6.14, and Figure 7.7).

- Second, the "measured penetration force" in the ballistic tests on GFRP laminates (Figures 7.9 to 7.16) is not measured directly from the experiments. They are calculated after the experiments by double-differentiating the ELVS measured projectile displacement time history. Successive differentiation deteriorates the accuracy of the results. Therefore, the measured penetration force from these tests has more inherent scatter that has to be known in mind when they are compared with the predictions.

8.2. Conclusions

The present model provides a useful and computationally efficient tool for analyses of penetrating/non-penetrating impact and transient nonlinear structural responses of laminated composites. Through extensive numerical parametric studies and verifications on the structural and impact response of composite structures, the following conclusions can be drawn:

- The present non-linear finite element formulation based upon super elements is efficient in accurately predicting the non-linear (contact/impact load, elasto-plastic material, and large deflections) structural response of plain and stiffened composite plates and shells.

- The hole expansion mechanism, where the target material is crushed and pushed aside by a conical projectile (indenter); flexural deformation of a delaminated target (split-plate model); and transverse plugging (shear failure) are the three major penetration mechanisms that have been identified from experimental studies. These mechanisms capture the nature and essence of local deformation state and penetration damage development of composite materials. Thus they are very useful in building the present penetration model.

- The ballistic limit of composite targets predicted by the present penetration model compares very well with the experimental measurements, where the error is generally less than 10%. Whether the target is "perforated" or "not perforated" as predicted by the present model is shown to be consistent with the experimental observations. Although the same accuracy in the ballistic limit prediction has already been attained by some authors (Cantwell *et al.* 1990, Zhu *et al.* 1992b, and Sun *et al.* 1996), the ability to predict the ballistic limit for various geometric conditions of the projectile and the target (e. g., nose shape of a conical projectile, target thickness, etc.) and type of composite material (e. g., CFRP and GFRP laminate) has not been demonstrated by these models. The model presented here aims to fill this gap.

- The cone angle of a conical projectile plays a major role in whether or not it will penetrate a given target. For CFRP and GFRP laminates studied in the present thesis, a projectile with an obtuse (flat) cone angle generally dissipates less impact energy to penetrate through the laminates than that with an acute angle.

- The global response has a minimal effect on the ballistic response when a target is impacted by a low mass projectile with a very high impact velocity. The impact energy absorbed in global deformation and motion is also small in the case where a target has a small planar size.

8.3. Future Work

Although the present penetration model can represent the local impact behaviour of composite structures fairly accurately, the penetration model is still semi-empirically and based upon the experimental observations of penetration behaviour under static loading. In order to capture the dynamic characteristics of the local penetration response, further experimental investigations have to be carried out leading to model improvements. The following work is suggested for future research:

- Investigate dynamic characteristics of the present penetration mechanisms (hole expansion and flexural deflection of a split-plate) and the strain-rate effects on the derived empirical parameters (hole expansion pressure, coefficient of friction, delamination initiation stress, and transverse shear strength).

- Develop proper models to account for the local permanent deformation due to the gap (displacement discontinuity) between delaminated interfaces.

- Conduct penetration tests statically and dynamically using projectiles (or indenters) with a wide range of included cone angles (15°, 60°, 90°, and 150°) and targets with different thicknesses to verify the conclusions derived from the present penetration model.

- In the present model (see Figure 6.1), either delamination or transverse plugging initiates when a certain criterion is met. Experimental investigations found that in the case shown in Figure 5.6, the delamination and transverse plugging can coexist in the target. Therefore, there is a need to add other interacting relations between delamination and transverse plugging mechanism in order to predict the perforation in this case more accurately.

References

Abrate, S., Impact on laminated composite materials, Applied Mechanics Review, 44 (4), pp 155- 190, 1991.

Abrate, S., Impact on laminated composite materials: Recent advances, Applied Mechanics Review, 47 (11), pp 517-544, 1994.

Aoki, R. M., Damage propagation in CFRP stiffened structural elements, Proceedings of the 10th International Conference on Composite Materials, Volume I, pp. 295-302, Whistler, B. C., Canada, August 1995.

Arenburg, R. T., and Reddy, J. N., Applications of the aboudi micromechanics theory to metal matrix composites, Mechanics of Composite Materials and Structures, ASME AMD-Vol. 100, Reddy and Teply, Ed., 1989.

Ashton, J. E., and Whitney, J.M., *Theory of Laminated Plates*, Technomic Publ. Co., 1970.

Awerbuch, J., and Bodner, S. R., Analysis of the mechanics of perforation of projectiles in metallic plates, International Journal of Solids Structures, 10, pp. 671-684, 1974.

Bachrach W. E., and Hansen R. S. Mixed finite-element method for composite cylinder subjected to impact, AIAA Journal, 27 (5), pp. 632-638, 1989.

Backman, M.E., and Goldsmith, W., The mechanics of penetration of projectiles into targets, International Journal of Engineering Science, 16, pp 1-99, 1978.

Basque, D., and Aoki, R. M., Phenomenological study of impact damaged CFRP stiffened panel elements, CANCOM 93, pp. 415-424, 1993.

Blanas, A. M., Finite element modelling of fragment penetration of thin structural composite laminates, 49p, *AD-A 245 069*, December, 1991.

Bless, S. J., Hartman, D. R., Ballistic penetration of S-2 glass laminates, The 21st International SAMPE Technical Conference, September 25-28, 1989.

Brockman, R. A., Lung, F. Y., and Braisted, W. R., Probabilistic finite element analysis of dynamic structural response, *AFWAL-TR-88-2149*, pp. 100-103, 1989.

Bucci, A., and Mercurio, U., CFRP stiffened panels under compresssion, Composite Structures, 27, pp. 181-191, 1994.

Bucinell. R. B., Nuismer, R. J., and Koury, J. L., Response of composite plates to quasi-static impact events, Composite Materials: Fatigue and Fracture (Third Volume), ASTM STP 1110, T. K. O'Brien, Ed., ASTM, Philadelphia, pp. 528-549, 1991.

Cantwell, W. J., The influence of target geometry on the high velocity impact response of CFRP, Composite Structures, 10, pp. 247-265, 1988.

Cantwell, W. J., and Morton, J., Impact perforation of carbon fibre reinforced plastic, Composite Science and Technology, 38, pp. 119-141, 1990.

Chandrashekhara, K., and Schroeder, T., Nonlinear impact analysis of laminated cylindrical and doubly curved shells, Journal of Composite Materials, 29 (16), pp. 2160-2179, 1995.

Chang, F. K., and Chang, K. Y., A progressive damage model for laminated composites containnig stress concentration, Journal of Composite Materials, 21, pp. 809-855, 1987.

Chen, J. K., and Sun, C. T., Dynamic large response of composite laminates subjected to impact, Composite Structures, 4, pp. 59-73, 1985.

Christoforou, A. P., Swanson, S. R., and Beckwith, S. W., Lateral impact of composite cylinders, Composite Materials: Fatigue and Fracture (Second Volume), ASTM STP 1012, P. A. Lagace, Ed., Philadelphia, pp. 373-386, 1989.

Christoforou, A. P., and Swanson, S. R., Analysis of simply-supported orthotropic cylindrical shells subject to lateral impact loads, Journal of Applied Mechanics, Transaction of ASME 57, pp. 376-382, June 1990.

Clough, R.W., and Wilson, E.L., Dynamic finite element analysis of arbitrary thin shells, Computers & Structures, 1, pp 33 - 56, 1971.

Cook, R. D., Malkus, D. S., and Plesha, M. E., *Concepts and Applications of Finite Element Analysis*, John Wiley & Sons, pp 408, 1989.

Corbett, G. G., Reid, S. R., and Johnson, W., Impact loading of plates and shells by free-flying projectiles: A review, International Journal of Impact Engineering, 18 (2), pp. 141-230, 1996.

Crouch, I. G., and Woodward, R. L., Modelling the penetration of plates by blunt missiles, Journal De Physique, 49 (9), pp. c3 567- c3 573, September 1988.

Delfosse, D., Pageau, G., Bennett, R., and Poursartip, A., Instrumented impact testing at high velocities, Journal of Composites Technology and Research, 15 (1), pp. 38-45, 1993a.

Delfosse, D., Vaziri, R., Pierson, M.O., and Poursartip, A. Analysis of the non-penetrating impact behaviour of CFRP laminates, Proceedings of The Ninth International Conference on Composite Materials, Madrid, Spain, pp. 366-373, July 1993b.

Delfosse, D., Poursartip, A., Coxon, B. C., and Dost, E. F., Non-penetrating impact behaviour of CFRP at low and intermediate velocities, Composite Materials: Fatigue and Fracture (Fifth Volume), ASTM STP 1230, ASTM, Philadelphia, 1994a.

Delfosse, D., Experimental results from static and dynamic out-of-plane loading of laminated composite materials, contract report submitted jointly to Directorate Research And Development Land (DRDL), National Defence Head Quarters, Ottawa, and Defence Research Establishment Valcartier (DREV), Department of National Defence, 1994b.

Dobyns, A. L., Analysis of simply-supported orthotropic plates subject to static and dynamic loads, AIAA Journal, 19 (5), pp. 642-650, May 1981.

Dost, E.F., Avery, W. B., Ilcewicz, L. B., Grande, D. H., and Coxon, B. R., Impact damage resistance of composite fuselage structures, Part I, Proc. 9th DOD/NASA/FAA Conf. on Fibrous Composites in Structural Design, FAA Publication, 1991.

Goldsmith, W. and Finnegan S. A., Normal and oblique impact of cylindro-conical and cylindrical projectiles on metallic plates. International Journal of Impact Engineering, 4 (2), pp. 83-105, 1986.

Goldsmith, W., Dharan, C. K. H., and Chang, H., Quasi-static and ballistic perforation of carbon fiber laminates, International Journal of Solids Structures, 32 (1), pp 89-103, 1995.

Gong, S. W., Toh, S. L., and Shim, V. P. W., The elastic response of orthotropic laminated cylindrical shells to low velocity impact, Composite Engineering, 4 (2), pp. 247-266, 1994.

Gong, S. W., Shim, V. P. W., and Toh, S. L., Impact response of laminated shells with orthogonal curvatures, Composite Engineering, 5 (3), pp. 257-275, 1995.

Goswami, S., and Mukhopadhyay, M., Finite element analysis of laminated composite stiffened shell, Journal of Reinforced Plastics and Composites, 13, pp. 574-616, July 1994.

Greaves, L. J., Failure mechanisms in glass fibre reinforced plastic armour, Memorandum 12/92, *Chertsey Memorandum 92003*, Defence Research Agency, Military Division, RARDE Chertsey, UK R0001001, December 1992.

Greaves, L. J., Through-thickness compression and tensile tests on an E-glass/polyester composites, *DRA/FV&S/FV&S7/TR93001/1.0*, 37p, December 1993.

Hearmon, R.F.S., On the transverse vibrations of rectangular orthotropic plates, Journal of Applied Mechanics, 25 (2), pp 307-309, June 1959.

Hill, R., *Plasticity*, Clarendon Press, Oxford, pp 307, 1950.

Hills, D.A., Nowell, D., and Sackfield, A., *Mechanics of Elastic Contacts*, Butterworth & Heinemann, 1992.

Howlett, S., and Greaves, L., The penetration behaviour of glass fibre reinforced plastic materials, Proceedings of the 10th International Conference on Composite Materials, Volume V, Whistler, BC, Canada, pp 727-734, August 1995.

Huffington, Jr., N. J., Authors Closure to "Comments on 'On the Transverse Vibrations of Rectangular Orthotropic Plates' ", Journal of Applied Mechanics, 25 (2), pp 308, June 1959.

Jackson, W. C., Impact damage resistance of textile composites, The 28th International SAMPE Technical Conference, Seattle, WA, USA, November 4-7, 1996.

Jiang, J., and Olson, M. D., Nonlinear dynamic analysis of blast loaded cylindrical shell structures, Computers & Structures, 41 (1), pp. 41-52, 1991.

Jiang, J., and Olson, M. D., A super finite element model for large deflection elastoplastic analysis of stiffened cylindrical shell structures, Structural Engineering Review, 5 (3), pp. 219-229, 1993.

Johnson, K. L., The correlation of indentation experiments, Journal of Mechanics Physics Solids, 18, pp. 115-126, 1970.

Johnson, W., *Impact Strength of Materials*, Edward Arnold, 1972.

Johnson, W., Chitkara, N.R., Ibrahim, A.H., Dasgupta, A.K., Hole flanging and punching of circular plates with conically headed cylindrical punches, Journal of Strain Analysis, 8 (3), pp. 228-241, 1973.

Johnson, W., Ghosh, S.K., Mamalis, A.G., Reddy, T.Y., and Reid, S.R., The quasi-static piercing of cylindrical tubes or shells, International Journal of Mechanical Science, 22, pp. 9-20, 1980.

Koko, T. S., and Olson, M. D., Non-linear analysis of stiffened plates using super elements, International Journal For Numerical Methods in Engineering, 31, pp 319-343, 1991a.

Koko, T. S., and Olson, M. D., Nonlinear transient response of stiffened plates to air blast loading by a super element approach, Computer Methods in Applied Mechanics and Engineering, 90, pp 737-760, 1991b.

Koko, T. S., and Olson, M. D., Vibration analysis of stiffened by super elements, Journal of Sound and Vibration, 151 (1), pp 149-167, 1992.

Landkof, B., and Goldsmith, W., Petalling of thin, metallic plates during penetration by cylindro-conical projectiles, International Journal of Solids Structures, 21 (3), pp 245-266, 1985.

Langseth, M., and Larsen, P. K., Dropped objects' plugging capacity of steel plates: an experimental investigation, International Journal of Impact Engineering, 9 (3), pp. 289-316, 1990.

Lau, W., Determination of E_1^f and G_{13}, for AS4/3501-6 and IM7/8551-7 specimens using 3-point bending tests, interim report in *Composites Group, Department of Metals and Materials Engineering, The University of British Columbia*, December, 1997.

Lee, L. J., Huang, K. Y., Hwang, D. G., and Pai, C. K., Geometrical nonlinear analysis of composite cylindrical shell panels subjected to impact, Finite Elements in Analysis and Design, 15, pp 135-149, 1993.

Lee, S.-W. R., and Sun, C. T., Dynamic penetration of graphite/epoxy laminates impacted by a blunt-ended projectile, Composite Science and Technology, 49, pp. 369-380, 1993a.

Lee, S.-W. R., and Sun, C. T., A quasi-static penetration model for composite laminates, Journal of Composite Materials, 27 (3), 251, 1993b.

Liss, J., and Goldsmith, W., Plate perforation phenomena due to normal impact by blunt cylinders, International Journal of Impact Engineering, 2 (1), pp. 37-64, 1984.

Lu, P. F., and Vaziri, R., A review of constitutive and failure models for numerical analysis of the impact response of composite materials. Contract Report submitted to Defence

Research Establishment Valcartier (DREV), Department of National Defence, Canada, February 1994.

Madan, R. C., Influence of low-velocity impact on composite structures, Composite Materials: Fatigue and Fracture (Third Volume), ASTM STP 1110, T. K. O'Brien, Ed., Philadelphia, pp. 457-475, 1991.

Madan, R. C., and Shuart, M. J., Impact damage and residual strength analysis of composite panels with bonded stiffeners, Composite Materials: Testing and Design (Ninth Volume), ASTM STP 1059, S. P. Garbo Ed., Philadelphia, pp. 64-85, 1990.

Malvern, L., Sun, C. T., and Liu, D., Delamination damage in central impacts at subperforation speeds on laminated Kevlar/Epoxy plates, Composite Materials: Fatigue and Fracture, 2nd volume, ASTM STP 1012, P. A. Lagace, Ed., Philadelphia, pp. 387-405, 1989.

Matsuhashi, H., Graves, M. J., Dugundji, J., and Lagace, P. A., Effect of membrane stiffening in transient impact analysis of laminated composite plates, AIAA-93-1611-CP, 1993.

Matzenmiller, A., Lubliner, J., and Taylor, R. L., An Anisotropic damage model for fiber-composites. *Report UCB-SEMM-91/09*, Department of Civil Engineering, University of California at Berkeley, Berkeley, CA, 1991.

Montermurro, M. P., Hansen, J. S., and Houde, M. J. L., Finite element analysis of the impact response of composite plates and shells, Proceedings of The 10th International Conference on Composite Materials: Volume V, pp. 639-644, 1995.

Navarro, C., Rodriguez, J., and Cortes, R., Analytical modelling of composite panels subjected to impact loading, Journal De Physique IV, Colloque C8, supplement au journal de Physique III, 4, pp. C8-515 - 520, September 1994.

Newmark, N. M., A method of computation for structural dynamics, Journal of Engineering Mechanics Division, Proc. of ASCE., pp 67-94, July 1959.

Ochoa, O. O., and Reddy, J. N., *Finite Element Analysis of Composite Laminates*, Kluwer Academic Publishers, 1992.

Olson, M. D. , Efficient modelling of blast loaded stiffened plate and cylindrical shell structures, Computers & Structures, 40 (5), pp 1139-1149, 1991.

Owen, D.R.J., and Figueiras, J.A., Anisotropic elasto-plastic finite element analysis of thick and thin plates and shells, International Journal for Numerical Methods in Engineering, 19, pp 541-566, 1983.

Pagano, N.J., Exact solutions for rectangular bidirectional composites and sandwich plates, Journal of Composite Materials, 4, pp 20-34, January 1970.

Pierson, M. O., Delfosse, D., Vaziri, R., and Poursartip, A., Penetration of laminated composite plates due to impact, Ballistics 93, 1993.

Pierson, M. O., and Vaziri, R., Analytical solution for low-velocity impact response of composite plates, AIAA Journal, 34 (10), October 1996.

Potti, S. V., and Sun, C. T., Prediction of impacted induced penetration and delamination in thick composite laminates, International Journal of Impact Engineering, 19 (1), pp. 31-48, 1997.

Qian, Y., and Swanson, S. R., A comparison of solution techniques for impact response of composite plates, Composite Structures, 14, pp. 177-192, 1990.

Quan, X., Vaziri, R., Ursenbach, D., and Delfosse, D., A simple analytical approach for analysis of laminated plates with partial delamination, The 28th International SAMPE Technical Conference, pp 163-176, Seattle, Washington, November 4-7, 1996.

Rahman, S., and Pecknold, D. A., Micromechanics-based analysis of fiber-reinforced laminated composites, Department of Civil Engineering, University of Illinois at Urbana-Champaign, September 1992.

Ramkumar, R. L., and Thakar, Y. R., Dynamic response of curved laminated plates subjected to low velocity impact, Journal of Engineering Materials and Technology, Transactions of ASME, 109, pp. 67-71, 1987.

Razi, H., and Kobayashi, A. S., Delamination in cross-ply laminated composite subjected to low-velocity impact, AIAA Journal, 31 (8), pp. 1498, 1993.

Recht, R. F., and Ipson, T. W., Ballistic perforation dynamics, Journal of Applied Mechanics, Transactions of the ASME, pp. 384-390, September 1963.

Rudrapatna, N., Olson, M. D., and Vaziri, R., Numerical simulation of tearing and rupture of thin square plates under blast loading, Symposium on Structures Response under Impact and Blast (SRIB), Israel, Oct. 6-13, 1996.

Saigal, S., Kapania, R. K., and Yang, T. Y., Geometrically nonlinear finite element analysis of imperfect laminated shells, Journal of Composite Material, 20, pp. 197-214, 1986.

Sanders, T., Penetration of composite laminates by conical indenters and projectiles, Master Thesis, Department of Civil Engineering, The University of British Columbia, Vancouver, BC, Canada, 1997.

Scott, M. L., and Rees, D. A. Analysis and test of thin integrally stiffened fibre composite panels, 10th International Conference on Composite Materials, Volume V, pp. 117-124, Whistler, B. C., Canada, August 1995.

Starratt, D., Sanders, T., Cepuš, E., Poursartip, A., and Vaziri, R., An efficient method for continuous measurement of projectile motion in ballistic impact experiments, Submitted to International Journal of Impact Engineering, 1998.

Sun, C. T., and Chattopadhyay, S., Dynamic response of anisotropic laminated plates under initial stresses to impact of mass, Journal of Applied Mechanics, Transaction of ASME, 42, pp. 693-698, September 1975.

Sun, C. T., and Chen, J. K., On the impact of initially stressed composite laminates, Journal of Composite Materials, 19, pp. 490-504, November 1985.

Sun, C. T., and Potti, S. V., A simple model to predict residual velocities of thick composite laminates subjected to high velocity impact, International Journal of Impact Engineering, 18 (3), pp. 339-353, 1996.

Tabor, D., *The hardness of metals*, Oxford, 1951.

Tan, T. M., and Sun, C. T., Use of statical indentation laws in the impact analysis of laminated composite plates, Journal of Applied Mechanics, Transaction of ASME, 52 (6), pp. 6-12, 1985.

Taylor, G. I., The formation and enlargement of a circular hole in a thin plastic sheet, Quarterly Journal of Mechanics and Applied Mathematics, 1, pp 103-124, 1948.

Thomson, W. T., An approximate theory of armor penetration, Journal of Applied Physics, 26 (1), pp 80-82, 1955.

Timoshenko, S., and Woinowsky-Krieger, *Theory of Plates and Shells, 2nd Edition*, McGraw-Hill Book Company, 1959.

Tsai, C. T., and Palazotto, A. N., On the finite element analysis of non-linear vibration for cylindrical shells with high-order shear deformation theory, International Journal of Non-Linear Mechanics, 26 (3/4), pp 379-388, 1991.

Ursenbach, D. O., Vaziri, R., and Delfosse, D., An engineering model for deformation of CFRP plates during penetration. The 8th International Conference on Composite Structures, University of Paisley, Paisley, Scotland, September 11-13th, 1995.

Varizi, R., Olson, M. D., and Anderson, D. L., Finite Element Analysis of Fibrous Composite Structures: A Plasticity Approach, Computers & Structures, 44 (1/2), pp 103-116, 1992.

Vaziri, R., Pageau, G, and Poursartip, A, Review of computer codes for penetration modelling of metal matrix composite materials, *Technical Report, Department of Metals and Materials Engineering, University of British Columbia*, 1989.

Vaziri, R., Quan, X., and Olson, M.D., Impact analysis of laminated composite plates and shells by super finite elements, International Journal of Impact Engineering, 18 (7/8), pp 765-782, October/December 1996.

Venkatesh, A., and Rao, K. P., Analysis of laminated shells with laminated stiffeners using rectangular shell finite elements, Computer Methods in Applied Mechanics and Engineering, 38, pp. 255-272, 1983.

Venkatesh, A., and Rao, K. P., Analysis of laminated shells of revolution with laminated stiffeners using a doubly curved quadrilateral finite element, Computers & Structures, 20 (4), pp. 669-682, 1985.

Virostek, S. P., Dual, J., and Goldsmith, W., Direct force measurement in normal and oblique impact of plates by projectiles, International Journal of Impact Engineering, 6 (4), pp. 247-269, 1987.

Whitney, J.M., *Structural Analysis of Laminated Anisotropic Plates*, Technomic Publ. Co., 1987.

Whitney, J. M., and Pagano, N. J., Shear deformation in heterogeneous anisotropic plates, Journal of Applied Mechanics, 92, pp. 1031-1036, 1970.

Williams, K., and Vaziri, R., Finite element analysis of the impact response of CFRP composite plates, Proceedings of 10th International Conference on Composite Materials, Whistler, BC, Canada, pp. 647-654, August 1995.

Williams, K., A physically-based continuum damage mechanics model for numerical prediction of damage growth in laminated composite plates, PhD Thesis, Composites Group, Depts. of Metals and Materials Engineering and Civil Engineering, The University of British Columbia, Vancouver, BC, Canada, 1998.

Woodward, R. L., The penetration of metal targets by conical projectiles, International Journal of Mechanical Sciences, 20, pp. 349-359, 1978a.

Woodward, R. L., The penetration of metal targets which fail by adiabatic shear plugging, International Journal of Mechanical Sciences, 20, pp. 599-607, 1978b.

Woodward, R. L., The interrelation of failure modes observed in the penetration of metallic targets, International Journal of Impact Engineering, 2 (2), pp 121-129, 1984.

Woodward, R. L., and Cimpoeru, S. J., A study of the perforation of aluminum laminate targets, accepted for publication in International Journal of Impact Engineering, 1997.

Woodward, R. L., Egglestone, G. T., Baxter, B. J., and Challis, K., Resistance to penetration and compression of fibre-reinforced composite materials, Composites Engineering, 4 (3), pp. 329-341, 1994.

Wu, E., and Chang, L.-C., Woven glass/epoxy laminates subject to projectile impact, International Journal of Impact Engineering, 16 (4), pp. 607-619, 1995.

Wu, E., Tsai, C.-Z., and Chen, Y.-C., Penetration into glass/epoxy composite laminates. Journal of Composite Materials, 28 (18), pp. 1783-1802, 1994.

Zaghloul, S. A., and Kennedy, J. B., Nonlinear behavior of symmetrically laminated plates. Journal of Composite Materials, Transaction of the ASME, 4, pp. 234-236, 1975.

Zaid, M., and Paul, B. Mechanics of high speed projectile perforation, J. F. L., pp. 117-126, 1957.

Zhu, G., Goldsmith, W., and Dharan, C. K. H., Penetration of laminated Kevlar by Projectiles-I: Experimental Investigation, International Journal of Solids Structures, 29 (4), pp. 421-436, 1992a.

Zhu, G., Goldsmith, W., and Dharan, C. K. H., Penetration of laminated Kevlar by Projectiles-II: Analytical model, International Journal of Solids Structures, 29 (4), pp. 421-436, 1992b.

Zukas, J. A., Nicholas, T., Swift, H. F., Greszczuk, L. B., and Curren, D.R., *Impact Dynamics*, John Wiley & Sons, 1982.

Appendix A: Shape Functions for Super Shell and Beam Elements

A.1 Super Shell Element

The matrix of shape functions for a super shell element, which is denoted as $[N]$ in Equation (2.1), is given by

$$
[N]=\begin{bmatrix}
N_1^u & 0 & 0 & N_2^u & 0 & 0 & 0 & 0 & N_3^u & 0 \\
0 & N_1^v & 0 & 0 & N_2^v & 0 & 0 & 0 & 0 & N_3^v \\
0 & 0 & N_1^w & 0 & 0 & N_2^w & N_3^w & N_4^w & 0 & 0
\end{bmatrix}
$$

$$
\begin{bmatrix}
0 & N_4^u & 0 & 0 & 0 & 0 & N_5^u & 0 & 0 & N_6^u \\
0 & 0 & N_4^v & 0 & 0 & 0 & 0 & N_5^v & 0 & 0 \\
N_5^w & 0 & 0 & N_6^w & N_7^w & N_8^w & 0 & 0 & N_9^w & 0
\end{bmatrix}
$$

$$
\begin{bmatrix}
0 & 0 & 0 & 0 & N_7^u & 0 & 0 & N_8^u & 0 & 0 \\
N_6^v & 0 & 0 & 0 & 0 & N_7^v & 0 & 0 & N_8^v & 0 \\
0 & N_{10}^w & N_{11}^w & N_{12}^w & 0 & 0 & N_{13}^w & 0 & 0 & N_{14}^w
\end{bmatrix}
$$

$$
\begin{bmatrix}
0 & 0 & N_9^u & 0 & 0 & N_{12}^u & N_{15}^u & 0 & 0 & 0 \\
0 & 0 & 0 & 0 & 0 & 0 & 0 & N_9^v & 0 & 0 \\
N_{15}^w & N_{16}^w & 0 & N_{17}^w & N_{18}^w & 0 & 0 & 0 & N_{19}^w & N_{20}^w
\end{bmatrix}
$$

$$
\begin{bmatrix}
0 & 0 & N_{10}^u & 0 & 0 & N_{13}^u & N_{16}^u & 0 & 0 & 0 \\
N_{13}^v & N_{16}^v & 0 & 0 & 0 & 0 & 0 & N_{10}^v & 0 & 0 \\
0 & 0 & 0 & N_{21}^w & N_{22}^w & 0 & 0 & 0 & N_{23}^w & N_{24}^w
\end{bmatrix}
$$

$$
\begin{bmatrix}
0 & 0 & N_{11}^u & 0 & 0 & N_{14}^u & 0 & N_{17}^u & 0 \\
N_{12}^v & N_{15}^v & 0 & N_{11}^v & 0 & 0 & N_{14}^v & 0 & N_{17}^v \\
0 & 0 & 0 & 0 & N_{25}^w & 0 & 0 & 0 & 0
\end{bmatrix}
\tag{A.1}
$$

The element nodal variable vector $\{\delta_e\}$ is defined as

$$\begin{aligned}\{\delta_e\}^T = \{ & u_1 \quad v_1 \quad w_1 \quad u_{,y1} \quad v_{,x1} \quad w_{,x1} \quad w_{,y1} \quad w_{,xy1} \quad u_2 \quad v_2 \\ & w_2 \quad u_{,y2} \quad v_{,x2} \quad w_{,x2} \quad w_{,y2} \quad w_{,xy2} \quad u_3 \quad v_3 \quad w_3 \quad u_{,y3} \\ & v_{,x3} \quad w_{,x3} \quad w_{,y3} \quad w_{,xy3} \quad u_4 \quad v_4 \quad w_4 \quad u_{,y4} \quad v_{,x4} \quad w_{,x4} \\ & w_{,y4} \quad w_{,xy4} \quad u_5 \quad w_5 \quad w_{,y5} \quad u_8 \quad u_{11} \quad v_5 \quad w_6 \quad w_{,x6} \\ & v_9 \quad v_{12} \quad u_6 \quad w_7 \quad w_{,y7} \quad u_9 \quad u_{12} \quad v_6 \quad w_8 \quad w_{,x8} \\ & v_8 \quad v_{11} \quad u_7 \quad v_7 \quad w_9 \quad u_{10} \quad v_{10} \quad u_{13} \quad v_{13} \quad \}\end{aligned} \tag{A.2}$$

The shape functions N_i^u, N_i^v, and N_j^w in Equation (A.1) are explicitly given by

$$\begin{aligned}
&N_1^u = L_1(\xi)H_1(\eta) \qquad N_2^u = L_1(\xi)H_2(\eta) \qquad N_3^u = L_2(\xi)H_1(\eta) \\
&N_4^u = L_2(\xi)H_2(\eta) \qquad N_5^u = L_2(\xi)H_3(\eta) \qquad N_6^u = L_2(\xi)H_4(\eta) \\
&N_7^u = L_1(\xi)H_3(\eta) \qquad N_8^u = L_1(\xi)H_4(\eta) \qquad N_9^u = L_3(\xi)L_1(\eta) \\
&N_{10}^u = L_3(\xi)L_2(\eta) \qquad N_{11}^u = L_3(\xi)L_3(\eta) \qquad N_{12}^u = \sin(2\pi\xi)L_1(\eta) \\
&N_{13}^u = \sin(2\pi\xi)L_2(\eta) \qquad N_{14}^u = \sin(2\pi\xi)L_3(\eta) \qquad N_{15}^u = \sin(4\pi\xi)L_1(\eta) \\
&N_{16}^u = \sin(4\pi\xi)L_2(\eta) \qquad N_{17}^u = \sin(4\pi\xi)L_3(\eta)
\end{aligned} \tag{A.3}$$

$$\begin{aligned}
&N_1^v = H_1(\xi)L_1(\eta) \qquad N_2^v = H_2(\xi)L_1(\eta) \qquad N_3^v = H_3(\xi)L_1(\eta) \\
&N_4^v = H_4(\xi)L_1(\eta) \qquad N_5^v = H_3(\xi)L_2(\eta) \qquad N_6^v = H_4(\xi)L_2(\eta) \\
&N_7^v = H_1(\xi)L_2(\eta) \qquad N_8^v = H_2(\xi)L_2(\eta) \qquad N_9^v = L_2(\xi)L_3(\eta) \\
&N_{10}^v = L_1(\xi)L_3(\eta) \qquad N_{11}^v = L_3(\xi)L_3(\eta) \qquad N_{12}^v = L_1(\xi)\sin(2\pi\eta) \\
&N_{13}^v = L_2(\xi)\sin(2\pi\eta) \qquad N_{14}^v = L_3(\xi)\sin(2\pi\eta) \qquad N_{15}^v = L_1(\xi)\sin(4\pi\eta) \\
&N_{16}^v = L_2(\xi)\sin(4\pi\eta) \qquad N_{17}^v = L_3(\xi)\sin(4\pi\eta)
\end{aligned} \tag{A.4}$$

$$N_1^w = H_1(\xi)H_1(\eta) \qquad N_2^w = H_2(\xi)H_1(\eta) \qquad N_3^w = H_1(\xi)H_2(\eta)$$

$$
\begin{aligned}
&N_4^w = H_2(\xi)H_2(\eta) \qquad N_5^w = H_3(\xi)H_1(\eta) \qquad N_6^w = H_4(\xi)H_1(\eta)\\
&N_7^w = H_3(\xi)H_2(\eta) \qquad N_8^w = H_4(\xi)H_2(\eta) \qquad N_9^w = H_3(\xi)H_3(\eta)\\
&N_{10}^w = H_4(\xi)H_3(\eta) \qquad N_{11}^w = H_3(\xi)H_4(\eta) \qquad N_{12}^w = H_4(\xi)H_4(\eta)\\
&N_{13}^w = H_1(\xi)H_3(\eta) \qquad N_{14}^w = H_2(\xi)H_3(\eta) \qquad N_{15}^w = H_1(\xi)H_4(\eta)\\
&N_{16}^w = H_2(\xi)H_4(\eta) \qquad N_{17}^w = \phi(\xi)H_1(\eta) \qquad N_{18}^w = \phi(\xi)H_2(\eta)\\
&N_{19}^w = H_3(\xi)\phi(\eta) \qquad N_{20}^w = H_4(\xi)\phi(\eta) \qquad N_{21}^w = \phi(\xi)H_3(\eta)\\
&N_{22}^w = \phi(\xi)H_4(\eta) \qquad N_{23}^w = H_1(\xi)\phi(\eta) \qquad N_{24}^w = H_2(\xi)\phi(\eta)\\
&N_{25}^w = \phi(\xi)\phi(\eta)
\end{aligned}
\tag{A.5}
$$

The quadratic Lagrange polynomials are

$$
L_1(\xi) = 2\xi^2 - 3\xi + 1 \qquad L_2(\xi) = 2\xi^2 - \xi \qquad L_3(\xi) = 4(\xi - \xi^2) \tag{A.6}
$$

The cubic Hermitian polynomials are

$$
\begin{aligned}
&H_1(\xi) = 1 - 3\xi^2 + 2\xi^3 \qquad H_2(\xi) = a(\xi - 2\xi^2 + \xi^3)\\
&H_3(\xi) = 3\xi^2 - 2\xi^3 \qquad H_4(\xi) = a(-\xi^2 + \xi^3)
\end{aligned}
\tag{A.7}
$$

The ϕ function is given by

$$
\phi(\xi) = \frac{\alpha(\sinh\beta\xi - \sin\beta\xi) + (\cosh\beta\xi - \cos\beta\xi)}{A_\phi} \tag{A.8}
$$

where

$$
A_\phi = \alpha(\sinh\frac{\beta}{2} - \sin\frac{\beta}{2}) + (\cosh\frac{\beta}{2} - \cos\frac{\beta}{2})
$$

$$
\alpha = \frac{\cos\beta - \cosh\beta}{\sinh\beta - \sin\beta} \quad \text{and} \quad \beta = 4.7300407448
$$

A.2 Super Beam Element

The matrix of shape functions for a super shell element, which is denoted as $[\overline{N}]$ in Equation (2.2), is given by

$$[\overline{N}]=\begin{bmatrix} L_1(\xi) & 0 & eH_1'(\xi) & 0 & eH_2'(\xi) & 0 & 0 \\ 0 & 0 & H_1(\xi) & 0 & H_2(\xi) & 0 & 0 \\ 0 & 0 & 0 & 0 & 0 & H_1(\xi) & H_2(\xi) \\ 0 & H_1(\xi) & 0 & H_2(\xi) & 0 & eH_1(\xi) & eH_2(\xi) \end{bmatrix}$$

$$\begin{matrix} L_2(\xi) & 0 & eH_3'(\xi) & 0 & eH_4'(\xi) & 0 & 0 \\ 0 & 0 & H_3(\xi) & 0 & H_4(\xi) & 0 & 0 \\ 0 & 0 & 0 & 0 & 0 & H_3(\xi) & H_4(\xi) \\ 0 & H_3(\xi) & 0 & H_4(\xi) & 0 & eH_3(\xi) & eH_4(\xi) \end{matrix} \qquad \text{(A.9)}$$

$$\begin{bmatrix} L_3(\xi) & e\phi'(\xi) & 0 & \sin 2\pi\xi & \sin 4\pi\xi \\ 0 & \phi(\xi) & 0 & 0 & 0 \\ 0 & 0 & \phi(\xi) & 0 & 0 \\ 0 & 0 & e\phi(\xi) & 0 & 0 \end{bmatrix}$$

The element nodal variable vector $\{\overline{\delta}_e\}$ is defined as

$$\{\overline{\delta}_e\}^T = \{u_1 \quad v_1 \quad w_1 \quad v_{,x1} \quad w_{,x1} \quad \theta_1 \quad \theta_{,x1} \quad u_2 \quad v_2 \quad w_2 \quad v_{,x2} \quad w_{,x2} \quad \theta_2 \quad \theta_{,x2} \quad u_3 \quad w_3 \quad \theta_3 \quad u_4 \quad u_5 \}$$ (A.10)

Appendix B: Elastic and Plastic Constitutive Matrices

The elastic constitutive matrix is written in the following form (Vaziri *et al.*, 1992)

$$[Q_e]=\begin{bmatrix} \dfrac{E_1}{1-\nu_{12}\nu_{21}} & \dfrac{\nu_{21}E_1}{1-\nu_{12}\nu_{21}} & 0 \\ \dfrac{\nu_{21}E_1}{1-\nu_{12}\nu_{21}} & \dfrac{E_2}{1-\nu_{12}\nu_{21}} & 0 \\ 0 & 0 & G \end{bmatrix} \tag{B.1}$$

where E_1 and E_2 are the elastic moduli of the lamina in the longitudinal and lateral directions; ν_{12} and ν_{21} are the major and minor Poisson's ratios of the lamina, G is the elastic in-plane shear modulus.

The constitutive matrices for anisotropic yielding and hardening is written in the following form (Vaziri *et al.*, 1992)

$$[Q_p]=\frac{[Q_e]\{a\}\{a\}^T[Q_e]}{\mu_y H'+\{a\}^T[Q_e]\{a\}} \tag{B.2}$$

Where $\{a\}$ is the plastic flow vector defined by

$$a_i=\frac{1}{k_y}A_{ij}\sigma_j,\ i,j=1,2,6; \tag{B.3}$$

μ_y is an anisotropy parameter ($\mu_y=1$ for isotropic yielding and hardening) defined as

$$\mu_y=1-\frac{1}{2k_y}\{\sigma\}^T\left[\frac{\partial A}{\partial k_y}\right]\{\sigma\} \tag{B.4}$$

Appendix C: Numerical Verifications and Structural Applications of SENACS

In this Appendix, the super finite element method and the associated computer program, SENACS, will be verified by comparing its results with available experimental, analytical, and other numerical results in the literature. At the same time, some numerical applications will be presented for future reference. These examples cover static, eigenvalue, and transient problems involving linear and non-linear geometries as well as elastic and elasto-plastic analysis of laminated composite structures.

C.1. Static Problems

C.1.1 Small Deflection, Linear-Elastic Analysis

C.1.1.1 Laminated square plate under sinusoidally-distributed pressure load

This is a typical example for elastic laminated composite plates subjected to lateral loading, which has been used extensively to verify a theoretical formulation and computer program. Consider a simply-supported graphite/epoxy laminated plate with a lay-up of [0/90/0] under transverse sinusoidal pressure load

$$q(x,y) = q_0 \sin(\frac{\pi x}{a}) \sin(\frac{\pi y}{b})$$

The material constants are

$$E_{11} = 25\,E_{22},\quad G_{12} = 0.5\,E_{22},\quad \nu_{12} = 0.25,\quad E_{22} = 10^6 \text{ psi}.$$

The ratio of side length to panel thickness is $\frac{a}{h} = 100$. The comparison of present results with finite element and analytical results in Ochoa *et al.* (1992), and exact solutions in Pagano (1970) for a square plate ($a = b$) and a rectangular plate ($b = 3a$) are shown in Table C.1 and Table C.2, respectively, where the non-dimensional central deflection and stress components are defined as

$$\overline{w} = \frac{100 E_2 w h^3}{q_0 a^4}$$

$$(\overline{\sigma}_x, \overline{\sigma}_y, \overline{\tau}_{xy}) = 10h^2 \frac{(\sigma_x, \sigma_y, \tau_{xy})}{q_0 a^2}$$

In the present formulation, one shell super element is used to model the whole plate. The element mesh used in Ochoa *et al.* (1992) was 2×2 and 6×6 QHD40 elements (an eight-node quadrilateral plate element with 40 degrees of freedom) for a quarter plate. The analytical solutions were obtained by using the elasticity theory [Pagano (1970)] and classical lamination plate theory (CLPT) [Ochoa *et al.* (1992)]. The results in Table C.1 and Table C.2 show that the super element converges more quickly than QHD40. One super shell element solution is in good agreement with analytical solutions, and numerical results by Ochoa *et al.* using 4×4 or 12×12 QHD40 elements.

C.1.1.2 Laminated stiffened cylindrical shell panel under a point load

This example concerns the static analysis of a glass/epoxy stiffened cylindrical shell, which was first presented by Venkatesh *et al.* (1983) and then verified by Venkatesh *et al.* (1985) and Goswani *et al.* (1994). A layered cantilevered cylindrical shell panel reinforced with eccentrically mounted layered stiffeners is loaded by a single concentrated force at one of its free corners as shown in Figure C.1. The material properties, geometric sizes, and lay-ups are given in Table C.3. Table C.4 shows a comparison between the present results and those obtained by Venkatesh *et al.* (1983), Venkatesh *et al.* (1985), and Goswani *et al.* (1994). The present mesh consists of 2×3 (axial×circumferential) elements for the whole shell panel.

C.1.2 Large Deflection, Linear-Elastic Analysis

C.1.2.1 Laminated square plate under uniformly-distributed pressure load

Present results are also compared with experimental data and numerical results for laminated square plates with lay-ups of [0] and [0/90/90/0] in linear-elastic and large deflection analysis. The geometric sizes and material properties are shown in Table C.5.

Comparing the load-deflection curves shown in Figure C.2 for a simply-supported square plate, it is evident that present analysis with moveable boundary ($u_{,y} \neq 0$ along the edge perpendicular to x-axis and $v_{,x} \neq 0$ along the edge perpendicular to y-axis) is closer to the experimental data much more than that with immoveable boundary ($u_{,y} = 0$ and $v_{,x} = 0$ on those edges). This is because the experimental set-up generally cannot produce fully immoveable boundary as assumed in the finite element analysis.

From the comparison of load-deflection relationship for a fully-clamped plate as shown in Figure C.3, the present results, although not in good agreement with the experimental data, are very close to the finite element predictions by Ochoa *et al.* (1992). This is also attributed to the improper finite element representation of the actual boundary conditions in the experiment. As we expected, present results are on the stiff side of Ochoa *et al.* (1992)'s which take into account the transverse shear deformations.

The same phenomenon occurred in Matsuhashi *et al.* (1993) when comparing the impact response of a clamped laminated composite plate using Rayleigh-Ritz method with experimental results. A geometrical non-linear factor β was applied to the large deflection term due to in-plane displacements in the system of equations of motion, where $\beta = 0$ represents a clamped-perfectly sliding boundary condition and $\beta = 1$ is equivalent to a clamped-fixed boundary condition. It was found from Matsuhashi *et al.* (1993)'s study that $\beta = 0.05$ would give closer results to the experiments. Putting $\beta = 1$, which is equivalent to the boundary condition used in the present analysis, over-predicts the peak impact force and under-predicts the impact duration.

C.1.2.2 Laminated composite cylindrical shell panel under a point load

A composite cylindrical shell panel with a $[0_4/90_4/0_4]$ lay-up is considered here. The geometric conditions and material constants are shown in Table C.6. This shell panel is subjected to a radially-directed point load P at the centre of the panel. The super element mesh is 2×4 for the whole panel, where 2 elements are arranged along the axial direction and 4 elements along the circumferential direction.

The present results are successfully compared in Table C.5 with finite element solutions by Lee *et al.*'s (1993) which account for the transverse shear deformation and Saigal *et al.*' (1986) which are based on CLPT. Because the shell panel is hinged along two straight edges and free on two curved edges, compressive deformation will occur around the panel centre if a point force is applied there. The panel will buckle when the force is increased to its critical buckling load. In the present case, when the load level approaches 1.1 kN, the number of iterations in the analysis increases significantly first and then the solution diverges due to the buckling of the shell.

C.1.3 Small Deflection, Elasto-Plastic Analysis

C.1.3.1 Boron/Aluminium plate under uniformly-distributed pressure load

This example is concerned with a simply-supported orthotropic square plate which was analysed by Arenburg *et al.* (1989) and Rahman *et al.* (1992) using micro-mechanics based models. The material constants are shown in Table C.7. The plate dimensions are $a = 0.254$ *m*, and $h = 2.54$ *mm*. The mesh used in SENACS consists of 2×2 elements for a quarter plate

and the results agree very well with micro-mechanics models as shown in Figure C.6. In the micro-mechanics analysis by Rahman *et al.* (1992), 6×6×2 elements were used for a quarter plate, where 2 elements are arranged through the plate thickness.

C.1.3.2 Laminated plate under a uniformly-distributed pressure load, elasto-plastic analysis

This example is adopted from Owen *et al.* (1983) where elasto-plastic analysis of an orthotropic plate was undertaken by using the finite element method accounting for transverse shear deformation. The material constants and geometric conditions are shown in Table C.8.

A comparison between the present results and numerical results of Owen *et al.* is shown in Figure C.7 on a plot of the non-dimensional central deflection of the plate, $\frac{100D}{M_p a^2} w_0$, versus the non-dimensional external load, $\frac{a^2}{10 M_p} q$, for both isotropic and anisotropic cases, where M_p denotes the plastic bending moment on the cross-section per unit length (MN·m/m), D denotes the plate's bending rigidity, and q is the transverse pressure load (MPa). For the isotropic material considered by Owen *et al.* (1983), the present analysis using only one element for a quarter plate can almost represent the same results obtained by Owen *et al.* in 3×3 element mesh for a quarter plate.

For the anisotropic case, the load-deflection relationship for the present analysis using 3×3 elements for a quarter plate are in good agreement with that obtained by Owen *et al.* as shown in Figure C.7. The values used by Owen *et al.* for the yield stresses are given in Table C.8.

C.1.3.3 Laminated plate under a uniformly-distributed pressure load, elasto-plastic analysis with either anisotropic or isotropic hardening

This is the same example except that the plastic tangent modulus or initial yield stress are raised in the 1-direction while they are kept the same in the 2-direction. Then different hardening rules (isotropic and anisotropic) are used to investigate their effects on the load-deflection relationship. As shown in Figure C.8, for high anisotropy in plastic tangent modulus, there is a big difference on the load-deflection relationship between the results using anisotropic hardening rule and those obtained using isotropic hardening rule. However, if high anisotropy comes from initial yielding, it will not cause any visible difference in the load-deflection relationship as shown in Figure C.9.

C.1.3.4 Laminated cylindrical shell panel under a uniformly-distributed vertical load

This example is also adopted from Owen *et al.* (1983) and is a classical example of the cylindrical shell roof analysed in the literature. The isotropic case was compared with the four anisotropic cases in which one material constant is varied at a time to get material anisotropy.

The cylindrical shell which is subjected to a self-weight loading and the corresponding mesh as shown in Figure C.10 (a). In Owen *et al.*'s results, one quarter shell was discretized by 6 elements and 6 equal layers were taken through the thickness. The material constants and geometric dimensions are shown in Table C.9.

Different finite element meshes and Gauss integration points are used to compute the isotropic case. There is a small difference between the results for the same mesh but different arrangements of Gauss integration points through the thickness, such as 6×1, or 6×2. Therefore, one Gauss integration point is used through the thickness of each layer instead of two to improve the computational efficiency. Then, the different finite element meshes $n \times m$ are used, where the first number "n" is the number of finite elements in the direction of the shell axis, and the second number "m" is the number of finite elements in the circumferential direction. The results of the 2×4 mesh for the whole shell and the 2×2 mesh for a quarter shell are found to be close to the results of Owen *et al.* Therefore, the first mesh is chosen for the analysis.

The relationships between the load and the vertical displacement at point A on the free edge are shown in Figure C.10 (b)-(e). Figure C.10 (b) shows this relationship for the isotropic case, while Figure C.10 (c)-(f) show the relationships for the four following anisotropic cases: $E_1 = 2E_0$; $E_2 = 2E_0$; $\sigma_{01} = 2\sigma_0$; $\sigma_{02} = 2\sigma_0$.

The present results agree with Owen *et al.* (1983)'s very well. In the case of $\sigma_{02} = 2\sigma_0$ in Figure C.10 (f), the mesh 2×2 for a quarter shell is used to approach the problem.

C.1.4 Large Deflection and Elasto-Plastic Analysis

C.1.4.1 Laminated cylindrical shell panel under a uniform vertical load

This example is again adopted from Owen *et al.* (1983). For large deflection and elastic-perfectly plastic case, the 2×2 mesh for a quarter plate is chosen in the analysis. In Figure C.10 (b) and Figure C.11 (a), isotropic and anisotropic results for the case $E_1 = 2E_0$ are compared with Owen *et al.*'s and they agree very well. In Figure C.11 (b), a 2×3 mesh for a quarter shell is used to obtain load-deflection relationship for the anisotropic case $\sigma_{01} = 2\sigma_0$. The present results agree very well with Owen *et al.*'s.

C.2 Eigenvalue Problems

C.2.1 Fundamental Frequencies of Square Orthotropic Plywood Plates

The fundamental frequencies of an orthotropic plate [0] made of plywood for different boundary conditions are shown in Table C.11, where f is the fundamental frequency and D_2 is the bending rigidity in the 2-direction. It is found that these results, which are calculated by using only one element for the whole plate are in good agreement with available analytical results given by Hearmon (1959) and Huffington (1959). Material constants and geometric sizes are given in Table C.10.

C.2.2 Natural Frequencies of Boron/Epoxy Plates

The natural frequencies of [0] and [45] boron/epoxy square plates with fully-clamped boundary conditions are calculated and compared with the results by Whitney (1987). In order to take account of high-frequency and anti-symmetric vibration modes, three meshes, namely, 1×1, 3×3 and 3×6 for the whole plate are considered in the present analysis, where in "n×m", the first number "n" denotes the number of elements along the 0° direction of the laminate, while the second number "m" denotes the number of elements along the 90° direction. More elements are taken along the 90° direction because the plate is more flexible in that direction.

The material constants and geometric sizes are given in Table C.12 and a comparison of natural frequencies with other analytical results and experimental data are provided in Table C.13. It is expected that the results from SENACS will be a little stiffer than the analytical results. Natural frequencies obtained from experiments are always lower than the analytical and numerical ones, because it is difficult to produce fully "clamped" boundary conditions in an experimental set-up.

C.2.3 Simply-Supported Laminated Plate

The natural frequencies for a rectangular [0/90/0] laminated plate are compared with the analytical solution by Ashton *et al.* (1970) and other available finite element solution by Brockman *et al.* (1989) in Table C.14. The plate size is a = 30 cm, b = 10 cm, h = 0.03 cm. The material constants are $\frac{E_L}{E_T} = 25$, $\frac{G_{LT}}{E_T} = 0.5$, $\nu_{LT} = 0.25$, ρ = 0.0001 kg/cm^3, where E_L, E_T, G_{LT}, ν_{LT} denote the elastic modulus in the lamina longitudinal direction and transverse direction, and in-plane shear modulus and Poisson's ratio of the lamina. All four edges are simply-supported.

First, a 1×1 mesh for the whole plate is used to obtain the first two natural frequencies. As expected, present results agree well only for the first mode of natural frequency and a large error occurs in computing the second and higher modes of natural frequencies because the one element representation is not sufficient to capture the higher modes of vibration.

A more refined 4×2 mesh was used for the whole plate. The corresponding results are close to Ashton *et al.*'s and Brockman *et al.*'s. The discrepancies are due to the fact that unlike the

other two analyses transverse shear deformations were not considered in the present formulation. The normalised natural frequencies in Table C.14 are calculated as

$$\overline{\omega} = \omega \frac{b^2}{\pi^2} \sqrt{\frac{\rho h}{D_{22}}}$$

C.3 Transient Problems

C.3.1. Isotropic cylindrical shell roof under time-dependent uniformly-distributed vertical load

Because there are not many examples on transient analysis of composite structures available in the literature for comparison with the present analysis, some examples of isotropic materials are used to verify the present approach.

The transient response of an isotropic cylindrical shell roof subjected to a vertically uniformly-distributed half-sinusoidal impulsive loading are analysed using SENACS and compared with the results of Tsai *et al.* (1991). The geometric sizes and material constants are shown in Table C.15.

First, the response of the shell roof without the inertia force for both small and large deflection cases are calculated and compared with Tsai *et al.* (1991). The present static results agree very well with Tsai *et al.*'s. The finite element mesh used in the present analysis is the same as in Figure C.10 (a).

Then transient analysis is performed for the same shell panel using the same mesh. The first natural frequency of the shell is 1.53 Hz. The time increment in each load step is taken to be 0.02 sec.

A comparison of transient responses is shown in Figure C.12. It seems that they both exhibit the same trends and vibration periods. The small difference in the amplitudes of free vibration can be attributed to the fact that the transverse shear deformations are ignored in the present analysis.

C.3.2 Isotropic cylindrical stiffened shell panel under time-dependent uniformly distributed vertical load

This example is an isotropic stiffened cylindrical shell roof, which is supported by a rigid shear diaphragm at the curved ends and is loaded by a step vertical uniform pressure due to its own dead weight as shown in Figure C.13 (a-b). Its geometric size and material properties are shown in Table C.15. The 3×3 super finite element mesh was used to discretize one

quadrant of the stiffened panel, which involves nine shell and three beam elements. The fundamental frequency of the stiffened shell is 1.95 Hz. A time step of 7 ms taken from Jiang *et al.* (1991) is used in the linear and non-linear transient analysis. The results obtained are compared with the finite strip solution by Jiang *et al.* (1991) and are shown in Figure C.13 (c-d). Figure C.13 (c) shows the linear transient response for vertical displacements at the central point of the shell. In Figure C.13 (d), the time histories of the same vertical displacement using large deflection analysis option are compared. It can be seen that the present results are very close to the finite strip predictions in both cases.

Table C.1 Comparison of normalised stress components and transverse deflection with Table 3.7-6 in Ochoa *et al.* (1992) for a simply-supported square graphite/epoxy plate with a lay-up of [0/90/0] subjected to transverse sinusoidal pressure load.

Approach	SENACS (1×1)	Ochoa (4×4)	Ochoa (12×12)	Pagano Elasticity	CLPT
$\overline{w}(\frac{a}{2},\frac{a}{2})$	0.432	—	—	—	0.435
$\overline{\sigma}_x(\frac{a}{2},\frac{a}{2},\pm\frac{h}{2})$	0.545	0.566	0.542	0.539	0.539
$\overline{\sigma}_y(\frac{a}{2},\frac{a}{2},\pm\frac{h}{6})$	0.181	0.174	0.167	0.181	0.180
$\overline{\tau}_{xy}(0,0,\pm\frac{h}{2})$	0.0230	0.0224	0.0215	0.0213	0.0213

Table C.2 Comparison of normalised stress components and transverse deflection with Table 3.7-8 in Ochoa *et al.* (1992) for a simply-supported rectangular graphite/epoxy plate with a lay-up of [0/90/0] subjected to transverse sinusoidal pressure load.

Approach	SENACS (1×1)	Ochoa (4×4)	Ochoa (12×12)	Pagano Elasticity	CLPT
$\overline{w}(\frac{a}{2},\frac{a}{2})$	0.504	0.507	0.509	0.508	0.503
$\overline{\sigma}_x(\frac{a}{2},\frac{a}{2},\pm\frac{h}{2})$	0.630	0.657	0.628	0.624	0.623
$\overline{\sigma}_y(\frac{a}{2},\frac{a}{2},\pm\frac{h}{6})$	0.0253	0.0259	0.0231	0.0253	0.0252
$\overline{\tau}_{xy}(0,0,\pm\frac{h}{2})$	0.0089	0.0086	0.0084	0.0083	0.0083

Table C.3 Constants of a laminated stiffened cylindrical shell panel subjected to a point load as shown in Figure C.1 (Goswami *et al.*, 1994).

Material properties	skin: $E_1 = 51.6$ GPa, $E_2 = 13.7$ GPa, $G_{12} = 8.61$ GPa, $\nu_{12} = 0.25$ stiffener: $E = 25.85$ GPa, $\nu = 0.36$ (equivalent isotropic properties)
Skin thickness	$h = 10.0$ mm
Lay-up	skin $[45/-45/-45/45]_T$ straight stiffener $[45/30/-45/-30/45/30]_{2T}$ curved stiffener $[-45/45/-45]_{2s}$.
Stiffener size	shape of cross-section: rectangular web thickness: 10.0 mm web height: 60.0 mm No. of stiffeners: 2 straight, one above and the other below; 2 curved, both below the skin.

Table C.4 Static deflection of a laminated stiffened cylindrical shell panel at the loading point as shown in Figure C.1.

Source	Radial displacement (mm)	Tangential displacement (mm)
Venkatesh *et al.* (1983)	2.1100	—
Venkatesh *et al.* (1985)	2.0254	0.4231
Goswami *et al.* (1994)	2.2269	0.4160
SENACS	2.3704	0.3819

Table C.5 Constants of laminated square plates with lay-ups of [0] and [0/90/90/0] under uniform pressure load in large deflection analysis (Ochoa *et al.*, 1992).

[0]	Material Properties: $E_1 = 3\times10^6$ psi, $E_2 = 1.28\times10^6$ psi, $G_{12} = 0.37\times10^6$ psi, $\nu_{12} = 0.32$ Plate Dimensions: $a = b = 12$ in, $h = 0.138$ in
[0/90/90/0]	Material Properties: $E_1 = 1.8282\times10^6$ psi, $E_2 = 1.9315\times10^6$ psi, $G_{12} = 0.3125\times10^6$ psi, $\nu_{12} = 0.2395$ Plate Dimensions: $a = b = 12$ in, $h = 0.096$ in

Table C.6 Constants of a laminated cylindrical shell panel with a lay-up of $[0_4/90_4/0_4]$ subjected to a point load as shown in Figure C.4 (Lee *et al.*, 1993).

Material constants (MPa)	$E_1 = E_2 = 1100$, $\nu_{12} = 0.25$, $G_{12} = 660.0$
Dimensions (m)	$L = 0.254$, $R = 2.54$, $h = 0.0126$, $\phi = 0.1$ rad

Table C.7 Material constants for [0] boron/aluminum plate subjected to uniformly-distributed pressure load (Rahman *et al.*, 1992). Units: GPa.

Elastic	$E_{11} = 210$, $E_{22} = 107$, $\nu_{12} = 0.2$, $G_{12} = 32$
Plastic	$E_{T11} = 203$, $E_{T22} = 24$, $G_{T12} = 1.5$
	$X_0 = 1.21$, $Y_0 = 0.089$, $S_0 = 0.045$

Table C.8 Constants of an orthotropic plate $[0]_8$ subjected to uniformly-distributed pressure load (Owen *et al.*, 1983).

Isotropic (MPa)	Elastic $E_1 = E_2 = 30000.0$, $\nu_{12} = 0.3$, $G_{12} = 11540.0$
	Yield stresses $\sigma_{01} = \sigma_{02} = \sigma_{045} = 30.0$, $\tau_{012} = 17.32$
	Plastic $E_p = 300.0$, $G_p = 100.0$
Anisotropic (MPa)	$\sigma_{01} = 30.0$, $\sigma_{02} = 40.0$, $\sigma_{045} = 35.0$, $\tau_{012} = 20.0$
	the remaining values are the same as for isotropic case
Dimensions (m)	$a = 6.0$, $h = 0.2$

Table C.9 Constants of an orthotropic cylindrical shell panel $[0]_6$ subjected to uniform pressure load as shown in Figure C.10 (a) (Owen *et al.*, 1983).

Isotropic (MPa)	Elastic $E_0 = E_1 = E_2 = 21000$, $\nu_{12} = 0.0$, $G_{12} = 10500$
	Yield Stresses $\sigma_0 = \sigma_{01} = \sigma_{02} = 4.1$, $\tau_{012} = 2.367$
	Plastic $E_p = 0.0$, $G_p = 0.0$
Anisotropic	$E_1 = 2E_0$; $E_2 = 2E_0$; $\sigma_{01} = 2\sigma_0$; $\sigma_{02} = 2\sigma_0$
Size (m)	$L = R = 7.60$, $h = 0.076$, $\phi = 40°$

Table C.10 Properties of [0] plywood plate (Hearmon, 1959).

Material constants	$E_1 = 1870.0$ ksi, $E_2 = 600.0$ ksi, $\nu_{12} = 0.12$
	$G_{12} = 159.0$ ksi, $\rho = 2.52 \times 10^{-4}$ lb s^2 / in^4.
Geometric sizes (in)	$a = 100.0$, $b = 50.0$, $h = 1.0$

Table C.11 Fundamental frequencies for [0] plywood plate under various boundary conditions.

Boundary Condition	Normalised Frequency $\frac{2\pi f a^2}{\sqrt{D_2 / \rho h}}$		
	SENACS	Hearmon (1959)	Huffington (1959)
SCSC	94.55	94.57	94.56
SSSC	68.56	68.53	68.52
SSSS	48.65	48.65	48.65
SFSC	26.06	26.22	26.06
SSFS	20.65	20.70	20.65
SFSF	17.39	17.42	17.39

Table C.12 Constants of a [0] boron/epoxy plate (Whitney, 1987).

Material constants	$E_1 = 31000.0$ ksi, $E_2 = 2700.0$ ksi, $G_{12} = 750.0$ ksi
	$\nu_{12} = 0.28$, $\rho = 0.000192$ lb·s^2/in^4
Geometric sizes (in)	$a = b = 12.0$, $h = 0.0424$

Table C.13 Natural frequencies of [0] and [45] boron/epoxy plates.

Plate	Mode No.		Natural Frequencies (Hz)			
	M	N	SENACS 3×3	SENACS 6×3	Analytical	Experiment
[0]	1	1	130	130	125	107
	2	1	165	165	159	123
	3	1	241	241	232	204
	1	2	343	342	329	233
	2	2	364	363	350	301
	4	1	362	363	343	343
	3	2	413	413	397	360
	4	2	503	505	482	451
	5	1	523	525	490	475
	1	3	665	664	639	555
	2	3	689	681	655	545
[45]	1		110	110	106	92
	2		184	186	178	156
	3		256	254	244	215
	4		270	276	264	239
	5		373	377	359	329

Table C.14 Normalised natural frequencies for a rectangular simply-supported laminated plate with a lay-up of [0/90/0].

Mode	M	N	Exact	Brockman (15×5)	SENACS (4×2)
1	1	1	1.415	1.473	1.569
2	2	1	2.626	2.733	2.774
3	1	2	4.420	4.864	5.623
4	3	1	4.622	5.056	5.269
5	2	2	5.659	6.358	6.249

Table C.15 Constants for the isotropic cylindrical shell panel shown in Figure C.4.

Shell Weight	90 lb/sq.ft.
Elastic Constants	$E = 3.0\times10^6$ psi, $\nu = 0.0$
Geometry Size	$L = 600$ in, $R = 300$ in, $h = 3.0$ in, $\phi = 20^\circ$
Mass Density	$\rho = \frac{W}{hg} = 11.18 lbs^2 ft^{-4}$

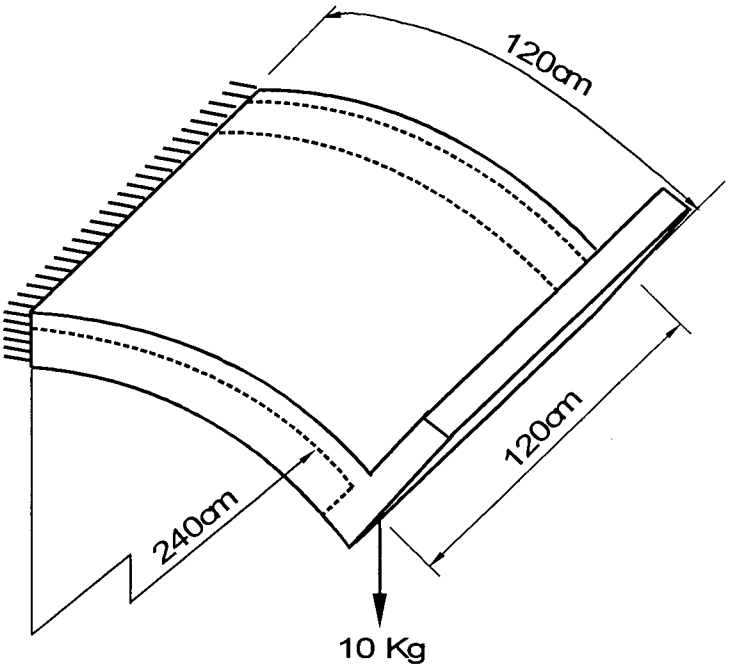

Figure C.1 A cantilever laminated composite cylindrical shell with eccentrically mounted composite stiffeners in axial and circumferential directions (Venkatesh *et al.*, 1983).

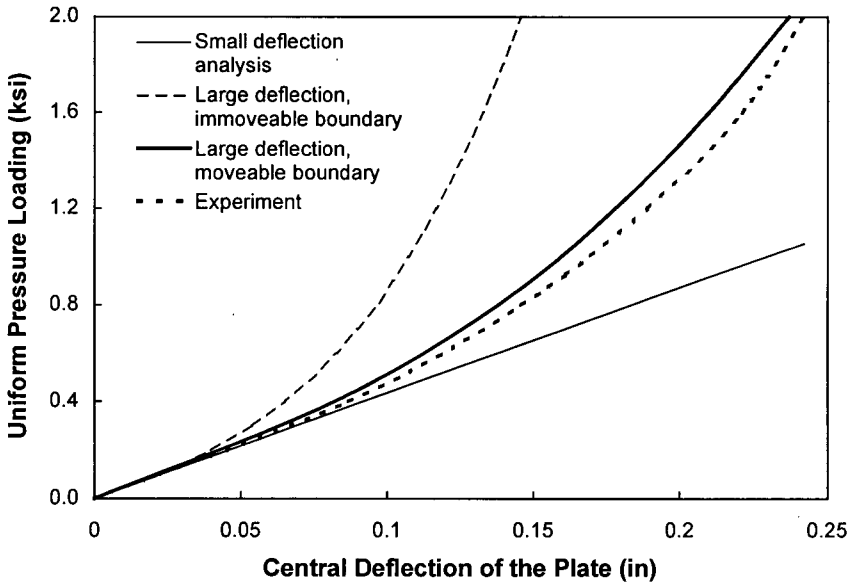

Figure C.2 Comparison of the present relationship of load and deflection with experimental data in Zaghloul *et al.* (1975) for large deflection analysis of a simply-supported plate [0] with in-plane moveable or immoveable boundary conditions.

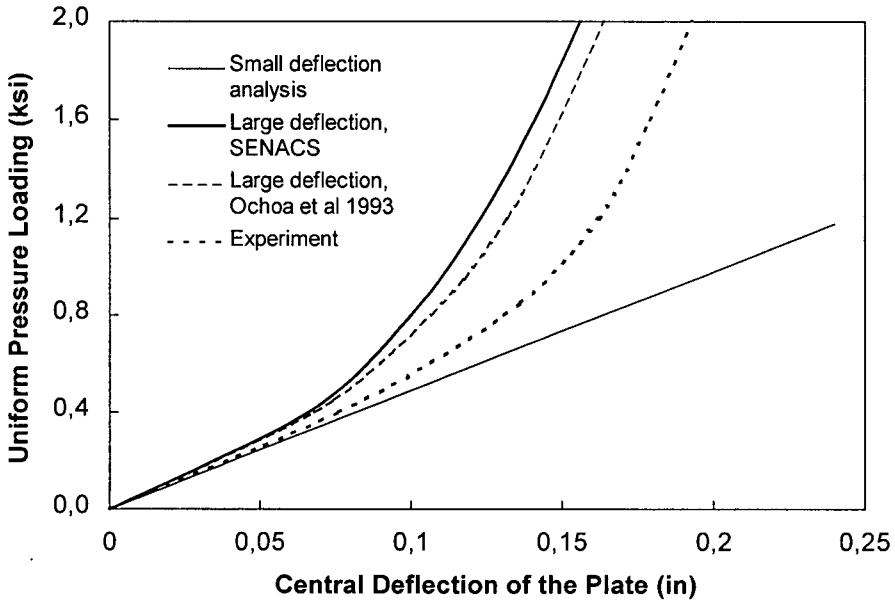

Figure C.3 Comparison of the present relationship of load and deflection with experimental data in Zaghloul *et al.* (1975) and finite element results in Ochoa *et al.* (1992) for large deflection analysis of an fully-clamped plate [0/90/90/0].

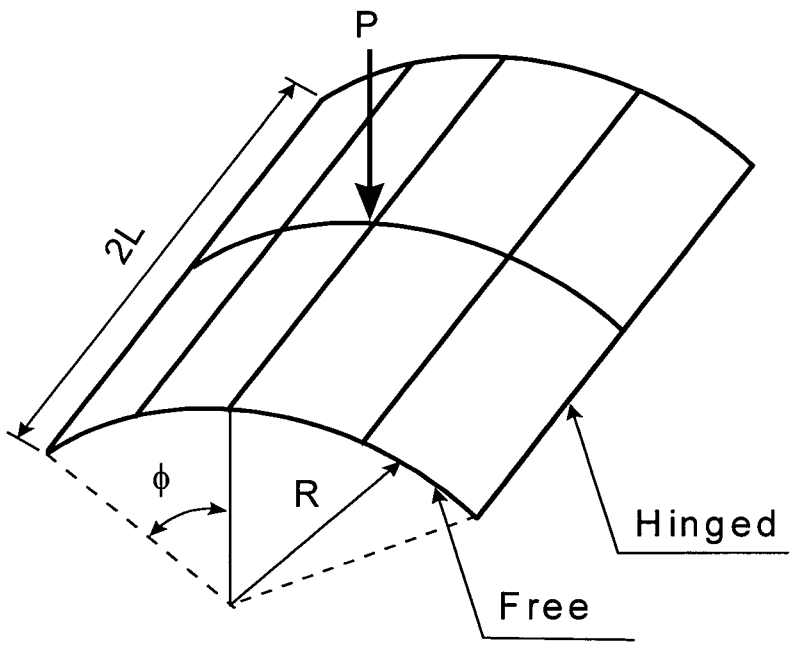

Figure C.4 Schematic illustration of laminated composite cylindrical shell panel with a lay-up of $[0_4/90_4/0_4]$ subjected to a point load (Lee *et al.*, 1993).

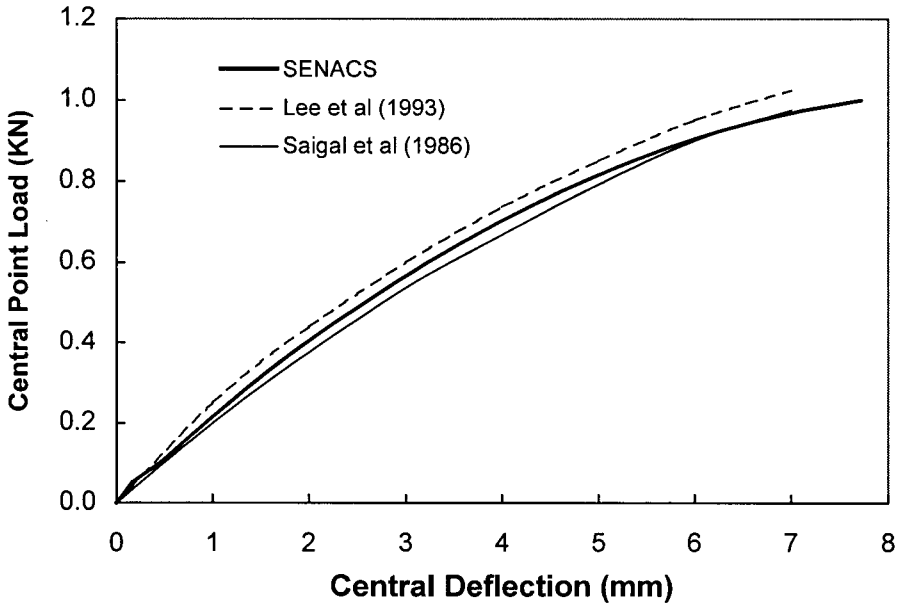

Figure C.5 Comparison of the present results with other finite element results by Lee *et al.*'s (1993) and Saigal *et al.*'s (1986) for linear-elastic material with large deflection analysis of laminated composite cylindrical shell with lay-up of $[0_4/90_4/0_4]$.

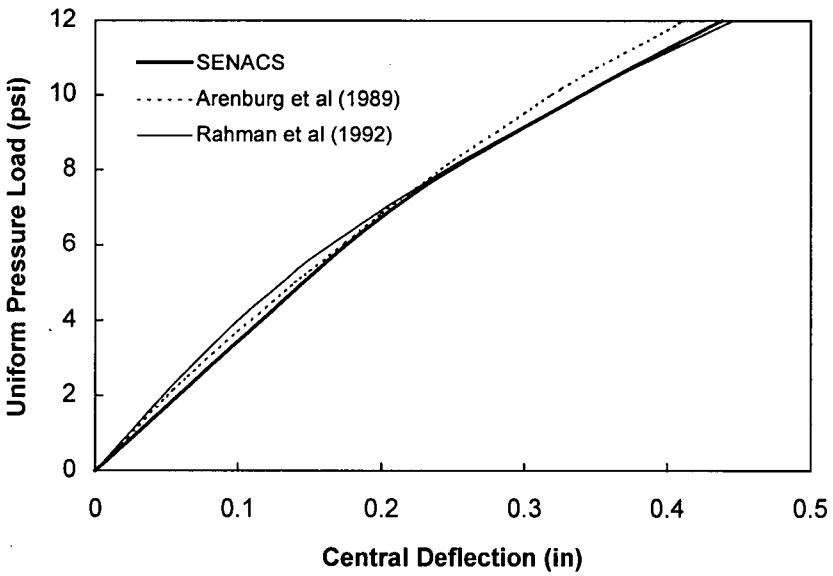

Figure C.6 Comparison of the present results with predictions of micro-mechanics models in Arenburg *et al.* (1989) and Rahman *et al.* (1992) for elasto-plastic material in small deflection analysis.

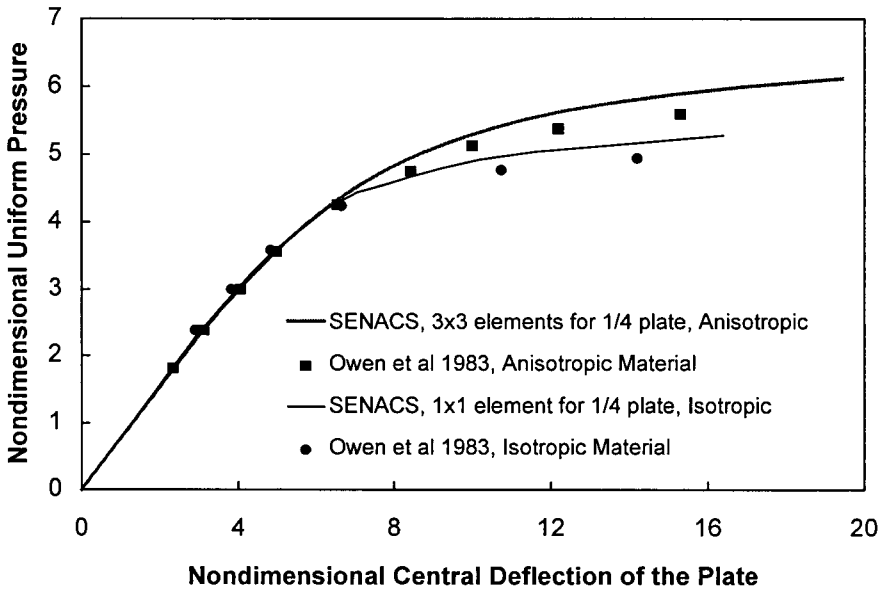

Figure C.7 Comparison of relationship of non-dimensional load vs. non-dimensional deflection between the present analysis and Owen *et al.* (1983) for a fully-clamped laminated square plate $[0_8]$ in isotropic or anisotropic elasto-plastic material and small deflection analysis.

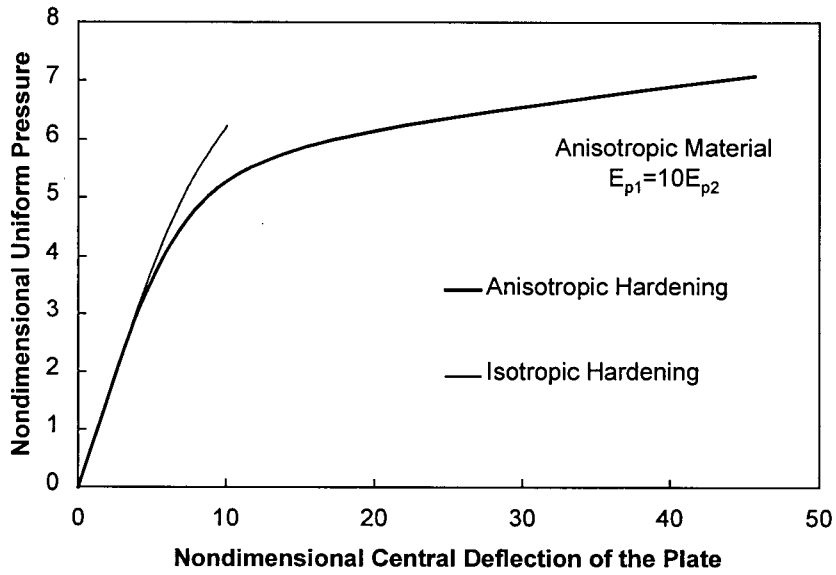

Figure C.8 Comparison of the predicted load-deflection relationships using isotropic and anisotropic hardening rule in the case of high anisotropy in plastic tangent modulus.

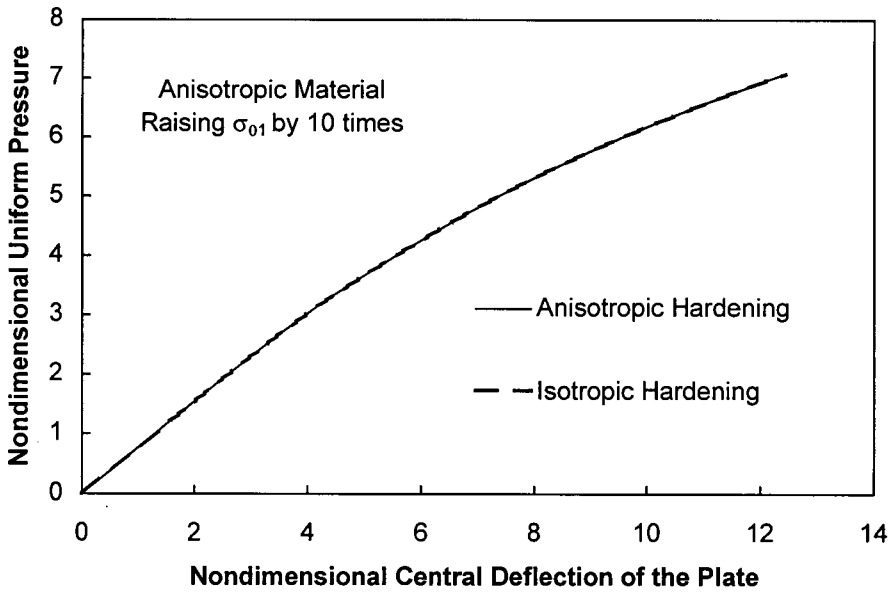

Figure C.9 Comparison of the predicted load-deflection relationships using isotropic and anisotropic hardening rule in the case of high anisotropy in initial yielding stress.

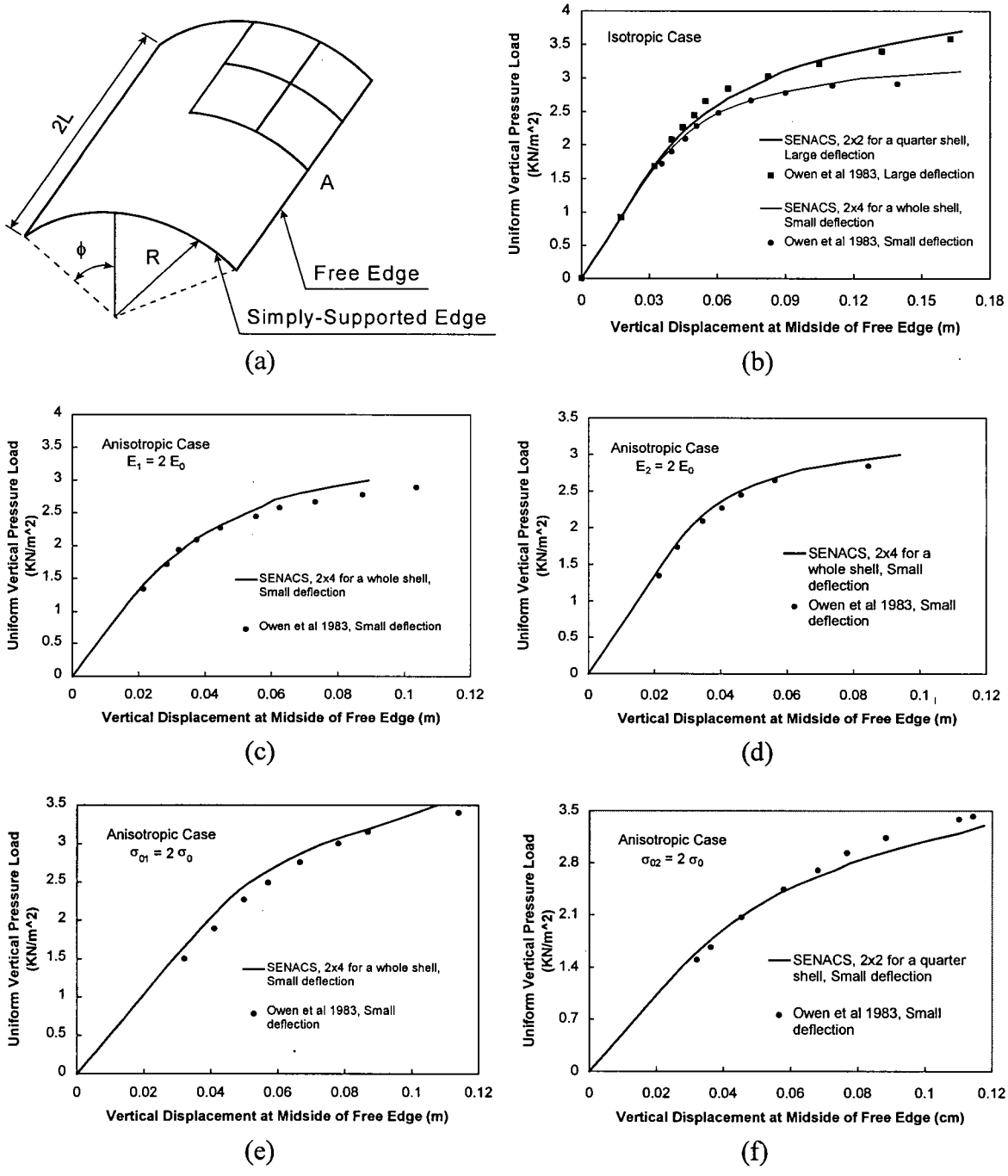

Figure C.10 Comparison of the present results with Owen *et al.* (1983) for laminated cylindrical shell panel $[0_6]$ in elasto-plastic and large deflection analysis. (a). Schematic illustration of cylindrical shell panel. (b-f). Relationship of load vs. downward deflection at midside of free edge for one isotropic and four anisotropic cases of $E_1=2E_0$, $E_2=2E_0$, $\sigma_1=2\sigma_0$, $\sigma_2=2\sigma_0$.

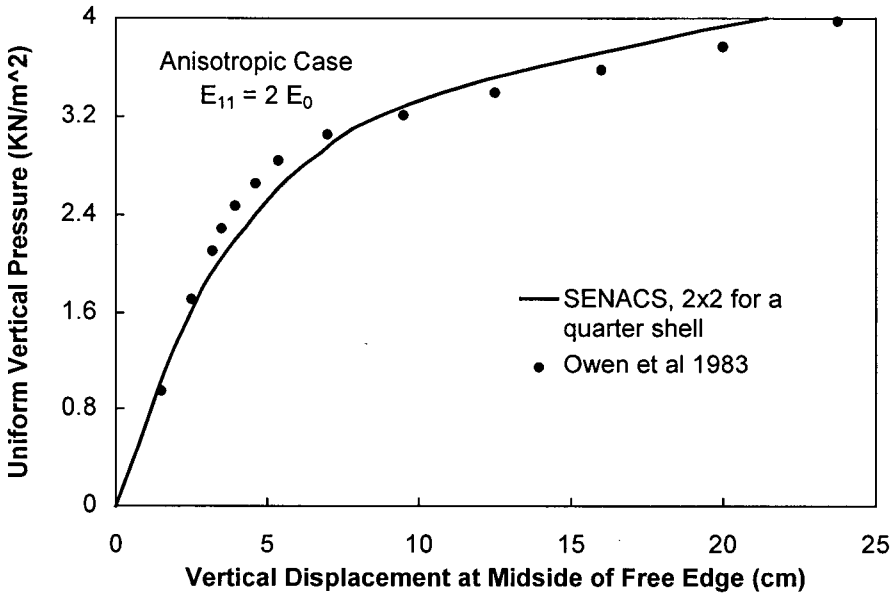

(a)

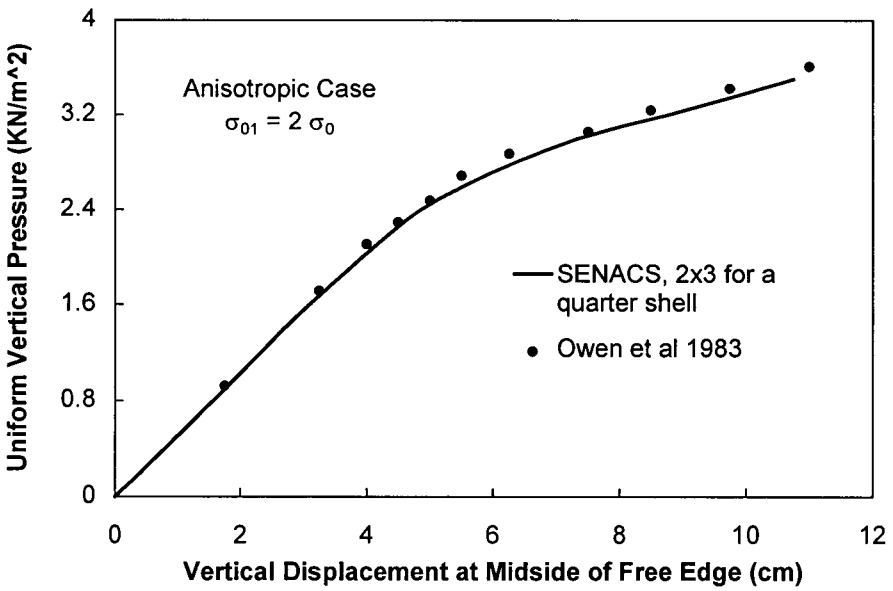

(b)

Figure C.11 Comparison of the present results with Owen *et al.* (1983) for laminated cylindrical shell panel $[0_6]$ in elasto-plastic and large deflection analysis: (a) $E_1=2E_0$, (b) $\sigma_1=2\sigma_0$.

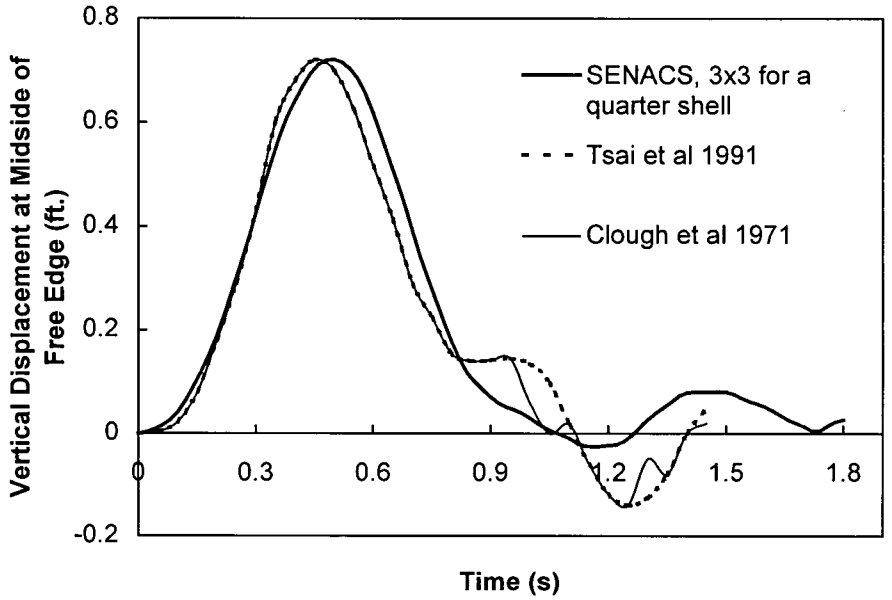

(a)

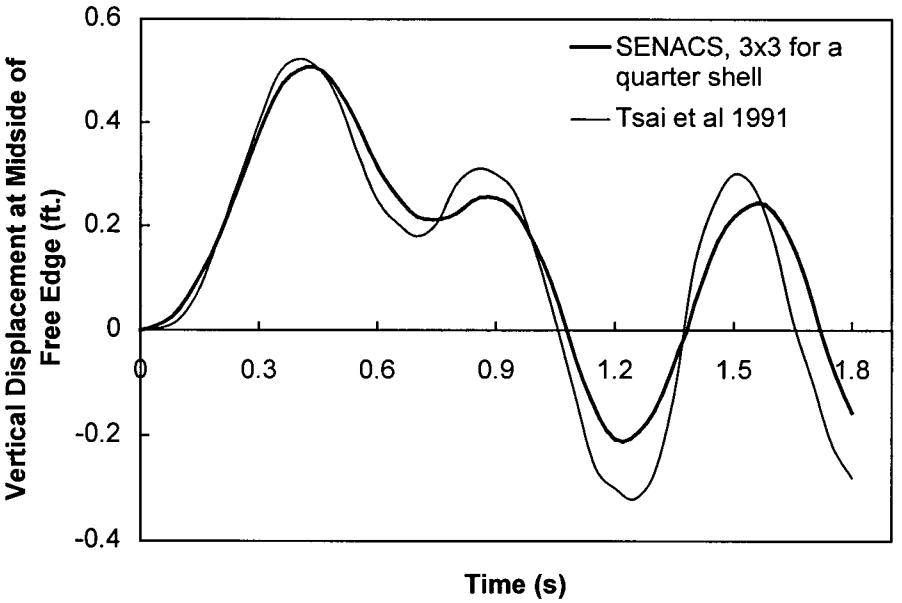

(b)

Figure C.12 Comparison of the present deflection-time history with Tsai *et al.* (1991) for transient response of an isotropic cylindrical shell roof subjected to a uniformly-distributed vertical half-sinusoidal impulsive load in linear-elastic and (a) small deflection and (b) large deflection analyses.

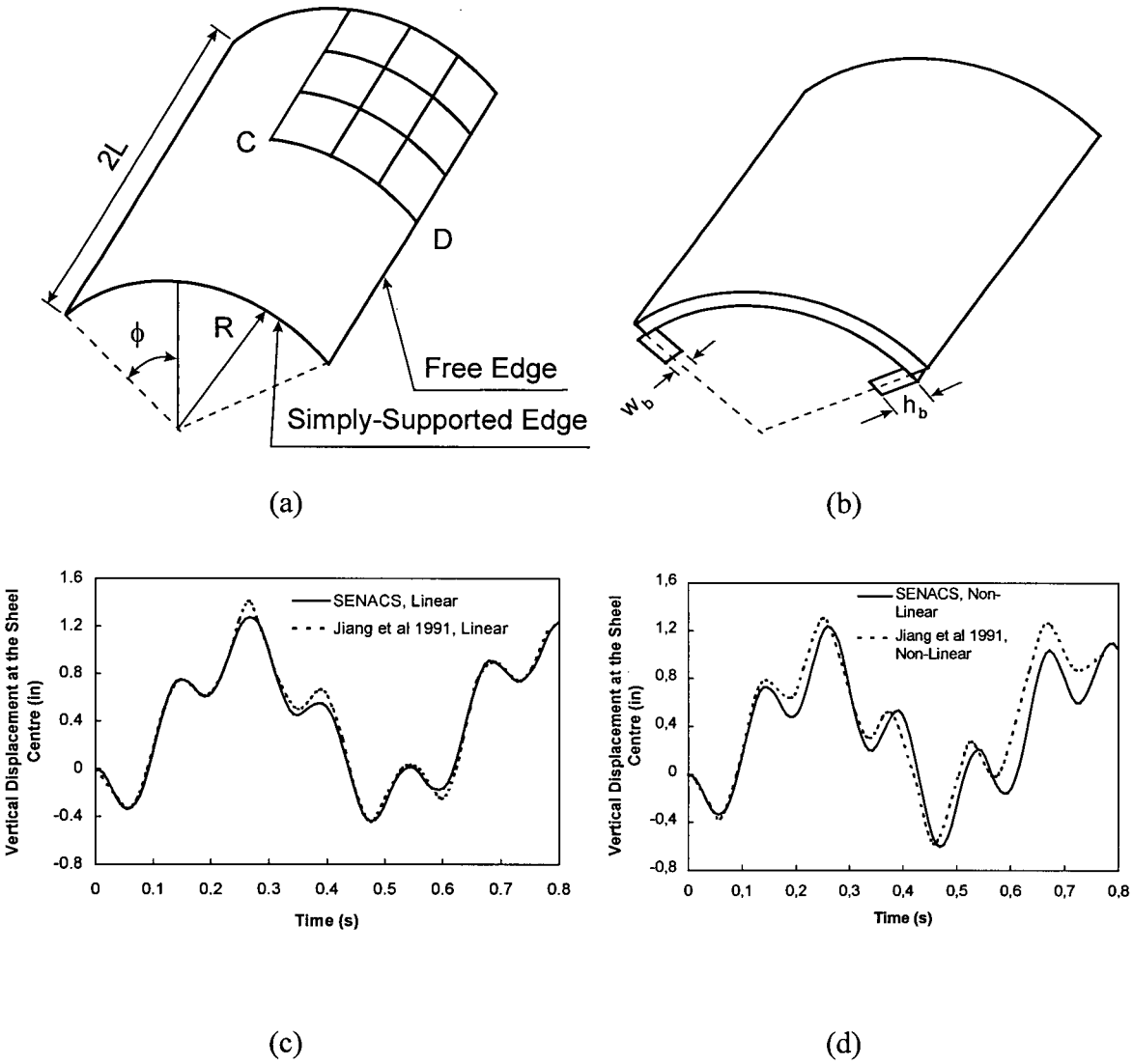

Figure C.13 Comparison of the present results with finite strip analysis by Jiang *et al.* (1991) for transient response of an isotropic stiffened cylindrical shell panel. (a-b) Schematic illustration of the stiffened shell panel. (c) Results in small deflection and linear-elastic analysis. (d) Results in large deflection and linear-elastic analysis.

Appendix D: High Frequency Oscillations in Contact Force-Time Histories

A two degrees of freedom, spring-mass model was proposed by Bucinell *et al.* (1991) to investigate the response of composite plates subjected to transverse impact. The model consists of a projectile and a target plate. The projectile mass is m_1 and the effective mass of the target plate is m_2. The representation of the model is illustrated in Figure D.1.

The first type of displacement was the indentation α, which was associated with the contact spring stiffness k_1 and the natural circular frequency of the contact spring ω_1. The second one is the transverse displacement of the plate, associated with the structural stiffness of the plate k_2 and fundamental circular frequency of the plate ω_2.

By solving the equations of motion of the two-degree-of-freedom system, the natural frequencies of the system can be written as

$$\omega_{I,II}^2 = \frac{(k_1+k_2)m_1 + k_1 m_2 \mp \sqrt{\left[(k_1+k_2)m_1 + k_1 m_2\right]^2 - 4k_1 k_2 m_1 m_2}}{2m_1 m_2} \tag{D.1}$$

where ω_I corresponds to the vibration mode of indentation α, and ω_{II} corresponds to the transverse vibration mode of the plate.

The non-penetrating impact responses of T800H/3900-2 CFRP plates with $[45/90/-45/0]_{3s}$ lay-up using present approach with and without artificial damping are shown in Figure D.2 - Figure D.5. The same results with artificial damping are also shown in the Figures 3.4-3.7.

The periods of high frequency oscillations in the force time history are shown in the graphs. These periods are compared with the periods calculated from ω_{II} in Equation (D.1) and shown in the Table D.1. The fairly agreement between the results indicate that these superposed secondary oscillations on the force-time curves are a reflection of the plate vibration. Any other efforts, such as refining the finite element mesh, using a patch load instead of a point load, or decreasing the time step, does not diminish the high-frequency oscillations. Only introducing artificial damping can decrease their magnitudes or make them disappear.

The energy absorption of the target during the projectile impact can also be estimated from the spring-mass model of Bucinell *et al.* (1991). The solution to the 2DOF spring-mass system is also given in Bucinell *et al.*'s work,

$$\begin{aligned} x_1(t) &= V_s(A_I \sin\omega_I t + A_{II} \sin\omega_{II} t) \\ x_2(t) &= V_s(X_I A_I \sin\omega_I t + X_{II} A_{II} \sin\omega_{II} t) \end{aligned} \tag{D.2}$$

where V_s is the projectile impact velocity, A_I and A_{II} are the amplitudes of the vibration, and X_I and X_{II} are the mode shapes of the system. They can be written as follows

$$A_I = \frac{1}{(1-\frac{X_I}{X_{II}})\omega_I} \tag{D.3-1}$$

$$A_{II} = \frac{1}{(1-\frac{X_{II}}{X_I})\omega_{II}} \tag{D.3-2}$$

$$X_I = (1-\frac{m_1}{k_1})\omega_I^2 \tag{D.4-1}$$

$$X_{II} = (1-\frac{m_1}{k_1})\omega_{II}^2 \tag{D.4-2}$$

The energy absorbed in the global deformation and motion of the target can be written as

$$E_{global} = \frac{1}{2} m_2 \omega_2^2 x_{2max}^2 \tag{D.5}$$

where x_{2max} is the maximum deflection of the target.

Ignoring the energy absorbed by the second mode of vibration, the maximum target deflection can be derived from Equation (D.2), as

$$x_{2\max} = V_s X_I A_I \tag{D.6}$$

Let E_{impact} denote the kinetic energy of the projectile, $E_{impact} = \frac{1}{2} m_1 V_s^2$. The relationship between the ratio of the global energy absorption to the total impact energy, $\frac{E_{global}}{E_{impact}}$, and the frequency ratio of target to contact springs, $\frac{\omega_2}{\omega_1}$, can be calculated using the above equations. The curves shown in Figure D.6 are plotted for different ratios of the projectile to target mass, $M = \frac{m_1}{m_2}$. In the calculation, m_1 and k_1 are kept constant. It can be seen from the graph that the stiffer structures ($\frac{\omega_2}{\omega_1} >> 1$) absorb less impact energy as expected. Also high mass

impact events ($M = \frac{m_1}{m_2} >> 1$) lead to more impact energy being absorbed by the target than low mass impact.

Table D.1 Comparison of periods of high frequency oscillations in impact force time history of T800H/3900-2 CFRP plates.

Projectile Mass (kG)	Projectile Velocity (m/s)	Predicted Oscillation Period (ms)	Bucinell's Oscillation Period (ms)	Error %
6.14	1.76	0.183	0.149	22
6.14	2.68	0.178	0.139	28
0.314	7.70	0.191	0.247	30
0.314	11.85	0.175	0.137	28

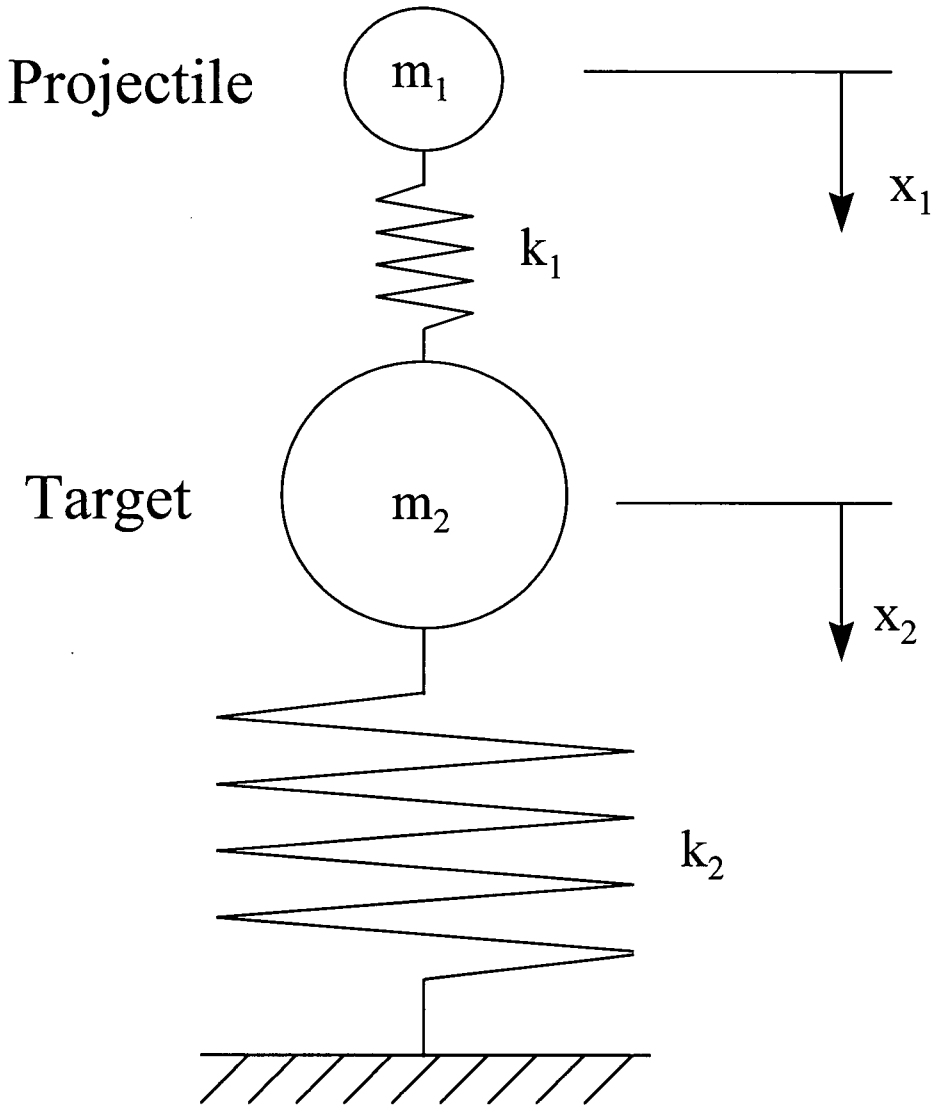

Figure D.1 Two degree of freedom, spring-mass system used in Bucinell *et al.* (1991) to investigate the nonpenetrating impact responses of composite plates.

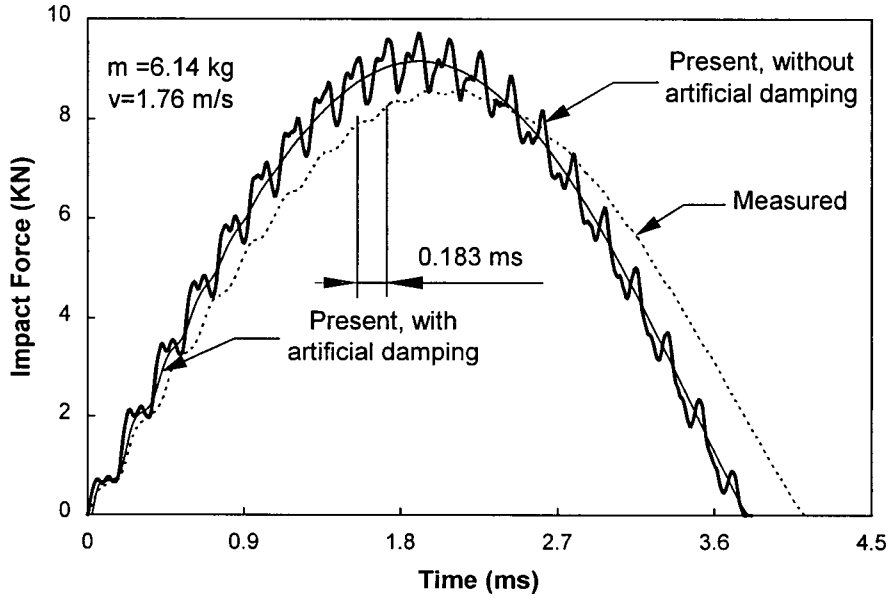

Figure D.2 Contact force history for 6.14 kg, 1.76 m/s impact on the laminate defined in Chapter Three; the predicted results with and without artificial damping are compared with drop-weight test results (Delfosse *et al.*, 1993).

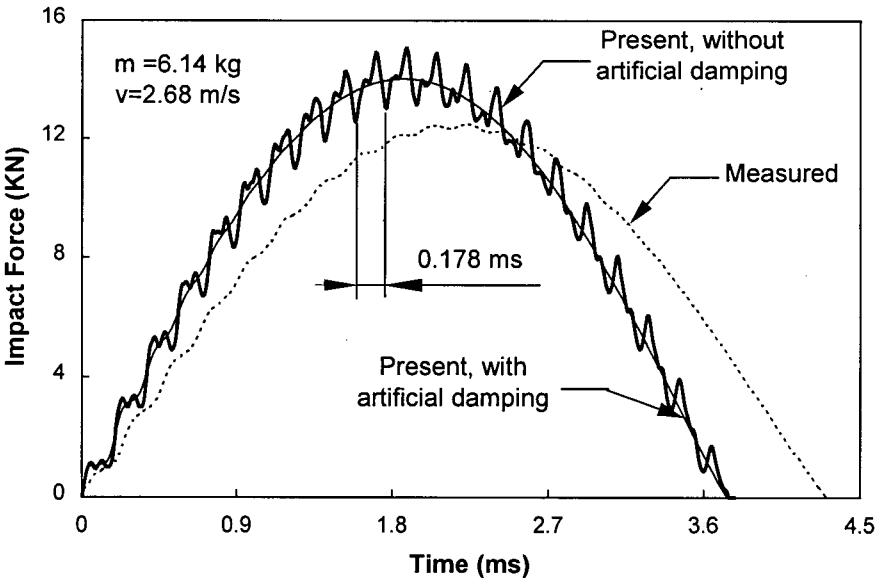

Figure D.3 Contact force history for 6.14 kg, 2.68 m/s impact on the laminate defined in Chapter Three; the predicted results with and without artificial damping are compared with drop-weight test results (Delfosse *et al.*, 1993).

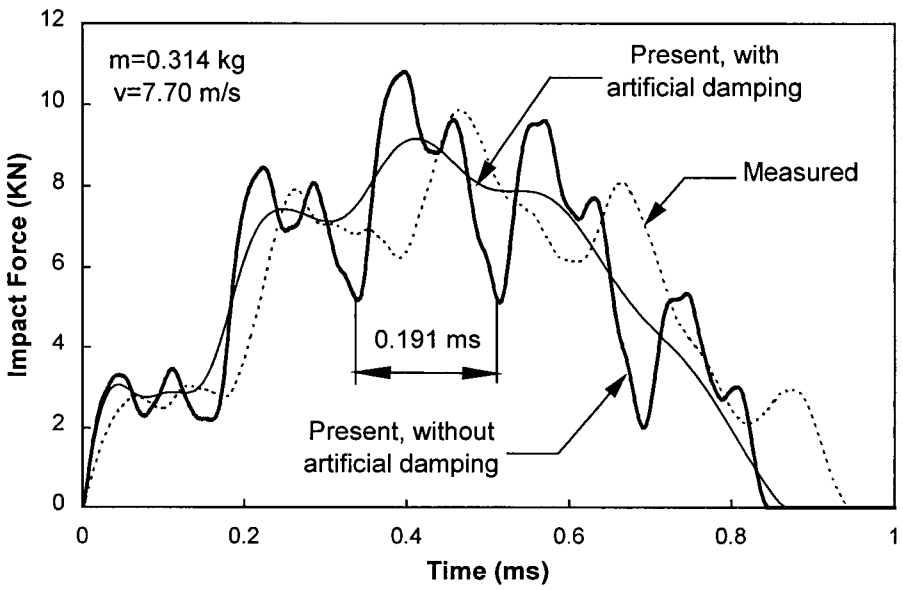

Figure D.4 Contact force history for 0.314 kg, 7.70 m/s impact on the laminate defined in Chapter Three; the predicted results with and without artificial damping are compared with drop-weight test results (Delfosse *et al.*, 1993).

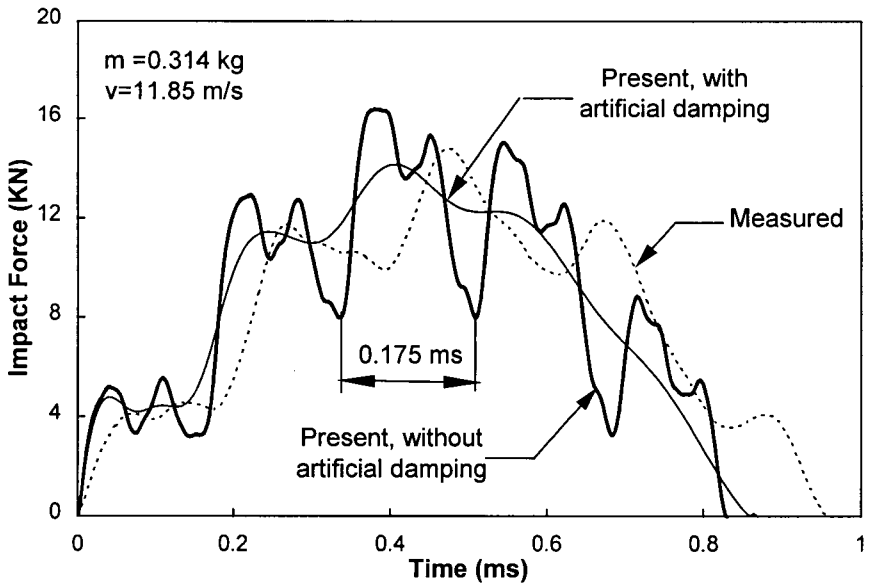

Figure D.5 Contact force history for 0.314 kg, 11.85 m/s impact on the laminate defined in Chapter Three; the predicted results with and without artificial damping are compared with drop-weight test results (Delfosse *et al.*, 1993).

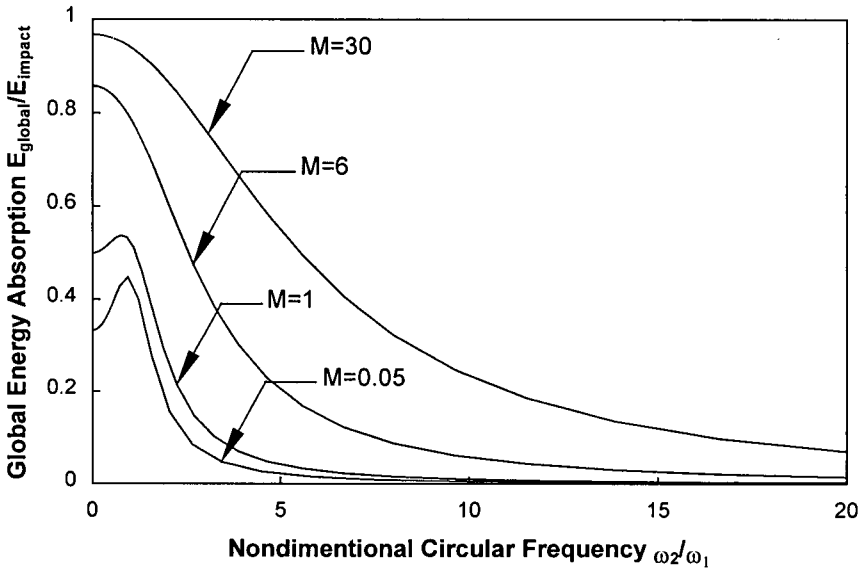

Figure D.6 Predicted relationship between energy absorbed in the deformation and motion of the target and the non-dimensional frequency ratio.

Appendix E: Derivation of Bending Compliance of a Clamped Circular Ring

Consider a circular ring, fully clamped on its boundary, with an inner radius b and outer radius a as shown in Figure E.1. Suppose that there is a transverse uniformly distributed shearing force Q_0 acting along ring's inner edge.

Let Q denote the transverse shearing force at radial distance $r = a$. Then

$$Q = \frac{Q_0 b}{r} = \frac{P}{2\pi r} \tag{E.1}$$

where $P = 2\pi b Q_0$ is the magnitude of the transversal load.

The differential equation of equilibrium of the circular ring according to Timoshenko and Woinowsky-Krieger (1959) is

$$\frac{d}{dr}\left[\frac{1}{r}\frac{d}{dr}\left(r\frac{dw}{dr}\right)\right] = \frac{Q}{D} = \frac{P}{2\pi r D} \tag{E.2}$$

where D is the bending rigidity of the circular ring.

Integrating Equation (E.2),

$$\frac{dw}{dr} = \frac{P}{8\pi D} r\left(2\ln\frac{r}{a} - 1\right) - \frac{C_1}{2} r - \frac{C_2}{r} \tag{E.3a}$$

$$w = \frac{P}{8\pi D} r^2\left(\ln\frac{r}{a} - 1\right) - \frac{C_1}{4} r^2 - C_2 \ln\frac{r}{a} + C_3 \tag{E.3b}$$

$$\frac{d^2 w}{dr^2} = \frac{P}{8\pi D}\left(2\ln\frac{r}{a} + 1\right) - \frac{C_1}{2} + \frac{C_2}{r^2} \tag{E.3c}$$

Applying the boundary conditions of the ring yields

$$w\big|_{r=a} = 0: \qquad C_3 = \frac{P a^2}{8\pi D} + \frac{C_1}{4} a^2 \tag{E.4a}$$

$$\left.\frac{dw}{dr}\right|_{r=a} = 0: \qquad \frac{C_1}{2} + \frac{C_2}{a^2} = -\frac{P}{8\pi D} \tag{E.4b}$$

$$M_r|_{r=b} = -D\left(\frac{d^2w}{dr^2} + \frac{\nu}{r}\frac{dw}{dr}\right)\Bigg|_{r=b} = 0: \quad \left(\frac{d^2w}{dr^2} + \frac{\nu}{r}\frac{dw}{dr}\right)\Bigg|_{r=b} = 0$$

i.e., $$\frac{P}{8\pi D}\left(2\ln\frac{b}{a}+1\right) - \frac{C_1}{2} + \frac{C_2}{b^2} + \nu\frac{P}{8\pi D}\left(2\ln\frac{b}{a}-1\right) - \frac{\nu C_1}{2} - \frac{\nu C_2}{b^2} = 0$$

Rearranging

$$\frac{C_1}{2} - \frac{C_2}{b^2}\frac{1-\nu}{1+\nu} = \frac{P}{4\pi D}\ln\frac{b}{a} + \frac{P}{8\pi D}\frac{1-\nu}{1+\nu} \tag{E.4c}$$

Subtracting Equation (E.4c) from Equation (E.4b), we obtain

$$C_2 = -\frac{Pa^2}{4\pi D}\frac{\ln\frac{b}{a} + \frac{1}{1+\nu}}{1 + \frac{a^2}{b^2}\frac{1-\nu}{1+\nu}} \tag{E.5}$$

Substituting Equation (E.5) into (E.4b), and Equation (E.6) into (E.4a),

$$C_1 = -\frac{P}{4\pi D} + \frac{P}{2\pi D}\frac{\ln\frac{b}{a} + \frac{1}{1+\nu}}{1 + \frac{a^2}{b^2}\frac{1-\nu}{1+\nu}} \tag{E.6}$$

$$C_3 = \frac{Pa^2}{16\pi D} + \frac{Pa^2}{8\pi D}\frac{\ln\frac{b}{a} + \frac{1}{1+\nu}}{1 + \frac{a^2}{b^2}\frac{1-\nu}{1+\nu}} \tag{E.7}$$

Substituting Equations (E.5-7) into (E.3b),

$$w = \frac{P}{8\pi D}r^2\left(\ln\frac{r}{a} - 1\right) + \frac{P}{16\pi D}(r^2 + a^2) - \frac{P}{8\pi D}\frac{\ln\frac{b}{a} + \frac{1}{1+\nu}}{1 + \frac{a^2}{b^2}\frac{1-\nu}{1+\nu}}(r^2 - a^2) \tag{E.8}$$

$$+\frac{Pa^2}{4\pi D}\frac{\ln\frac{b}{a}+\frac{1}{1+\nu}}{1+\frac{a^2}{b^2}\frac{1-\nu}{1+\nu}}\ln\frac{r}{a}$$

The flexural deflection at the inner edge of the ring is

$$w|_{r=b}=\frac{Pb^2}{8\pi D}(\ln\frac{b}{a}-1)+\frac{P}{16\pi D}(b^2+a^2)-\frac{P}{8\pi D}\frac{\ln\frac{b}{a}+\frac{1}{1+\nu}}{1+\frac{a^2}{b^2}\frac{1-\nu}{1+\nu}}(b^2-a^2)+\frac{Pa^2}{4\pi D}\frac{\ln\frac{b}{a}+\frac{1}{1+\nu}}{1+\frac{a^2}{b^2}\frac{1-\nu}{1+\nu}}\ln\frac{b}{a}$$

Therefore, the bending compliance of the circular ring is

$$f=\frac{b^2}{8\pi D}(\ln\frac{b}{a}-1)+\frac{1}{16\pi D}(b^2+a^2)-\frac{1}{8\pi D}\frac{\ln\frac{b}{a}+\frac{1}{1+\nu}}{1+\frac{a^2}{b^2}\frac{1-\nu}{1+\nu}}(b^2-a^2-2a^2\ln\frac{b}{a}) \qquad \text{(E.9)}$$

where $D=\frac{Eh^3}{12(1-\nu^2)}$. E is the elastic modulus, and h is the ring thickness.

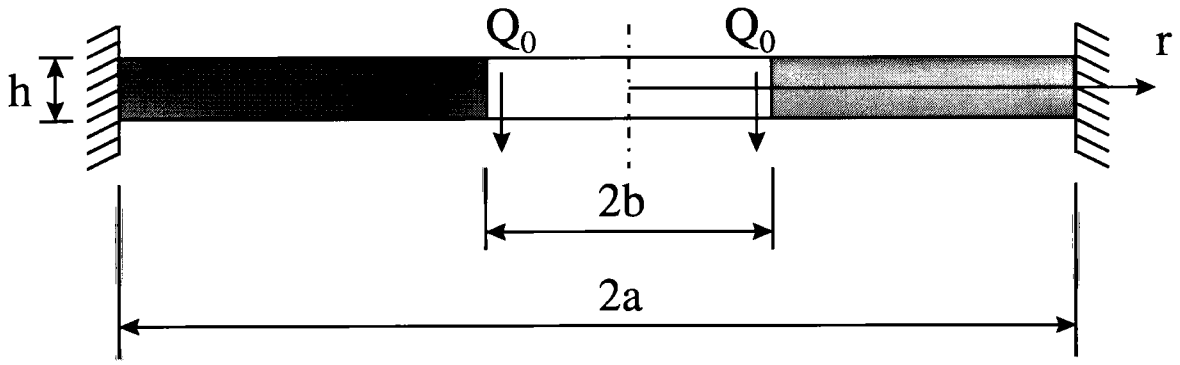

Figure E.1 Illustration of a circular ring fully clamped along its outer edge. A transverse uniformly distributed shearing force Q_0 acts along the inner edge.